DNA Methylation Dynamics and Epigenetic Diversity in Development

THE UNIVERSITY OF EDINBURGH

Nur Annies Binti Abd Hadi

Thesis submitted for the degree of
Doctor of Philosophy
2017

Declaration of Originality

I hereby declare that, this thesis and the research work reported herein was composed and originated entirely by myself except where specifically indicated.

Nur Annies Binti Abd Hadi

April 2017

Abstract

Epigenetics refers to heritable changes in phenotype without alterations to the genotype. Epigenetic changes involve two main mechanisms: DNA methylation and histone modification. Methylation of DNA at cytosine bases is the best-studied epigenetic process to date. CpG methylation states are thought to be maintained throughout cell divisions. However, loss of DNA methylation or DNA demethylation has been observed in specific stages of mammalian development. Such prominent examples of developmental DNA demethylation processes occur in developing primordial germ cells and in preimplantation embryos. However, little is known about DNA methylation changes of other tissues in mammalian development. Therefore, the first aim of this PhD study was to investigate changing nuclear distributions and levels of DNA methylation during development in order to discover dynamic variations amongst developing mouse tissues. In addition, a transgenic MBD-GFP mouse was employed to visualise DNA methylation in tissues.

Several hypothetical mechanisms for the enzymatic removal of 5mC have been proposed. One of the proposed candidates is Tet-mediated successive oxidation of 5mC to generate 5hmC, 5fC and 5caC. 5hmC has therefore been considered as a transient intermediate in an active cytosine demethylation pathway. Nevertheless, some studies suggest that 5hmC may also function as an epigenetic modification in its own right. Thus, the second aim of this study was to address the research question of how and where 5hmC originates during development.

In order to be able to identify tissues undergoing dynamic nuclear changes in DNA methylation and hydroxymethylation states during early mouse development, new working protocols for immunodetection of 5mC and 5hmC on tissue cryosections were required. The protocol optimisation for 5mC immunodetection is discussed in greater detail in Chapter 3. It was found that DNA methylation immunostaining of cryosections required heat-mediated DNA denaturation, which was partly compatible with protein immunostaining.

Next, Chapter 4 focuses on identifying tissues undergoing dynamic changes in 5mC and 5hmC patterns during development from E9.5 to E14.5 mouse embryonic stages, using optimised immunohistochemistry protocols. These protocols revealed interesting dynamic observations of 5mC and 5hmC in the developing cerebral neocortex, surface ectoderm, liver, red blood cells, diaphragm and heart. These findings suggested that dynamic changes of 5mC and 5hmC during neocortical and compact myocardial development were in good agreement with a model where the formation of 5hmC may correlate with the loss of old 5mC, but the observations were also consistent with an involvement of *de novo* methylation in the generation of 5hmC. In other developing tissues, including surface ectoderm, liver, red blood cells, diaphragm and cardiac trabeculae, dynamic changes in 5mC and 5hmC levels were in line with a model where the 5hmC may act as a new epigenetic mark that functions independently. The optimised protocol also confirmed DNA demethylation of the germ cells at E12.5. The presence of three Tet family enzymes (Tet1, Tet2, Tet3) and *de novo* methyltransferase DNMT3A in mouse E12.5 tissues is reported in the second part of Chapter 4. It was found that Tet1, Tet2, Tet3 and Dnmt3a were present at detectable levels in neocortex, liver, diaphragm and heart. Contrastingly, no apparent signals for Tet1, Tet2, Tet3 and Dnmt3a were observed in red blood cells. This result was expected due to the very low levels of 5hmC staining in E12.5 red blood cells.

The third aim of the present study was to investigate the existence of crosstalk between various epigenetic mechanisms. Thus, Chapter 5 focuses on exploring the relationship between 5mC and repressive histone marks, H3K9me3 and H3K27me3. Histone methylation dynamics at H3K9 and H3K27 were observed during mouse fetal development in neocortex and heart. The overall distribution patterns of H3K9me3 and H3K27me3 demonstrated strong association with developmental changes in 5mC, suggesting that these three repressive epigenetic marks work in concert to establish a silenced state of heterochromatin.

Chapter 6, on the other hand, focuses on visualising DNA methylation in tissues using mouse transgenic tools. It was found that brain, liver, heart and neural tube expressed high levels of GFP. But no apparent developmental dynamics of GFP was observed.

In conclusion, this study will contribute scientific understanding of dynamic DNA methylation and nuclear heterochromatin organisation during mammalian development, and its role in the specification and maintenance of cell lineages forming tissues and organs. This knowledge will provide insight into current barriers to cell fate reprogramming, which will be of benefit to cell regenerative biomedical technologies.

Lay Summary

Well known examples of epigenetic DNA demethylation processes occur in early mammalian development; nonetheless, little is known about the DNA methylation dynamics of other developing tissues. It is important to discover DNA methylation changes in other mammalian tissues and investigate whether the role of 5hmC is as an intermediate product of cytosine demethylation or as a stable epigenetic modification that functions independently. Furthermore, recent studies reported that DNA methylation and histone modifications appear to be associated with one another. It was therefore important to investigate the relationship between DNA methylation and histone modifications.

Optimised immunohistochemistry protocols revealed new observations of DNA methylation dynamics at 5mC and 5hmC during mouse embryo development in brain neocortex, surface ectoderm, liver, red blood cells, diaphragm and heart. Moreover, the results suggested that the generation of 5hmC may correlate with the loss of old 5mC, but the observations were also consistent with an involvement of *de novo* methylation in the formation of 5hmC. Some results were in agreement with the model where 5hmC may possess independent functions. Furthermore, this study also discovered a strong correlation between 5mC and histone methylation at H3K9 and H3K27.

Together, this study provides advanced scientific understanding of the nuclear epigenetic dynamics during development, which is of relevance to cell reprogramming for regenerative medicine.

Acknowledgements

Undertaking this PhD has been a very exciting and challenging experience for me and it would not have been possible without the constant advice and support that I received from many people. I would like to take this opportunity to convey my sincere appreciation to those who have helped and supported me towards the successful completion of my PhD study.

First and foremost, my deepest gratitude goes to my supervisor, Dr. Sari Pennings, who has been a tremendous mentor for me. I would like to thank you for giving me the opportunity to broaden my skill and expand my knowledge in the evolving field of epigenetics. I would not be where I am today without your priceless support, help and guidance. Thank you very much indeed for your valuable suggestions, insightful criticisms, boundless patience and endless encouragement throughout the entire period of my PhD study. The profound and invaluable knowledge that I gained from you will benefit me in my future career. I could not have imagined having a better advisor for my PhD study.

With profound respect, I would like to express my gratitude to my co-advisor, Professor Richard Meehan. Your brilliant comments, suggestions, ideas and insights are very much appreciated. I am pleased to have you as my co-advisor. I also wish to express my appreciation towards Dr. Ian Adams, Chairman of my PhD committee, for fruitful discussions, wise advice and helpful feedback.

I would like to take this opportunity to sincerely thank Dr. Tatiana Chebotareva, who has provided me with a wide range of skills and knowledge during my research work. I also wish to address special thanks to my lovely colleague, Dr. Cristina Aguilar, who has been very helpful and kind to me. Your friendly assistance and warm encouragement have meant so much for me.

Furthermore, I would like to gratefully acknowledge and deeply appreciate the funding and support received towards my PhD from Majlis Amanah Rakyat (MARA). I also thank the University of Edinburgh for providing me with excellent facilities and administrative supports during my study.

To my dear husband, Dr. Wan Fahmi, there are not enough words to describe how grateful I am to be able to share the journey full of ups and downs with you. Thanks for patiently walking beside me through all sorts of difficulties, challenges and sacrifices. Your unconditional love, encouraging words and sense of humour have lifted me up and given me strength and confidence. This accomplishment would not have been possible without you.

Finally, I must express my special thanks to my family for providing me with constant support and motivation. I am forever grateful and indebted to my father, Abd Hadi, and my mother, Mazinah, for their indefinite love, patience, advice, endless prayers and help. To my sisters, Nur Ziehan and Nur Azureen, thank you for all your support and best wishes. I would also like to extend heartfelt appreciation to my father-in-law, Wan Mohamad Nazarie, and my mother-in-law, Norsina, for their understanding, endless patience, words of encouragement and prayers.

Table of Contents

List of Figures

Chapter 1

Chapter 2

Chapter 3

Chapter 4

Chapter 5

Chapter 6

List of Tables

Chapter 2

Chapter 3

List of Acronyms and Abbreviations

2OG	2-oxoglutarate
α-KG	α-ketoglutarate
ATP	adenosine triphosphate
BER	base excision repair
bp	base pairs
CAF	chromatin assembly factor
CGIs	CpG islands
CO_2	carbon dioxide
CpG	cytosine-phosphate-guanine
DAPI	4′,6-Diamidino-2-phenylindole dihydrochloride
DNA	deoxyribonucleic acid
DNMTs	DNA methyltransferases
EZH2	enhancer of zeste homolog 2
$Fe2^+$	ferrous ion
FITC	fluorescein isothiocyanate
GFP	green fluorescent protein
GMO	genetically modified organism
H3K4me3	trimethylation of lysine 4 at histone H3
H3K9me1	monomethylation of lysine 9 at histone H3
H3K9me3	trimethylation of lysine 9 at histone H3
H3K27me3	trimethylation of lysine 27 at histone H3
HATs	histone acetyltransferases
HCl	hydrochloric acid
HDACs	histone deacetylases
HMTs	histone methyltransferases
HP1	heterochromatin protein 1
KDMs	lysine demethylases
KMTs	histone lysine methyltransferases
MBD	methyl-CpG binding domain

MBPs	methyl-CpG binding proteins
me0	unmethylated
me1	monomethylated
me2	dimethylated
me3	trimethylated
mRNA	messenger ribonucleic acid
O_2	Oxygen
PGCs	primordial germ cells
PRC2	polycomb repressive complex 2
PTMs	post-translational modifications
RNA	ribonucleic acid
SAH	S-adenosyl-L-homocysteine
SAM	S-adenosyl-L-methionine
SET	suppressor of variegation, enhancer of zeste and trithorax
SETDB1	SET domain, bifurcated 1
SMUG1	single-strand-selective monofunctional uracil DNA glycosylase 1
ssDNA	single-stranded DNA
TDG	thymine-DNA glycosylase
Tet	ten-eleven translocation
TRITC	tetramethyl rhodamine isothiocyanate
trxG	trithorax group
5caC	5-carboxylcytosine
5fC	5-formylcytosine
5hmC	5-hydroxymethylcytosine
5hmU	5-hydroxymethyluracil
5mC	5-methylcytosine
Xi	X chromosome inactivation

List of Publications

In this study

Nathalie Beaujean, Juliette Salvaing, **Nur Annies Abd Hadi** and Sari Pennings. Antibody based detection of global nuclear DNA methylation in cells, tissue sections and mammalian embryos. (2017). *Methods in Molecular Biology Springer* (in press).

Conference poster

Nur Annies Abd Hadi, Richard Meehan, Sari Pennings. 5mC & 5hmC DNA methylation dynamics in developing mouse embryonic heart and liver. Centre for Cardiovascular Science Symposium, Edinburgh, UK. June 2016

Nur Annies Abd Hadi, Richard Meehan, Sari Pennings. 5mC & 5hmC DNA modification dynamics in developing mouse tissues. 4th Munich Chromatin Symposium, Munich, Germany. March 2016

Nur Annies Abd Hadi, Richard Meehan, Sari Pennings. Optimised immunostaining for studying DNA methylation dynamics and epigenetic diversity in development. Wellcome Trust Waddington Symposium, Edinburgh, UK. June 2015

Previous study

Nur Annies Abd Hadi, Siti Nor Akmar Abdullah, Azzreena Mohamad Azzeme, Ahmed Al-Shanfari, Halimi Mohd Saud. Effects of over-expressing ethylene responsive transcription factor on expression of selected fruit ripening-related genes in oil palm (*Elaeis guineensis* Jacq.) mesocarp. (2015). *Pertanika Journal of Tropical Agricultural Science.* 38(143-159)

Chapter 1 - Introduction

1.1 What is epigenetics?

Transcription, translation and subsequent protein modification are processes by which the information coded in a strand of deoxyribonucleic acid (DNA) is expressed into a new molecule of messenger ribonucleic acid (mRNA) for production of protein. Although all cells in an organism have identical genetic instructions, cell types and functions vary due to qualitative and quantitative differences in their gene expression, and control of gene expression is therefore important for differentiation and development (Meehan et al., 2005). During development, the patterns of gene expression that characterise differentiated cells are established and maintained as the cells divide by mitosis. Thus, in addition to inheriting genetic information, cells inherit and propagate functionally relevant expression instructions to the genome that do not involve a change in the nucleotide sequence, and this has been termed epigenetic information (Gilbert, 2012; Waddington, 1942). Epigenetics is now considered a vital mechanism for controlling gene expression in a potentially heritable way (Portela and Esteller, 2010).

The Greek prefix ‘epi-’ in epigenetics means ‘on top of’ or ‘in addition to’ genetics. So, the term ‘Epigenetics’ refers to an additional layer of information coded ‘on top of’ the organism’s underlying DNA sequence (Nightingale, 2015). The term epigenetics was coined by the British developmental biologist Conrad H. Waddington in 1942. He defined epigenetics as “the branch of biology that studies the causal interactions between genes and their products which bring the phenotype into being” (Deans and Maggert, 2015; Waddington, 1942). In 1957, Waddington developed the idea of epigenetic landscape **(Figure 1.1)** to illustrate cellular decision-making through the processes of development (Noble, 2015; Waddington, 1957). Today, epigenetics is widely known as “the study of changes in gene function that are mitotically and/or meiotically heritable and that do not entail a change in DNA sequence” (Meloni, 2016). In other words, epigenetics basically refers to any process that alters gene expression without affecting the original base sequence (Bonasio et al., 2010).

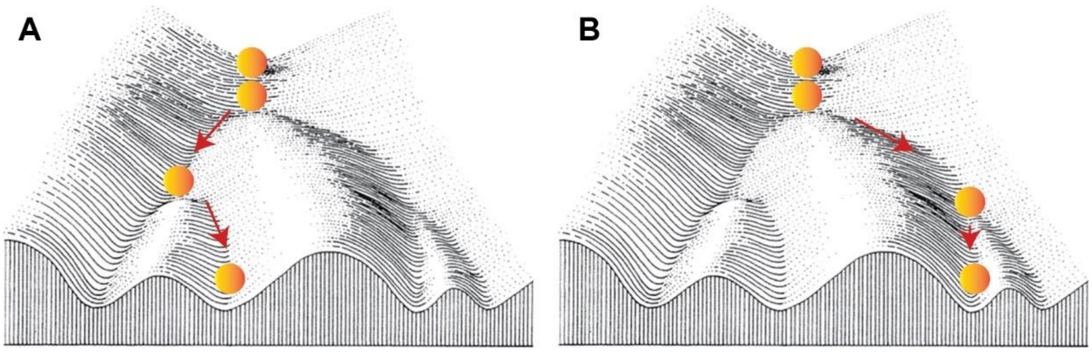

Figure 1.1: Waddington's epigenetic landscape. The landscape of dividing valleys and the cell (represented by a ball) at the top of the hill are from his initial drawing. The images of the cell rolling down the epigenetic landscape have been added to explain that the cell makes different choices by taking only one of several possible valleys **(A or B)**, leading to different cell fates. Figure redrawn from Noble (2015).

1.1.1 Chromatin

To understand the phenomenon of epigenetics requires an understanding of the chromatin structure and organisation as is foundations. Chromatin is the conformational state in which DNA is packed tightly inside the nucleus of every cell (Margueron and Reinberg, 2010). Chromatin is the complex of DNA, protein, and RNA that constitutes chromosomes, and is organised into small repeat units known as nucleosomes (Flaus and Owen-Hughes, 2017; Westhorpe and Straight, 2015). In a nucleosome, 147 base pairs (bp) of DNA are wrapped around an octamer of histone proteins which is composed of two copies of each of the four core histone proteins H2A, H2B, H3, and H4 (Pastore, 2017; Tessarz and Kouzarides, 2014). Each of the core histones, in addition to their globular C-terminal domain, also contain an unstructured, flexible, highly conserved N-terminal domain which is described as the histone 'tail'. A distinct feature of the core histones, especially their protruding N-terminal tails, is the large number and type of covalently modified residues they can possess (McGinty and Tan, 2015).

In addition to the four core histones, there is another type of histone called linker histone, also known as histone H1 (Hergeth and Schneider, 2015). The linker histone H1 plays pivotal roles in various cellular functions, including condensation of chromatin, regulation of transcription, nucleosome spacing and chromosome spacing (Kalashnikova et al., 2016). Furthermore, histone H1 can interact with linker DNA between nucleosomes and promotes compaction of chromatin by coiling nucleosomes from the smaller “beads-on-a-string” fibres of approximately 10-11 nm into higher-order chromatin structures known as the 30 nm chromatin fibres (Gross et al., 2015; Harshman et al., 2013).

The dynamics of 30 nm higher-order chromatin fibres are key regulators of transcription as well as other biological processes involving DNA (Li and Reinberg, 2011). Altering higher-order chromatin structures through the control of DNA-binding proteins and/or complexes is essential in order to gain access to the DNA for transcription, DNA repair, and DNA replication (Bell et al., 2011). A number of factors, including DNA methylation, histone modifications, histone variants and architectural proteins have now been well recognised for their important function in the modulation of higher-order chromatin structure that carries epigenetically inherited information (Kaufman and Rando, 2010; Li and Reinberg, 2011).

As the chromatin structure may be transmissible from mother to daughter cells through mitotic division, chromatin modifications can serve as major carriers of epigenetic information that influence the expression of the underlying genes (Bintu et al., 2016; Budhavarapu et al., 2013). The epigenetic marking of chromatin is required to define each cell's identity during development, in which cells develop different identities despite the fact that they are genetically similar (Cantone and Fisher, 2013). The unique property of DNA and histones, specifically their ability to recruit epigenetic modifications, allows chromatin to assimilate cellular ‘memory’ (D’Urso and Brickner, 2014) and cellular plasticity (Duncan et al., 2014; Liu et al., 2016b; Rajagopal and Stanger, 2016). Epigenetic regulation involving covalent modification of DNA and histone proteins, may add a further layer of regulatory complexity to the chromatin (Soshnev et al., 2016).

1.1.2 Epigenetic mechanisms

Epigenetic mechanisms including DNA methylation, histone modifications as well as regulation of gene expression by non-coding RNAs play essential roles in numerous fundamental biological processes (Feinberg AP and Fallin M, 2015; Yao et al., 2016). Together, they work in concert to organise DNA into chromatin and contribute to shaping the gene expression profile that defines the exact phenotype of a cell (Boland et al., 2014). Epigenetic mechanisms are necessary for proper development and maintenance of tissue-specific gene expression programs through mitotic cell division in mammals (Fedoriw et al., 2012; Handy et al., 2011). Epigenetic changes can be influenced by numerous factors, including aging, disease development, and environmental exposure (Cacabelos, 2016). Furthermore, epigenetic changes have been found to be involved in a variety of disease conditions, including various monogenic and multifactorial disorders (Maarel, 2008). However, epigenetic changes are potentially reversible and thus can be promising targets for pharmacological interventions (Cacabelos and Torrellas, 2015).

The two most extensively studied and well-characterised epigenetic modifications are DNA methylation and histone modifications **(Figure 1.2)** (Putiri and Robertson, 2010), while the role of non-coding RNAs in epigenetic regulation had been relatively less studied but is gaining interest (Roundtree and He, 2016). DNA methylation and histone modification can impact chromatin accessibility through controlling the chromatin structure, and thereby regulate gene expression patterns (Rothbart and Strahl, 2014). In mammals, DNA and histone methylation marks can be inherited (Chen and Dent, 2014). These epigenetic marks can be transmitted through mitotic cell divisions (Probst et al., 2009) and, in some cases, the marks could be potentially passed on to the subsequent generations through meiosis, a phenomenon known as transgenerational epigenetic inheritance (Daxinger and Whitelaw, 2010).

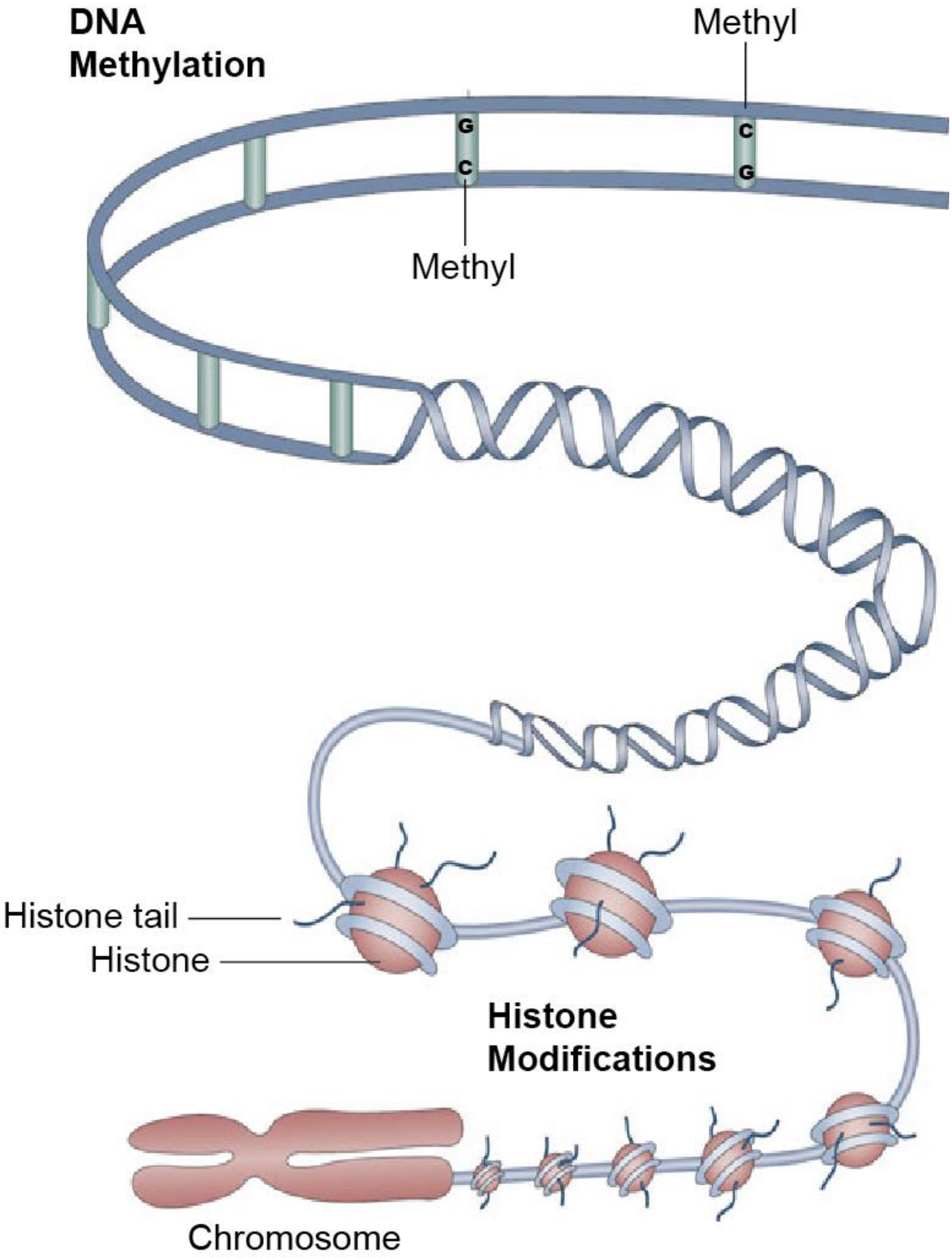

Figure 1.2: Schematic representation of two major mechanisms of epigenetic gene regulation. DNA methylation refers to the addition of methyl groups to cytosine (C) residues in DNA (shown in light blue) and thereby repress gene expression. Histone modifications, on the other hand, refer to the addition of various functional groups for instance methyl or acetyl to specific amino acid residues on the tails (shown in dark blue) of histone proteins (shown in pink) and thereby either activate or repress gene expression. Figure redrawn from Walker and Gore (2011).

Faithful transmission of these epigenetic marks during each cellular division as well as across generations is critical in order for cells to retain their non-DNA sequence information (Alabert and Groth, 2012; He et al., 2014). Both epigenetic marks must avoid being erased in the process called epigenetic reprogramming in order for epigenetic inheritance to occur (Whitelaw, 2015). Epigenetic inheritance is critically important in numerous fundamental biological processes, including expression of genes during early embryogenesis, genomic imprinting and transposon silencing (Migicovsky and Kovalchuk, 2011; Triantaphyllopoulos et al., 2016). Improper maintenance of heritable epigenetic marks can lead to developmental abnormalities and common diseases such as cancer (Lorthongpanich et al., 2013; Peters, 2014; Tomizawa and Sasaki, 2012). In addition, poor maternal nutrition can lead to epigenetic changes increases the risk of certain diseases, including obesity and diabetes. These changes are proposed to be passed on to the subsequent generation via transgenerational epigenetic inheritance, indicating that parental eating disorders may raise the risk of diabetes and obesity in offspring (Huypens et al., 2016).

1.1.3 Epigenetic mechanisms determine chromatin state

From the functional point of view, chromatin can be classified into two major types of material, euchromatin and heterochromatin **(Figure 1.3)**, depending on the degree of compaction and gene activity profile (Wang et al., 2014). The concepts of euchromatin and heterochromatin were first described in the late 1920s by Emil Heitz (Heitz, 1928). The initial classification of chromatin was based on its appearance, where euchromatin described the regions of chromatin that were decondensed and were no longer visible during interphase, while, on the other hand, heterochromatin described the regions that remained visibly condensed throughout most of interphase (Heitz, 1928; Pueschel et al., 2016).

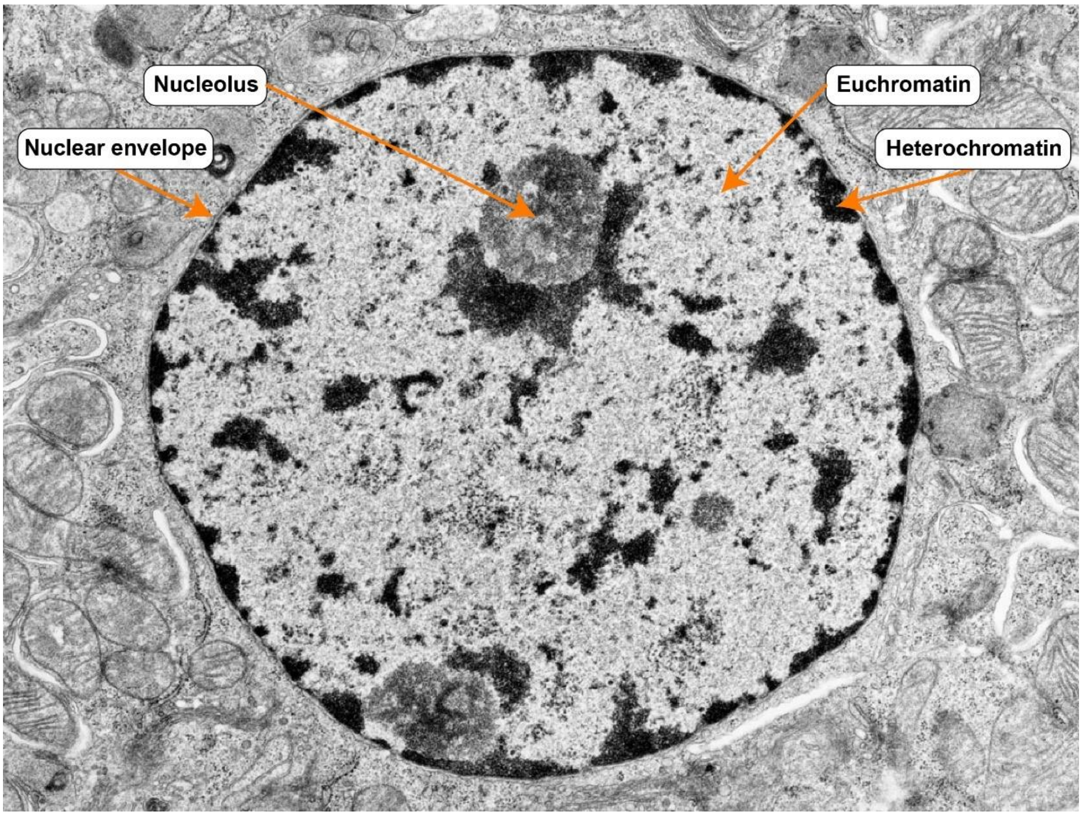

Figure 1.3: Electron micrograph of euchromatin and heterochromatin in an interphase nucleus. Regions of chromatin that are less condensed and lightly stained in interphase are known as euchromatin. The rest of the chromatin, which appears highly condensed, darkly stained, scattered throughout the nucleus but concentrated close to the nuclear envelope, is called heterochromatin. The DNA in loosely packed euchromatin is accessible for transcription, whereas the DNA in tightly packed heterochromatin is transcriptionally inactive. Figure relabelled from http://medcell.med.yale.edu/histology/cell_lab/euchromatin_and_heterochromatin.php.

The less condensed euchromatin contains high concentrations of genes that participate in the active transcription. On the contrary, the condensed heterochromatin contains very few genes that are mostly transcriptionally silent (Allis and Jenuwein, 2016). In addition, heterochromatic state can be further divided into two main subtypes according to their distinct molecular signatures: constitutive heterochromatin and facultative heterochromatin (Grewal and Jia, 2007). Constitutive heterochromatin refers to the chromosomal regions that are permanently condensed and transcriptionally silent throughout the cell cycle. The majority of constitutive heterochromatin is located at the pericentromeric regions and telomeres, and these gene-poor regions are composed of repetitive tandem satellite repeats

(Saksouk et al., 2015). In contrast, facultative heterochromatin refers to the chromosomal region that are not permanently kept in the condensed state, instead, they can be unwound to form euchromatin in response to cellular signals that regulate activity of specific genes (Trojer and Reinberg, 2007). A classic example of the formation of facultative heterochromatin is the silent X chromosome in female mammals (Chow et al., 2010; Vallot et al., 2016).

The partition of the genome into active euchromatin and inactive heterochromatin regions is largely determined by epigenetic modifications (Tamaru, 2010). Epigenetic mechanisms are capable of organising chromatin into “open” (euchromatin) or “closed” (heterochromatin) states, and thereby control the “on” and “off” status of the target genes (Hahn et al., 2010; Williamson et al., 2012; Wright and Saul, 2013). Open chromatin structure may allow access of the transcriptional machinery, thereby resulting in transcriptional activation, on the other hand, in the closed chromatin structure, the accessibility of genes to the transcriptional machinery could be restricted leading to transcriptional repression (Allan, 2015). Therefore, the patterns of epigenetic modifications may serve as markers to represent transcriptional activity and gene expression as well as chromatin state for a genomic region (Baker, 2011; Bernstein et al., 2007; Li and Zhang, 2012). In addition, chromatin remodeling alone, without affecting transcription, is sufficient to drive nuclear reorganisation during differentiation (Therizols et al., 2014).

1.2 DNA methylation

DNA methylation is one of the best studied epigenetic modifications and the most mechanistically understood (Smith and Meissner, 2013). It is found in most mammalians and many other organisms, as well as in plants (Meyer, 2015; Moffat et al., 2012). Chemically, it refers to the covalent transfer of a methyl group (CH_3) from S-adenosyl-L-methionine (SAM) to the fifth position of the pyrimidine ring of cytosine, mostly within cytosine-phosphate-guanine (CpG) dinucleotides to produce 5-methylcytosine (5mC), often referred as the ‘fifth base’ of DNA **(Figure 1.4)** (Moore et al., 2013). DNA methylation is typically associated with transcriptional repression (Jones, 2012). The repressive function of DNA methylation is involved in various forms of stable silencing mechanism, including genomic imprinting, X-chromosome inactivation and silencing of repetitive DNA (Schübeler, 2015).

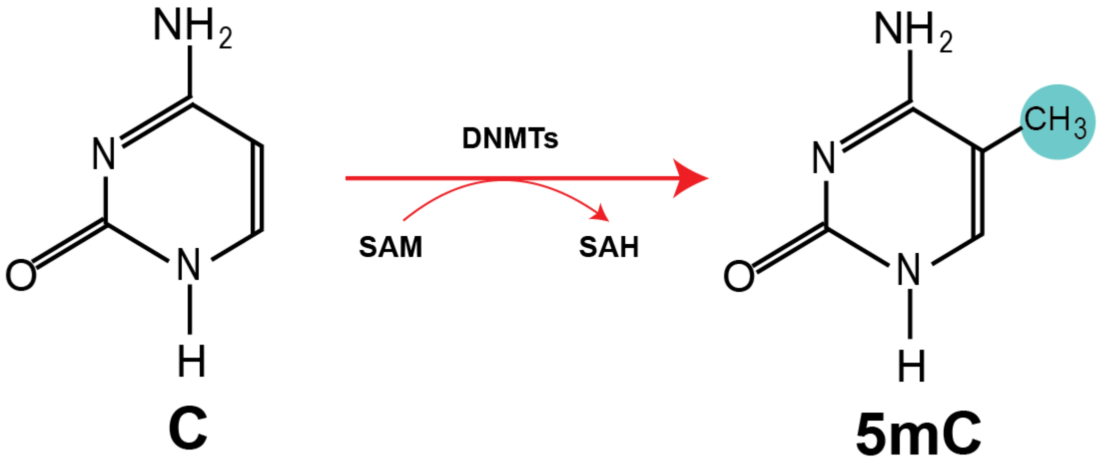

Figure 1.4: Schematic representation of DNA methylation. DNMT enzymes catalyse the transfer of a methyl group (CH_3) from the methyl donor SAM to the carbon 5 position of the pyrimidine ring of cytosine. SAM donates the methyl group and is transformed into S-adenosyl-L-homocysteine (SAH). Figure redrawn from Maresca et al. (2015).

1.2.1 DNA methylation machinery

Methylation of mammalian genomic DNA is regulated by a family of enzymes called DNA methyltransferases (DNMTs), which are recognised as key factors in epigenetic silencing of transcription. The DNMT family has four known members, including DNMT1, DNMT3A, DNMT3B as well as DNMT3L. Three catalytically active enzymes, DNMT1, DNMT3A and DNMT3B, are vital for establishment and maintenance of DNA methylation patterns during development of an embryo. DNMT1 preferentially methylates hemimethylated CpG dinucleotides that are produced upon replication and thus acts as a maintenance methyltransferase. On the other hand, DNMT3A and DNMT3B have preference for unmethylated CpG dinucleotides and thus are known as *de novo* methyltransferases. Unlike the other DNMTs, DNMT3L has no catalytic activity because it lacks some regions that are required for methyltransferase activity, but it modulates the DNA methylation activity of DNMT3A and DNMT3B by directly binding to these enzymes **(Figure 1.5)** (Duymich et al., 2016; He et al., 2011a).

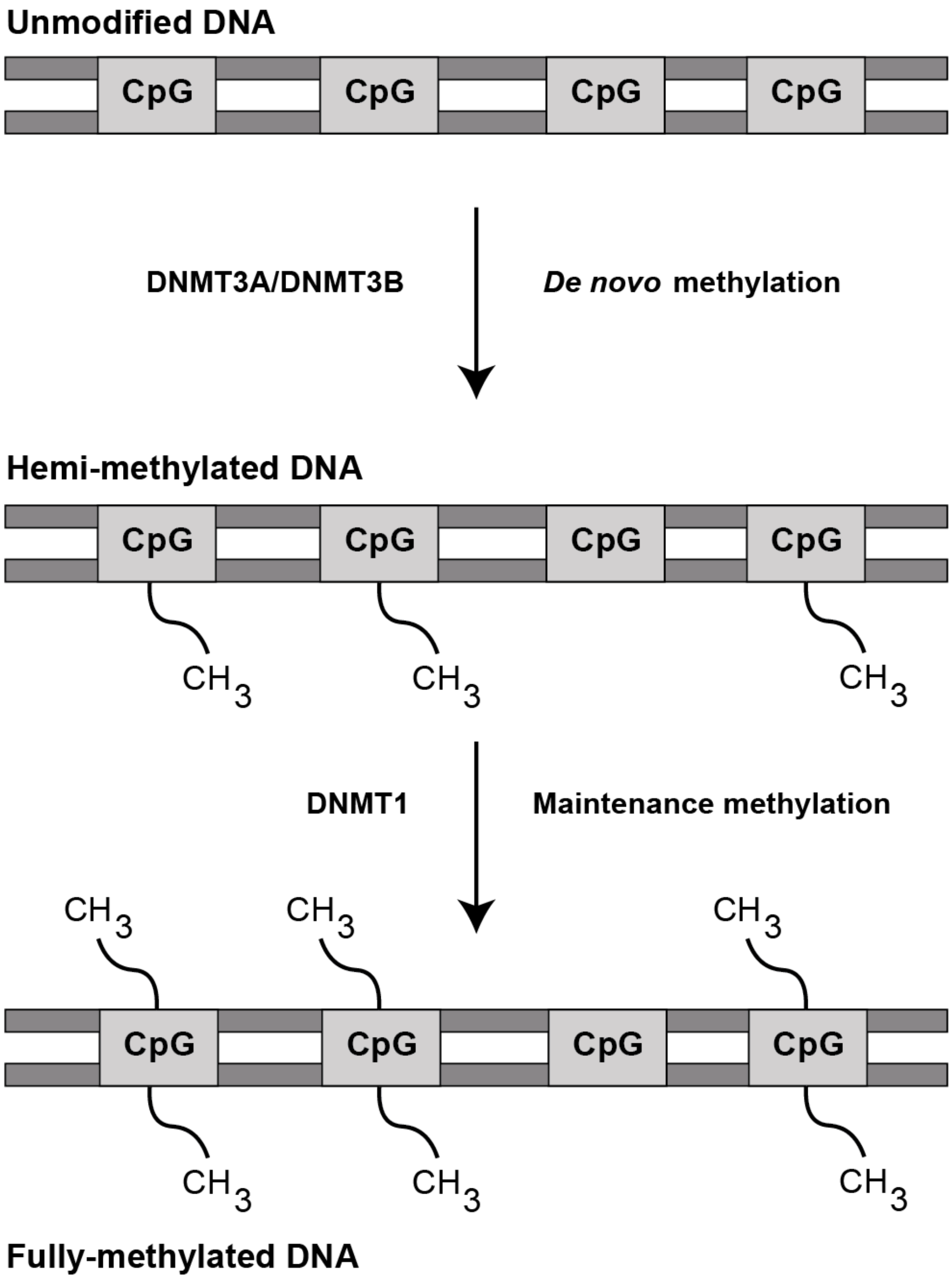

Figure 1.5: A schematic representation of *de novo* and maintenance methylation in mammals. DNMT3A and DNMT3B act as *de novo* methyltransferases that methylate unmethylated cytosines at CpG sites, whereas DNMT1 acts as a maintenance methyltransferase that preferentially methylates hemimethylated cytosines at CpG sites, thus maintaining DNA methylation patterns during replication. Figure redrawn from Maresca et al. (2015).

Early reports invoked direct interference of the methyl group at gene promoters, which is known to affect the binding sites of specific transcription factors (Deaton et al., 2011; Domcke et al., 2015; Maurano et al., 2015). A more general mechanism is provided by proteins specifically binding to the methyl groups. Once CpG sites are methylated, they can be specifically recognised and read by the methyl-CpG binding proteins (MBPs), which then recruit chromatin remodelling corepressor complexes to methylated DNA sequences to suppress the expression of gene and/or to form a higher order compacted chromatin structure called heterochromatin, thereby establishing a transcriptionally inactive chromatin state (Li and Zhang, 2014). MPBs are grouped into three different families according to their structural similarity: MBD (methyl-CpG binding domain), Kaiso and SRA domain proteins (Gibney and Nolan, 2010). The MBD protein family comprises seven members, namely MBD1, MBD2, MBD3, MBD4, MBD5, MBD6, and MeCP2. MBD1, MBD2, MBD4 and MeCP2 have a conserved methyl CpG binding domain that enables them to bind to methylated DNA. However, unlike the other family members, MBD3, MBD5, and MBD6 fail to bind to methylated DNA due to the lack of numerous essential amino acids in the MBD domain that are crucial for the DNA binding activity (Menafra et al., 2014).

1.2.2 CpG islands

In mammalian genomes, DNA methylation occurs most often at CpG sites, where a cytosine is directly followed by a guanine in the sequence of the DNA (Klose and Bird, 2006). While methylated CpGs are distributed globally throughout the genome, those that seem to be protected from the methylation exhibit dramatic clustering. These clusters of unmethylated CpG dinucleotides tend to reside in regions known as CpG islands (CGIs) and frequently located at the 5' ends of genes (Bird, 1986, 1987; Gardiner-Garden and Frommer, 1987; Reddington et al., 2013a). CGIs are stretches of DNA approximately 1000 bp in length that have an elevated G + C content, little CpG depletion, and normally free from DNA methylation (Blackledge and Klose, 2011; Deaton and Bird, 2011).

Up to 70% of human genes are associated with CGIs (Saxonov et al., 2006). It has been predicted that the human genome contains roughly 29,000 CGIs (Lander et al., 2001), most of which are associated with the 5' ends of genes, including the promoters of housekeeping genes which are often embedded in CGIs as well as a proportion of tissue-restricted genes and developmental regulator genes (Harraghy et al., 2015; Chatterjee and Vinson, 2012; Zhu et al., 2008). Based on their location in the promoters, it has been hypothesized that CGIs may play key roles in gene regulation (Beck et al., 2014), most likely by the recruitment of the CXXC finger protein 1 (Cfp1) and possibly other CpG-binding proteins (Clouaire et al., 2012; Thomson et al., 2010).

CGIs, however, avoid the phenomenon of CpG dinucleotide suppression and preserve their CpGs. A mechanism involved in protecting these DNA regions against *de novo* methylation is under intense investigation (Sormani et al., 2016). Some results suggest that the protection mechanisms of promoter-associated CGIs from *de novo* methylation are DNA-encoded and evolutionarily conserved, regardless of host species (Long et al., 2016). Moreover, CGIs may escape DNA methylation machinery through a conserved property of unmethylated CGI promoters known as GC skew by forming R-loop structures upon transcription (Hartono et al., 2015; Ginno et al., 2012). Even more, by hosting DNA-binding proteins, particularly transcription factors, CGIs could make them resistant to the DNMTs (Saadeh and Schulz, 2014). Alternatively, CGIs are targeted by a DNA demethylation mechanism through direct removal of a methyl moiety from the cytosine residue, thus making CGIs remain free of methylation (Jin et al., 2014). However, while most CGIs remain unmethylated, promoter CGIs located on the inactive X chromosome in females readily acquire DNA methylation (Gendrel et al., 2013).

The CGI promoter methylation can impair transcription factor binding and results in stable silencing of gene expression (Deaton et al., 2011). The phenomenon of aberrant promoter CGI hypermethylation has been well recognised as a hallmark of cancer involved in transcriptional inactivation of tumour suppressor genes and activation of oncogenes (Sproul and Meehan, 2013). These hypermethylated promoter CGIs can completely block the transcription of tumour suppressor genes, causing uncontrolled growth of abnormal cells, which subsequently leads to cancerous tumour formation (Rodríguez-Paredes and Esteller, 2011). Furthermore, a reduction in Tet1 activity at CGIs may induce hypermethylation events in many cancers (Thomson et al., 2016).

1.2.3 DNA demethylation

DNA methylation has long been thought to be a relatively stable epigenetic modification. However, recent evidence demonstrated that this modification may be more dynamic and complex than previously thought. In theory, loss of DNA methylation, or DNA demethylation can occur through passive or active processes. Passive DNA demethylation is caused by the failure of maintenance methylation during several cycles of DNA replication. By contrast, active DNA demethylation occurs via direct enzymatic removal of the methyl group from 5mC **(Figure 1.6)**. Passive DNA demethylation is well understood and accepted, however the mechanism of active DNA demethylation has been a controversial subject in recent decades (Wu and Zhang, 2014).

DNA methylation marks are comprehensively reprogrammed across the genome via DNA demethylation in a process known to occur at two major points in mammalian development. DNA methylation reprogramming occurs firstly following fertilization in the zygote and secondly occurs in PGCs (primordial germ cells) which are the embryonic progenitors of sperm or oocytes. In both cases, a unique set of mechanisms regulates the global DNA demethylation followed by extensive remethylation (Seisenberger et al., 2013a). This reprogramming is necessary for resetting parental imprints, erasing acquired epimutations, returning the genome to a pluripotent or totipotent state and potentially for the activation of transposable elements (Popp et al., 2010; Surani, 2015).

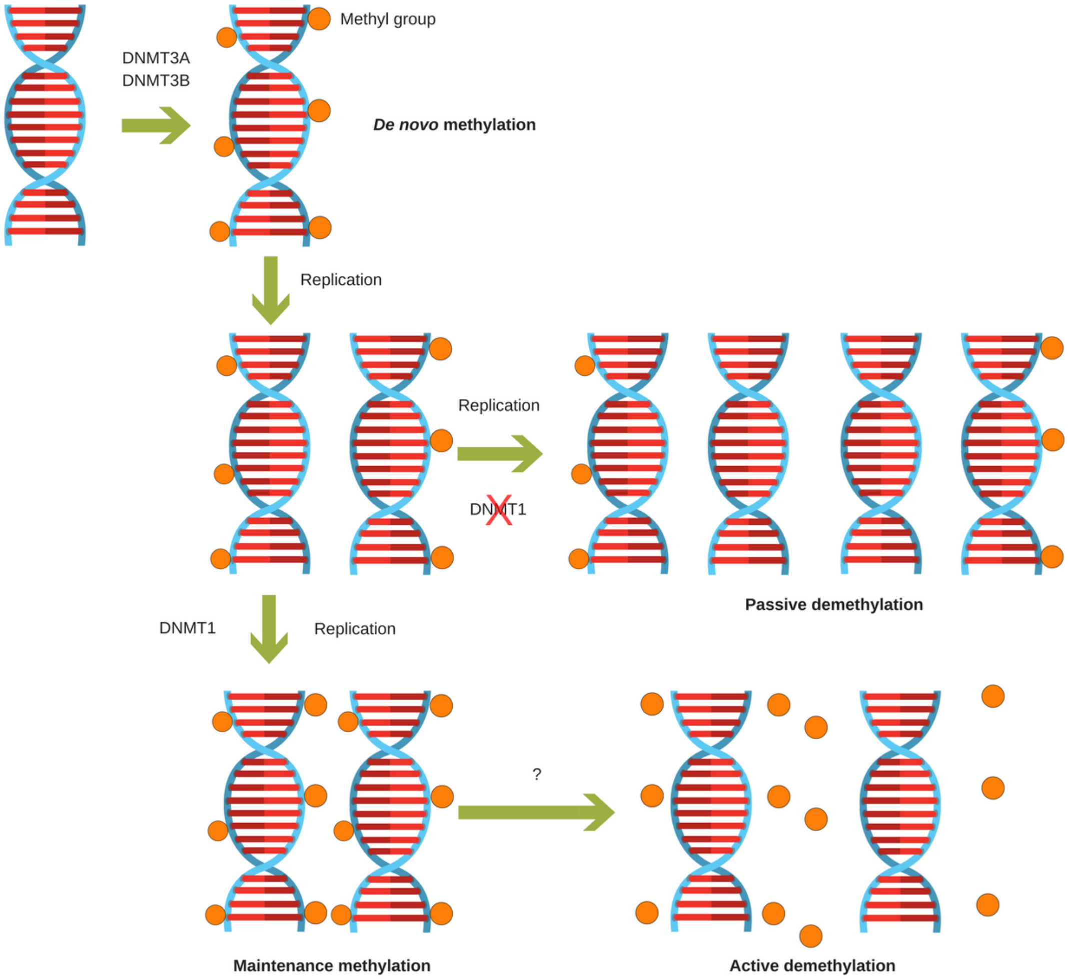

Figure 1.6: Passive and active mechanisms of DNA demethylation. Loss of 5mC can occur through passive or active mechanisms. Passive demethylation refers to the loss of 5mC due to poor of maintenance methylation during several rounds of replication. On the contrary, active demethylation refers to the enzymatic removal of methyl groups directly from 5mC. Figure redrawn from Wu and Zhang (2010).

1.3 DNA hydroxymethylation

Several molecular mechanisms for the enzymatic removal of the methyl group from 5mC have been proposed to play a role in reprogramming. One potential active demethylation mechanism involves enzymatic oxidation of 5mC to generate 5-hydroxymethylcytosine (5hmC) **(Figure 1.7A)** (Hill et al., 2014). Current evidence suggests that 5hmC may play an intermediate role in the process of oxidative demethylation (Pfeifer et al., 2013).

The existence of 5hmC was initially discovered in the DNA of T-even bacteriophage (Wyatt and Cohen, 1952). Later on, in the early 1970s, 5hmC was further reported in mammalian genomes (Penn et al., 1972). However, this finding did not draw much attention as it could not be reproduced in subsequent studies (Kothari and Shankar, 1976), therefore 5hmC was simply thought to be a by-product of oxidative damage of DNA in mammalian genomes, rather than serving as a functional epigenetic mark. For that reason, 5hmC was largely ignored and it took almost 40 years to confirm the presence of 5hmC and gain insights into its molecular function (Kriukienė et al., 2012).

1.3.1 Tet-mediated 5mC oxidation

Progress was made in 2009 when 5hmC was independently re-discovered by the groups of Nathaniel Heintz at Rockefeller University and Anjana Rao at Harvard Medical School. Heintz’ and Rao’s groups confirmed the presence of 5hmC in mouse brain cells (Kriaucionis and Heintz, 2009) and mouse embryonic stem (ES) cells (Tahiliani et al., 2009). By using thin layer chromatography (TLC), high pressure liquid chromatography (HPLC) and mass spectrometry (MS), Kriaucionis and Heintz detected the presence of 5hmC in Purkinje cells and granule cells comprising approximately 0.6% and 0.2% of total nucleotides, respectively (Kriaucionis and Heintz, 2009). Coinciding with this observation, Rao and co-workers discovered the key player responsible for active DNA demethylation, the Ten-eleven translocation (Tet) gene; Tet1. They found that Tet1 can catalyse the conversion of 5mC to 5hmC in a 2-oxoglutarate (2OG)- and Fe(ll)-dependent manner (Tahiliani et al., 2009).

Soon after, two other Tet family members, Tet2 and Tet3, were also identified as being able to catalyse a similar reaction (Ito et al., 2010). Tet family proteins share a conserved C-terminal catalytic domain (Cys-rich and DSBH regions) that belongs to the dioxygenase superfamily (Gao et al., 2016). The Zhang group discovered that all three Tet proteins can further oxidize 5hmC to 5-formylcytosine (5fC) and 5-carboxylcytosine (5caC) in an enzymatic activity-dependent manner **(Figure 1.7B and 1.7C)** (Ito et al., 2011). Their potential redundancy adds a degree of complexity to revealing the role of Tet proteins and 5hmC in epigenetic regulation during development (Tan and Shi, 2012).

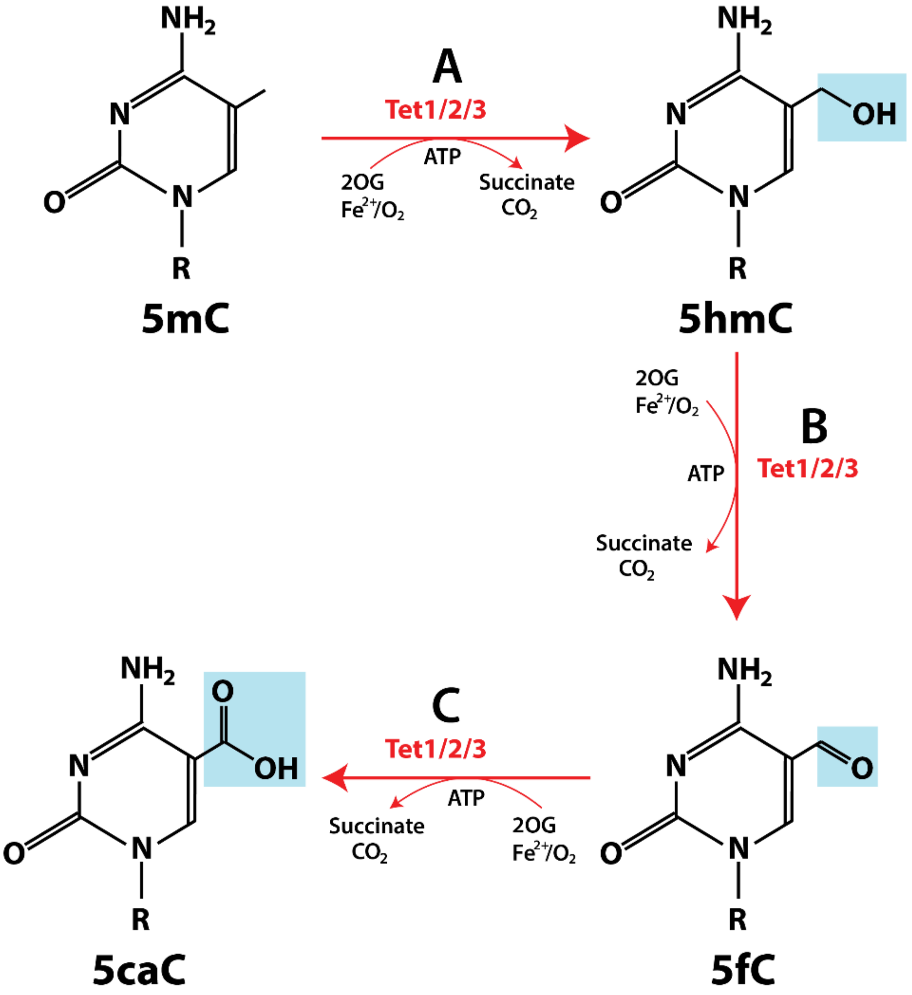

Figure 1.7: Oxidative reactions catalysed by Tet enzymes. (A) All three mammalian Tet proteins, Tet1, Tet2 and Tet3, catalyse the oxidation of 5mC to generate 5hmC. This chemical reaction requires 2OG, ferrous ion (Fe^{2+}), oxygen (O_2) and adenosine triphosphate (ATP) and yields succinate and carbon dioxide (CO_2). **(B,C)** Similar reactions oxidise 5hmC further to generate 5fC and 5caC. Figure redrawn from Huang and Rao (2014).

1.3.2 Tet-mediated DNA demethylation

Tet proteins play vital roles in the active DNA demethylation through iterative oxidation of 5mC followed by the conversion of 5caC to cytosine (Wu and Zhang, 2015). Restoration of 5mC back to unmodified cytosine cannot happen spontaneously. It is likely that there are a number of chemically plausible pathways responsible for the reversal of DNA methylation, and that Tet proteins are involved in several of these (Pastor et al., 2013).

Several proposed DNA replication-independent active DNA demethylation pathways involving Tet-mediated oxidation for the conversion of 5mC to unmodified cytosine are outlined in **(Figure 1.8)**. Such pathways were mostly inferred from *in vitro* studies. One possibility is that Tet-catalysed 5hmC conversion into 5fC and 5caC can be efficiently excised from DNA by the DNA repair enzyme thymine-DNA glycosylase (TDG) and subsequently repaired via base excision repair (BER). Subsequent repair of the resulting abasic site via BER can generate an unmodified cytosine residue, thus completing the process of DNA demethylation (Weber et al., 2016). It has been revealed that TDG possesses robust excision activity towards 5fC- and 5caC-containing DNA, but not 5hmC- and 5mC-containing DNA (He et al., 2011b; Maiti and Drohat, 2011).

Another possibility is that 5fC and 5caC can be directly deformylated or decarboxylated by a putative DNA deformylase or DNA decarboxylase enzyme, which eventually leads to the restoration of unmodified cytosine (Branco et al., 2012). Intriguingly, 5caC decarboxylase activity has been detected in mouse embryonic stem cell (mESC) lysates, but no putative decarboxylase has yet been identified (Schiesser et al., 2012). First *in vitro* evidence for direct decarboxylation of 5caC to unmodified cytosine by an enzyme was found by Xu et al. (2013), which demonstrated that IDCases (isoorotate decarboxylases) possess decarboxylase function albeit with weak activity. Another study found that C5-MTases (cytosine-5-*S*-Adenosylmethionine-dependent DNA methyltransferases) can convert 5caC directly to unmodified cytosine *in vitro* but are lacking the ability toward 5fC (Liutkevičiūtė et al., 2014). However, the existence of 5fC DNA deformylase and

5caC DNA decarboxylase remains uncertain and has yet to be identified (Shukla et al., 2015).

Alternatively, 5mC or 5hmC can be deaminated by cytidine deaminases, leading to replacement of the residue with an unmodified cytosine residue and resulting in active DNA demethylation. The activation-induced cytidine deaminase (AID)/apolipoprotein B mRNA editing enzyme, catalytic polypeptide-like (APOBEC) family of cytidine deaminases are well characterised for their ability to deaminate 5mC or 5hmC to generate thymidine (T) or 5-hydroxymethyluracil (5hmU), respectively. As these are present in mismatched T:G and 5hmU:G basepairs, they have been suggested to be excised by TDG or single-strand-selective monofunctional uracil DNA glycosylase 1 (SMUG1), another DNA glycosylase, leaving intact abasic sites in DNA. The resulting abasic sites are repaired by BER to restore unmodified cytosines (Nabel et al., 2012).

On the other hand, a recent study presented *in vitro* evidence that the mammalian *de novo* DNA methyltransferases DNMT-3A and -3B, in addition to their well-known methyltransferase activity, could also function as reduction-oxidation (redox) state-dependent DNA dehydroxymethylases that can convert 5hmC directly to unmodified cytosine, although the exact pathways are yet to be better defined (Chen et al., 2012). Interestingly, the direct conversion of 5mC to unmodified cytosine might be catalysed by DNMT-3A and -3B in the context of SAM deficiency, although the physiological relevance of DNMT-3A and -3B needs to be investigated (Wijst et al., 2015).

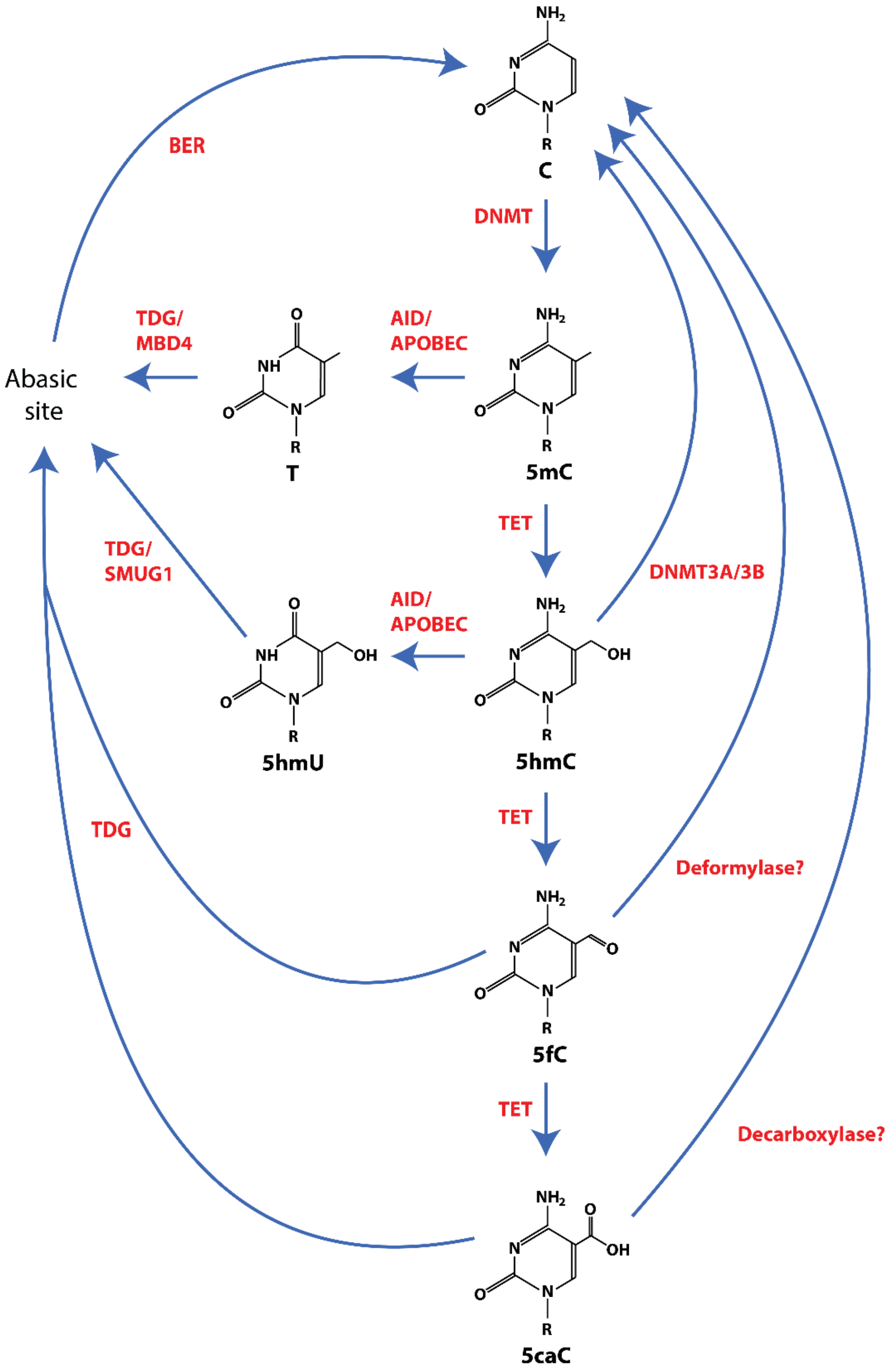

Figure 1.8: Mechanisms of Tet protein-mediated DNA demethylation. A number of potential mechanisms for active DNA demethylation, in which 5mC is converted back to a naked cytosine, have been proposed. Tet family proteins consecutively oxidise 5mC to 5hmC, 5fC and 5caC. The oxidation products 5fC and 5caC are subject to removal by TDG to generate abasic sites. The resulting abasic sites are

further repaired by the BER mechanism to reinstate unmodified cytosines. Other less well-characterised mechanisms include deformylation of 5fC and decarboxylation of 5caC by as yet unidentified deformylases and decarboxylases, respectively. These enzymes could directly remove the formyl and carboxyl groups from fC and caC, respectively, leading to the restoration of unmodified cytosines. Alternatively, 5mC and 5hmC may be deaminated by AID or APOBEC, producing T:G and 5hmU:G mismatches, respectively, which can subsequently be removed by DNA glycosylases and then repaired by BER. Another possibility is that DNMT-3A and -3B could directly remove the hydroxymethyl group of 5hmC to generate unmodified cytosine. Figure redrawn from Branco et al. (2012).

1.3.3 5hmC in brain

The relative abundance of cytosine modifications tends to vary in the order of 5mC>5hmC>5fC>5caC in tissues (Delatte et al., 2014). The overall levels of 5hmC are substantially lower than 5mC in the mammalian genome, which have been reported to be approximately 10% of 5mC and 0.4% of all cytosines (Branco et al., 2012; Malan-Müller et al., 2014). However, initial studies of 5hmC in 2009 uncovered that 5hmC occurs at relatively high levels in the brain and neural tissues, suggesting a unique role for 5hmC in neuronal function through epigenetic control of gene expression (Kriaucionis and Heintz, 2009). Indeed, in a study published by Khare et al. (2012), the enrichment of 5hmC was detected in the vicinity of genes with synapse-related functions.

Unlike 5mC, which is detected at similar levels in numerous cell types, the global levels of 5hmC vary markedly between different tissues and cell types (Nestor et al., 2012). Interestingly, research into the 5hmC distribution across different tissues discovered that brain tissue has the highest abundance of 5hmC compared to other tissues (Li and Liu, 2011), in agreement with the previous study reported on 5hmC (Kriaucionis and Heintz, 2009). A more detailed survey of various brain tissues revealed that the 5hmC was particularly prominent in cerebral cortex and hippocampus, which are the areas of the brain that involved in higher cognitive functions (Münzel et al., 2010).

Another interesting observation is the discovery that the 5hmC content in mouse hippocampi seems to increase with age. It was found that the amount of 5hmC in the hippocampus tissue of 90 day old mice was significantly increased by approximately 75% from one day old mice (Münzel et al., 2010). Soon after, a study by Song et al. (2011) also observed the developmental stage-dependent increase of 5hmC in mouse cerebellum. A similar correlation was later shown in human brain tissues, which suggest that the amount of 5hmC in the brain is age dependent (Kraus et al., 2014; Wagner et al., 2015), consistent with the overall observations of prior studies in mice (Münzel et al., 2010; Song et al., 2011). Together, these discoveries suggest that 5hmC might play a crucial role in brain maturation and neuronal development (Münzel et al., 2010; Zheng et al., 2015).

The presence of high levels of 5hmC in the brain suggests that 5hmC is necessary for proper neurodevelopment, thus dysregulation of 5hmC may lead to severe neurological and neurodegenerative diseases (Cheng et al., 2015). Mounting evidence has recently demonstrated that 5hmC is involved in the pathology of numerous neurological diseases, among them ischemic brain injury (Miao et al., 2015), fragile X-associated tremor/ataxia syndrome (Yao et al., 2014), Alzheimer's disease (Chouliaras et al., 2013), and Huntington's disease (Wang et al., 2013), suggesting that 5hmC may play a vital role in the mechanisms underlying neurological diseases (Sun et al., 2014).

5hmC is now widely recognised as an important epigenetic mark that is linked to both normal neurodevelopment and neurological diseases and has become the subject of many new studies (Cheng et al., 2015). It is not fully known yet what the functions are of 5hmC, but evidence suggests that 5hmC could also perform as a stable epigenetic marker exerting a specific regulatory role during brain development and ageing, in addition to being an intermediate in demethylation (Kraus et al., 2015). However, further studies on biochemical and molecular interactions between 5hmC and neural tissue are necessary to more deeply understand the critical function of 5hmC in the brain where it may play an important role in neural development, as well as neurological diseases (Kato and Iwamoto, 2014).

1.3.4 Potential roles of 5hmC

Although 5hmC has been well characterized as a transient intermediate in an active DNA demethylation pathway, increasing data are suggesting that 5hmC may also be a stable epigenetic mark in its own right that possesses unique regulatory functions (Hahn et al., 2014). 5hmC is enriched in euchromatic regions of the genome, suggesting that it is associated with increased gene expression (Ficz et al., 2011). 5hmC might prime specific genes for rapid activation, either by triggering active DNA demethylation or perhaps through recruitment of a specific set of transcriptional regulators that recognise 5hmC (Pastor et al., 2011).

The conversion of 5mC to 5hmC by Tet proteins may be required to protect the genome from any unwanted DNA methylation by preventing DNA methyltransferase activity (Jeong et al., 2014). 5hmC is recognised poorly by DNMT1 during DNA replication, therefore the oxidation of 5mC to 5hmC may aid passive DNA methylation dilution in proliferating cells by impairing methylation maintenance machinery (Giehr et al., 2016). Thus, Tet protein-mediated oxidation of 5mC may contribute to dynamic changes in global or locus-specific 5mC and/or 5hmC levels by facilitating both active DNA demethylation and passive DNA methylation dilution, thereby modulating gene transcription (Li et al., 2015a). 5hmC could also be involved in fine-tuning of the regulation of gene expression (Ehrlich and Ehrlich, 2014).

According to a number of reports 5hmC levels are remarkably depleted in numerous types of cancer cells (Jin et al., 2011; Thomson et al., 2016; Yang et al., 2013), which indicates that a lack of 5hmC could be developed into a beneficial molecular biomarker for cancer detection and diagnosis (Munari et al., 2016). For this reason, the detection of 5hmC has gradually become a major focus of epigenomic research (Yang et al., 2015).

1.4 Post-translational modifications (PTMs) of histone proteins

Post-translational modifications (PTMs) of histone proteins in conjunction with DNA methylation play an important role in determining the state of chromatin structure (Winter and Fischle, 2010). Importantly, most of the epigenetic marks on the chromatin platform do not function alone, but rather crosstalk with one another (Fischle, 2008), and this regulatory crosstalk can be mediated by the interaction of numerous epigenetic modifier proteins (Cedar and Bergman, 2009). Interestingly, accumulating evidence suggests that extensive crosstalk exists between different epigenetic pathways in mammals (Wang and Zhu, 2015).

Alongside histone modifications on the amino-terminal tails of histones, the nucleosome structure itself can also play a decisive role in the regulation of gene expression. In the last two decades, it has become clear that the function of nucleosomes is much broader than just facilitating the packaging of large amounts of DNA into the small volume of a cell nucleus. Nucleosomes may participate in the regulation of gene expression by modulating access of transcription factors and transcription machinery to DNA (Bai and Morozov, 2010; Wight et al., 2016). Emerging data have revealed that nucleosome positioning works in tight concert with histone modifications as well as DNA methylation to determine the epigenetic regulation of the genome (Pennings et al., 2005; Portela and Esteller, 2010; Rhie et al., 2014). It has been suggested that nucleosome positioning and histone modification are able to switch on or off, temporally and spatially, specific genes in order to establish cellular identity at different stages of development or differentiation (Teif et al., 2012, 2014).

The histone core of a nucleosome contains two copies of each of the four core histone proteins H2A, H2B, H3 and H4 (Luger et al., 2012). The four core histones can undergo a wide variety of post-translational modifications, including acetylation of lysines, methylation of lysines and arginines, phosphorylation of serines and threonines, ubiquitylation and sumoylation of lysines, as well as glycosylation, adenosine diphosphate ribosylation and carbonylation (Kouzarides, 2007). These modifications are carried out by an equally large number of histone modifying enzyme complexes specialised in adding or removing the covalent modifications at particular sites on the histone proteins (Lalonde et al., 2014).

Additionally, these various histone modifications are further separable into different degrees of chemical modification, for instance, a single lysine residue can accept up to three methyl groups, thus forming four different methylation states; unmethylated (me0), monomethylated (me1), dimethylated (me2), and trimethylated (me3) (Zhou et al., 2011). Multiple lines of evidence indicate that different methylation states on the same protein are often associated with distinct biological functions (Fuchs et al., 2012; Schwämmle et al., 2016).

The histone tails of the nucleosome are the most common regions of extensive post-translational modification (DesJarlais and Tummino, 2016). Histone tails, which refer to the disordered N-termini, extend beyond the surface of the nucleosome core particle, making them more accessible. The N-terminal histone tails are required for stabilizing higher order chromatin structures (Allan et al., 1982; Pepenella et al., 2014). Firstly, histone tail modifications appear to modulate the interactions between histones and DNA, thereby altering nucleosome stability (Iwasaki et al., 2013). In addition, these histone tail modifications may also contribute to defining the condensed state of the chromatin fibre by controlling interactions between nucleosomes to form higher order structures, which also require linker histone H1 (Allan et al., 1981; Bowman and Poirier, 2015). By weakening histone-DNA and nucleosome-nucleosome interactions, post-translational modifications of histone tails modulate access of DNA-binding proteins that regulate biological processes (Biswas et al., 2011). In this way, histone tail modifications are crucial for the fundamental cellular processes of transcription, replication, recombination, and DNA repair (Iwasaki et al., 2013; Simon et al., 2011).

Histone modification patterns are established through a highly regulated interplay between histone modification enzymes, which have been categorised as histone ‘writers’, ‘erasers’, and ‘readers’ (Zhang et al., 2015). Histone writers such as histone acetyltransferases (HATs), histone methyltransferases (HMTs), protein arginine methyltransferases (PRMTs) and kinases are the histone modifying enzymes that add covalent post-translational modifications to the histone tails. Histone erasers such as histone deacetylases (HDACs), lysine demethylases (KDMs) and phosphatases are the enzymes that can remove post-translational marks from histone substrates. On the other hand, histone readers such as proteins containing bromodomains, chromodomains and Tudor domains are the proteins that recognise and bind to post-translational marks on histones (Falkenberg and Johnstone, 2014; Gillette and Hill, 2015). Disruption of histone writers, erasers, and readers can lead to malfunction including cancer (Chi et al., 2010; Højfeldt et al., 2013; Liu et al., 2016a).

1.4.1 Histone code

The total number of possible combinations of histone modifications within a single nucleosome runs into many thousands, creating an abundance of regulatory potential (Schwämmle et al., 2014). Interestingly, multiple post-translational modifications of core histones appear to work synergistically to fine tune a precise chromatin state, forming a so-called ‘histone code’ that can be read and interpreted by specialised proteins to bring about distinct downstream events (Fischle et al., 2015; Tian et al., 2012). In general, histone code is the term that often used to describe how different combinations of histone modifications affect gene expression at a transcriptional level (Strahl and Allis, 2000; Turner, 2000). Specifically, certain combinations of histone modifications are capable of driving gene expression up, while others are capable of driving it down (Dong and Weng, 2013).

According to the histone code hypothesis initially proposed by Strahl and Allis (2000) and Turner (2000), distinct combinations of covalent post-translational modifications of histones can have a dramatic impact on chromatin structure and function, leading to varied transcriptional outputs (Strahl and Allis, 2000). Jenuwein and Allis (2001) further generalized the concept to the idea that numerous combinations of histone modifications are linked to specific chromatin-related mechanisms and functions. For instance, various histone modifications have been strongly associated with apoptosis-induced chromatin changes, providing cumulative evidence for a potential ‘apoptotic histone code’ (Füllgrabe et al., 2010).

1.4.2 Histone acetylation and histone methylation

The most widely studied and best understood post-translational modifications of histones constituting a putative histone code are histone acetylation and histone methylation, which occur predominantly at lysine (K) residues **(Figure 1.9)** (Sun et al., 2013). The presence of histone acetylation was first observed by Allfrey et al. (1964) in 1964. In this pioneering study, it was demonstrated that histones were hyperacetylated at the promoters of actively transcribed genes, whereas at silenced genes histones were hypoacetylated (Allfrey et al., 1964). Since then, it has been revealed that the acetylation of lysine residues is highly dynamic and dependent on the opposing actions of two classes of enzymes, HATs and HDACs (Verdin and Ott, 2015).

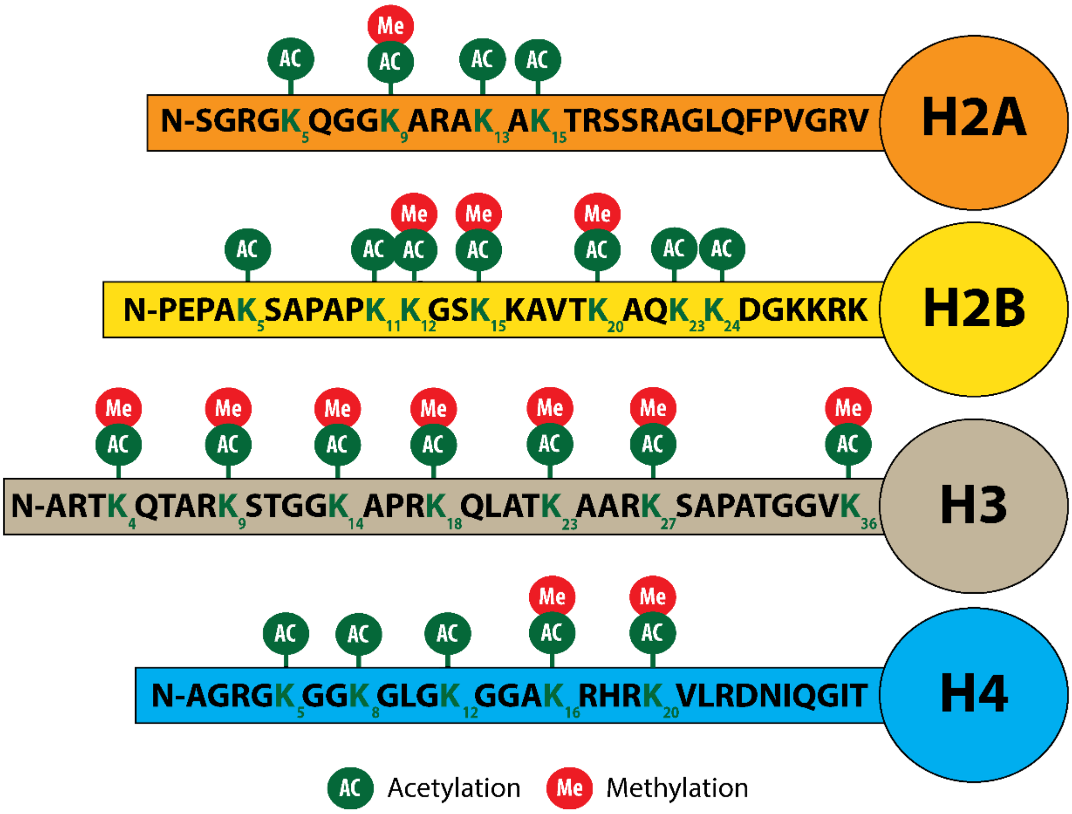

Figure 1.9: Acetylation and methylation of lysine (K) residues in histones. The nucleosome core histones (H2A, H2B, H3 and H4) are subjected to a variety of post-translational modifications at their N-terminal tails that protrude out of the

nucleosome. Two major modifications, histone acetylation and histone methylation, which occur predominantly at the lysine residues, are highlighted. Figure redrawn from www.psych.mpg.de/1496016/deussing.

The HATs utilise acetyl-coenzyme A as the acetyl group donor and catalyse the transfer of an acetyl group to the ε-amino group of a target lysine side-chain within a histone. This is associated with a relaxed chromatin structure that allows binding of transcription factors and thus constitutes an activating gene transcription mark (Marmorstein and Zhou, 2014; Taylor et al., 2013). Acetylated histones regulate transcription via interaction with proteins that contain a motif called a bromodomain, which consists of approximately 110 amino acid residues predominantly found in a variety of transcription factors as well as in some chromatin remodeling complexes (Filippakopoulos and Knapp, 2014). HAT activity can be counteracted by HDACs through the removal of the acetyl groups (deacetylation) from the histone tails, leading to hypoacetylation. This is associated with compaction of the chromatin structure, and consequently shutting down transcription (Seto and Yoshida, 2014).

Unlike histone acetylation, where only one acetyl group can be added to a lysine residue within a histone tail, histone methylation can lead to the addition of either one, two or three methyl groups per lysine residue (Rivera et al., 2014). Histone methylation can occur at different amino acid residues, including lysine, arginine and histidine. Amongst these, methylation of lysines has been extensively studied and is considered one of the most versatile covalent histone modifications (Musselman et al., 2014). This is because lysine residues can exist in monomethylated, dimethylated, or trimethylated states and depending on the site and methylation state, can be associated with either an active or a silent state of gene expression (Zhang et al., 2012b).

The attachment of methyl groups occurs predominantly, but not exclusively, on lysine residues of histones H3 and H4 and is carried out by specific histone lysine methyltransferases (KMTs) (Black et al., 2012). KMTs mediate the transfer of one to three methyl groups from the methyl donor cofactor SAM to specific lysine residues on histones (Mohan et al., 2012). All KMTs, with the exception of DOT1-like protein (DOT1L; also known as KMT4), contain a conserved suppressor of variegation, enhancer of zeste and trithorax (SET) domain, which is crucial for the binding of SAM and the interaction with the targeted lysine to mediate the transfer of the methyl group (Mozzetta et al., 2015). SET domain KMTs catalyse the methylation of lysine residue in a site- and state-specific manner (Izzo and Schneider, 2010; Wagner et al., 2014).

Initially, histone methylation was considered to be stable and irreversible. Its dynamic nature was not confirmed until 2004 when Shi and co-workers broke new ground with their discovery of the first lysine-specific histone demethylase (LSD1; also known as KDM1A) (Shi et al., 2004b). Soon afterward, a second and larger family of histone demethylases consisting of the Jumonji C (JmjC)-domain containing proteins was discovered, another module that possesses enzymatic activity to remove the methyl groups from lysine residues (Tsukada et al., 2006). Two evolutionarily conserved families of histone demethylases with distinct cofactor requirements and reaction mechanisms have thus far been identified (McAllister et al., 2016). First is the FAD (flavin adenine dinucleotide)-dependent amine oxidase LSD1 family, and the second is the Fe(II) and alpha-KG (alpha-ketoglutarate)-dependent dioxygenase JHDM family (JmjC domain-containing histone demethylase) (Dimitrova et al., 2015; Nowak et al., 2016). LSD1 can theoretically catalyse only demethylation of monomethylated and dimethylated lysine residues, whereas JHDM enzymes can demethylate all three lysine methylation states (Suzuki and Miyata, 2011).

The transcriptional consequences of histone methylation depend on the specific amino acid residues in the histone tails that are modified, and can also depend on the degree of methylation. While methylation of certain lysine residues is associated with active transcription, methylation of other lysines is associated with the opposite effect on gene activity (Bannister and Kouzarides, 2011). For instance, trimethylation of lysine 27 at histone H3 (H3K27me3) by polycomb repressive complex 2 (PRC2) contributes to gene repression (Justin et al., 2016). On the contrary, trimethylation of lysine 4 at histone H3 (H3K4me3) through trithorax group (trxG) proteins counteracts PRC2-mediated repressive activity and activates gene expression (Geisler and Paro, 2015; Schuettengruber et al., 2011). For other lysine residues in histones, the degree of methylation determines the effect on gene expression. For example, in mammalian chromatin, monomethylation of lysine 9 at histone H3 (H3K9me1) is associated with gene activation (Barski et al., 2007), whereas dimethylation and trimethylation of the same lysine residue, H3K9me2 and H3K9me3, respectively, are associated with gene silencing (Boros et al., 2014).

To date, the most widely investigated histone lysine methylation sites include H3K4, H3K9, H3K27, H3K36, H3K79, and H4K20, although numerous methylations of lysine residues have also been found in histones H1, H2A, H2B, and in further positions within H3 and H4 (Morera et al., 2016). Multiple lines of evidence suggest that aberrant histone methylation, which is often caused by a gene mutation, translocation, or dysregulated expression is likely to play a critical role in the development and progression of cancer. In addition, altered expression and mutations of genes that encode histone methyl modifiers and readers correlate with increased incidence of many different types of cancers. (Albert and Helin, 2010; Greer and Shi, 2012; Song et al., 2016; Thinnes et al., 2014). Furthermore, a genetic change, such as an insertion of a transposable element has been suggested for causing aberrant expression or function of histone modifying enzymes, which may subsequently lead to aberrant histone methylation (Ezponda and Licht, 2014; Grégoire et al., 2016).

1.4.3 Histone lysine methylation and linking with DNA methylation

Among the different histone lysine methylation states, H3K9 and H3K27 methylation appear to be the best candidates for epigenetic histone modifications that can be propagated through cell division, not only because they are critical for classic epigenetic phenomena such as position effect variegation, Polycomb silencing, and X chromosome inactivation, but also because these two modified histones have been shown to possess certain characteristics of a prototype-guided information duplication system (Huang et al., 2013). It has recently become apparent that the DNA and histone lysine methylation systems are highly interconnected and can be dependent on one another to play a part in establishing patterns of gene repression during development (Reddington et al., 2013b; Rose and Klose, 2014). It seems that the DNA methylation and histone lysine methylation reciprocally influence each other in the deposition: histone lysine methylation state of chromatin may help to direct DNA methylation patterns, while DNA methylation may serve as a template for the establishment of certain methylation states on accompanying histones in chromatin after DNA replication (Cedar and Bergman, 2009).

At the molecular level, the interplay between DNA methylation and histone methylation during gene silencing can be mediated through direct interactions between DNA methyltransferases and SET domain histone methyltransferases (Vaissière et al., 2008). Furthermore, the presence of methylated CpGs attracts methyl-CpG-binding domain proteins, which in turn recruit repressor complexes that induce repressive histone modifications, resulting in a compact chromatin structure with repressed gene transcription (Du et al., 2015b).

MBD1, for instance, which specifically binds to methylated DNA, can induce transcriptional repression by recruiting the H3K9 methyltransferase SET domain, bifurcated 1 (SETDB1), an enzyme that responsible for the deposition of H3K9me3. Additionally, during S-phase, MBD1 recruits SETDB1 through its TRD domain to the large chromatin assembly factor (CAF)-1 subunit to form an S-phase specific complex to establish new repressive H3K9 methyl marks within pericentric heterochromatin during replication-coupled chromatin assembly (Sarraf and Stancheva, 2004). The S-phase specific complex mediates methylation of H3K9 with the help of heterochromatin protein 1 (HP1), which is a reader of H3K9me3, and promotes the formation of heterochromatic structure (Hiragami-Hamada et al., 2016). The involvement of MBD1 in the formation of condensed heterochromatin suggests that this protein can act as a histone modulator and a chromatin assembler (Li et al., 2015b). A recent study suggested that this complex may also play a crucial role in the maintenance of the silent state of the X chromosome inactivation in female mammalian cells (Minkovsky et al., 2014).

The crosstalk between DNA methylation and PRC2-dependent modification of histone H3K27me3 has been revealed in several organisms (Bogdanovic et al., 2011; Brinkman et al., 2012; van Heeringen et al., 2014; Irimia et al., 2012; Landan et al., 2012; Nakamura et al., 2014; Potok et al., 2013), and both marks are important for normal cell function (de la Calle Mustienes et al., 2015). The first connection between DNA methylation and H3K27 methylation was made when it was observed that Polycomb group protein enhancer of zeste homolog 2 (EZH2) can interact directly with all three DNMTs *in vitro,* implicating a role for PRC2 in directing DNA methylation (Viré et al., 2006). However, subsequent studies in cancer cells discovered that tumor-suppressor gene silencing by EZH2-mediated H3K27me3 is independent of promoter DNA methylation, a finding that seems to contradict with previous studies (Kondo et al., 2008). In addition, Meehan and co-workers have uncovered an unappreciated plausible role for the DNA methylome in ensuring the correct PRC2-targeting and hence the H3K27me3 deposition on chromatin (Reddington et al., 2013b). Therefore, aberrant DNA methylation patterns could possibly affect the affinity of PRC2 binding, leading to Polycomb mis-targeting, and consequently drive carcinogenesis and disease progression (Reddington et al., 2014).

1.5 Epigenetic reprogramming

During mammalian development, epigenetic states of early embryos and PGCs are extensively reprogrammed on a genome-wide scale (Saitou et al., 2012). The genome-wide demethylation of DNA appears to be part of a comprehensive epigenetic reprogramming, together with global changes of histones and their modifications (Feng et al., 2010). This epigenetic reprogramming involves the erasure of previously established epigenetic states followed by the initiation of new epigenetic marks for the totipotency programme (Hill et al., 2014). The reprogramming process plays a pivotal role in the re-establishment of the correct epigenetic marks in early embryogenesis and germ cell development, resetting the patterns associated with somatic differentiation thus preventing incorrect epigenetic information being passed down from one generation to the next (Bunkar et al., 2016; Rose et al., 2013). Moreover, the reprogramming process in the germline may also be important in resetting parent-specific epigenetic states, such as genomic imprints in order to protect the offspring from epigenetic errors (Barlow and Bartolomei, 2014; Hajkova, 2011; Stringer et al., 2013).

Two recent studies have shown the distribution and dynamics of 5mC and 5hmC during mouse germ cell development. These results demonstrate a temporal increment of 5hmC in PGCs between E9.5-E10.5, accompanied by decreased levels of 5mC followed by a significant depletion of 5hmC levels between E11.2-E12.5 (Hackett et al., 2013; Yamaguchi et al., 2013). Meanwhile, other studies revealed the distribution patterns of histone modifications in the developing mouse germ line. These immunofluorescence studies show that H3K9me3 and H3K27me3 were maintained at relatively high levels in PGCs between E10.5 to E12.5 (Kagiwada et al., 2013; Prokopuk et al., 2017; Tang et al., 2016). On the other hand, in mouse embryonic brain, a recent study has found that the levels of 5hmC were elevated during neurogenesis, whereas no significant changes in 5mC levels were detected. Moreover, the formation of 5hmC was often accompanied by the loss of H3K27me3 (Hahn et al., 2013).

Extensive erasure of epigenetic modifications can occur both naturally at two points in the life cycle of mammals, but also artificially using various cell fate reprogramming strategies (Cantone and Fisher, 2013). This artificial reprogramming system in which differentiated somatic cells are converted into a pluripotent state holds great promise for the emerging field of regenerative medicine (Hochberg et al., 2011; Takahashi and Yamanaka, 2013). Artificially reprogrammed cells were called induced pluripotent stem cells (iPSCs) and were first generated by Shinya Yamanaka’s research group in 2006 (Takahashi and Yamanaka, 2006).

Yamanaka’s group discovered that the generation of iPSCs from differentiated somatic cells can be obtained through ectopic expression of four embryonic transcription factors, octamer-binding transcription factor 3/4 (Oct3/4), SRY (sex determining region Y)-box 2 (Sox2), c-myc proto-oncogene (c-Myc), and Kruppel-like factor 4 (Klf4), under the culture conditions for ES cells (Takahashi and Yamanaka, 2006, 2016). These four essential reprogramming factors have become known as the “Yamanaka factors” (Cyranoski, 2014). In addition to regenerative medicine, iPSCs technology may open up new opportunities for disease modeling and drug discovery (Avior et al., 2016; Grskovic et al., 2011).

In addition to iPSCs derivation, there are a number of strategies proven to facilitate the reprogramming of somatic cells to pluripotent cells, including somatic cell nuclear transfer, cell fusion, reprogramming through cell extracts and direct reprogramming (Patel and Yang, 2010). The iPSCs derivation technique has been broadly investigated for the mechanisms underlying direct cell reprogramming, which are not fully understood (Hirschi et al., 2014). However, research into direct reprogramming, in which fully differentiated somatic cells are directly reprogrammed into another differentiated cell type while bypassing the intermediate pluripotent stage, is at a more preliminary stage than work on iPSCs but may eventually provide a safer, quicker method for regenerative medicine (Eisenstein, 2016; Kelaini et al., 2014).

1.6 Aims of the thesis

This PhD study aims to advance scientific understanding of the nuclear epigenetic dynamics during mammalian development. Dynamic developmental DNA methylation changes have been observed in zygotes and germ cells. Nevertheless, DNA methylation dynamics of other tissues in mammalian development have been less studied. Therefore, this study investigated changing nuclear distributions and levels of DNA methylation during development to discover dynamic variations amongst developing mouse tissues. These changes were characterised to report on developmental tissue-specific differences in DNA methylation states.

Therefore, the objectives of this study were:

1. To discover dynamic nuclear changes in DNA methylation and hydroxymethylation in the developing mouse embryonic tissues.

2. To investigate the origin of 5hmC, either as a demethylation intermediate or an independent epigenetic mark.

3. To explore the relationship between DNA methylation (5mC) and histone lysine methylation.

4. To visualise DNA methylation in transgenic MBD-GFP mouse and further characterise the transgenic.

Chapter 2 – Materials and methods

2.1 Animals

Wild type CD-1 outbred mouse line and transgenic methyl binding domain-green fluorescent protein (MBD-GFP) mice in the same CD-1 background used in this study were generated and maintained in the animal facility at the MRC Human Genetics Unit (HGU), Institute of Genetics and Molecular Medicine, The University of Edinburgh, Edinburgh, United Kingdom. Heterozygous transgenic MBD-GFP embryos and wild-type (non-GFP) siblings were obtained from crosses between heterozygous transgenic MBD-GFP males and CD-1 females of matching wild type background. Female mice that had reached sexual maturity at about 6 weeks of age were used to generate embryos at specific developmental stages. To establish natural matings, male and female mice were housed together overnight and the females were checked the following morning for the presence of vaginal plugs.

2.1.1 Staging of mouse embryos

The presence of a vaginal plug the next morning was referred to as embryonic day E0.5 (in the literature also described as 0.5 days post-conception or DPC). However, this system is not a reliable indicator of the anatomical stage, thus unable to stage mouse embryos comprehensively. Furthermore, there is considerable uncertainty about the precise time of conception, which can result in inter-litter variation in embryo development as a consequence of variable implantation time and disproportionate supply of nutrients. Nevertheless, mouse embryos can be accurately staged by observing morphological landmarks including eye development, limb and tail formation through a dissecting microscope (Wong et al., 2015).

In the present study, natural matings were used to obtain embryos at E9.5, E10.5, E11.5, E12.5, E13.5 and E14.5 stages of development **(Figure 2.1)**.

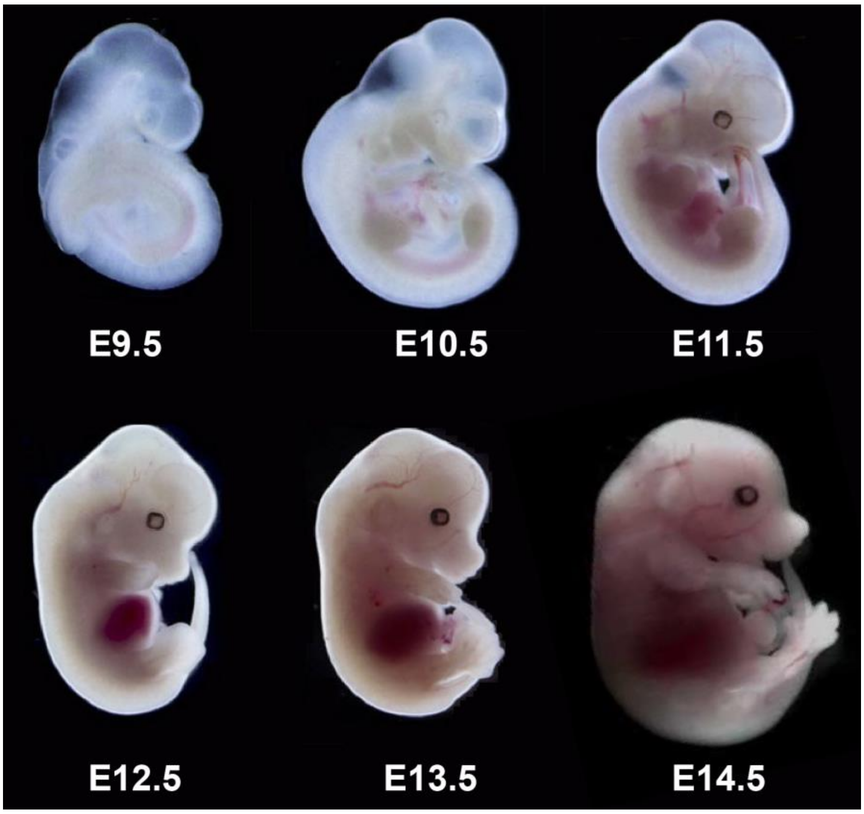

Figure 2.1: Early-stage mouse embryos. Embryos at day 9.5, 10.5, 11.5, 12.5, 13.5, 14.5 (E9.5, E10.5, E11.5, E12.5, E13.5, E14.5) stages of embryonic development were used in this study. Figure relabelled from www.pdn.cam.ac.uk/directory/watson-erica.

2.1.2 Mouse tissue dissection

Plug-positive females were considered as pregnant. Pregnant mice were sacrificed at specific stages by cervical dislocation. A midline laparotomy was then performed to expose the pregnant uterus. The paired uterine horns were dissected out and flushed with Dulbecco's phosphate-buffered saline (DPBS) (Life Technologies). The uterine horns were placed in sterile 15 ml centrifuge tubes (Corning) containing 10 ml DPBS and immediately transported on ice to the laboratory within 0.5 hours.

All mouse work, including mating setup and laparotomy, was performed by David Read at HGU.

2.1.3 Embryo collection

Individual embryos were dissected under a Leica MZ7.5 dissecting microscope (Leica, Bensheim, Germany) from the uterine horns while in DPBS. With a pair of surgical scissors, each embryo was first separated by cutting between implantation sites along uterine horns. Following separation, the embryos were then dissected out of the uterus with the placenta and yolk sac attached and intact. Using fine forceps, conceptuses with embryos within their yolk and amniotic sacs were opened and Reichert's membranes surrounding the yolk sacs were subsequently removed. After that, the umbilical vessels were cut with fine scissors to separate the embryos from the placentas with the yolk sacs intact. Finally, the yolk sacs were cut and the thin amniotic sacs surrounding the embryos were removed to release the embryos. The embryos were placed in an individual well of a 24-well plate containing DPBS for microscopic observation. A fluorescent microscope with a eGFP Bandpass Emission filter set (Chroma 41017) was used to examine GFP positive and GFP negative embryos.

The protocol described above is representative of that used for dissecting embryos from E9.5 to E14.5. Typically, 11-17 embryos were collected per pair of uterine horns.

2.2 Tissue embedding for cryopreservation

A simple freezing technique for the cryopreservation of mouse whole embryos was used in this study based on comparative method testing in the lab (Aguilar-Sanchez, 2016). After dissection, individual embryos were embedded in optimal cutting temperature (OCT) (Tissue-Tek) compound and snap frozen on dry ice. Embedding in OCT followed by snap freezing not only preserves cellular morphology and retains the antigenicity of the target molecules of epigenetic markers, but also allows for easier sectioning of the frozen tissue.

To prepare the frozen tissues for cryosectioning, a few drops of OCT were first placed onto the centre of the bottom of a cryomold [Simport base mould 15 x 15 x 5mm, Scientific Lab Supplies (SLS)]. This was followed by pat drying of the dissected embryos with tissue paper until all surface liquid was absorbed. Excess liquid on the surface of the tissue can form ice crystals, which can be responsible for tissue cracks during the sectioning procedure. Using forceps, the surface dry embryos were then transferred to the OCT-filled cryomolds and gently submerged into the media. The embryos were carefully oriented in the cryomolds near the bottom to ensure maximum exposure for cutting. More OCT was added to fully cover the exposed embryos. It was crucial to avoid formation of air bubbles when adding the OCT as this may cause problems when cutting cryosections. Moreover, it was also important to ensure that the top surface of the OCT compound was completely level and covering the embryos. The embryos were allowed to sit in OCT for a few minutes to promote adhesion of the OCT to the embryos during sectioning.

Cryomolds were immediately placed on dry ice for a few minutes until the OCT turned into a solid white colour, indicating that the embryos were sufficiently frozen. After hardening of the OCT compound, the frozen blocks were then stored in an air-tight container at -70ºC until ready to proceed with cryosectioning.

2.3 Cryosectioning

All sectioning steps described in this procedure were performed using a Bright cryostat (Bright Instruments, Huntingdon, UK). Before cryosectioning, the cryostat chuck was first covered with a thin layer of OCT embedding compound. Then, the frozen tissue block was immediately placed on the OCT-coated chuck in the appropriate orientation. The tissue/OCT/chuck complex was allowed to freeze solid (10 to 15 minutes at -20°C) inside the cryostat. The positioning of the frozen block was adjusted to align the block with the knife blade. The tissue block was trimmed to expose the tissue surface to a level where a representative section could be cut. Trimming was normally performed at a thickness of 10 to 20 µm.

After trimming, the cryostat was set to cut sections at a thickness of 5 µm. Several serial 5 µm sections were then cut. A paint brush was used to help guide the emerging sections over the microtome blade knife (MX35 Premier microtome blade, Thermo Scientific). The sections were immediately transferred to a room temperature microscope slide (Superfrost Plus, ThermoFisher) by touching the slides to the sections. This step was accomplished within 1 minute of cutting the sections to avoid freeze-drying of the tissues. A maximum of two sections was collected on each slide. To maximize the adherence, the sections were allowed to air-dry at room temperature until the sections firmly adhered to the slides. After drying at room temperature, the slides were ready for fixation.

2.4 Immunofluorescence staining

Indirect immunofluorescence studies were performed on cryostat sections on the day of cutting. Immunofluorescent staining of epigenetic modifications allowed for the nuclear presence and distribution of these epigenetic marks to be examined. Mouse embryonic tissues from stages E9.5 to E14.5 were used in this study as 5 µm cryosections of whole embryos adhered on microscope slides. In addition, MBD-GFP mouse embryonic tissues from stages E10.5 to E14.5 were also used as 5 µm cryosections of whole embryos adhered on microscope slides to visualise DNA methylation in tissues and subsequently characterise the transgenic model.

Standard immunofluorescence staining procedures were used. The standard protocols were tested on both mouse embryonic fibroblasts and cryosections to ensure that the protocols were working reliably. The protocol for 5mC detection on cryosections, however, required methodology changes and optimisation. The protocol optimisation for 5mC immunodetection is discussed in greater detail in Chapter 3.

Standard immunofluorescence staining protocols for detecting histone modifications and DNA methylation on mouse embryonic fibroblasts and cryosections are described below. An optimised 5mC immunodetection protocol is also presented.

2.4.1 Histone immunostaining in mouse embryonic fibroblasts

Mouse E13.5 fibroblasts used in this study were grown on 13 mm No. 1.5 round coverslips (VWR) inside a 24-well plate (Greiner). The cells were washed with PBS containing 1 mM $CaCl_2$ (calcium chloride 2-hydrate, BDH) twice for 5 minutes each. The cells were fixed in 200 µl of 4% of PFA (paraformaldehyde, Sigma Aldrich) for

10 minutes at room temperature. PFA solution was removed and cells were washed with 200 µl of PBS (phosphate buffered saline, Bioline) twice for 5 minutes each. The cells were permeabilised with 200 µl of 0.4% of Triton X-100 (VWR) for 15 minutes. Triton X-100 was removed and cells were washed with PBS twice for 10 minutes each. The cells were blocked with 200 µl of 2% of BSA in PBS (bovine serum albumin, Sigma Aldrich) for 1 hour. The blocking solution was removed and the cells were incubated with 200 µl of anti-H3K9me3 primary antibody (rabbit polyclonal antibody, Millipore) at 1:1000 dilution in blocking solution overnight at 4^{o}C. The antibody was removed and cells were washed with 200 µl of PBST (containing 0.05% of Tween 20, BDH) three times for 15 minutes each. The cells were incubated with 200 µl of Alexa Fluor 488 donkey anti-rabbit secondary antibody (Invitrogen Molecular Probes) at 1:200 dilution in blocking solution for 1 hour. The antibody was removed and cells were washed with PBST for 15 minutes. The cells were incubated with 200 µl of 0.3 µM of DAPI (4′,6-Diamidino-2-phenylindole dihydrochloride, Sigma Aldrich) for 15 minutes. DAPI solution was removed and cells were washed with PBST twice for 15 minutes each. The coverslips carrying the cells were mounted onto slides with mounting medium (Prolong Gold, Invitrogen Molecular Probes). The cells were left to cure overnight in the dark at room temperature and stored at 4°C.

2.4.2 Histone immunostaining in mouse embryonic tissues

The following staining procedure was performed at room temperature in a dark humidity chamber unless indicated otherwise. PAP pen liquid blocker (a water-repellent marking pen; Sigma) was used to help retain reagents during incubation. The cryosectioned tissues were fixed in 200 µl of 4% of PFA for 50 minutes at room temperature within a PAP pen traced area of the slide. The PFA solution was removed from the slide by gently tapping the side onto paper tissue and tissues were washed with 200 µl of PBS twice for 5 minutes each. The tissues were permeabilised with 200 µl of 0.4% of Triton X-100 for 30 minutes. Triton X-100 was removed and tissues were washed with PBS twice for 10 minutes each. The tissues were blocked with 200 µl of 2% of BSA for 1 hour. Blocking solution was removed and tissues were incubated with either 200 µl of anti-H3K9me3 primary antibody (Millipore) at

1:1000 dilution in blocking solution or 200 µl of anti-H3K27me3 primary antibody (Millipore) at 1:500 dilution overnight at 4°C. The antibody was removed and tissues were washed with 200 µl of 0.05% of PBST three times for 15 minutes each. The tissues were incubated with 200 µl of Alexa Fluor 488 donkey anti-rabbit **(see Chapter 3)** or 200 µl of Alexa Fluor 568 donkey anti-rabbit (Invitrogen Molecular Probes) **(see Chapter 5)** secondary antibodies at 1:200 dilution in blocking solution for 1 hour. The antibody was removed and tissues were washed with PBST for 15 minutes. The tissues were incubated with 200 µl of 0.3 µM of DAPI for 15 minutes. DAPI solution was removed and tissues were washed with PBST twice for 15 minutes each. The tissues were mounted using Prolong Gold antifade reagent (Molecular Probes, Life technologies) and covered with a coverslip. The tissues were left to cure overnight in the dark at room temperature and stored at 4°C.

2.4.3 DNA methylation immunostaining in mouse embryonic fibroblasts

Mouse embryonic fibroblasts were grown on 13 mm round coverslips and handled as stated in section 2.4.1. The cells were washed with PBS containing 1 mM $CaCl_2$ twice for 5 minutes each. The cells were fixed in 200 µl of 4% of PFA for 10 minutes at room temperature. PFA solution was removed and cells were washed with 200 µl of PBS twice for 5 minutes each. The cells were treated with 200 µl of 4 M of HCl (hydrochloric acid, VWR) for 10 minutes to denature the DNA. HCl solution was removed and cells were washed with PBS three times for 5 minutes each. The cells were permeabilised with 200 µl of 0.4% of Triton X-100 for 15 minutes. Triton X-100 was removed and the cells were washed with PBS twice for 10 minutes each. The cells were blocked with 200 µl of 2% of BSA for 1 hour. The blocking solution was removed and the cells were incubated with 200 µl of anti-5mC primary antibody (mouse monoclonal antibody 33D3, Diagenode) at 1:300 dilution in blocking solution for 2 hours at room temperature. The antibody was removed and cells were washed with 200 µl of 0.05% of PBST three times for 15 minutes each. The cells were incubated with 200 µl of Alexa Fluor 488 donkey anti-mouse secondary antibody (Invitrogen Molecular Probes) at 1:200 dilution in blocking solution for 1 hour. The antibody was removed and cells were washed with PBST for 15 minutes.

The cells were incubated with 200 µl of 0.3 µM of DAPI for 15 minutes. DAPI solution was removed and cells were washed with PBST twice for 15 minutes each. The coverslips were mounted onto slides as described before.

ssDNA primary antibody (rabbit polyclonal antibody, Demeditec Diagnostics) followed by Alexa Fluor 488 donkey-anti rabbit secondary antibody was used as a control immunostaining performed in parallel.

2.4.4 DNA methylation immunostaining in mouse embryonic tissues (before optimisation)

Described below is the standard tissue immunostaining procedure (before optimisation), performed at room temperature in a dark humidity chamber unless indicated otherwise.

Tissues were fixed by overlaying with 200 µl of 4% of PFA for 50 minutes at room temperature within a PAP pen traced area of the slide as described in section 2.4.2. PFA solution was removed and tissues were washed with 200 µl of PBS twice for 5 minutes each. Tissues were treated with 200 µl of 4 M of HCl for 15 minutes to denature the DNA. HCl solution was removed and tissues were washed with PBS three times for 5 minutes each. The tissues were permeabilised with 200 µl of 0.4% of Triton X-100 for 30 minutes. Triton X-100 was removed and tissues were washed with PBS twice for 10 minutes each. The tissues were blocked with 200 µl of 2% of BSA for 1 hour. This blocking solution was removed and tissues were incubated with 200 µl of anti-5mC primary antibody for 2 hours at room temperature at 1:300 dilution in blocking solution. The antibody was removed and tissues were washed with 200 µl of 0.05% of PBST three times for 15 minutes each. The tissues were incubated with 200 µl of Alexa Fluor 488 donkey anti-mouse secondary antibody for 1 hour at 1:200 dilution in blocking solution. The antibody was removed and tissues were washed with PBST for 15 minutes. The tissues were incubated with 200 µl of 0.3 µM of DAPI for 15 minutes. DAPI solution was removed and the tissues were washed with PBST twice for 15 minutes each. The tissues were mounted with mounting medium and covered with a coverslip as described before in section 2.4.2.

Three controls were used in this immunostaining procedure. The first control, for DNA denaturation and antibody specificity, used ssDNA primary antibody followed by Alexa Fluor 488 donkey anti-rabbit secondary antibody; the second control for nonspecific background used Alexa Fluor 488 donkey anti-mouse secondary antibody without primary antibody; and the third control for auto-fluorescence was without both primary and secondary antibodies.

2.4.5 DNA methylation immunostaining in mouse embryonic tissues (after optimisation)

Described below is the optimised tissue immunostaining procedure, performed at room temperature in a dark humidity chamber unless indicated otherwise.

Tissues were fixed by overlaying with 200 µl of 2% of PFA for 50 minutes at room temperature within a PAP pen traced area of the slide as described in section 2.4.2. PFA solution was removed and tissues were washed with 200 µl of PBS twice for 5 minutes each. The tissues were permeabilised with 200 µl of 0.5% of Triton X-100 for 30 minutes. Triton X-100 was removed and tissues were washed with PBS twice for 10 minutes each. Tissues were boiled in 10 mM sodium citrate pH 6 either using hot plate or microwave techniques **(section 2.4.5.1)** to denature the DNA. Tissues were washed in 250 ml of PBS on a rocking jar for 15 minutes. The tissues were blocked with 200 µl of blocking buffer, a mixture of 2% of BSA and 2% of donkey serum in PBS for 1 hour. This blocking solution was removed and tissues were incubated with 200 µl of anti-5mC primary antibody for 2 hours at room temperature at 1:300 dilution in BSA solution. The antibody was removed and tissues were washed with 200 µl of PBST three times for 15 minutes each. The tissues were incubated with either 200 µl of Alexa Fluor 488 donkey anti-mouse **(see Chapter 3)** or 200 µl of Alexa Fluor 568 donkey anti-mouse (Invitrogen Molecular Probes) **(see Chapter 4)** secondary antibodies for 1 hour at 1:200 dilution in BSA solution. The antibody was removed and tissues were washed with PBST for 15 minutes. The tissues were incubated with 200 µl of 0.3 µM of DAPI for 15 minutes. DAPI solution was removed and the tissues were washed with PBST twice for 15 minutes each. The tissues were mounted with mounting medium and covered with a coverslip as described in section 2.4.2.

2.4.5.1 DNA denaturation for immunostaining

Heat-mediated antigen retrieval was used in this study to replace a problematic acid-dependent DNA denaturation step in the standard tissue immunostaining procedure. Antigen retrieval (also known as epitope retrieval or unmasking) refers to any technique in which the masking effects of aldehyde fixation on some antigens are reversed and epitope-antibody binding is restored. But, in this case, heat-induced antigen retrieval approach also denatured DNA double-strands to make the nucleotides accessible to antibody detection, at the same time as it retrieved antigen epitopes. Two methods of DNA denaturation were successfully optimised; using a hot plate and microwave techniques. But only the microwave technique was taken forward in Chapter 4 due to several practical advantages. Described below are the two methods of DNA denaturation.

For hot plate technique, a heat resistant beaker containing 0.01 M sodium citrate pH 6.0 was first preheated on a hot plate to near boiling point. The slides were then transferred in a holder to the beaker containing preheated 0.01 M sodium citrate pH 6.0. The beaker was immediately brought to a boil on the hot plate. Boiling was continued for a further 10 minutes to complete DNA denaturation and antigen retrieval. The beaker was carefully removed from the hot plate and the heated slides were allowed to cool for 10 minutes while submerged in solution. The slides were finally rinsed in a rocking jar containing 250 ml of PBS for 15 minutes to remove any loose material.

For microwave technique, a wide microwavable dish filled with 2.5 cm of H_2O was first preheated in a microwave oven for 8 minutes at full power. In parallel, a Schieferdecker jar was filled with 0.01 M sodium citrate pH 6.0 and the slides were then put in. It was important to ensure that the slides were completely covered with the buffer. The jar (without the lid) was placed in the previously preheated dish, which contained hot H_2O in the bottom. The jar containing the slides was heated in the microwave oven at full power for 3 minutes. It was very important to ensure that the antigen retrieval solution was not evaporated to the point that the tissue sections dried. More antigen retrieval solution was added if necessary. The slides were again heated for an additional 3 minutes to complete DNA denaturation and antigen retrieval. The Schieferdecker jar was carefully removed from the microwave oven and the heated slides were allowed to cool for 10 minutes while submerged in solution. The slides were finally rinsed in a rocking jar containing 250 ml of PBS for 15 minutes to remove any loose material.

2.4.6 DNA hydroxymethylation immunostaining in mouse embryonic tissues

The optimised tissue immunostaining protocol used for staining 5mC **(section 2.4.5)** was employed for the staining of 5hmC. Like anti-5mC antibody, anti-5hmC antibody also required denatured DNA as the native context of double-stranded DNA may sterically hinder the primary antibody from binding to its target. Anti-5hmC primary antibody followed by either Alexa Fluor 568 donkey-anti rabbit **(see Chapter 3)** or Alexa Fluor 488 donkey-anti rabbit **(see Chapter 4)** secondary antibodies was used for immunodetection of 5hmC. Tissues were incubated with anti-5hmC primary antibody (Active Motif) in the dark for 2 hours at room temperature at 1:500 dilution in BSA solution.

2.4.7 GFP immunostaining in MBD-GFP mouse embryonic tissues

The optimised tissue immunostaining protocol used for staining 5mC **(section 2.4.5)** was employed for the detection of GFP in transgenic mouse embryonic tissues. Double staining of GFP and 5mC **(see Chapter 3)** was initially performed to ensure that the MBD-GFP and 5mC results observed in transgenic mouse tissues were well correlated before performing single staining of GFP. No denaturation step was performed for single staining of GFP in Chapter 6. GFP double immunostaining was only successful when using the microwave-heating denaturation method. The protocol optimisation for combinatorial applications of the GFP immunostaining method with the procedure requiring heat treatment is discussed in more detail in Chapter 3.

Anti-GFP primary antibody (Invitrogen) followed by Alexa Fluor 488 donkey-anti rabbit was used for immunodetection of GFP to overcome weak fluorescent signals of native GFP. GFP-booster Atto488 (Chromotek) was also used in the protocol optimisation for the preservation of native GFP proteins. Tissues were incubated with anti-GFP primary antibody in the dark for 2 hours at room temperature at 1:200 dilution in BSA solution. For GFP booster, tissues were incubated with the GFP booster primary antibody at 1:200 dilution in BSA solution using the same conditions as anti-GFP.

2.4.8 Immunostaining for epigenetic modifier enzymes in mouse embryonic tissues

Enzymes responsible for active DNA demethylation and methylation events were also investigated in this study using the indirect immunofluorescence technique. These enzymes included Tet1, Tet2, Tet3 and DNMT3A. The standard tissue immunostaining procedure used for staining histone modifications **(section 2.4.2)** was used in this study to stain for Tet1, Tet2, Tet3 and DNMT3A. For Tet1 staining, Tet1 primary antibody (GeneTex) followed by Alexa Fluor 488 donkey-anti rabbit was used. For Tet2 staining, Tet2 primary antibody (Abcam) followed by Alexa Fluor 488 donkey-anti rabbit was used. For Tet3 staining, Tet3 primary antibody (Millipore) followed by Alexa Fluor 488 donkey-anti rabbit was used and for DNMT3A staining, DNMT3A primary antibody (Santa Cruz Biotechnology) followed by Alexa Fluor 568 donkey-anti goat (Invitrogen Molecular Probes) was used. Tissues were incubated with primary antibodies in the dark at specific dilutions in BSA solution **(Table 2.1)** overnight at 4^{o}C.

2.4.9 Tissue-specific marker immunostaining in wild-type and transgenic mouse embryonic tissues

Tissue-specific markers used in this study were cTnT (cardiac marker), HNF4α (hepatic marker), RC2 (nestin marker) and Vasa (DDX4/MVH) (germ cell marker). For double staining of cTnT and RC2 with histone modifications in wild-type mouse embryonic heart and brain tissues, respectively, the standard tissue immunostaining procedure used for staining histone modifications **(section 2.4.2)** was used. For double staining of cTnT, HNF4α and RC2 with GFP in transgenic mouse embryonic heart, liver and brain tissues, respectively, the optimised tissue immunostaining protocol used for staining 5mC **(section 2.4.5)** was used, but with the omission of the denaturation step. For double staining of Vasa and 5mC in wild-type mouse embryonic gonadal tissues, the optimised tissue immunostaining protocol for staining 5mC was used to observe the genome-wide DNA demethylation proses in mouse primordial germ cells.

For cardiac staining, anti-cTnT primary antibody (DHSB) followed by either Alexa Fluor 488 donkey-anti mouse or Alexa Fluor 568 donkey-anti mouse was used. For hepatic staining, anti-HNF4α primary antibody (Santa Cruz Biotechnology) followed by Alexa Fluor 568 donkey-anti goat was used. For nestin staining, RC2 primary antibody (DHSB) followed by either Alexa Fluor 488 donkey-anti mouse or Alexa Fluor 568 donkey-anti mouse was used. For primordial germ cell staining, anti-DDX4/MVH primary antibody (Abcam) followed by Alexa Fluor 488 donkey-anti rabbit was used. Tissues were incubated with primary antibodies in the dark at specific dilutions in BSA solution **(Table 2.1)** either overnight at 4^{o}C or for 2 hours at room temperature.

2.5 Immunofluorescence microscopy

The immunostained tissues were analysed using advanced microscopic imaging techniques. The fluorescent molecules can be visualised either by fluorescence widefield microscopy or confocal microscopy. Immunofluorescence microscopy is an extremely useful technique for detecting and localising particular antigens within tissue sections via fluorescently-labeled antibodies. After staining, the slides were viewed using a Nikon Eclipse-Ti inverted fluorescence microscope (Nikon, Tokyo, Japan) **(see Chapter 3 and Chapter 6)** and Zeiss LSM 780 confocal microscope with an oil immersion 40X objective **(see Chapter 4 and Chapter 5, unless indicated otherwise)**. The slides were examined under a fluorescence microscope using DAPI/FITC/tetramethyl rhodamine isothiocyanate (TRITC) triple band-pass filter sets, whereas under the confocal microscope, triple band-pass filter sets for DAPI/FITC/Cyanine 3 (Cy3) was used.

In Chapter 3, the fluorescence microscope was used to observe the presence and distribution pattern of epigenetic markers. In Chapter 4 and Chapter 5, the confocal microscope was used to observe the dynamic nuclear changes in DNA methylation (5mC and 5hmC) and histone modifications (H3K9me3 and H3K27me3) states during embryonic development as well as the enzymes (Tet1, Tet2, Tet3 and DNMT3A) that are responsible for the dynamic changes in DNA methylation. For dynamic studies, confocal microscopy imaging was performed under controlled conditions. A set of images of each tissue type for each epigenetic marker at different developmental stages was taken on the same day, using the exact same exposure and gain to ensure maximum reliability and informativeness of the imaging data.

Laser scanning confocal microscopy was used for dynamic studies due to several advantages it possessed over conventional widefield optical microscopy. One of the main advantages of confocal microscopy is the ability to control the depth of field. A key advantage of confocal microscopy is the ability to remove out-of-focus noise, thus producing sharp and high-resolution images. The confocal microscopy is also capable of eliminating or reducing the background information away from the focal plane.

2.6 Stage-specific embryonic tissue identification

For immunofluorescence staining of 5mC and 5hmC, no tissue-specific markers were used as immunodetection of 5mC and 5hmC required denaturation of the DNA which was totally incompatible with the preservation of most protein epitopes. Therefore, tissue identity was determined by morphology. Morphological structures of stage-specific embryonic tissues were identified by reference to ‘Kaufman’s Atlas’ (Kaufman, 1992) and the web publication of the open access mouse embryo eHistology resource (www.emouseatlas.org/emap/eHistology/) (Graham et al., 2015).

The Atlas of Mouse Development by Matthew H. Kaufman is an essential text and a much used reference for understanding mouse developmental anatomy. This atlas describes mouse developmental anatomy at the histological level. It provides clear and comprehensive descriptions of the anatomical attributes relevant to each stage of development.

2.7 Image processing and analysis

The obtained fluorescence images were processed and analysed using the free, open-source software ImageJ (Schneider et al., 2012). Using ImageJ, the contrast and brightness of individual channels in the stack were adjusted. But for confocal images, specific for dynamic studies, no adjustments were made. The confocal images with raw fluorescence intensities were used to avoid possible misinterpretation of the results.

2.8 Semi-quantitative image analysis

Standard imaging conditions were employed for all whole mount immunostained cryosections to allow for semi-quantitative comparative analysis of nuclei from different tissues. Zeiss LSM 780 confocal microscope images capturing DAPI, A488 and A568 signal were saved as three channels in lsm format and imported into ImageJ software as a stack. Outlines of multiple isolated nuclei were manually traced with the drawing tool (Shift key down) in the DAPI channel and selections were saved as filled objects on a mask layer using the ‘Fill’ command. Objects on the mask layer were thresholded using the ‘Threshold’ command and the corresponding intensities of these nuclei in the green and red channel were measured with the ‘Analyze Particles’ command. The list of values for each nucleus was exported to Excel for further analysis.

Table 2.1: Primary antibodies used in the experiments. Optimal dilutions for each of the antibodies are shown in the second column.

Antibody	Dilution in BSA solution	Supplier
H3K9me3	1:1000	Millipore
H3K27me3	1:500	Millipore
5mC	1:300	Diagenode
ssDNA	1:500	Demeditec Diagnostics
5hmC	1:500	Active Motif
GFP	1:200	Invitrogen
GFP-booster Atto488	1:200	Chromotek
Tet1	1:600	GeneTex
Tet2	1:250	Abcam
Tet3	1:250	Millipore
DNMT3A	1:100	Santa Cruz Biotechnology
cTnT	1:250	DHSB
HNF4α	1:250	Santa Cruz Biotechnology
RC2	1:100	DHSB
Vasa	1:300	Abcam

Table 2.2: Secondary antibodies used in the experiments. Optimal dilutions for each of the antibodies are shown in the second column.

Antibody	Dilution in BSA solution	Supplier
Alexa Fluor 488 donkey anti-rabbit	1:200	Invitrogen Molecular Probes
Alexa Fluor 568 donkey anti-rabbit	1:200	Invitrogen Molecular Probes
Alexa Fluor 488 donkey anti-mouse	1:200	Invitrogen Molecular Probes
Alexa Fluor 568 donkey anti-mouse	1:200	Invitrogen Molecular Probes
Alexa Fluor 568 donkey anti-goat	1:200	Invitrogen Molecular Probes

Chapter 3 – Optimised immunostaining for studying DNA methylation in tissues

3.1 Introduction

Immunostaining refers to an antibody-based method to identify the presence and localisation of a particular protein within individual cells or tissue sections (Maity et al., 2013). Detection of a specific protein or antigen within cells is known as immunocytochemistry (Burry, 2011), whereas antigen detection within tissues is generally known as immunohistochemistry (Shi and Stack, 2015). Visual detection of specific target antigens is achieved through the use of antibodies that have been chemically conjugated to fluorescent dyes such as fluorescein isothiocyanate (FITC) or tetramethyl rhodamine isothiocyanate (TRITC), a technique usually referred to as immunofluorescence of IF (Odell and Cook, 2013). Immunofluorescent-stained cells or tissue sections can then be visualised using fluorescence widefield or confocal microscopy (Wang and Matise, 2013).

There are two main methods of immunofluorescent staining, direct and indirect. For direct immunofluorescent staining, the antibody (called the primary antibody) against the antigen of interest is directly conjugated to a fluorescent dye (Pástor, 2010). On the other hand, for indirect immunofluorescence, the primary antibody is unconjugated and an additional fluorescence dye-conjugated antibody (called the secondary antibody) directed toward the primary antibody is used for detection of target antigen (Barbierato et al., 2012). The latter method, while requiring an additional step, results in secondary antibody clustering at the site of the epitope with amplification of the signal.

Immunofluorescence staining has been frequently used to study dynamic changes in DNA modification states at time points during mammalian development (Rose et al., 2014; Santos and Dean, 2006). In addition, highly specific antibodies raised against 5mC, and more recently, its derivatives 5hmC, 5fC and 5caC have been developed (Inoue et al., 2011; Wu and Zhang, 2011). However, for immunofluorescence staining of 5mC and 5hmC, DNA must first be denatured into single strands in order to increase the accessibility of the epitopes to the antibodies (Ito et al., 2010; Jørgensen et al., 2006; Li and O'Neill, 2013). The most commonly-employed method for the denaturation of DNA is acid treatment, but the denaturation method may vary depending on the application (Salvaing et al., 2012; Yamaguchi et al., 2013; Zhang et al., 2016a). Moreover, in the case of acid treatment, harsh denaturing conditions may compromise the integrity of the chromatin structure (Jørgensen et al., 2006).

A number of methodologies were acquired for this study, including DNA methylation immunostaining in mouse embryonic tissues. As this methodology is regarded as standard in the field, it was very important to have this working reliably on mouse embryo cryosections in order to be able to investigate tissues undergoing dynamic nuclear changes in DNA methylation and hydroxymethylation states. In particular, the study of their possible relationship with histone modifications during mouse embryonic development required comparable quality of immunostaining of these independent assays.

Therefore, the aims of this chapter were:

1. To test standard histone immunocytochemistry protocols specific for mouse E13.5 fibroblasts and cryosections, respectively.

2. To test standard DNA methylation immunocytochemistry protocols specific for mouse E13.5 fibroblasts and cryosections, respectively.

3. To optimise standard DNA methylation immunohistochemistry protocol on mouse E13.5 thin cryosections, and to perform this optimised protocol for DNA hydroxymethylation immunostaining.

4. To test optimised DNA methylation immunohistochemistry protocol on MBD-GFP mouse E11.5 cryosections, and to improve this protocol.

3.2 Histone immunostaining in mouse embryonic fibroblasts

Immunostaining was performed on fixed mouse E13.5 fibroblasts using a standard histone immunocytochemistry protocol, as outlined in Chapter 2 Section 2.4.1.

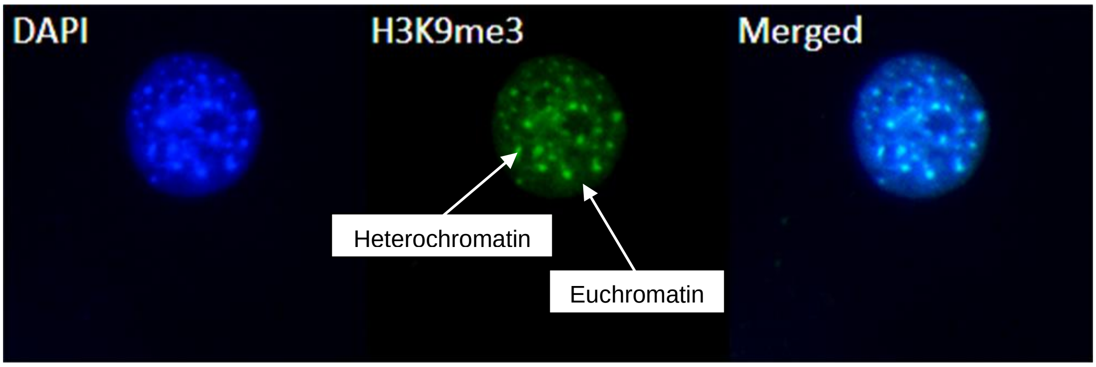

Figure 3.1: Histone immunostaining in E13.5 mouse embryonic fibroblasts. Representative staining of mouse embryonic fibroblasts is shown. Left panel: cell nuclear DNA counterstained with DAPI (blue). Middle panel: cell stained with anti-H3K9me3 primary antibody (green). Right panel: merged image. Antibody-specific histone immunostaining of cultured cells is confirmed by colocalisation of H3K9me3 in DNA dense heterochromatin foci.

Histone H3K9me3 immunostaining demonstrated colocalisation with DAPI-stained dense DNA regions representing heterochromatin (DAPI bright dots) **(Figure 3.1)**, where this epitope is expected. This shows that the method used for staining H3K9me3 in mouse embryonic fibroblasts was successful.

3.3 Histone immunostaining in mouse embryonic tissues

Immunostaining was performed on mouse E13.5 fixed cryosections using a standard histone immunohistochemistry protocol as outlined in Chapter 2 Section 2.4.2.

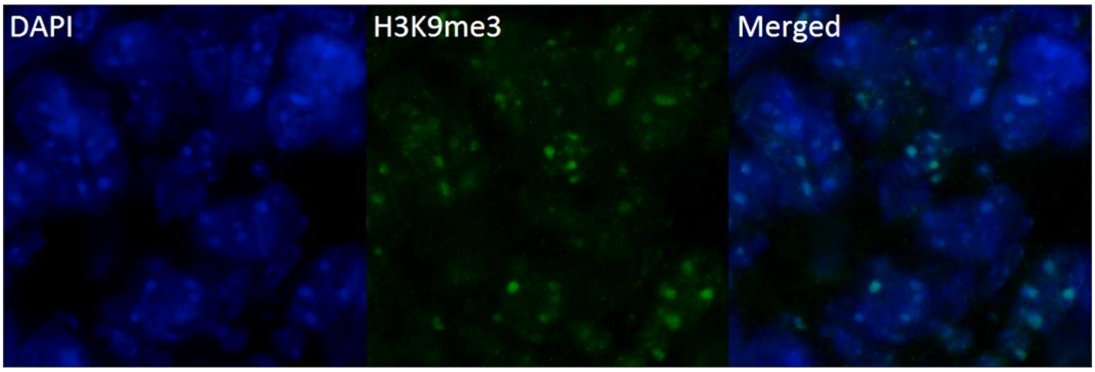

Figure 3.2: Histone immunostaining in E13.5 mouse embryonic brain tissues. Representative staining of mouse embryonic brain tissue sections is shown. Left panel: tissues nuclear DNA counterstained with DAPI (blue). Middle panel: tissues stained with anti-H3K9me3 primary antibody (green). Right panel: merged image. Antibody-specific histone immunostaining of cryosections is apparent by colocalisation of H3K9me3 in DNA dense heterochromatin foci.

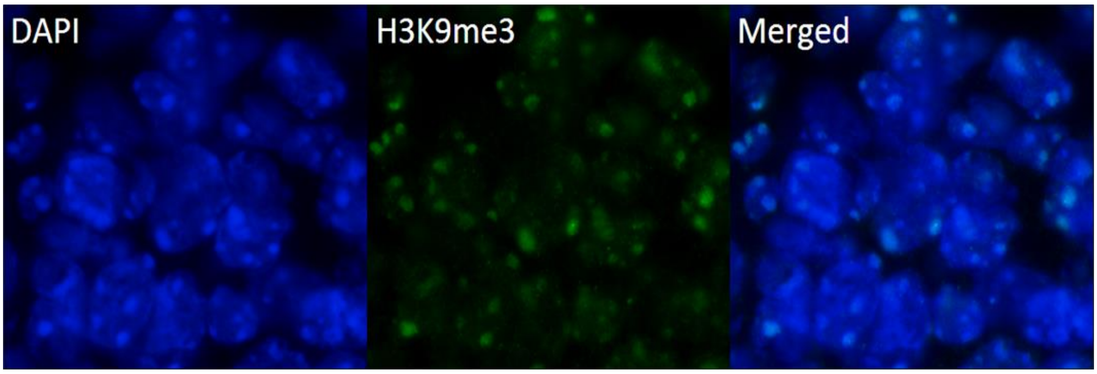

Figure 3.3: Histone immunostaining in E13.5 mouse embryonic liver tissues. Representative staining of mouse embryonic liver tissue sections is shown. Left panel: tissues nuclear DNA counterstained with DAPI (blue). Middle panel: tissues stained with anti-H3K9me3 primary antibody (green). Right panel: merged image. Antibody-specific histone immunostaining of cryosections is confirmed by colocalisation of H3K9me3 in DNA dense heterochromatin foci.

Histone H3K9me3 immunostaining showed colocalisation with DAPI-stained foci of high DNA density **(Figure 3.2 and 3.3)**, as expected. This demonstrates that the method used for immunostaining for H3K9me3 in mouse embryonic tissues was successful.

3.4 DNA methylation immunostaining in mouse embryonic fibroblasts

Immunostaining was performed on mouse E13.5 cultured fibroblasts following the standard DNA methylation immunocytochemistry protocol outlined in Chapter 2 Section 2.4.3.

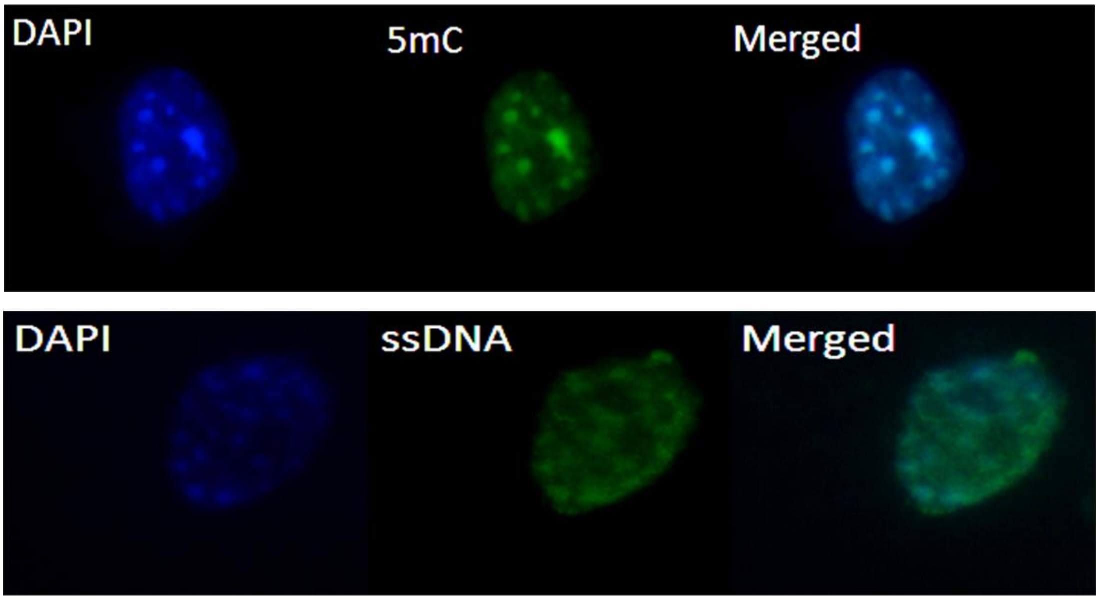

Figure 3.4: DNA methylation immunostaining in E13.5 mouse embryonic fibroblasts. Representative staining of mouse embryonic fibroblasts is shown. Left panel: cell nuclear DNA counterstained with DAPI (blue). Middle panel: cell stained with primary antibodies against, 5mC (green) and ssDNA (green), respectively. Right panel: merged images. Antibody-specific DNA immunostaining in cultured cells is apparent using the standard protocol.

Immunostaining for 5mC and ssDNA demonstrated colocalisation with DAPI-stained DNA **(Figure 3.4)**. DNA dense foci stained preferentially for 5mC, whereas nuclear DNA stained more evenly for ssDNA, as expected. This shows that the standard method used for staining 5mC in mouse embryonic fibroblasts was successful.

3.5 DNA methylation immunostaining in mouse embryonic tissues

Immunostaining was performed on mouse E13.5 thin cryosections following the standard DNA methylation immunohistochemistry protocol outlined in Chapter 2 Section 2.4.4.

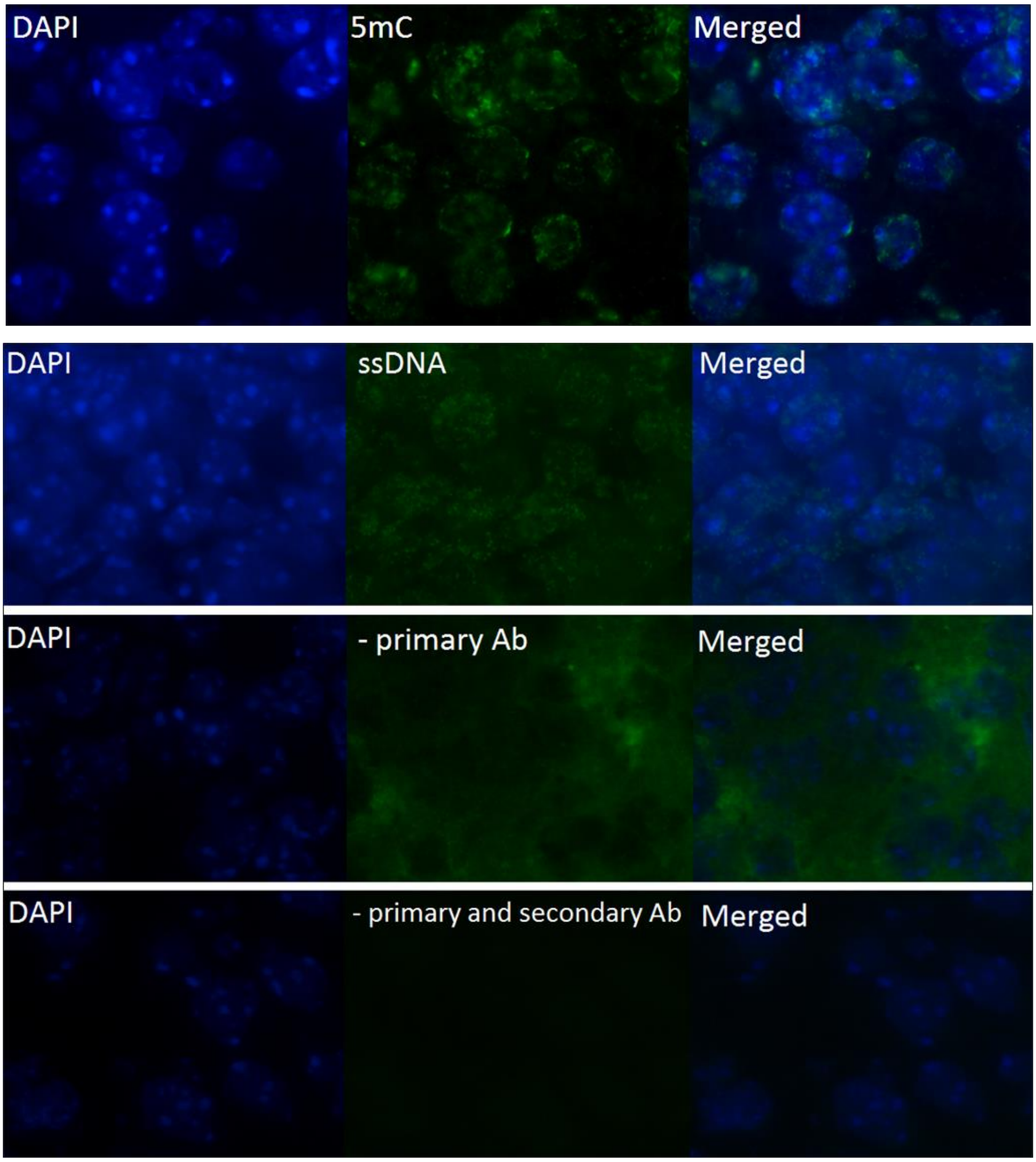

Figure 3.5: DNA methylation immunostaining in E13.5 mouse embryonic brain tissues. Representative stainings of mouse embryonic brain tissue sections are shown. Left panels: tissue nuclear DNA counterstained with DAPI (blue). Middle panels: from top to bottom, tissues stained with primary antibodies against 5mC (green), ssDNA (green), control without the primary antibody (green) and control without both primary and secondary antibodies (green). Right panels: merged images. Cryosection DNA immunostaining using the standard protocol resulted in non-specific signal, as no colocalisation was observed between antibody staining and DAPI signal.

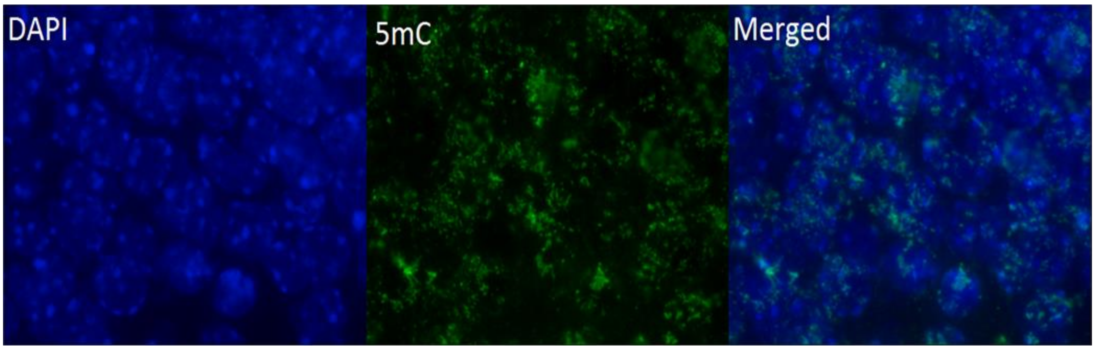

Figure 3.6: DNA methylation immunostaining in E13.5 mouse embryonic liver tissues. Representative staining of mouse embryonic liver tissue sections is shown. Left panel: tissue nuclear DNA counterstained with DAPI (blue). Middle panel: tissues stained with primary antibody against 5mC (green). Right panel: merged image. Non-specific DNA immunostaining using the standard protocol is confirmed for liver, as no colocalisation is observed between antibody staining and DAPI signal.

No significant colocalisation of 5mC and DAPI signal was detected following standard DNA methylation immunostaining protocol **(Figure 3.5 and 3.6)**. In addition, 5mC staining results show a too strong DAPI signal for DNA to be denatured. High background was also detected in 5mC staining. This might be due to a very strong non-specific staining, which despite poor colocalisation with DAPI sometimes appeared to be nuclear. Similar non-specific staining (strong DAPI signals and high background) was observed in ssDNA staining **(Figure 3.5)**. An antibody staining control was performed in this experiment. Omission of the primary or secondary antibody in the staining procedure resulted in complete absence of immunofluorescence staining **(Figure 3.5)**. The controls seemed fine, and the strong non-specific staining on tissues was seen regardless of primary antibody. In Figure

3.5 and 3.6, brain and liver location could be determined from whole embryo cryosection anatomy.

3.6 DNA methylation immunostaining in mouse embryonic tissues: protocol optimisation

Initially, the standard protocol of DNA methylation immunostaining was applied as described in Chapter 2 Section 2.4.4. The standard protocol was primarily developed for immunocytochemistry of cells. It was initially assumed to work on tissue sections adhered on microslides, on the basis of a few immunostained images in the literature (Hahn et al., 2013; Jin et al., 2011). However, the existing methodology was found not to work for mouse embryo tissue cryosections. Therefore, several tests were subsequently undertaken to optimise the protocol. These tests are described in the following sections.

3.6.1 pH test

In this test, pH was monitored at four different stages throughout the procedure: fixation, denaturation, permeabilisation and blocking **(Table 3.1)**. The pH was checked with a pH paper. This test was performed to determine whether the HCl step was sufficiently neutralised, as this could affect antibody performance.

Table 3.1: pH test for DNA methylation immunostaining in mouse embryonic tissues. pH was monitored at four different stages throughout the standard staining procedure, including after second wash of PFA, after third wash of HCl, after second wash of Triton X-100 and after blocking with BSA.

Step	Duration
Fix with 2% PFA	50 mins
Wash with PBS	**2 X 5 mins**
Denature DNA with 4 M HCl	15 mins
Wash with PBS	**3 X 5 mins**
Permeabilise with 0.4% Triton X-100	30 mins
Wash with PBS	**2 X 10 mins**
Block with 2% BSA	**1 hour**
5mC primary antibody	2 hours
Wash with PBST	3 X 15 mins
Alexa Fluor 488 secondary anti mouse	1 hour
Wash with PBST	15 mins
DAPI staining	15 mins
Wash with PBST	2 X 15 mins
Mounting	Overnight at RT

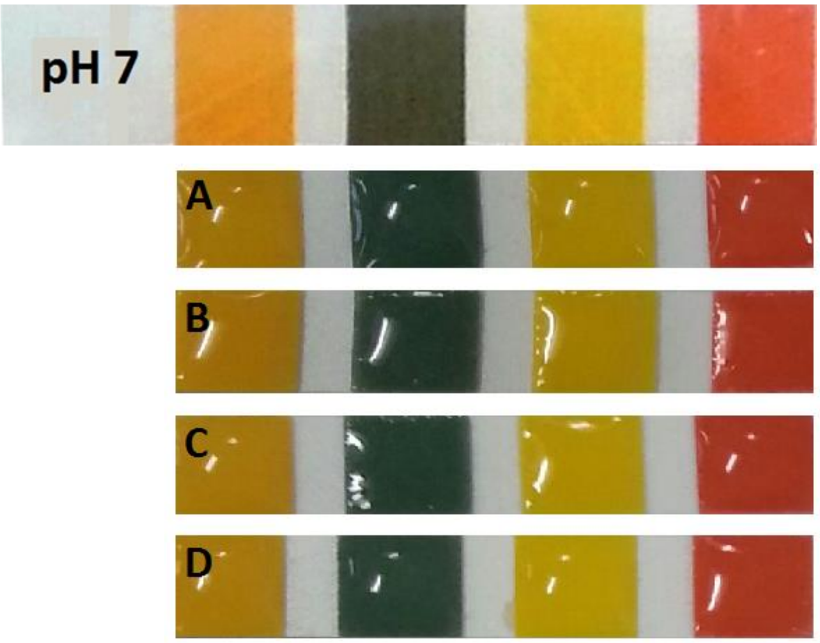

Figure 3.7: pH test. (A) pH after second wash of PFA. **(B)** pH after third wash of HCl. **(C)** pH after second wash of Triton X-100. **(D)** pH after blocking with BSA. The pH of all samples was neutral (pH 7.0).

One possibility was that the HCl step for DNA denaturation was not sufficiently neutralised when the antibody was added, causing the antibody to precipitate. As evident from A, B, C and D **(Figure 3.7)**, however, all stages show a pH near 7.0. This shows that the pH was maintained at pH 7.0 throughout the procedure. It was found that the pH was restored to neutral pH after only three PBS washes on the slide. This suggested that the antibody was not denatured or precipitated by any remaining acid.

3.6.2 Washing step test

In this test, the slide was washed thoroughly in a large volume of PBS on a rocking jar after the HCl step **(Table 3.2).** This test was performed to determine whether the acid denatured proteins or aggregates introduced by HCl step were completely removed. Acid denatured proteins might cause high background.

Table 3.2: Washing step test for DNA methylation immunostaining in mouse embryonic tissues. Vigorous washing was performed after HCl step for 15 minutes.

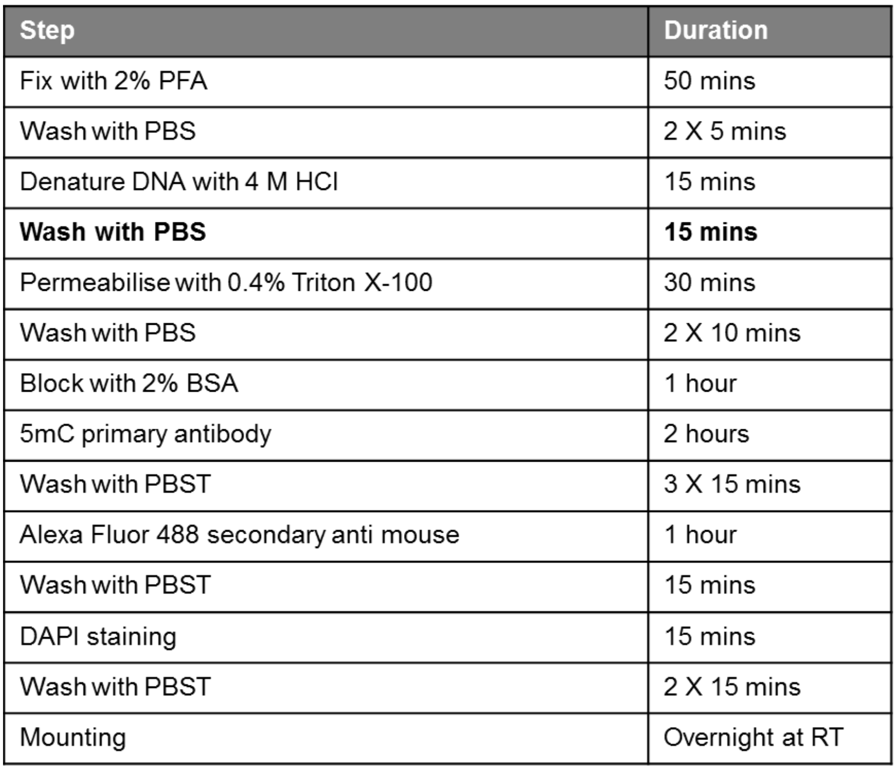

Step	Duration
Fix with 2% PFA	50 mins
Wash with PBS	2 X 5 mins
Denature DNA with 4 M HCl	15 mins
Wash with PBS	**15 mins**
Permeabilise with 0.4% Triton X-100	30 mins
Wash with PBS	2 X 10 mins
Block with 2% BSA	1 hour
5mC primary antibody	2 hours
Wash with PBST	3 X 15 mins
Alexa Fluor 488 secondary anti mouse	1 hour
Wash with PBST	15 mins
DAPI staining	15 mins
Wash with PBST	2 X 15 mins
Mounting	Overnight at RT

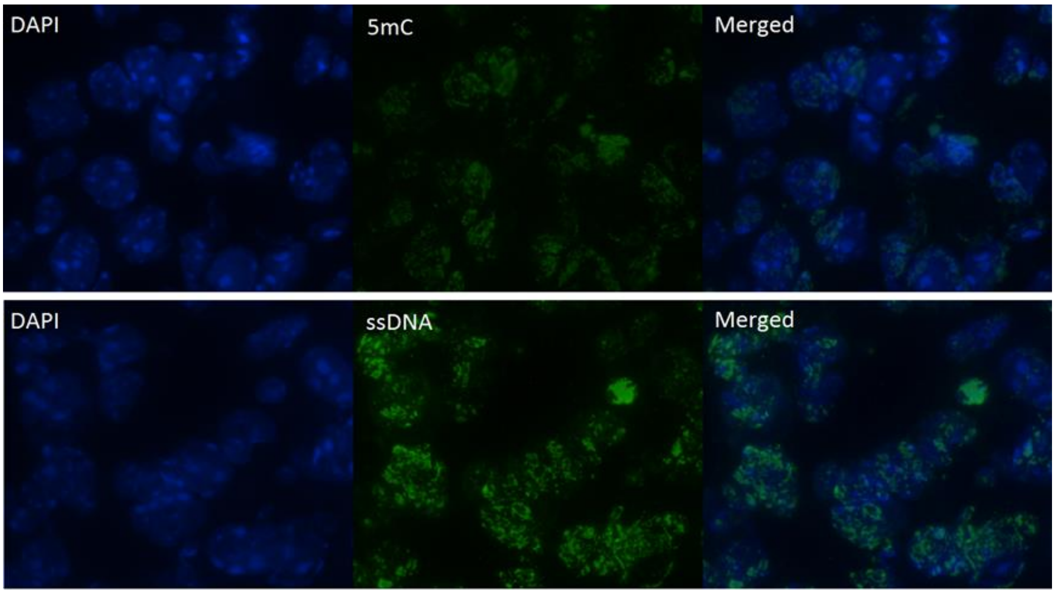

Figure 3.8: DNA methylation immunostaining in E13.5 mouse embryonic brain tissues. Representative stainings of mouse embryonic brain tissue sections are shown. Left panels: tissue nuclear DNA counterstained with DAPI (blue). Middle panels: tissues stained with 5mC (green) and ssDNA (green), respectively. Right panels: merged images. Non-specific immunostaining was not removed by intensive washing.

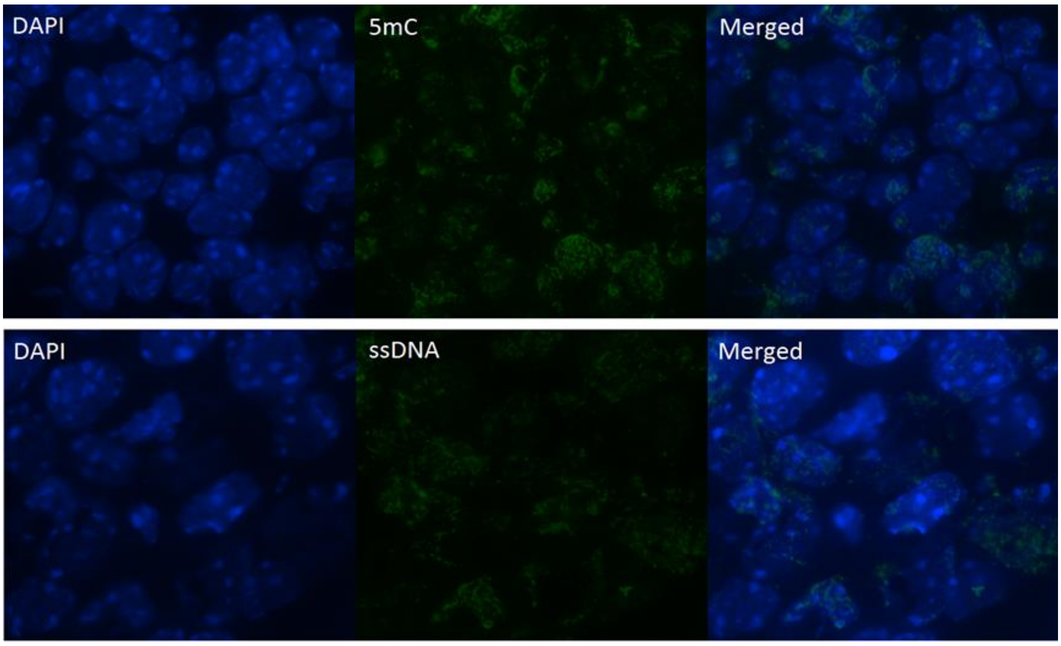

Figure 3.9: DNA methylation immunostaining in E13.5 mouse embryonic liver tissues. Representative stainings of mouse embryonic liver tissue sections are shown. Left panels: tissues counterstained with DAPI (blue). Middle panels: tissues stained with 5mC (green) and ssDNA (green), respectively. Right panels: merged images. Non-specific immunostaining is not removed by intensive washing in either brain (Figure 3.8) or liver tissue.

Since the histone protocol did not show these immunostaining issues, another possibility was that the HCl step introduced background from acid denatured or extracted protein. After including an intensive washing step often used in standard histochemistry protocols, still no colocalisation of 5mC and DAPI was detected in brain or in liver tissue sections **(Figure 3.8 and 3.9)**. 5mC staining results showed too strong DAPI signals for DNA to be denatured. However, less background was detected in 5mC staining. Similar conditions (strong DAPI signals and less background) were observed in ssDNA staining **(Figure 3.8 and 3.9)**. Washing in a rocking jar might remove acid denatured proteins trapped inside the tissue. These denatured proteins might cause high background as they would expose numerous epitopes normally engaged in protein-protein interactions. Unlike with nuclear protein immunostaining, washes can be more vigorous when staining the DNA. This test suggested that the two different primary antibodies bound non-specifically to nuclear surfaces after intensive washes, but showed more general debris after gentle washes. The strong signal did not look like an ordinary background but more like an incompatibility between protocol steps causing precipitation. The strong non-specific staining on tissues was seen regardless of washing. Washing in a rocking jar step was continually used in the subsequent test as background was seen to reduce using this step.

3.6.3 Inverted step and neutralisation test

In this test, the permeabilisation step was performed before the HCl step and HCl step was immediately neutralised with 100 mM Tris-HCl pH 8.5 **(Table 3.3)**. For tissues, the cell protocol might need specific adaptation of denaturation together with permeabilisation condition as one might affect the other.

Table 3.3: Inverted step and neutralisation test for DNA methylation immunostaining in mouse embryonic tissues. Permeabilisation step was performed before the HCl step and HCl step was immediately neutralised with 100 mM Tris-HCl pH 8.5.

Step	Duration
Fix with 2% PFA	50 mins
Wash with PBS	2 X 5 mins
Permeabilise with 0.4% Triton X-100	**30 mins**
Wash with PBS	2 X 10 mins
Denature DNA with 4 M HCl	**15 mins**
Neutralise with 100 mM Tris-HCl pH 8.5	**10 mins**
Wash with PBS	15 mins
Block with 2% BSA	1 hour
5mC primary antibody	2 hours
Wash with PBST	3 X 15 mins
Alexa Fluor 488 secondary anti mouse	1 hour
Wash with PBST	15 mins
DAPI staining	15 mins
Wash with PBST	2 X 15 mins
Mounting	Overnight at RT

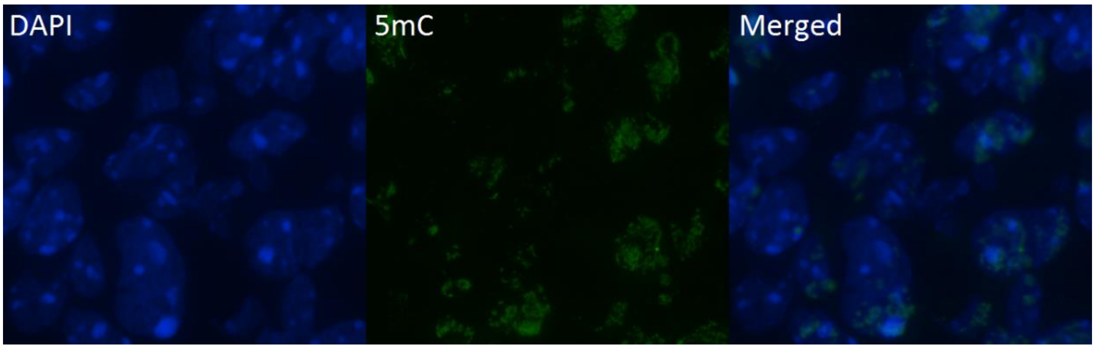

Figure 3.10: DNA methylation immunostaining in E13.5 mouse embryonic brain tissues. Representative staining of mouse embryonic brain tissue sections is shown. Left panel: tissue nuclear DNA counterstained with DAPI (blue). Middle panel: tissues stained with primary antibody against 5mC (green). Right panel: merged image. The protocol variation of performing the permeabilisation before the HCl denaturation did not result in less non-specific signal.

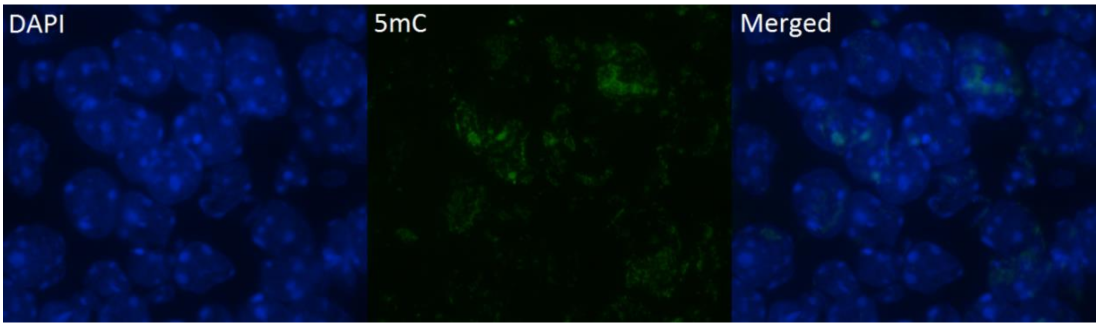

Figure 3.11: DNA methylation immunostaining in E13.5 mouse embryonic liver tissues. Representative staining of mouse embryonic liver tissue sections is shown. Left panel: tissue nuclear DNA counterstained with DAPI (blue). Middle panel: tissues stained with primary antibody against 5mC (green). Right panel: merged image. Performing the permeabilisation before the HCl denaturation did not result in less non-specific signal.

To further reduce the impact of possible acid-induced background signal, the HCl step was conducted after permeabilisation followed by immediate pH neutralisation, a variation based on some protocols. Yet, no colocalisation of 5mC and DAPI was detected in brain or in liver tissue sections **(Figure 3.10 and 3.11)**. 5mC staining results showed too strong DAPI signals for DNA to be denatured. Permeabilisation was performed before the HCl step in order for the denatured proteins to be washed out more effectively. Following permeabilisation and DNA denaturation by HCl, histones are expected to be released and other denatured proteins to be precipitated. Neutralisation was performed immediately to diminish precipitation while HCl debris was washed out using a rocking jar. This test was based on a suggestion that the standard protocol may work well in cells as flat cultured cells washed out HCl debris better and have less extracellular matrix. Inverted permeabilisation and neutralisation steps were continually used in the subsequent tests as background was seen to reduce using these steps.

3.6.4 Duration of 5mC antibody incubation test

Previously, 5mC was incubated for 2 hours at room temperature in the dark. In this test, 5mC antibody was incubated overnight at 4°C. The standard protocol was also slightly changed where the concentration of Triton X-100 was increased to 0.5% and 2% of donkey serum was used as an additional blocker **(Table 3.4)**. The first two changes were to verify possible antibody accessibility issues. The blocking solution might have to be adapted to mixed background types, therefore blocking were with a mix of BSA and donkey serum.

Table 3.4: Duration of 5mC antibody incubation test for DNA methylation immunostaining in mouse embryonic tissues. 5mC antibody incubation was performed overnight 4°C. In addition to overnight 5mC antibody incubation, the concentration of Triton X-100 was increased to 0.5% and an additional blocking reagent, 2% of donkey serum was used.

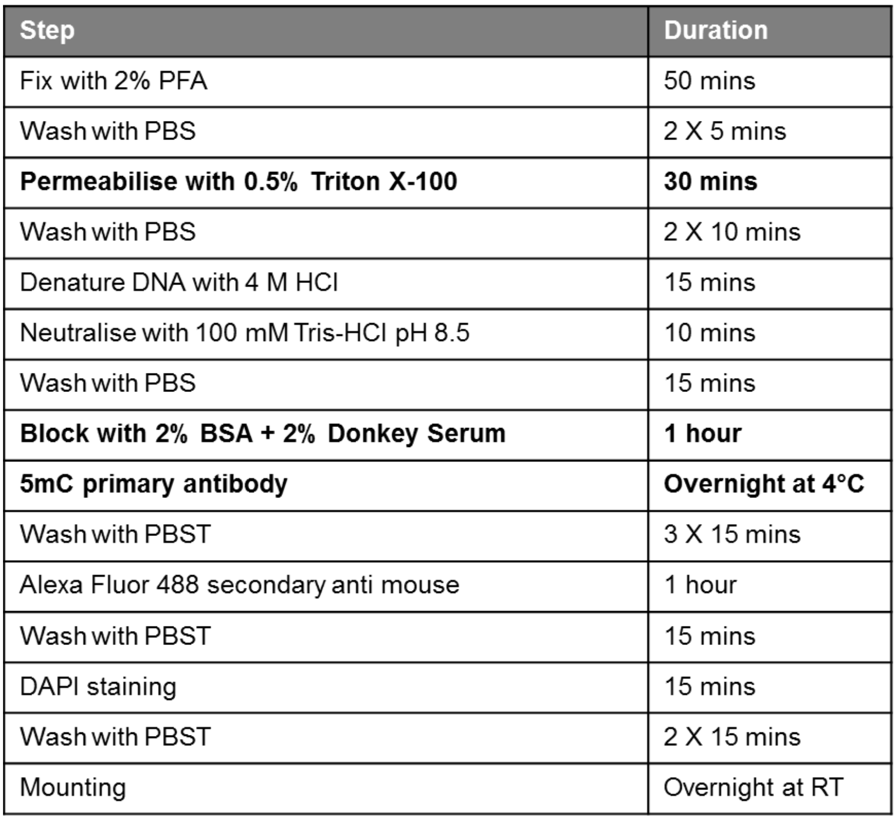

Step	Duration
Fix with 2% PFA	50 mins
Wash with PBS	2 X 5 mins
Permeabilise with 0.5% Triton X-100	**30 mins**
Wash with PBS	2 X 10 mins
Denature DNA with 4 M HCl	15 mins
Neutralise with 100 mM Tris-HCl pH 8.5	10 mins
Wash with PBS	15 mins
Block with 2% BSA + 2% Donkey Serum	**1 hour**
5mC primary antibody	**Overnight at 4°C**
Wash with PBST	3 X 15 mins
Alexa Fluor 488 secondary anti mouse	1 hour
Wash with PBST	15 mins
DAPI staining	15 mins
Wash with PBST	2 X 15 mins
Mounting	Overnight at RT

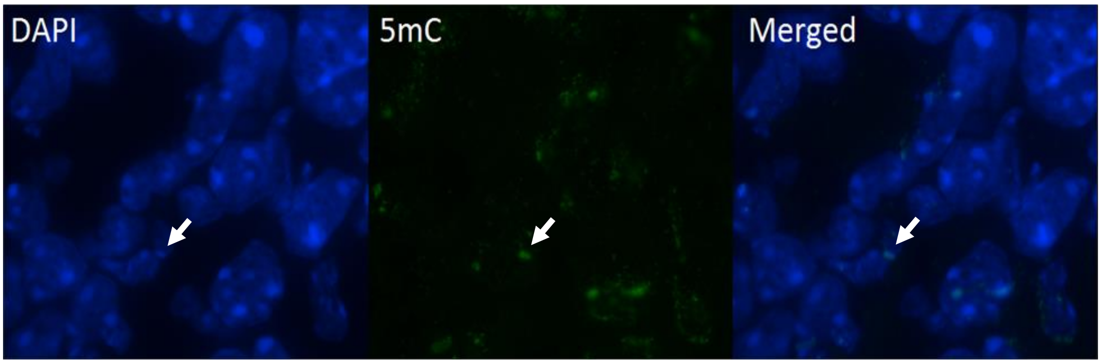

Figure 3.12: DNA methylation immunostaining in E13.5 mouse embryonic brain tissues. Representative staining of mouse embryonic brain tissue sections is shown. Left panel: tissue nuclear DNA counterstained with DAPI (blue). Middle panel: tissues stained with primary antibody against 5mC (green). Right panel: merged image. Partial colocalisation (arrows) between 5mC and DAPI dense foci was achieved by longer primary DNA antibody staining.

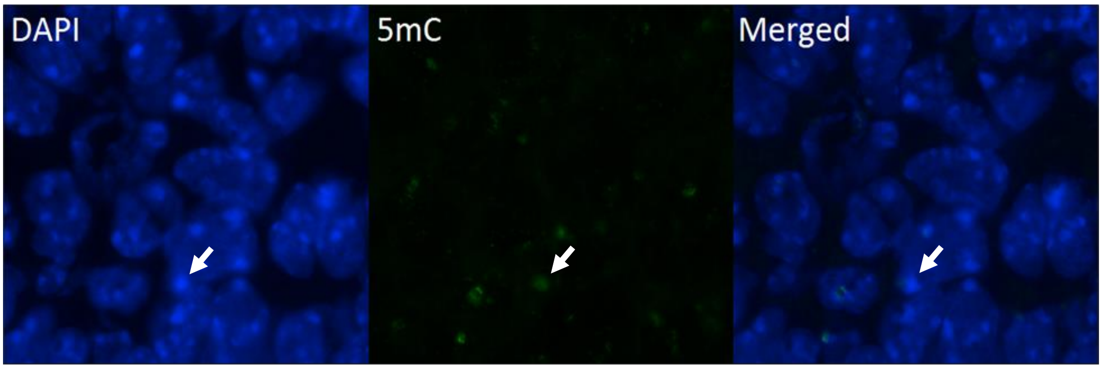

Figure 3.13: DNA methylation immunostaining in E13.5 mouse embryonic liver tissues. Representative staining of mouse embryonic liver tissue sections is shown. Left panel: tissue nuclear DNA counterstained with DAPI (blue). Middle panel: tissues stained with primary antibody against 5mC (green). Right panel: merged image. Partial colocalisation (arrows) by longer primary DNA antibody staining was confirmed.

The overnight 4°C incubation resulted in approximately 15% of nuclear regions demonstrating colocalisation of 5mC and DAPI in brain as well as in liver tissue sections **(Figure 3.12 and 3.13)**. Longer duration of 5mC antibody incubation therefore improved the antibody signal. The adhesive elements that caused non-specific staining were better covered by using additional blocking with donkey serum. The nature of the problem was still being reconsidered at the HCl step, as the strong non-specific binding seemed linked to DNA denaturation. For that reason, overnight 5mC antibody incubation was not used in the subsequent test until optimal condition for HCl step was found. However, 0.5% Triton X-100 and 2% donkey serum were continually used in the subsequent test as both conditions seemed to aid in the reduction of the background and non-specific staining, respectively.

3.6.5 Duration of HCl treatment test

In this test, the tissues were treated with HCl for 30 minutes **(Table 3.5)**. Longer duration of HCl treatment gives a higher possibility of DNA in each nucleus to be denatured.

Table 3.5: Duration of HCl treatment test for DNA methylation immunostaining in mouse embryonic tissues. HCl treatment was performed for 30 minutes.

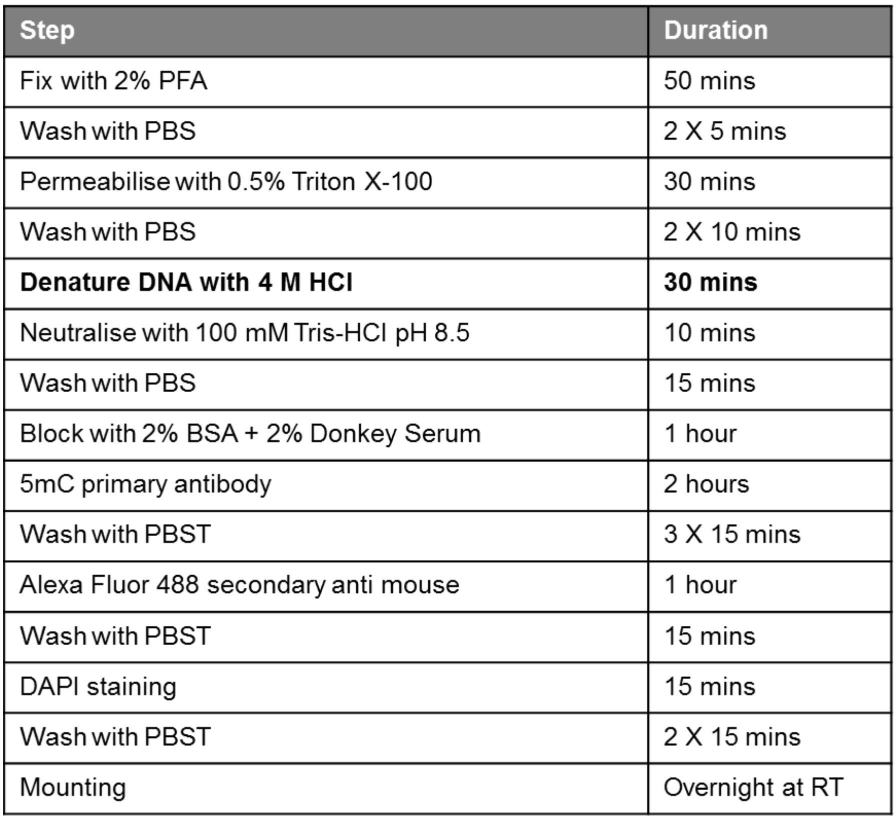

Step	Duration
Fix with 2% PFA	50 mins
Wash with PBS	2 X 5 mins
Permeabilise with 0.5% Triton X-100	30 mins
Wash with PBS	2 X 10 mins
Denature DNA with 4 M HCl	**30 mins**
Neutralise with 100 mM Tris-HCl pH 8.5	10 mins
Wash with PBS	15 mins
Block with 2% BSA + 2% Donkey Serum	1 hour
5mC primary antibody	2 hours
Wash with PBST	3 X 15 mins
Alexa Fluor 488 secondary anti mouse	1 hour
Wash with PBST	15 mins
DAPI staining	15 mins
Wash with PBST	2 X 15 mins
Mounting	Overnight at RT

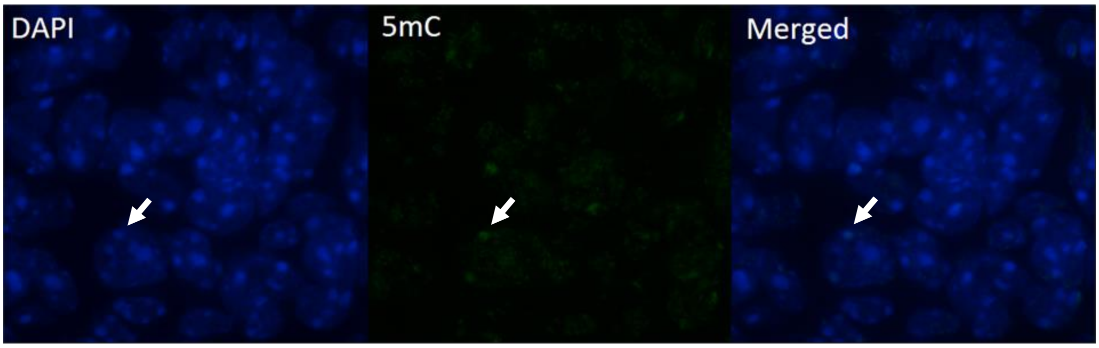

Figure 3.14: DNA methylation immunostaining in E13.5 mouse embryonic brain tissues. Representative staining of mouse embryonic brain tissue sections is shown. Left panel: tissue nuclear DNA counterstained with DAPI (blue). Middle panel: tissues stained with primary antibody for 5mC (green). Right panel: merged image. Partial colocalisation (arrows) between 5mC and DAPI dense foci was achieved by longer HCl treatment.

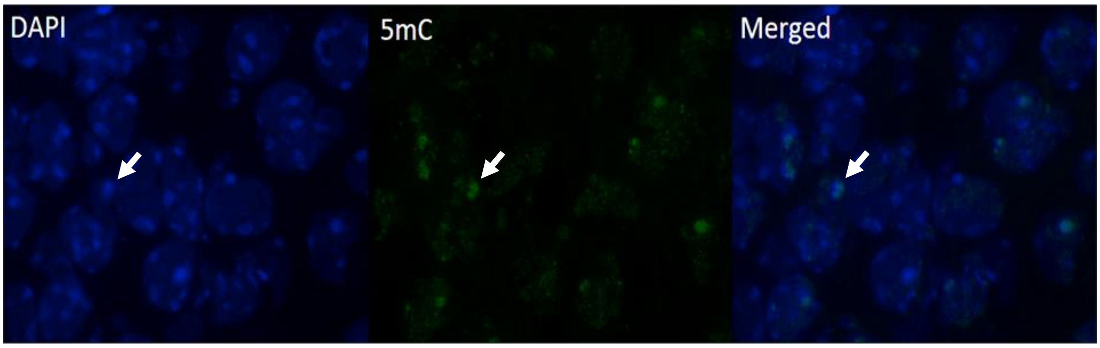

Figure 3.15: DNA methylation immunostaining in E13.5 mouse embryonic liver tissues. Representative staining of mouse embryonic liver tissue sections is shown. Left panel: tissue nuclear DNA counterstained with DAPI (blue). Middle panel: tissues stained with primary antibody against 5mC (green). Right panel: merged image. Partial colocalisation (arrows) by longer HCl treatment was confirmed.

In view of the persistence of strong DAPI staining despite the HCl denaturation step, it was possible that DNA denaturation was not complete. HCl treatment for 30 minutes resulted in approximately 15% of nuclear regions colocalising for 5mC and DAPI in brain as well as in liver tissue sections **(Figure 3.14 and 3.15)**. Longer duration of HCl treatment was employed to increase the possibility for DNA in each nucleus to be denatured. The denaturation time often needs to be recalibrated, as cells will denature quicker than tissues, and various tissues will also show differences. However, this test went beyond the 5 to 15 minutes range employed for cells and whole embryos.

3.6.6 Duration of HCl treatment test (2)

In this test, the duration of HCl treatment was further increased to 45 minutes **(Table 3.6)**. Longer duration of HCl treatment gives higher possibility of DNA in each nucleus to be denatured if tissue morphology is not affected.

Table 3.6: Duration of HCl treatment test for DNA methylation immunostaining in mouse embryonic tissues. HCl treatment was performed for 45 minutes.

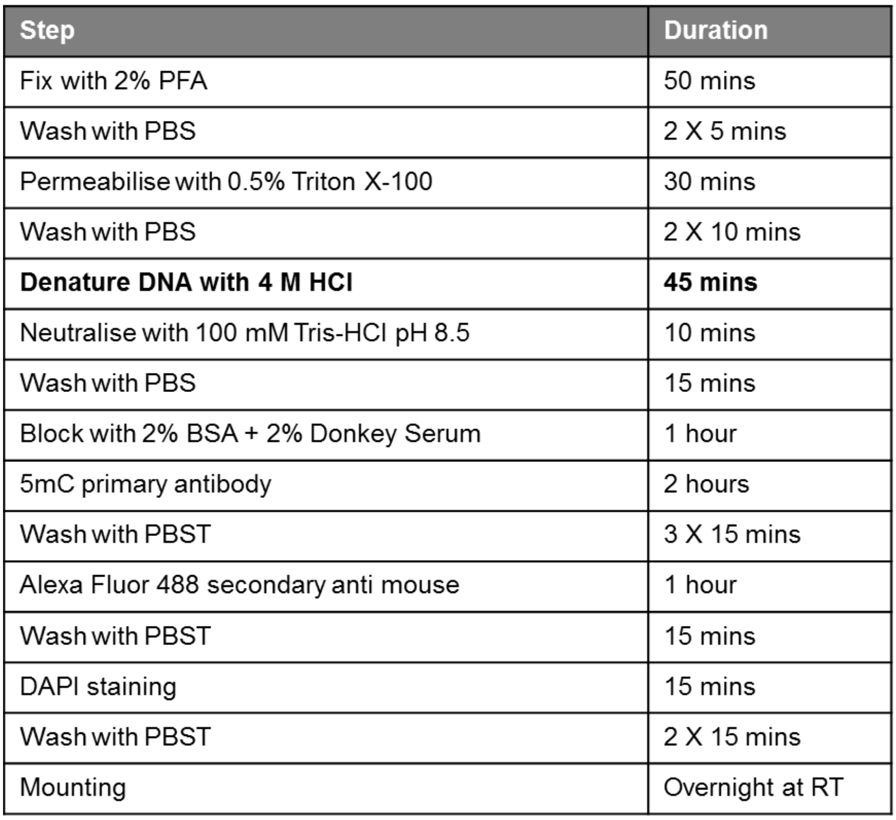

Step	Duration
Fix with 2% PFA	50 mins
Wash with PBS	2 X 5 mins
Permeabilise with 0.5% Triton X-100	30 mins
Wash with PBS	2 X 10 mins
Denature DNA with 4 M HCl	**45 mins**
Neutralise with 100 mM Tris-HCl pH 8.5	10 mins
Wash with PBS	15 mins
Block with 2% BSA + 2% Donkey Serum	1 hour
5mC primary antibody	2 hours
Wash with PBST	3 X 15 mins
Alexa Fluor 488 secondary anti mouse	1 hour
Wash with PBST	15 mins
DAPI staining	15 mins
Wash with PBST	2 X 15 mins
Mounting	Overnight at RT

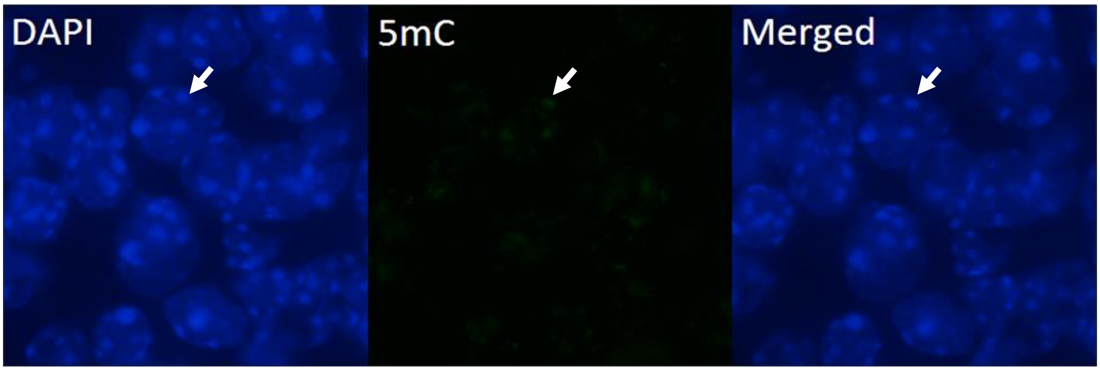

Figure 3.16: DNA methylation immunostaining in E13.5 mouse embryonic brain tissues. Representative staining of mouse embryonic brain tissue sections is shown. Left panel: tissue nuclear DNA counterstained with DAPI (blue). Middle panel: tissues stained with primary antbody against 5mC (green). Right panel: merged image. Partial colocalisation (arrows) between 5mC and DAPI dense foci was achieved by very long HCl treatment.

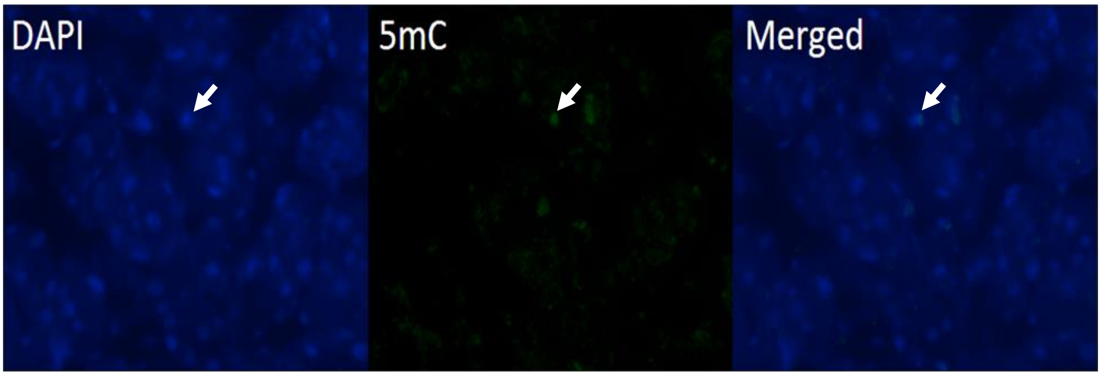

Figure 3.17: DNA methylation immunostaining in E13.5 mouse embryonic liver tissues. Representative staining of mouse embryonic liver tissue sections is shown. Left panel: tissue nuclear DNA counterstained with DAPI (blue). Middle panel: tissues stained with primary antibody against 5mC (green). Right panel: merged image. Partial colocalisation (arrows) by longer HCl treatment was confirmed.

HCl treatment for 45 minutes resulted in approximately 15% of nuclear regions colocalising for 5mC and DAPI in brain as well as in liver tissue sections **(Figure 3.16 and 3.17)**. Longer duration of HCl treatment was employed to increase the possibility for DNA in each nucleus to be denatured, but no further enhancement was seen at the expense of likely acid damage to the tissues. 45 minutes of HCl treatment was considered to be optimal denaturation condition for HCl step and was therefore used in the subsequent step.

3.6.7 Duration of HCl treatment and 5mC antibody incubation test

In this test, two conditions were combined: 45 minutes of HCl treatment and overnight incubation of 5mC antibody **(Table 3.7)**. Longer duration of HCl treatment gives higher possibility for DNA in each cell to be denatured and longer duration of antibody incubation gives higher possibility of antibody access and binding.

Table 3.7: Duration of HCl treatment and 5mC antibody incubation test for DNA methylation immunostaining in mouse embryonic tissues. 45 minutes of HCl treatment was performed in combination with the overnight incubation of 5mC antibody.

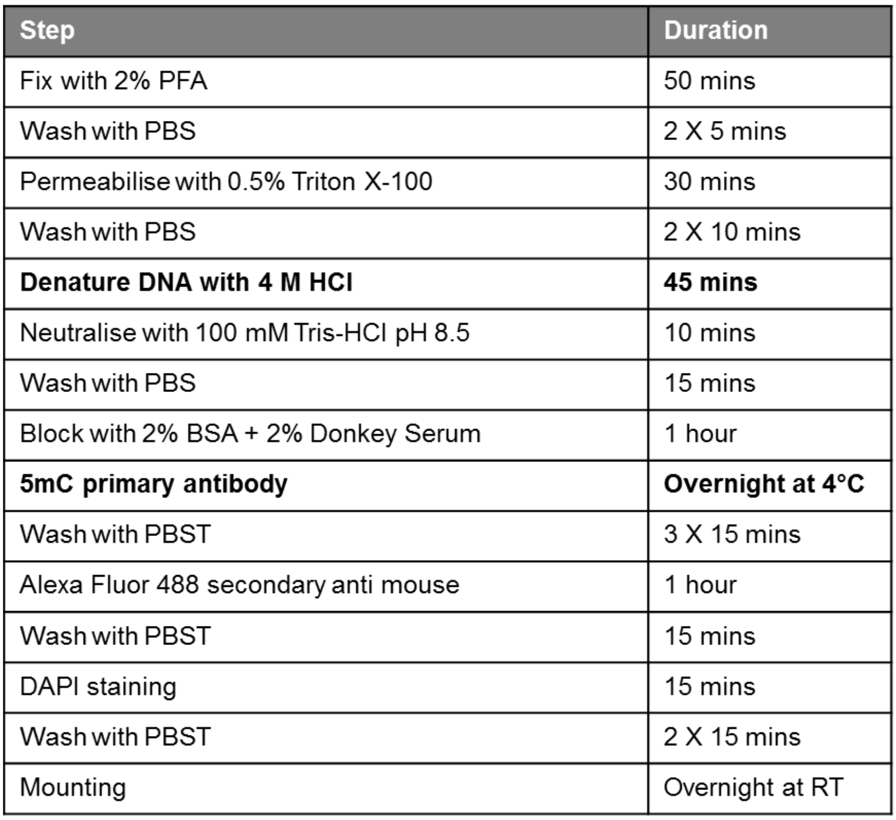

Step	Duration
Fix with 2% PFA	50 mins
Wash with PBS	2 X 5 mins
Permeabilise with 0.5% Triton X-100	30 mins
Wash with PBS	2 X 10 mins
Denature DNA with 4 M HCl	**45 mins**
Neutralise with 100 mM Tris-HCl pH 8.5	10 mins
Wash with PBS	15 mins
Block with 2% BSA + 2% Donkey Serum	1 hour
5mC primary antibody	**Overnight at 4°C**
Wash with PBST	3 X 15 mins
Alexa Fluor 488 secondary anti mouse	1 hour
Wash with PBST	15 mins
DAPI staining	15 mins
Wash with PBST	2 X 15 mins
Mounting	Overnight at RT

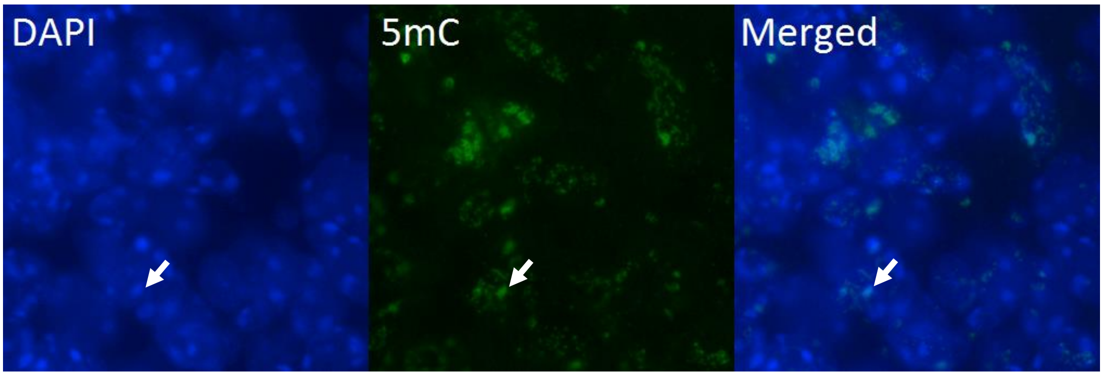

Figure 3.18: DNA methylation immunostaining in E13.5 mouse embryonic brain tissues. Representative staining of mouse embryonic brain tissue sections is shown. Left panel: tissue nuclear DNA counterstained with DAPI (blue). Middle panel: tissues stained with primary antibody against 5mC (green). Right panel: merged image. Partial colocalisation (arrows) between 5mC and DAPI dense foci was achieved by combining longer incubations.

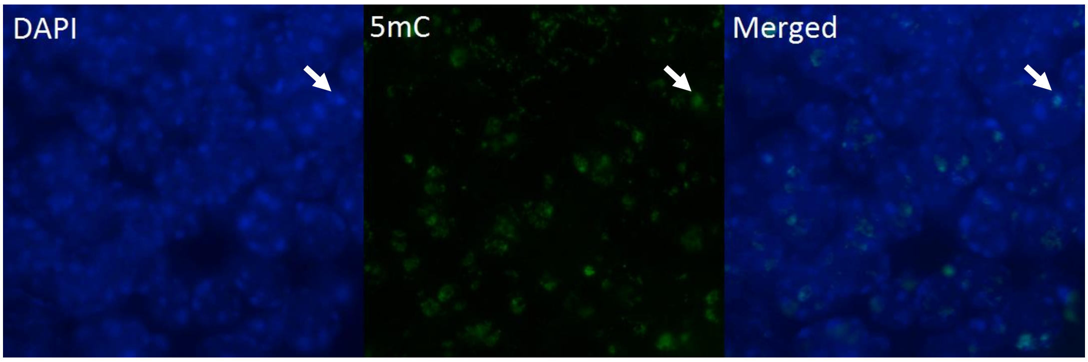

Figure 3.19: DNA methylation immunostaining in E13.5 mouse embryonic liver tissues. Representative staining of mouse embryonic liver tissue sections is shown. Left panel: tissue nuclear DNA counterstained with DAPI (blue). Middle panel: tissues stained with primary antibody against 5mC (green). Right panel: merged image. Partial colocalisation (arrows) between 5mC and DAPI dense foci was achieved by combining longer incubations.

Partial success with longer HCl treatment and longer primary antibody incubation suggested combining both conditions could produce further gains. Yet still approximately 15% of nuclear regions demonstrated colocalisation of 5mC and DAPI in brain as well as in liver tissue sections **(Figure 3.18 and 3.19)**. No further increase in colocalisation between 5mC and DAPI was observed. DNA denaturation is a critical step in this method as longer treatment of HCl might lead to tissue damage. Standard DNA methylation immunostaining method somehow caused 5mC antibody specificity problems in tissues but not in cultured cells. Further optimisation of the DNA denaturation step using HCl could not be considered. Although a further 37°C HCl treatment protocol variation was tested, this did not result in further gains (not shown). Therefore, an alternative denaturation step was employed to improve the antibody signals.

3.6.8 DNA denaturation by boiling test

In this test, after the permeabilisation step the slide was boiled for 10 minutes in 10 mM sodium citrate pH 6 **(Table 3.8)**. This alternative denaturation step was employed to denature the DNA as it is similar to an antigen retrieval step, which is recommended whenever antibody signals need to be improved (at the expense of some heat damage to the tissues). It is also related to the DNA denaturation step in in situ hybridisation experiments and had been used by some protocols using wax embedded tissue sections.

Table 3.8: DNA denaturation by boiling test for DNA methylation immunostaining in mouse embryonic tissues. DNA denaturation step was performed by boiling slide in 10 mM sodium citrate pH 6.0 for 10 minutes.

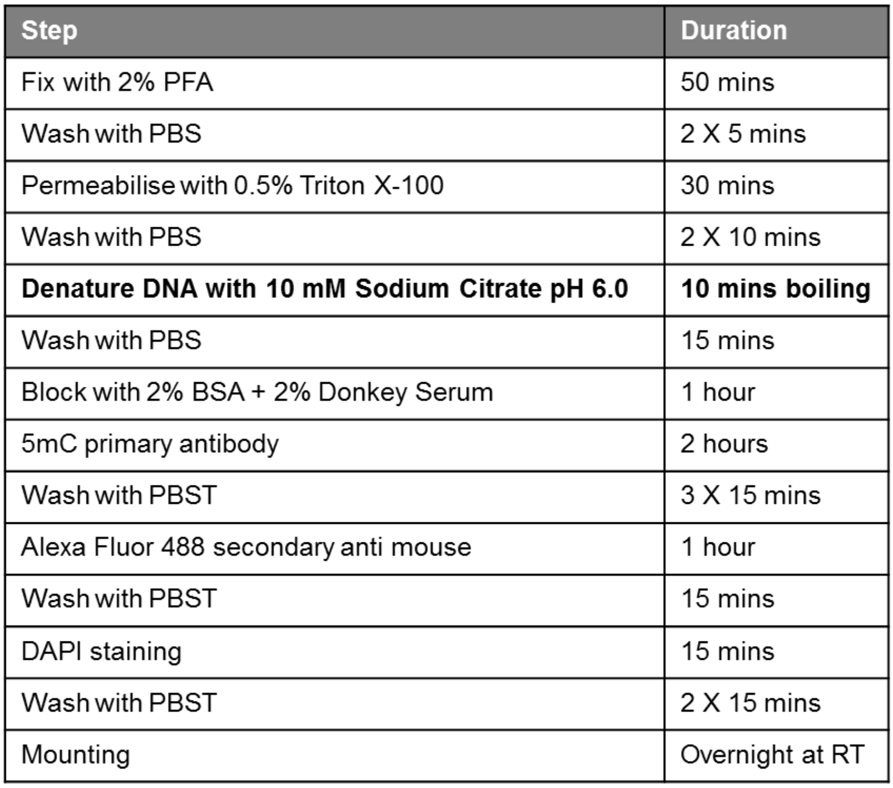

Step	Duration
Fix with 2% PFA	50 mins
Wash with PBS	2 X 5 mins
Permeabilise with 0.5% Triton X-100	30 mins
Wash with PBS	2 X 10 mins
Denature DNA with 10 mM Sodium Citrate pH 6.0	**10 mins boiling**
Wash with PBS	15 mins
Block with 2% BSA + 2% Donkey Serum	1 hour
5mC primary antibody	2 hours
Wash with PBST	3 X 15 mins
Alexa Fluor 488 secondary anti mouse	1 hour
Wash with PBST	15 mins
DAPI staining	15 mins
Wash with PBST	2 X 15 mins
Mounting	Overnight at RT

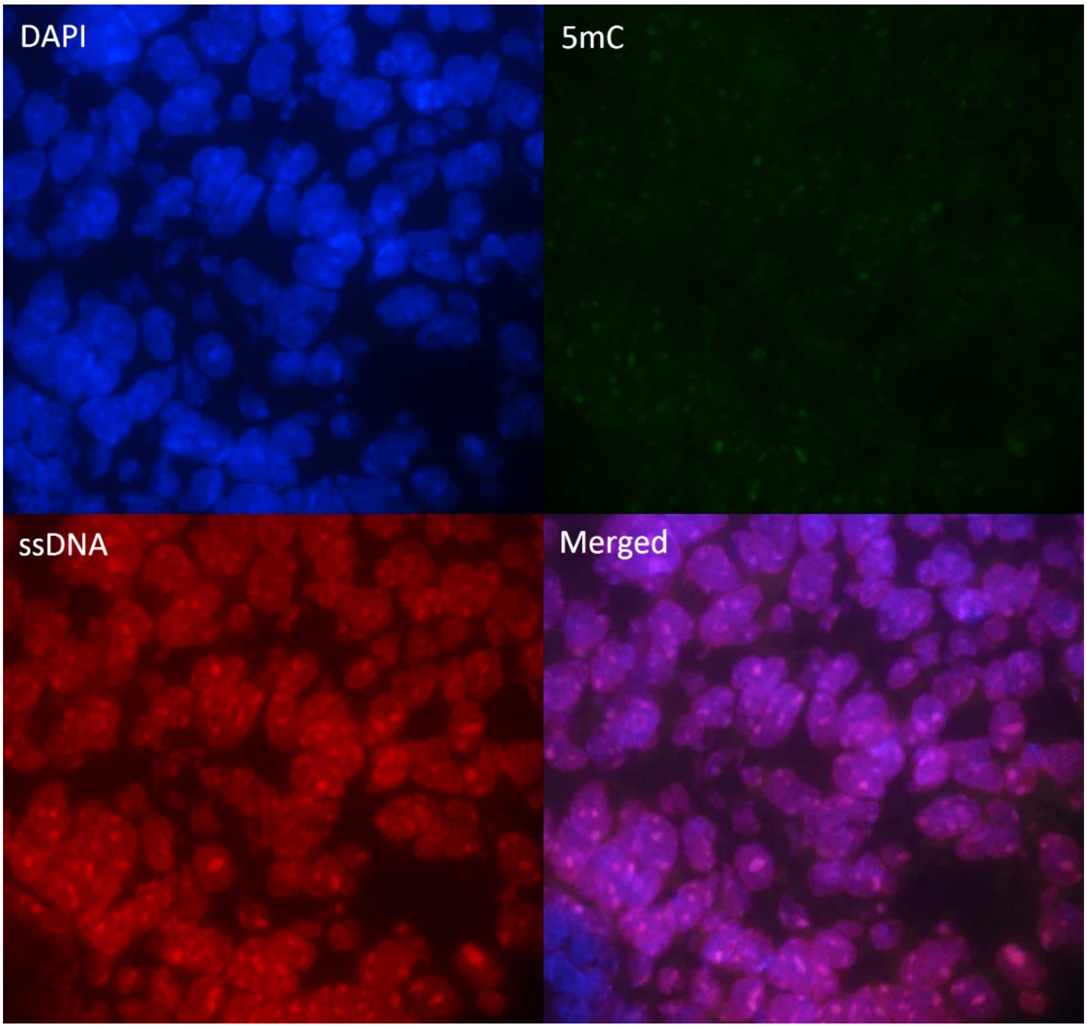

Figure 3.20: DNA methylation immunostaining in E13.5 mouse embryonic brain tissues. Representative stainings of mouse embryonic brain tissue sections are shown. Top left panel: tissue nuclear DNA counterstained with DAPI (blue). Top right panel: tissues stained with primary antibody against 5mC (green). Bottom left panel: tissues stained antibody against with ssDNA (red). Bottom right panel: merged image. Colocalisation between 5mC, ssDNA and DAPI is apparent after DNA denaturation by boiling in sodium citrate.

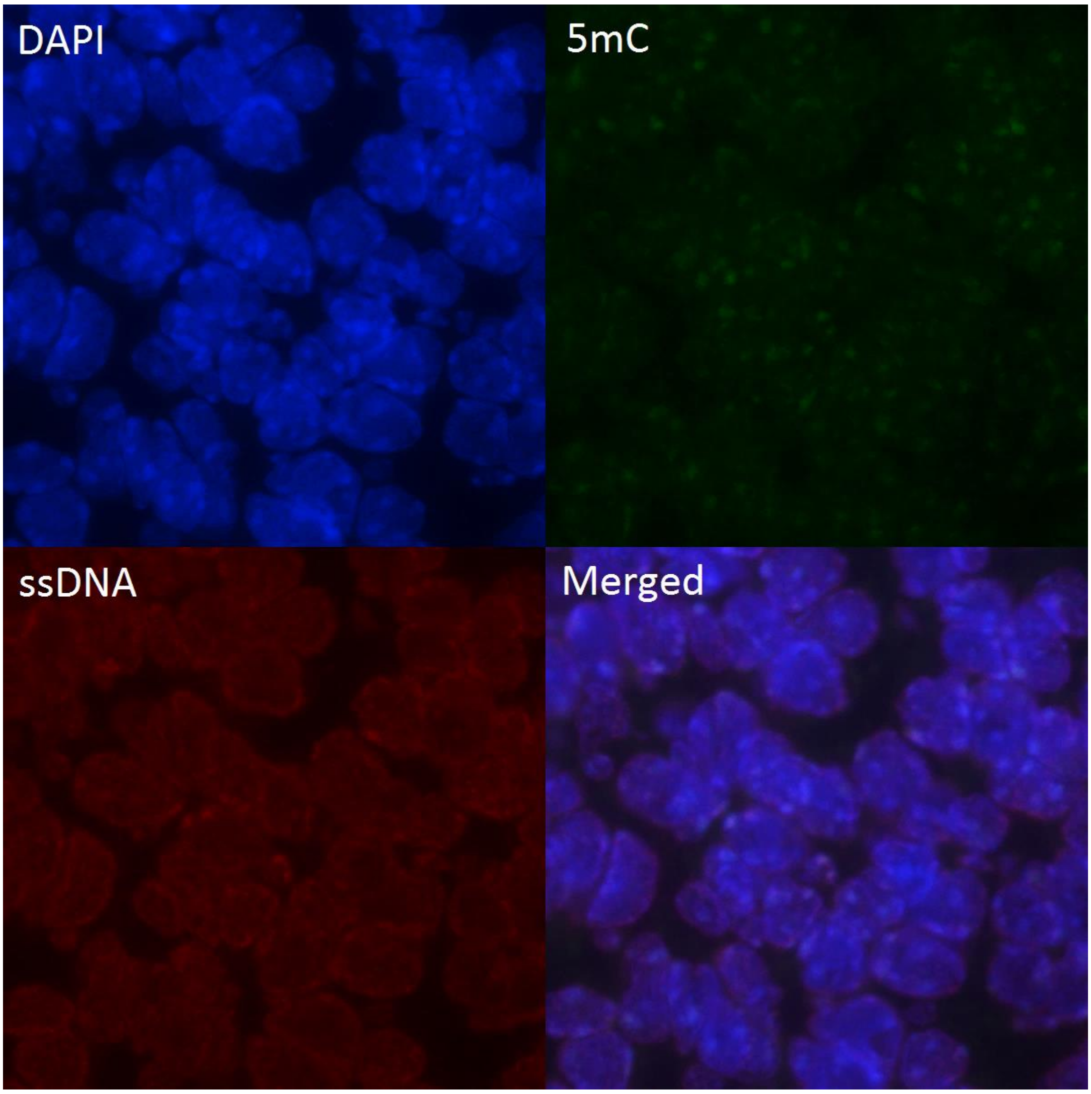

Figure 3.21: DNA methylation immunostaining in E13.5 mouse embryonic liver tissues. Representative staining of mouse embryonic liver tissue sections are shown. Top left panel: tissue nuclear DNA counterstained with DAPI (blue). Top right panel: tissues stained with primary antibody against 5mC (green). Bottom left panel: tissues stained with antibody against ssDNA (red). Bottom right panel: merged image. Colocalisation between 5mC, ssDNA and DAPI is confirmed after DNA denaturation by boiling in sodium citrate.

Figure 3.20 and **3.21** show that the change in method used for DNA denaturation in mouse embryonic tissues was successful in brain tissues as well as in liver tissues, as demonstrated by 5mC colocalisation with DAPI. Boiling in 10 mM of sodium citrate for denaturation of DNA was demonstrated to be much more effective in tissues than HCl treatment. Similar improvement was observed for 5mC and ssDNA staining. The immunostaining for ssDNA that was used as a control further reinforced the observed colocalisation with 5mC and DAPI. Patterns of observed signal were consistent with the partially immunostained images from HCl denatured cultured cells. The boiling step was derived from protocols for sodium citrate Southern hybridisation, fluorescent in situ hybridisation (FISH) and histochemistry staining of dehydrated paraffin sections. The method is also used for antigen retrieval; this generally retrieves protein epitopes but in this case included denaturation of DNA to expose DNA bases. The boiling step therefore retrieves antigen epitopes as well as denaturing DNA. Formalin or other aldehyde fixation may form protein cross-links that mask the antigenic sites in tissue specimens, thereby showing poor or false negative staining for immunohistochemical detection of certain proteins. The citrate based solution is designed to break the protein cross-links, thus unmask the antigens and epitopes in formalin-fixed and paraffin embedded tissue sections, therefore enhancing staining intensity of antibodies. Of further relevance is that DNA denaturation by sodium citrate boiling, as used in Southern hybridisation, FISH and paraffin section histochemistry may be better at dealing with dehydrated DNA on a substrate, including DNA adhered onto glass.

3.7 DNA hydroxymethylation immunostaining in mouse embryonic tissues

5hmC has been proposed to be an intermediate in an active DNA demethylation pathway. Thus, immunohistochemical detection of 5hmC was crucial in order to investigate tissues undergoing dynamic nuclear changes in DNA hydroxymethylation state during development. Therefore, the optimised immunohistochemistry method used for staining 5mC was used to stain 5hmC.

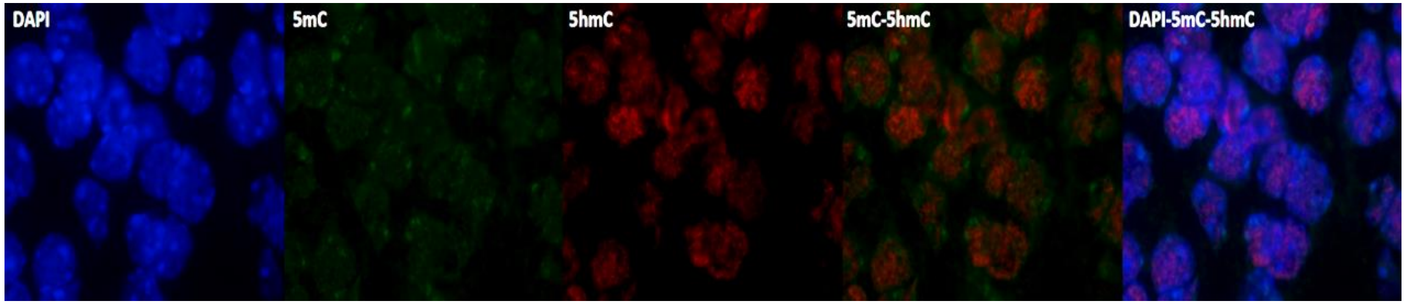

Figure 3.22: DNA hydroxymethylation immunostaining in E13.5 mouse embryonic brain tissues. Representative stainings of mouse embryonic brain tissue sections are shown. First panel: tissue nuclear DNA counterstained with DAPI (blue). Second panel: tissues stained with primary antibody against 5mC (green). Third panel: tissues stained with antibody against 5hmC (red). Fourth panel: merged image of 5mC and 5hmC. Fifth panel: merged image of DAPI, 5mC and 5hmC. 5hmC staining is excluded from DAPI-dense foci.

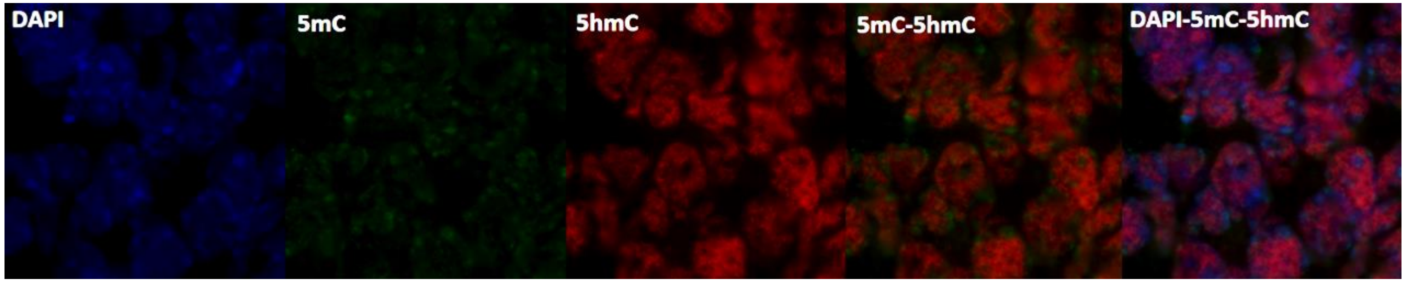

Figure 3.23: DNA hydroxymethylation immunostaining in E13.5 mouse embryonic liver tissues. Representative stainings of mouse embryonic liver tissue sections are shown. First panel: tissue nuclear DNA counterstained with DAPI (blue). Second panel: tissues stained with primary antibody against 5mC (green). Third panel: tissues stained with antibody against 5hmC (red). Fourth panel: merged image of 5mC and 5hmC. Fifth panel: merged image of DAPI, 5mC and 5hmC. 5hmC signals are confirmed.

It is shown that the method used for staining 5mC successfully stained for 5hmC. 5hmC and 5mC were expected to show overlap if 5hmC is a derivative, yet 5hmC signals were mainly enriched in euchromatic regions and excluded from DAPI-dense foci in brain tissues as well as in liver tissues **(Figure 3.22 and 3.23)**. This result has confirmed what the lab has observed for primary mouse embryonic fibroblast cultures (Nestor et al., 2015).

3.8 DNA methylation immunostaining in MBD-GFP mouse embryonic tissues

A transgenic mouse GFP reporter was under characterisation in the lab as an approach to visualise DNA methylation in tissues. Tissues carrying a GFP fusion with a CpG methyl-binding domain (human MBD1) were used in this study. In order to assess the effectiveness of this marker, it was very important to have the optimised protocol for 5mC detection working reliably on these MBD-GFP mouse embryo cryosections. This was because, for any GFP signals observed in transgenic mouse tissues, 5mC results were used as a necessary control for comparison. Thus, it was crucial for the working protocol to detect both markers together on the same cryosection in order to observe how well these two marks correlate.

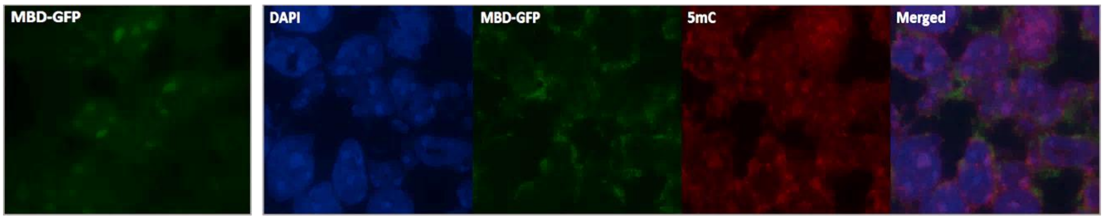

Figure 3.24: DNA methylation immunostaining in E11.5 MBD-GFP mouse embryonic brain tissues. Representative stainings of MBD-GFP mouse embryonic brain tissue sections are shown. First panel: GFP-expressing cells (green) were detected in PFA-fixed cryosection before the staining procedure. Second panel: tissue nuclear DNA counterstained with DAPI (blue). Third panel: tissues stained with anti-GFP antibody (green). Fourth panel: tissues stained with anti-5mC antibody (red). Fifth panel: merged image. The working protocol for 5mC detection did not preserve the native GFP fluorescent pattern present before the staining procedure (compare first and third panel).

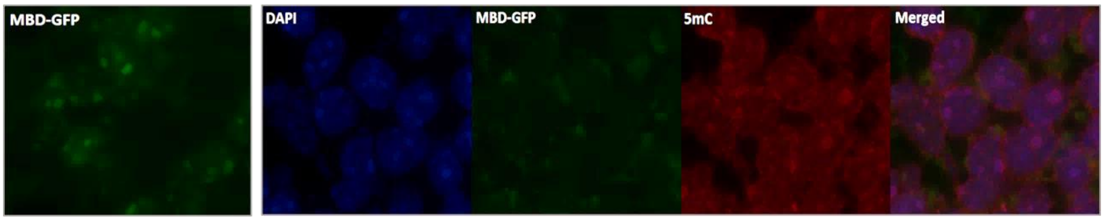

Figure 3.25: DNA methylation immunostaining in E11.5 MBD-GFP mouse embryonic liver tissues. Representative stainings of MBD-GFP mouse embryonic liver tissue sections are shown. First panel: GFP-expressing cells (green) were detected in PFA-fixed cryosection before the staining procedure. Second panel: tissue nuclear DNA counterstained with DAPI (blue). Third panel: tissues stained with anti-GFP antibody (green). Fourth panel: tissues stained with anti-5mC antibody (red). Fifth panel: merged image. The working protocol for 5mC detection did not preserve the native GFP fluorescence in either brain tissue (Figure 3.24) or liver tissue (compare first and third panel).

Figure 3.24 and **3.25** show that the working protocol for immunodetection of 5mC did not preserve the native GFP or its detection by anti-GFP antibody in either brain or liver tissue. As a control, the presence of GFP signal in PFA-fixed tissue cryosections was recorded prior to staining, showing that the GFP signals were detected in heterochromatic foci before the procedure. Another control, GFP immunostaining without denaturation step, also was performed (data not shown). Omission of this critical denaturation step in the staining procedure resulted in the detection of GFP signals. Anti-GFP antibody was incorporated into the 5mC staining protocol in order to overcome dim and degraded signals. However, anti-GFP immunostaining did not rescue detectable GFP signals apart from non-nuclear background.

It is shown that the method used for staining 5mC was successful but unfortunately it did not preserve the native GFP. The problem was considered at the denaturation step as heat denaturation leads to disruption of GFP signal. Therefore, an alternative refinement of the denaturation method was employed to preserve native GFP signals from harsh denaturing treatment.

3.9 DNA methylation immunostaining in MBD-GFP mouse embryonic tissues: preservation of native GFP proteins

GFP immunostaining using optimised 5mC immunodetection was unsuccessful. An alternative denaturation method was employed to preserve the native GFP signals whilst at the same time working reliably for 5mC immunodetection.

3.9.1 Formamide-based denaturation method

Heating is not the only way to denature DNA, an organic solvent such as formamide also has the ability to break the hydrogen bonds that hold the double helix together. Formamide is a well-known and the most frequently used denaturing agent for DNA. Therefore, an alternative denaturation method using 70% formamide, 2X saline sodium citrate (SSC) adapted from Shi et al. (2004a) was employed.

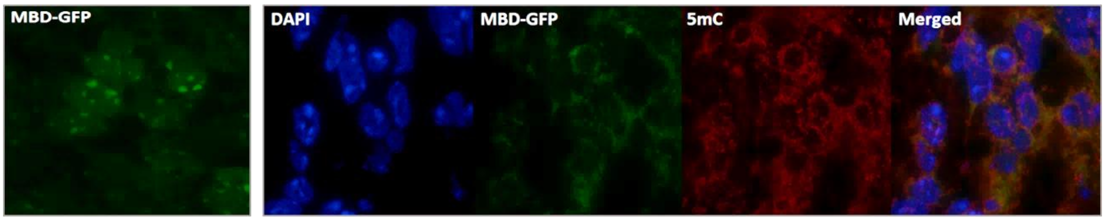

Figure 3.26: DNA methylation immunostaining in E11.5 MBD-GFP mouse embryonic brain tissues. Representative staining of MBD-GFP mouse embryonic brain tissue sections is shown. First panel: GFP-expressing cells (green) were detected in PFA-fixed cryosection before the staining procedure. Second panel: tissues counterstained with DAPI (blue). Third panel: same tissues stained with anti-GFP (green). Fourth panel: tissues stained with 5mC (red). Fifth panel: merged image. Formamide-based denaturation method did not detect 5mC as a nuclear signal, and neither did it preserve the native GFP.

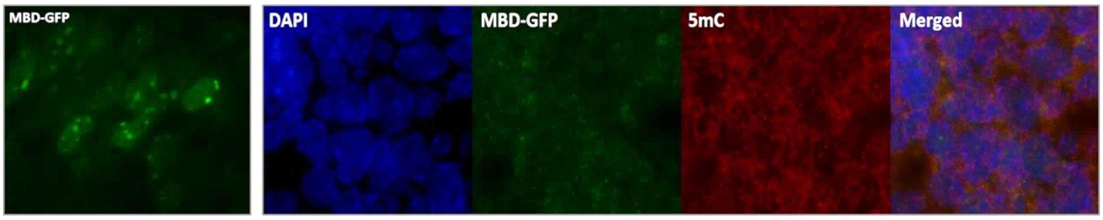

Figure 3.27: DNA methylation immunostaining in E11.5 MBD-GFP mouse embryonic liver tissues. Representative staining of MBD-GFP mouse embryonic liver tissue sections is shown. First panel: GFP-expressing cells (green) were detected in PFA-fixed cryosection before the staining procedure. Second panel: tissues counterstained with DAPI (blue). Third panel: same tissues stained with anti-GFP (green). Fourth panel: tissues stained with 5mC (red). Fifth panel: merged image. Formamide-based denaturation method did not detect 5mC as a nuclear signal, and neither did it preserve the native GFP in either tissue.

Figure 3.26 and **3.27** show that the alternative denaturation method using formamide did not work for either 5mC or as GFP detection. Positive GFP signals were detected in PFA-fixed tissue cryosections, indicating that the GFP was present before the staining procedure. The formamide-denatured DNA method showed no improvement; in fact, this method worked even worse than heat-denatured DNA. Therefore, no subsequent actions were taken to optimise it. For that reason, another method for DNA denaturation was sought in order to detect both markers.

3.9.2 Microwave-heating denaturation method

A further refinement of the denaturation method using the same heat treatment as previously was employed. The denaturation method was adapted from Piyathilake et al. (2004). But instead of boiling the slides in a sodium citrate-containing beaker on a hot plate, the alternative heating method employed a microwave, in which the slides were boiled in a sodium citrate-containing Schieferdecker jar in the microwave. Microwaving is commonly used as a heating method for heat-induced epitope retrieval in immunohistochemistry, but in this case, it also includes denaturation of DNA to expose DNA bases.

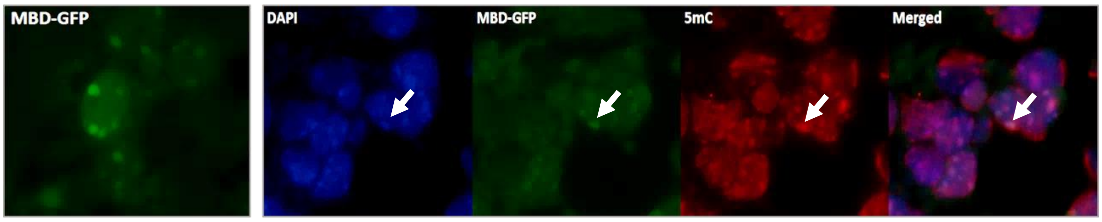

Figure 3.28: DNA methylation immunostaining in E11.5 MBD-GFP mouse embryonic brain tissues. Representative staining of MBD-GFP mouse embryonic brain tissue sections is shown. First panel: GFP-expressing cells (green) were detected in PFA-fixed cryosection before the staining procedure. Second panel: tissues counterstained with DAPI (blue). Third panel: same tissues stained with anti-GFP antibody (green). Fourth panel: tissues stained with 5mC (red). Fifth panel: merged image. 5mC immunostaining worked after microwave treatment with approximately 10% of GFP signals detectable by antibody after heat-mediated antigen retrieval (marked by arrows).

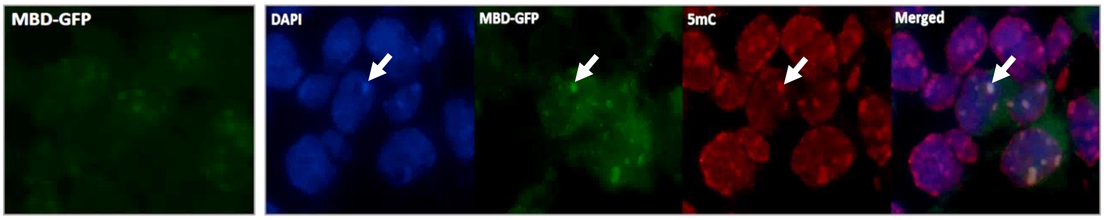

Figure 3.29: DNA methylation immunostaining in E11.5 MBD-GFP mouse embryonic liver tissues. Representative staining of MBD-GFP mouse embryonic liver tissue sections is shown. First panel: GFP-expressing cells (green) were detected in PFA-fixed cryosection before the staining procedure. Second panel: tissues counterstained with DAPI (blue). Third panel: same tissues stained with anti-GFP antibody (green). Fourth panel: tissues stained with 5mC (red). Fifth panel: merged image. 5mC immunostaining worked after microwave treatment with approximately 10% of GFP signals detectable by antibody after heat-mediated antigen retrieval (marked by arrows). Observations in brain (Figure 3.28) were confirmed in liver.

Figure 3.28 and **3.29** show that the change in heating method for DNA denaturation was partially successful. The microwave heating method allowed successful staining of 5mC and enabled the preservation of immunodetectable native GFP signals. However, only approximately 10% of GFP signals survived after heat-mediated antigen retrieval. Positive GFP signals were detected in PFA-fixed tissue cryosections, indicating that the GFP was present before the staining procedure. Furthermore, the antibody used for GFP immunostaining was compatible with the microwave treatment where it appeared to rescue detection of the natural fluorophore of GFP.

5mC and GFP signals demonstrated colocalisation with DAPI staining. A good overlap between 5mC and GFP signals was also observed, particularly in heterochromatic areas where both marks were highly enriched. It is shown that 5 minutes of microwave treatment resulted in detection of 5mC and preservation of approximately 10% of GFP signals. Suitable conditions for heat denaturation were further investigated to avoid potential risk of overheating. In particular, overheating may fully denature the GFP protein and destroy its ability to fluoresce.

3.9.2.1 Optimisation of microwave boiling duration

To improve the GFP retention, microwave boiling duration was optimised.

3.9.2.1.1 Duration of microwave boiling test (4 minutes)

In this test, the duration of microwave boiling was shortened from 5 minutes to 4 minutes. A short boiling time may preserve more GFP signals.

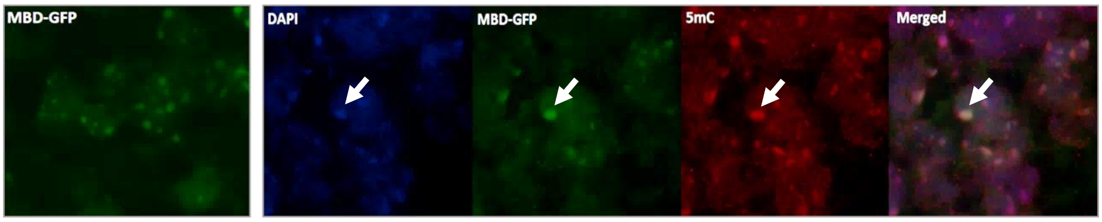

Figure 3.30: DNA methylation immunostaining in E11.5 MBD-GFP mouse embryonic brain tissues. Representative staining of MBD-GFP mouse embryonic brain tissue sections is shown. First panel: GFP-expressing cells (green) were detected in PFA-fixed cryosection before the staining procedure. Second panel: tissues counterstained with DAPI (blue). Third panel: same tissues stained with anti-GFP (green). Fourth panel: tissues stained with 5mC (red). Fifth panel: merged image. Four minutes of microwave treatment resulted in an increase of GFP signals to an estimated 20%, yet 5mC immunodetection was still effective (marked by arrows).

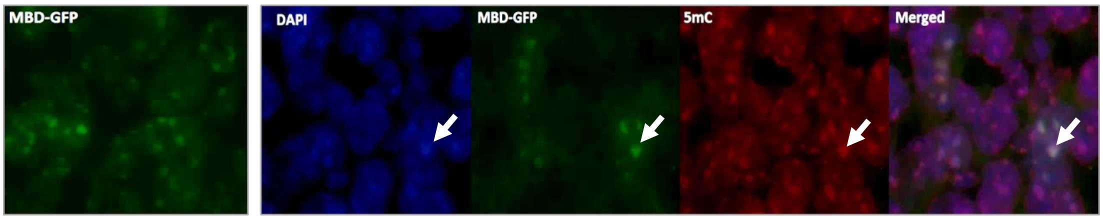

Figure 3.31: DNA methylation immunostaining in E11.5 MBD-GFP mouse embryonic liver tissues. Representative staining of MBD-GFP mouse embryonic liver tissue sections is shown. First panel: GFP-expressing cells (green) were detected in PFA-fixed cryosection before the staining procedure. Second panel: tissues counterstained with DAPI (blue). Third panel: same tissues stained with anti-GFP (green). Fourth panel: tissues stained with 5mC (red). Fifth panel: merged image. 4 minutes of microwave treatment resulted in an increase in GFP signals to an estimated 20%, yet 5mC immunodetection was still effective (marked by arrows). Observations in brain were confirmed in liver.

Figure 3.30 and **3.31** show that the 4 minutes of microwave treatment resulted in increased GFP signals to approximately 20%. This treatment was also compatible with 5mC immunodetection. Positive GFP signals were detected in PFA-fixed tissue cryosections, indicating that the GFP was present before the staining procedure. 5mC and GFP signals demonstrated colocalisation with DAPI staining. A good overlap between 5mC and GFP signals was also observed. Indeed, a shorter boiling time preserved more GFP signals.

3.9.2.1.2 Duration of microwave boiling test (3 minutes)

To further improve the GFP retention, the duration of microwave boiling was shortened to 3 minutes.

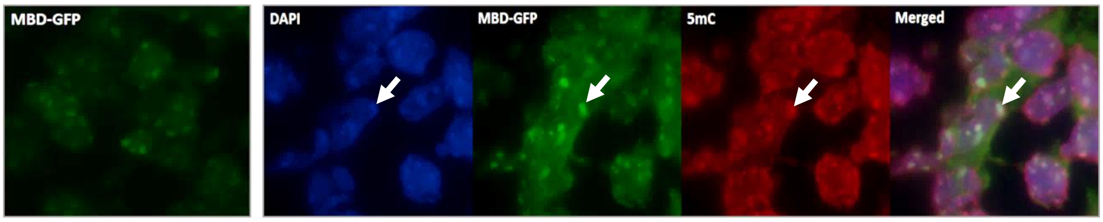

Figure 3.32: DNA methylation immunostaining in E11.5 MBD-GFP mouse embryonic brain tissues. Representative staining of MBD-GFP mouse embryonic brain tissue sections is shown. First panel: GFP-expressing cells (green) were detected in PFA-fixed cryosection before the staining procedure. Second panel: tissues counterstained with DAPI (blue). Third panel: same tissues stained with anti-GFP (green). Fourth panel: tissues stained with 5mC (red). Fifth panel: merged image. Three minutes of microwave treatment resulted in an increase in GFP signals to an estimated 45%, yet 5mC immunodetection was still effective (marked by arrows).

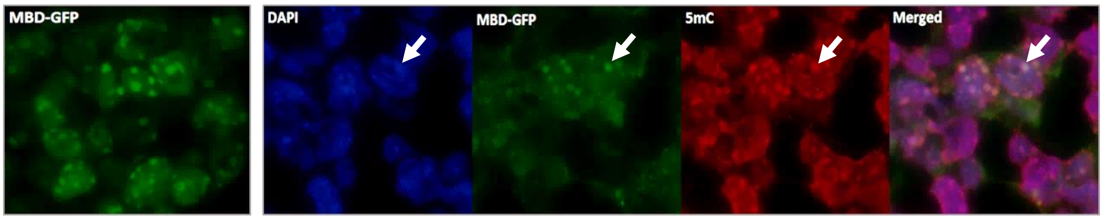

Figure 3.33: DNA methylation immunostaining in E11.5 MBD-GFP mouse embryonic liver tissues. Representative staining of MBD-GFP mouse embryonic liver tissue sections is shown. First panel: GFP-expressing cells (green) were detected in PFA-fixed cryosection before the staining procedure. Second panel: tissues counterstained with DAPI (blue). Third panel: same tissues stained with anti-GFP (green). Fourth panel: tissues stained with 5mC (red). Fifth panel: merged image. Three minutes of microwave treatment resulted in an increase in GFP signals to an estimated 45%, yet 5mC immunodetection was still effective (marked by arrows). Observations in brain were confirmed in liver.

Figure 3.32 and **3.33** show that the 3 minutes of microwave treatment resulted in a further increase in GFP signals to approximately 45%. This treatment was still compatible with 5mC immunodetection. Positive GFP signals were detected in PFA-fixed tissue cryosections, indicating that the GFP was present before the staining procedure. 5mC and GFP signals demonstrated colocalisation with DAPI staining. A good overlap between 5mC and GFP signals was also detected. Indeed, a further decrease in boiling time reduced fluorophore disruption and more GFP signals were immunodetectable.

3.9.2.1.3 Duration of microwave boiling test (2 minutes)

To determine the condition boundaries of the boiling duration, 2 minutes of microwave treatment was performed.

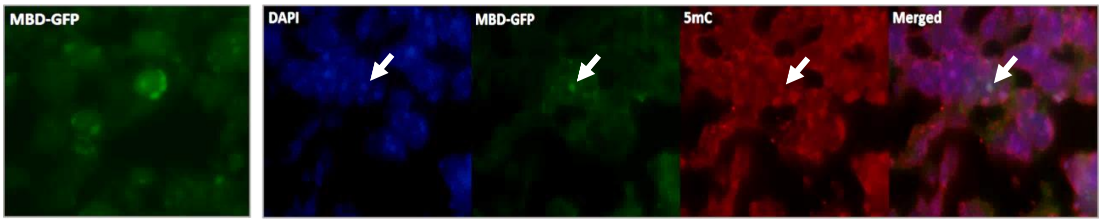

Figure 3.34: DNA methylation immunostaining in E11.5 MBD-GFP mouse embryonic brain tissues. Representative staining of MBD-GFP mouse embryonic brain tissue sections is shown. First panel: GFP-expressing cells (green) were detected in PFA-fixed cryosection before the staining procedure. Second panel: tissues counterstained with DAPI (blue). Third panel: same tissues stained with anti-GFP (green). Fourth panel: tissues stained with 5mC (red). Fifth panel: merged image. Two minutes of microwave treatment resulted in a decrease in GFP signals to an estimated 20% yet 5mC immunodetection was still effective (marked by arrows) but some areas started to show non-specific staining.

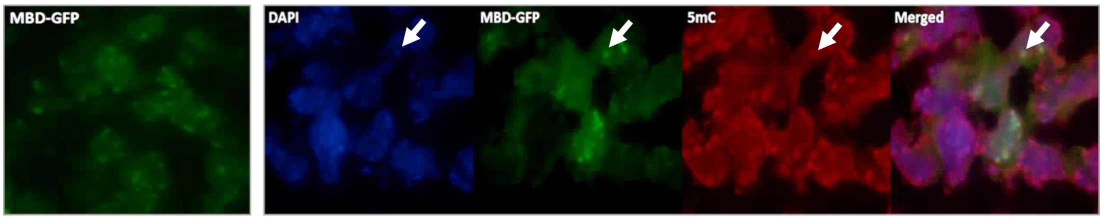

Figure 3.35: DNA methylation immunostaining in E11.5 MBD-GFP mouse embryonic liver tissues. Representative staining of MBD-GFP mouse embryonic liver tissue sections is shown. First panel: GFP-expressing cells (green) were detected in PFA-fixed cryosection before the staining procedure. Second panel: tissues counterstained with DAPI (blue). Third panel: same tissues stained with anti-GFP (green). Fourth panel: tissues stained with 5mC (red). Fifth panel: merged image. Two minutes of microwave treatment resulted in a decrease in GFP signals to an estimated 20% yet 5mC immunodetection was still effective (marked by arrows) but some areas started to show non-specific staining. Observations in brain (Figure 3.34) were confirmed in liver.

Figure 3.34 and **3.35** show that the 2 minutes of microwave treatment resulted in decreased GFP signals to approximately 20%. This treatment was still compatible with 5mC immunodetection, however some areas started to show non-specific staining. Positive GFP signals were detected in PFA-fixed tissue cryosections, indicating that the GFP was present before the staining procedure. 5mC and GFP signals demonstrated colocalisation with DAPI staining. A good overlap between 5mC and GFP signals was also detected. It is shown that reducing the boiling time did not result in further gains.

Therefore, 3 minutes of microwave boiling was considered an optimal condition and was used for subsequent experiment.

3.9.2.2 GFP antibody test

Detection of native GFP signals may be improved by using another GFP antibody. For that reason, the use of anti-GFP antibody was changed to GFP booster detection agent. GFP booster might give better results in detecting heat-denatured GFP as it is a single chain nanobody, claimed to have some advantages. Compared to indirect immunofluorescence, this GFP fusion nanobody has the potential to provide a more direct and dense staining, mainly due to its nanoscale size (2-3 nm). Furthermore, GFP nanobody is shown to react in mouse (manufacturer’s datasheet) and there are numerous published studies using it (Ridzuan et al., 2012; Rothbauer et al., 2006; Szymanska et al., 2016).

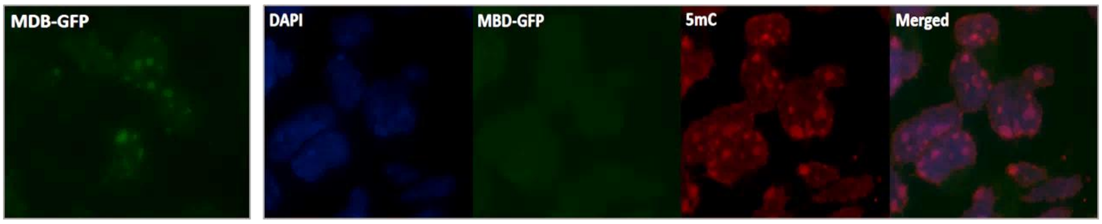

Figure 3.36: DNA methylation immunostaining in E11.5 MBD-GFP mouse embryonic brain tissues. Representative staining of MBD-GFP mouse embryonic brain tissue sections is shown. First panel: GFP-expressing cells (green) were detected in PFA-fixed cryosection before the staining procedure. Second panel: tissues counterstained with DAPI (blue). Third panel: same tissues stained with anti-GFP (green). Fourth panel: tissues stained with 5mC (red). Fifth panel: merged image. GFP booster did not preserve the native GFP.

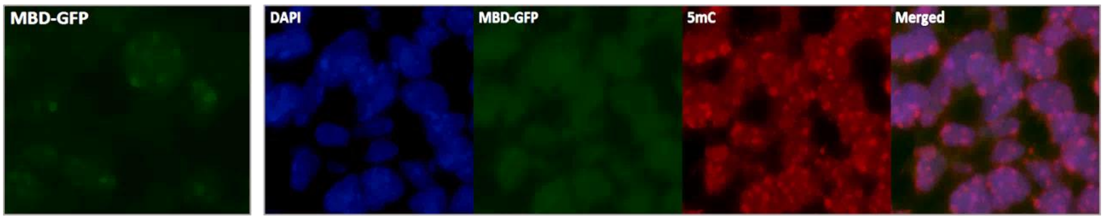

Figure 3.37: DNA methylation immunostaining in E11.5 MBD-GFP mouse embryonic liver tissues. Representative staining of MBD-GFP mouse embryonic liver tissue sections is shown. First panel: GFP-expressing cells (green) were detected in PFA-fixed cryosection before the staining procedure. Second panel: tissues counterstained with DAPI (blue). Third panel: same tissues stained with anti-GFP (green). Fourth panel: tissues stained with 5mC (red). Fifth panel: merged image. GFP booster did not preserve the native GFP in either brain or liver tissue.

Figure 3.36 and **3.37** show that the change in GFP antibody did not result in more rescue of native GFP signals. GFP signal detection using alternative GFP booster antibody showed weak nuclear staining but was unsuccessful in staining the native GFP pattern. Positive GFP signals were observed in PFA-fixed tissue cryosections, indicating that the GFP was present before the staining procedure. Therefore, anti-GFP was used for subsequent experiment.

3.9.2.3 Duration of PFA fixation test

PFA tends to quench fluorescence of the GFP fusion protein. Mild fixation may prevent the quenching of GFP fluorescence, thereby increasing its visibility. Therefore, in this test, the duration of PFA fixation was shortened from 50 minutes to 30 minutes.

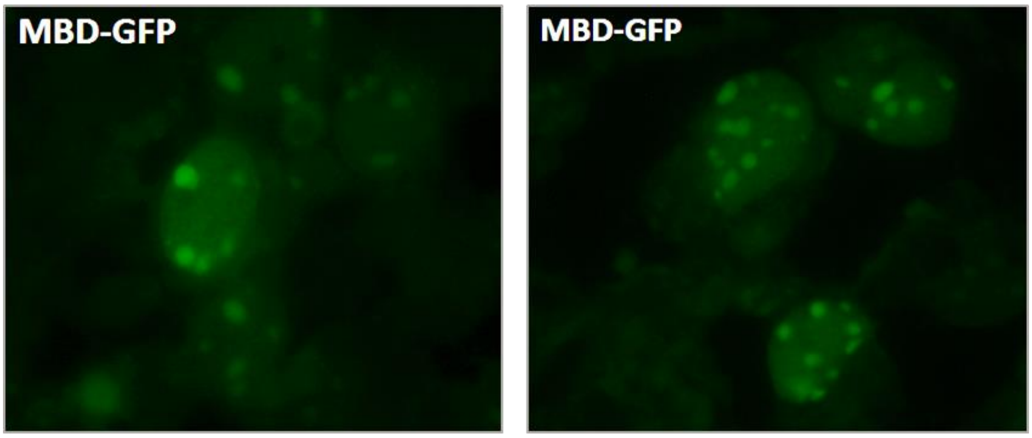

Figure 3.38: DNA methylation immunostaining in E11.5 MBD-GFP mouse embryonic brain tissues. Representative stainings of MBD-GFP mouse embryonic brain tissue sections are shown. First panel: GFP-expressing cells (green) after 50 minutes of PFA fixation. Second panel: GFP-expressing cells (green) after 30 minutes of PFA fixation. Mild fixation did not result in increased GFP signals.

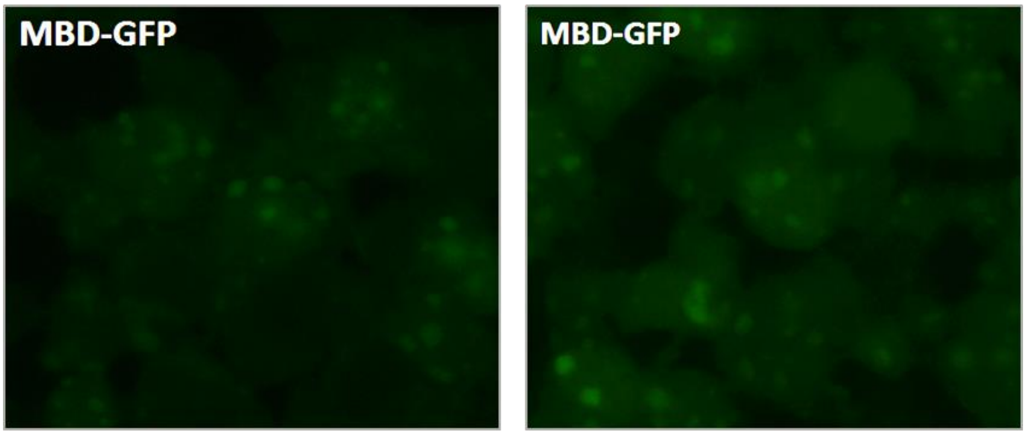

Figure 3.39: DNA methylation immunostaining in E11.5 MBD-GFP mouse embryonic liver tissues. Representative stainings of MBD-GFP mouse embryonic liver tissue sections are shown. First panel: GFP-expressing cells (green) after 50 minutes of PFA fixation. Second panel: GFP-expressing cells (green) after 30 minutes of PFA fixation. Mild fixation did not result in increased GFP signals in either tissue.

Figure 3.38 and **3.39** show that the mild fixation did not result in increased GFP signals, indicating that PFA did not quench the fluorescence of GFP. There was no significant difference in fluorescence intensity of GFP signals between 50 minutes and 30 minutes of PFA fixation. Therefore, a standard 50 minutes of PFA fixation employed for tissues was used for subsequent experiment.

3.9.2.4 ssDNA immunostaining using microwave-based denaturation method

As a control and to further confirm the denaturation of DNA, ssDNA immunostaining was performed using 3 minute microwave-heating denaturation method.

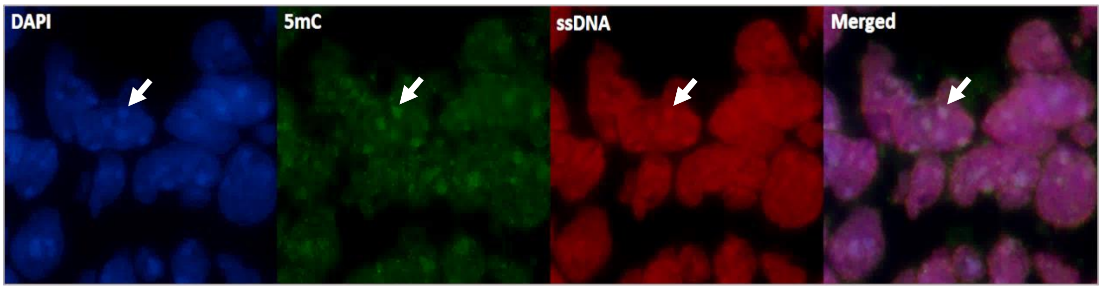

Figure 3.40: DNA methylation immunostaining in E11.5 MBD-GFP mouse embryonic brain tissues. Representative staining of MBD-GFP mouse embryonic brain tissue sections is shown. First panel: tissues counterstained with DAPI (blue). Second panel: same tissues stained with 5mC (green). Third panel: tissues stained with ssDNA (red). Fourth panel: merged image. ssDNA staining was observed using 3 minute microwave-heating denaturation method.

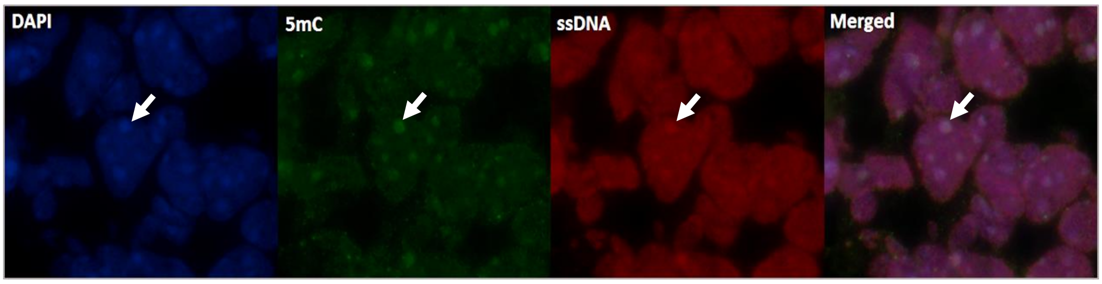

Figure 3.41: DNA methylation immunostaining in E11.5 MBD-GFP mouse embryonic liver tissues. Representative staining of MBD-GFP mouse embryonic liver tissue sections is shown. First panel: tissues counterstained with DAPI (blue). Second panel: same tissues stained with 5mC (green). Third panel: tissues stained with ssDNA (red). Fourth panel: merged image. ssDNA staining was confirmed in brain (Figure 3.40) and liver.

Figure 3.40 and **3.41** show that the presence of ssDNA was detected. ssDNA demonstrated colocalisation with 5mC and DAPI. The denaturation of DNA was confirmed by ssDNA staining in brain and in liver cryosections.

3.9.2.5 DNA hydroxymethylation immunostaining using microwave-based denaturation method

As 5hmC detection was crucial for this study, it was important to have the alternative microwave-heating denaturation method working reliably for 5hmC immunodetection.

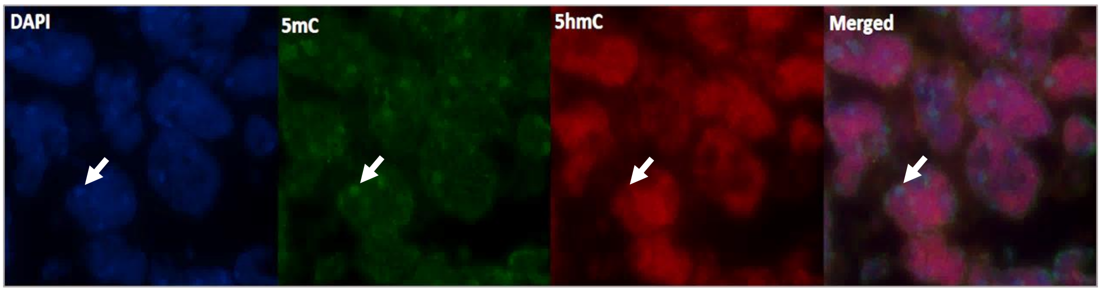

Figure 3.42: DNA methylation immunostaining in E11.5 MBD-GFP mouse embryonic brain tissues. Representative staining of MBD-GFP mouse embryonic brain tissue sections are shown. First panel: tissues counterstained with DAPI (blue). Second panel: same tissues stained with 5mC (green). Third panel: tissues stained with 5hmC (red). Fourth panel: merged image. 5hmC staining was observed using 3 minute microwave-heating denaturation method.

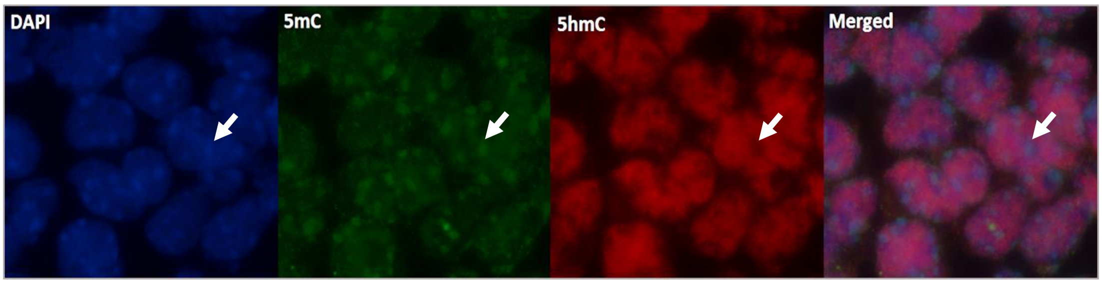

Figure 3.43: DNA methylation immunostaining in E11.5 MBD-GFP mouse embryonic liver tissues. Representative staining of MBD-GFP mouse embryonic liver tissue sections is shown. First panel: tissues counterstained with DAPI (blue). Second panel: same tissues stained with 5mC (green). Third panel: tissues stained with 5hmC (red). Fourth panel: merged image. 5hmC staining was confirmed in brain (Figure 3.42) and liver.

Figure 3.42 and **3.43** show that the alternative microwave-heating denaturation method used for staining 5mC successfully stained for 5hmC. It is shown that the 5hmC signals are mainly enriched in euchromatic regions and excluded from the DAPI-dense heterochromatin.

3.10 Discussion

This PhD study aims to investigate the changing nuclear distributions and levels of DNA methylation during development, to discover dynamic variations amongst developing mouse tissues, a topic which is currently under-investigated. In this study of DNA methylation dynamics, immunohistochemical technique has been employed as an investigative tool. Optimal immunohistochemistry protocols are fundamental to minimise the possibility of false negative results, whilst at the same time not introducing a false positive result. Furthermore, reliable immunohistochemical studies may represent an important source of information for accurately understanding the nuclear epigenetic dynamics during development with relevance to cell reprogramming for regenerative medicine. Therefore, this chapter focuses on the optimisation of DNA methylation immunohistochemistry protocol aiming to achieve the optimal conditions for the detection of DNA methylation and reports significant improvements on methods published in the literature.

3.10.1 DNA methylation immunostaining: protocol optimisation

The existing standard methodology for DNA methylation immunostaining using HCl DNA denaturation works for cultured cells, preimplantation embryos (mouse, rat and sheep) and embryos to larvae (zebrafish). These examples have shown that 5mC stains heterochromatin, 5hmC stains throughout nucleus except nucleoli and ssDNA staining copies the DAPI pattern. However, the existing methodology was found not to work for mouse embryo tissue cryosections, on which all antibodies for 5mC, 5hmC and ssDNA stain preferentially nuclei but without reference to the DAPI pattern. Therefore, all these antibodies have a similar non-specific nuclear appearance on cryosections, which could be potentially misleading when viewed at low magnification.

Examples of working protocols for DNA methylation immunostaining of cryosections in the literature were examined but not many tissues have been characterised for DNA methylation. Only a few images in the literature demonstrated a working technique and some images found for paraffin sections suffered from distinct issues of partial staining.

The standard protocol was assumed to work on tissues as it worked on cells but methodology changes and optimisation were required. The standard denaturation protocol uses HCl and rapid neutralisation with buffer, for example Ruzov et al. (2011). Somehow this causes 5mC antibody specificity problems in tissues but not in cultured cells or small whole embryos. Further optimisation of the DNA denaturation step using HCl needs to be considered. Overall, the existing protocol was found not to be a very reproducible method, yet it is a standard methodology and widely used.

Therefore, an alternative denaturation step was employed to improve the antibody detection. It is shown that this alternative method used for DNA denaturation in mouse embryonic tissues by boiling in 10 mM of sodium citrate was successful. During the process of heat-induced antigen unmasking, heat causes the cross-linked proteins to unfold in a manner similar to DNA denaturation (Fowler et al., 2011), whereas the citrate solution used during this heating may help to further unfold the proteins, resulting in the recovery of antigen reactivity (Hussaini et al., 2013). However, the precise mechanism of antigen retrieval is not properly understood (Vollert et al., 2015).

In this case, the antigen retrieval heating technique was successfully applied to denature the DNA, making it single-stranded and accessible for antibody binding. Using this method, it is shown in nuclei throughout the cryosection that 5mC stains heterochromatin, 5hmC stains nuclear euchromatin except for nucleoli and ssDNA staining copies the DAPI pattern.

To further confirm the results, three important controls had been performed to verify the specificity of both 5mC and 5hmC antibodies. The first control was 5mCimmunostaining in both cells and tissues, which showed immunofluorescence evidence for the presence of 5mC, suggesting that this monoclonal antibody worked perfectly specific in capturing methylated DNA in cells, as well as in tissues. The second control was 5mC immunostaining in hypomethylated mouse embryonic primordial germ cells, which demonstrated no apparent evidence of 5mC staining as expected, further confirming the specificity of this antibody against 5mC. The third control was single staining of 5mC and 5hmC, which displayed 5mC was mainly located in heterochromatic regions, whereas 5hmC enrichment was found in euchromatic regions, indicating that both antibodies were highly specific for their respective epitopes and did not cross-react with one another. Second and third controls are discussed in greater detail in Chapter 4.

5hmC immunostaining, however, was not particularly performed in cells and hypohydroxymethylated cells/tissues, therefore these controls should be carried out in order to further confirm the specificity of the 5hmC antibody. Nonetheless, anti-5hmC, as well as anti-5mC antibodies, are well-characterised antibodies whose antigenic specificity is well known and there are several published studies using the same antibodies (Diotel et al., 2017; Franco et al., 2017; Jafarpour et al., 2017; Lee et al., 2017). In addition, according to the manufacturer's datasheet, dotblot assay demonstrates no cross-reactivity of the 5mC antibody with 5hmC and cytosine. Similarly, for the 5hmC antibody, dotblot assay shows no cross-reactivity of this antibody with 5mC and cytosine (manufacturer's datasheet). Furthermore, both antibodies are shown to react in mouse (manufacturer's datasheet).

3.10.2 DNA methylation immunostaining: preservation of native GFP proteins

GFP is frequently used in molecular biology to generate fluorescent tagged/fusion proteins in order to visualise the subcellular localisation of specific proteins (Chalfie et al., 1994; Yamagata et al., 2007; Yamazaki et al., 2007). Nonetheless, being genetically encoded and not chemically engineered, there are a number of technical limitations of GFP as a subcellular marker. These limitations include the following: low expression level, photosensitive, weak signal intensity, insolubility, and instability at high temperature (Vela and Buja, 2016).

In the case of immunohistochemical staining, preservation of tissue morphology with chemical fixatives such as formaldehyde is necessary (Howat and Wilson, 2014). However, one shortcoming of fixation of GFP-expressing tissues is that it may lose its direct fluorescence during this process (Swenson et al., 2007). Moreover, the

DNA methylation immunostaining protocol used in this study to visualise GFP involves heat treatment. This approach has its limitations as GFP tends to lose its fluorescence in heat-treated tissue sections (Nakamura et al., 2008). It seems that treatment involving heat irreversibly denatures GFP, thus destroying its ability to emit fluorescence (Nakamura et al., 2008). To counter these limitations, immunostaining with commercially available antibodies is normally used to detect GFP (Jensen, 2012). Low fluorescence signals can be recovered using an anti-GFP antibody (Choudhury et al., 2016; Kohl et al., 2014).

Despite these limitations, this study has found that GFP immunostaining worked after optimising protocols for microwave treatment, with 45% of signals surviving after heat-mediated antigen retrieval. This opens up the possibility for combinatorial applications of the GFP immunodetection method with procedures requiring heat treatment.

3.10.3 Comparison between two methods of DNA denaturation

DNA methylation immunostaining of cryosections was found to require DNA denaturation by heat treatment (hot plate or microwave) **(Figure 3.44)** instead of HCl DNA denaturation. Most importantly, GFP immunostaining offered good compatibility with the microwave method, adding further advantage of using this method.

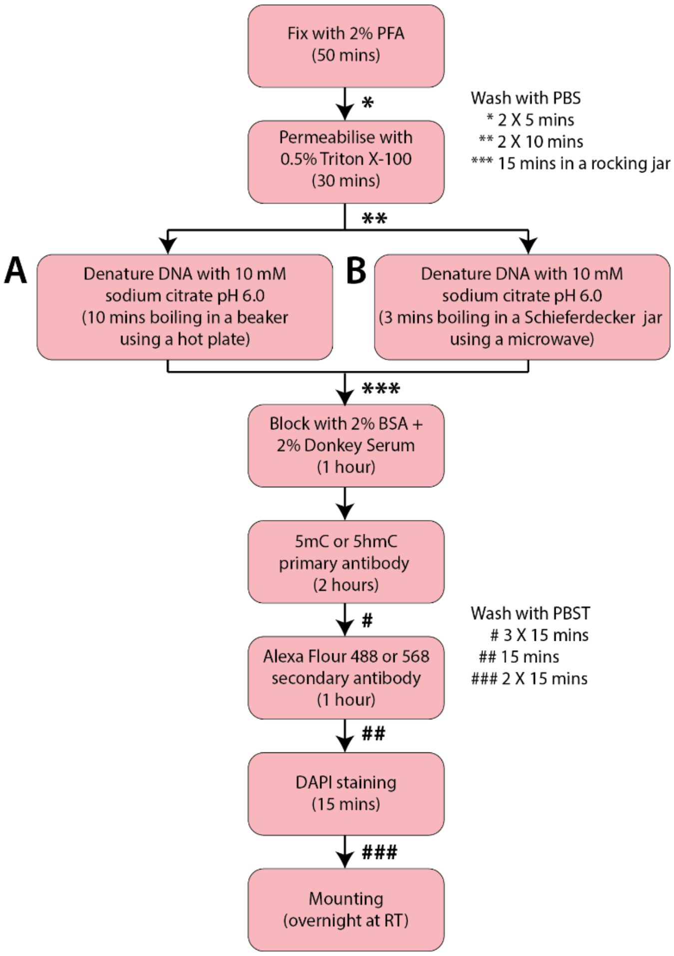

Figure 3.44: DNA methylation immunohistochemistry protocol. DNA methylation immunostaining of cryosections requires heat-mediated DNA denaturation either using **(A)** hot plate or **(B)** microwave techniques. Both methods are reported in Beaujean et al. (2017) (in press).

Immunohistochemistry has become the most valuable tool in many medical research laboratories as it permits visualisation of specific antigens in tissues (Goto et al., 2015). Therefore, ensuring the accuracy and reliability of the results obtained through visual inspection of stained tissues is critical. Based on this study, both methods that were optimised have proven to be very accurate and reliable in detecting DNA methylation in tissue cryosections. Furthermore, the ultimate aim when optimising immunohistochemistry protocols is to ensure consistent and reproducible results. Based on obtained results, both optimised methods were shown to be capable of producing high-quality, uniform staining, with a degree of consistency and reproducibility sufficient to allow comparison of staining results across experiments. In addition, the use of heat in the immunostaining procedure was generally considered too harsh and likely to destroy tissue morphology. Remarkably, both heat-mediated DNA denaturation methods did not show any apparent detrimental effects to nuclear detail and morphology of the tissue sections.

However, in subsequent experimental works, microwave heating became the method of choice due to several practical advantages. It has been shown that the application of microwave heating during the immunohistochemical staining process can significantly reduce the amount of time needed to perform the denaturation step, thus speeding up the entire staining process. Furthermore, the microwave oven has the potential to provide heat instantly, thus a significantly higher temperature can be reached more quickly. Moreover, with this method, the amount of heat delivered and time required can be manually set with the push of a button, which makes it easy to operate and convenient to use. Most importantly, microwave heating is safer than an external hot plate heating.

Nonetheless, the application of a domestic microwave is not ideal due to the presence of hot and cold spots in the oven, leading to uneven distribution of heat (Vinod et al., 2016). In order to overcome this problem, the built-in rotating platform has been employed to ensure substantially uniform heat distribution. Indeed, it has been demonstrated in this study that the microwave-assisted staining protocol uniformly stained DNA methylation throughout the tissue section.

Considering the advantages offered by microwave heating, this method was therefore employed in the next chapter to investigate tissues undergoing dynamic nuclear changes in DNA methylation and hydroxymethylation states during development from E9.5 to E14.5 mouse embryonic stages.

Chapter 4 - 5mC and 5hmC DNA methylation dynamics in developing mouse embryonic tissues

4.1 Introduction

Cytosine DNA methylation was historically viewed as a relatively stable gene-silencing epigenetic modification throughout the life cycle (Hackett et al., 2012). Nonetheless, compelling evidence suggests that DNA methylation patterns undergo a genome-wide dramatic change during mammalian development (Zhou et al., 2016). Such change involves both passive and active mechanisms of DNA demethylation (Seisenberger et al., 2013b). Well known examples of developmental DNA demethylation processes occur in the primordial germ cells (PGCs) and in zygotes (Messerschmidt et al., 2014). However, little is known about the DNA methylation dynamics of other tissues in mammalian development. With this rationale, the changing nuclear distributions and levels of DNA methylation during development were experimentally investigated in the present chapter in order to discover dynamic variations amongst developing mouse tissues. I hypothesised that variations in DNA methylation localisation and nuclear organisation were associated with differentiation to many tissues.

Several promising, and a few controversial, model pathways of active DNA demethylation have been proposed (Tammen et al., 2013). One of the potential candidate mechanisms that has gained acceptance in recent years involves iterative oxidation of 5mC by Tet proteins, which produces three oxidised cytosine bases (5hmC/5fC/5caC) (Neri et al., 2015). This finding indicates that 5hmC may act as an intermediate in the removal of 5mC (Zhong et al., 2017). Since 5mC is needed as a substrate for the oxidation reaction, a significant reduction in 5mC levels could possibly be explained by the generation of 5hmC (Hu et al., 2013). Together, these data are consistent with a model in which the gain of 5hmC may coincide with a concomitant loss of 5mC (Lan et al., 2017; Yoo et al., 2017). Furthermore, the suggested model of active oxidative demethylation through 5hmC formation is also in keeping with a recent study done by Amouroux et al. (2016) which demonstrated that the accumulation of 5hmC is dependent on the *de novo* DNA methylation activity. Using this separate *de novo* pathway, 5hmC is generated from 5mC and serves as a DNA demethylation intermediate, but 5hmC could also function as a stable epigenetic mark with its own regulatory role without apparently triggering active cytosine demethylation (Heras et al., 2017; Li et al., 2016).

Thus, it was of considerable interest to address the question about the origin of 5hmC during development. In an attempt to answer this important research question raised by the findings described above, confocal immunofluorescence experiments were performed in order to investigate the dynamics of DNA methylation of both 5mC and 5hmC. Furthermore, imaging mouse embryonic tissues from stages E9.5 to E14.5 also allowed accurate characterisation of 5mC and 5hmC changes across different tissues, which had not been systematically investigated previously. In addition, strong 5mC changes in the early PGCs of the embryo were investigated as well.

Therefore, the aims of this chapter were:

1. To investigate tissues undergoing dynamic nuclear changes in DNA methylation (5mC) state during development from E9.5 to E14.5 mouse whole embryonic stages using our optimised immunohistochemistry protocol.

2. To investigate tissues undergoing dynamic nuclear changes in DNA hydroxymethylation (5hmC) state during development from E9.5 to E14.5 mouse embryonic stages using our same standardised immunohistochemistry protocol.

3. To investigate the colocalisation and possible correlation between the levels of 5mC and 5hmC during mouse fetal development in brain neorcortex, surface ectoderm, liver, red blood cells, diaphragm and heart.

4. To detect a hypomethylated state of PGCs in cryosections of E12.5 mouse embryonic gonad.

5. To detect the presence of Tet1, Tet2, Tet3 enzymes and DNA methyltransferase DNMT3A in cryosections of E12.5 mouse embryonic neocortex, liver, red blood cells, diaphragm and heart.

4.2 Results

DNA methylation dynamics at 5mC and 5hmC were observed in whole embryo cryosections taken during mouse fetal development with results reported in brain neocortex surface ectoderm, liver, red blood cells, diaphragm and heart.

4.2.1 5mC and 5hmC DNA methylation dynamics in developing mouse embryonic neocortex

The dynamics of 5mC and 5hmC during development of the embryonic mouse neocortex, examined by confocal microscopy at a magnification of 40X, are shown in **Figure 4.1**. The resulting dynamics are also shown at a higher image resolution using zoomed observations in **Figure 4.2**. The neocortex is part of the cerebral cortex and is the hallmark of the mammalian brain. The exact location of the neocortex in the brain is shown in **Figure 4.3**. 5mC and 5hmC display interesting dynamic patterns in the developing cerebral neocortex. Immunofluorescence experiments showed that the levels of both 5mC and 5hmC are low at E9.5. 5mC levels begin to increase between E10.5 and E12.3, peak at E13.5 and remain high until E14.5 **(Figure 4.1 and 4.2 – 5mC)**. Remarkably, 5hmC exhibits the same pattern of dynamic changes in signal intensity as 5mC from E10.5 to E13.5, but at E14.5, in contrast to 5mC, the level of 5hmC appears to decline substantially **(Figure 4.1 and 4.2 – 5hmC)**. These results suggested that the dynamic nuclear changes in DNA methylation and hydroxymethylation states observed in neocortex were in good agreement with a model where the 5hmC may be an epigenetic modification in its own right. There was clearly no significant correlation between the loss of 5mC and the generation of 5hmC at the global nuclear level.

Analysis of immunofluorescence images also showed that the 5mC signals are mainly localised in the heterochromatic regions correlating with DAPI density **(Figure 4.2 – 5mC)**, whereas 5hmC signals are mainly localised in the euchromatic regions. In brain, they are excluded from DAPI-dense areas of the nuclei **(Figure 4.2 – 5hmC)**. The observed staining patterns of 5hmC and 5mC are in agreement with the results obtained in Chapter 3, indicating that the optimised 5mC and 5hmC immunostaining protocols demonstrate good reproducibility of results between cryosections of different stages of mouse embryonic development.

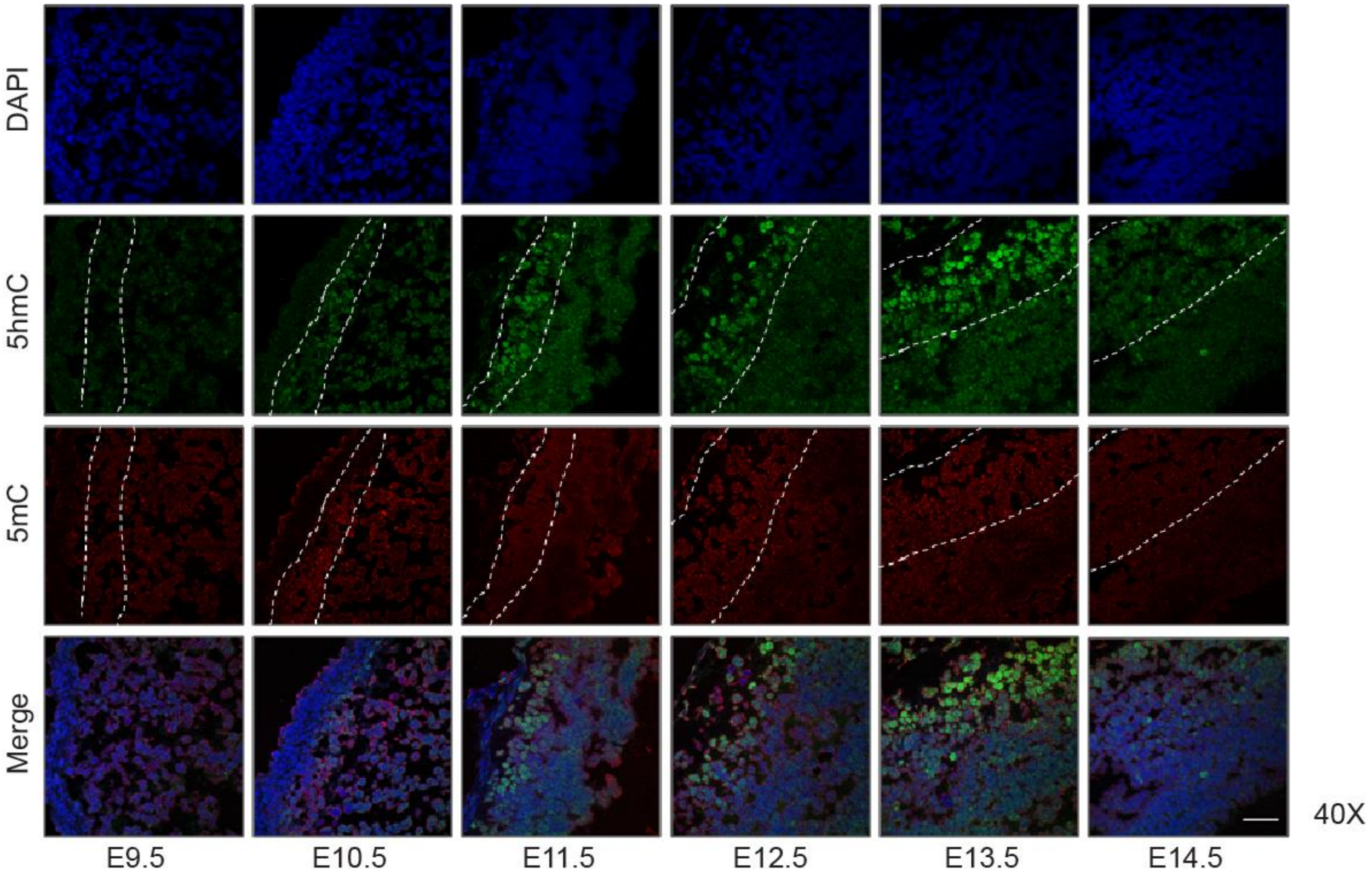

Figure 4.1: 5mC and 5hmC double immunostaining in E9.5 to E14.5 mouse embryonic brain neocortical tissues. First row: cryosectioned tissues showing nuclear DNA counterstained with DAPI (blue). Second row: primary antibody against 5hmC (green). Third row: antibody against 5mC (red). Fourth row: merged images of DAPI, 5hmC and 5mC. Columns 1 to 6: representative mouse embryonic brain neocortical tissue sections at stages from E9.5 to E14.5. Areas within the dashed lines represent a neocortical zone of interest. Dashed lines mark the neocortex starting at the stage where no differentiation has yet occurred. At this stage (E9.5), the majority of cells

are embryonic neural stem cells. The brighter cells continue through development until E13.5 when the preplate is formed. Specific markers that can be used to identify the regions of interest are Pax6/Sox2 (which serve as markers for radial glia cells), Tbr2 (which serves as a marker for basal progenitor cells in the neocortex), and Tbr1/Tuj1 (which serve as markers for neurons). Images were obtained using a confocal microscope with a 40X oil-immersion objective lens. Scale bar indicates 40 µm.

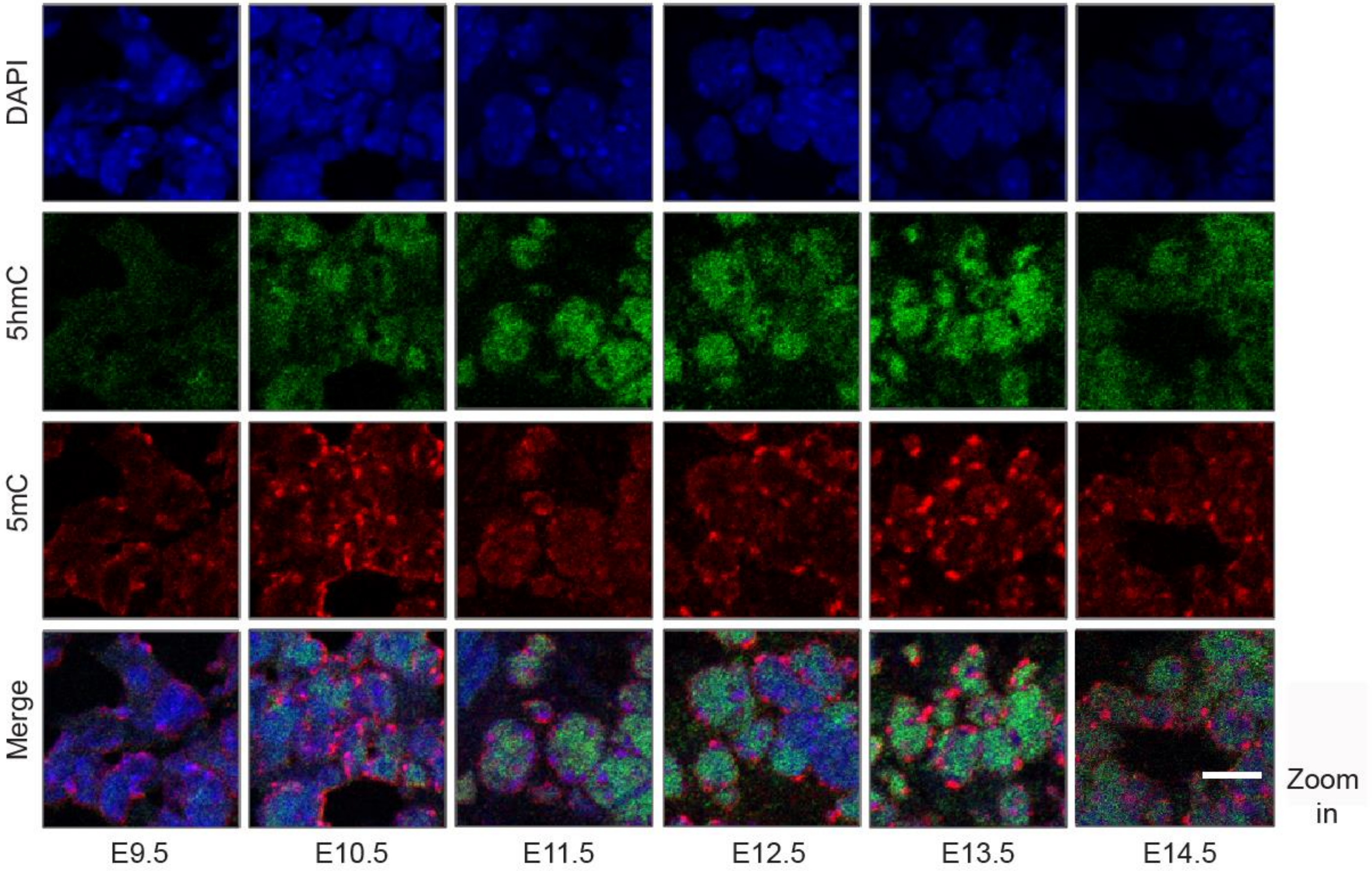

Figure 4.2: 5mC and 5hmC double immunostaining in E9.5 to E14.5 mouse embryonic brain neocortical cell nuclei. First row: cryosectioned tissues showing nuclear DNA counterstained with DAPI (blue). Second row: primary antibody against 5hmC (green). Third row: antibody against 5mC (red). Fourth row: merged images of DAPI, 5hmC and 5mC. Columns 1 to 6: representative mouse embryonic brain neocortical cell nuclei at stages from E9.5 to E14.5. The confocal images were obtained by zooming into areas within the dashed lines shown in Figure 4.1. Scale bar indicates 10 µm.

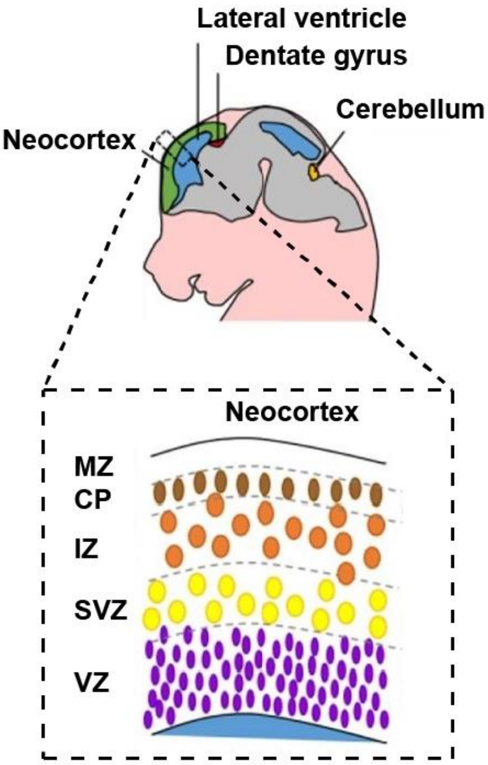

Figure 4.3: Sagittal view of an E14.5 mouse embryonic brain. The dashed line inset highlights the neocortex (green) and its location in the brain. At developmental stage of E14.5, the neocortex is divided into several functionally distinct layers: the ventricular and sub-ventricular zones (VZ/SVZ), which lie adjacent to the lateral walls of the lateral ventricles (blue), comprise the neural stem and intermediate progenitor cells; the intermediate zone (IZ), which is located above the VZ/SVZ, comprises migrating cells and axons; and the cortical plate (CP), which lies between the IZ and the superficial marginal zone (MZ), contains post-mitotic neurons (Barazzuol et al., 2015).

To identify these 5hmC- and 5mC-rich cell populations, immunohistochemical detection of nestin with RC2 antibody was performed on cryosections of E12.5 mouse embryo. Nestin is an intermediate filament protein that is widely used as a molecular marker for neural progenitor and stem cells. Adjacent serial sections were used for either nestin or 5hmC or 5mC staining, as immunodetection of 5hmC and 5mC required heat denaturation treatment which was incompatible with the preservation of most protein epitopes.

At E12.5, neocortex possesses relatively high abundance of 5hmC as well as 5mC and the intense staining of 5hmC and 5mC is closely correlated with high nestin-expressing cells, as shown in **Figure 4.4**. The location of these epigenetic marks was in the outer region, external to the neocortex rather than the ventricular zones where neural progenitors reside.

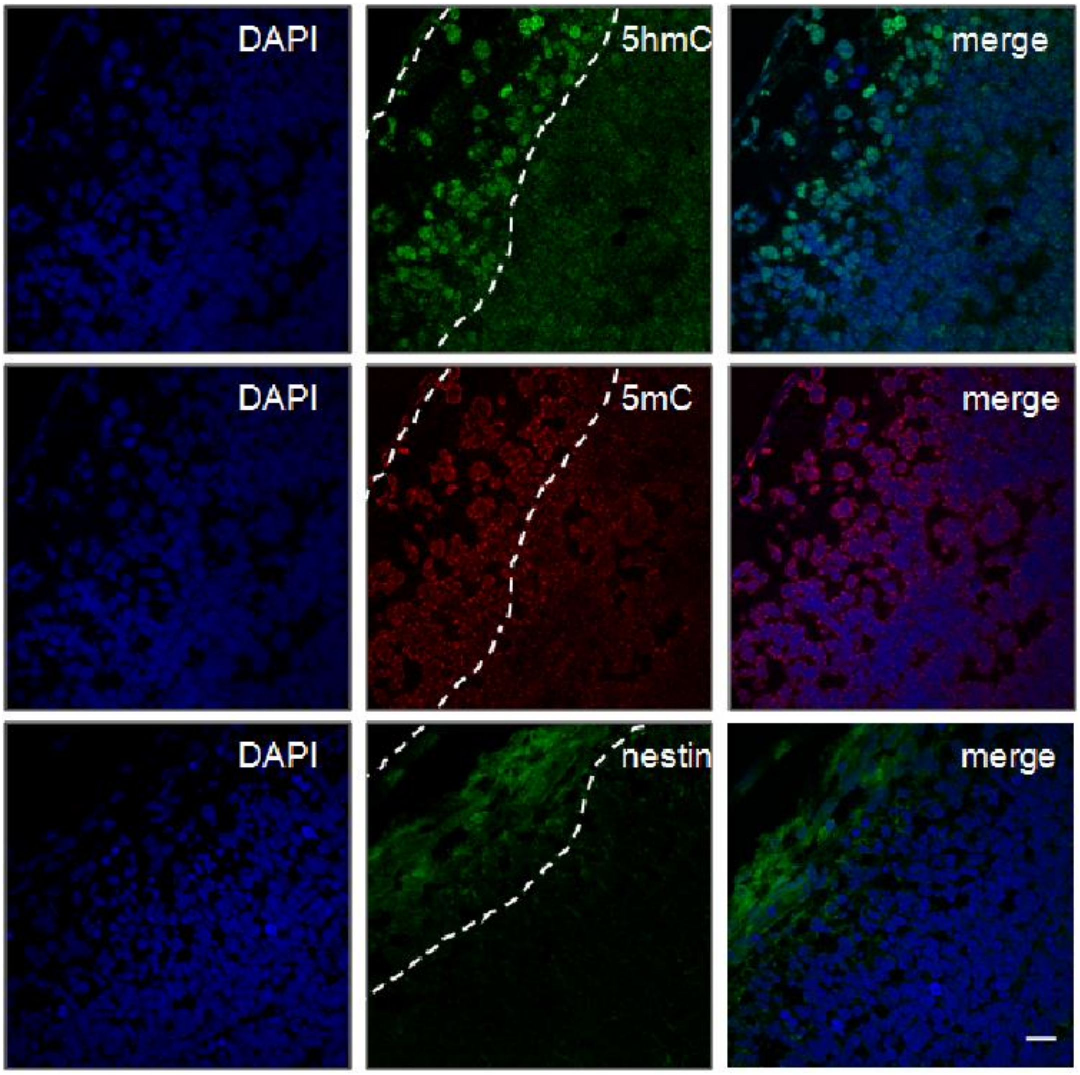

Figure 4.4: 5mC and 5hmC double immunostaining in E12.5 mouse embryonic brain neocortical tissues. Mouse embryonic neocortical tissue cryosection as shown in Fig 4.1 with a non-denatured cryosection immunostained for nestin. First column: nuclear DNA counterstained with DAPI (blue). Second column: from top to bottom, primary antibodies against 5hmC (green), 5mC (red) and nestin, RC2 (green). Third column: merged images. Areas within the dashed lines represent neocortical zones of interest. Images were obtained using a confocal microscope with a 40X oil-immersion objective lens. Intense staining of nestin is closely correlated with high levels of 5hmC and 5mC. Some non-specific nestin staining was observed in the region external to the neocortex. Scale bar indicates 20 µm.

4.2.2 5mC and 5hmC DNA methylation dynamics in developing mouse embryonic surface ectoderm

The dynamics of 5mC and 5hmC during development of the embryonic mouse surface ectoderm, examined at a magnification of 40X, are shown in **Figure 4.5**. The resulting dynamics are also shown at a higher image resolution using zoomed observations in **Figure 4.6**. Surface ectodermal tissues were identified using Kaufman's atlas of mouse development. The surface ectoderm, which is derived from ectoderm, is a single-layered epithelium that gives rise to tissues on the outer surface of the embryo, for instance, epidermis, hair, nails and lens of the eye (Rao P and Kumar D, 2016). The images of surface ectoderm were only taken at E9.5, E10.5 and E11.5, as at the early stages of development the tissues were thicker and became noticeably thinner and indistinguishable at the later stages (E12.5, E13.5 and E14.5). This was evidently due to a formation of other tissues. 5mC and 5hmC display interesting dynamic patterns in developing surface ectoderm. Immunofluorescence experiments showed very low levels of staining for 5mC from E9.5 to E11.5 **(Figure 4.5 and 4.6 – 5mC)**, whereas for 5hmC, the levels of staining at the same stages of embryonic development are moderate **(Figure 4.5 and 4.6 – 5hmC)**. These results suggested that the dynamic nuclear changes in DNA methylation and hydroxymethylation states observed in surface ectoderm were in good agreement with a model where the generation of 5hmC may correlate with the loss of old 5mC, but the observations were also consistent with an involvement of *de novo* methylation in the generation of 5hmC.

Closer inspection of immunofluorescence images also showed that the 5mC signals, where detectable, are mainly localised in the heterochromatic regions **(Figure 4.6 – 5mC)**, whereas 5hmC signals are predominantly localised in the euchromatic regions and are excluded from DAPI-dense foci **(Figure 4.6 – 5hmC)**. The observed staining patterns of 5hmC and 5mC are in agreement with the results obtained in Chapter 3, suggesting that the optimised immunofluorescence staining protocols for 5mC and 5hmC immunostaining protocols display high repeatability and reproducibility of results between cryosections of different stages of mouse embryonic development.

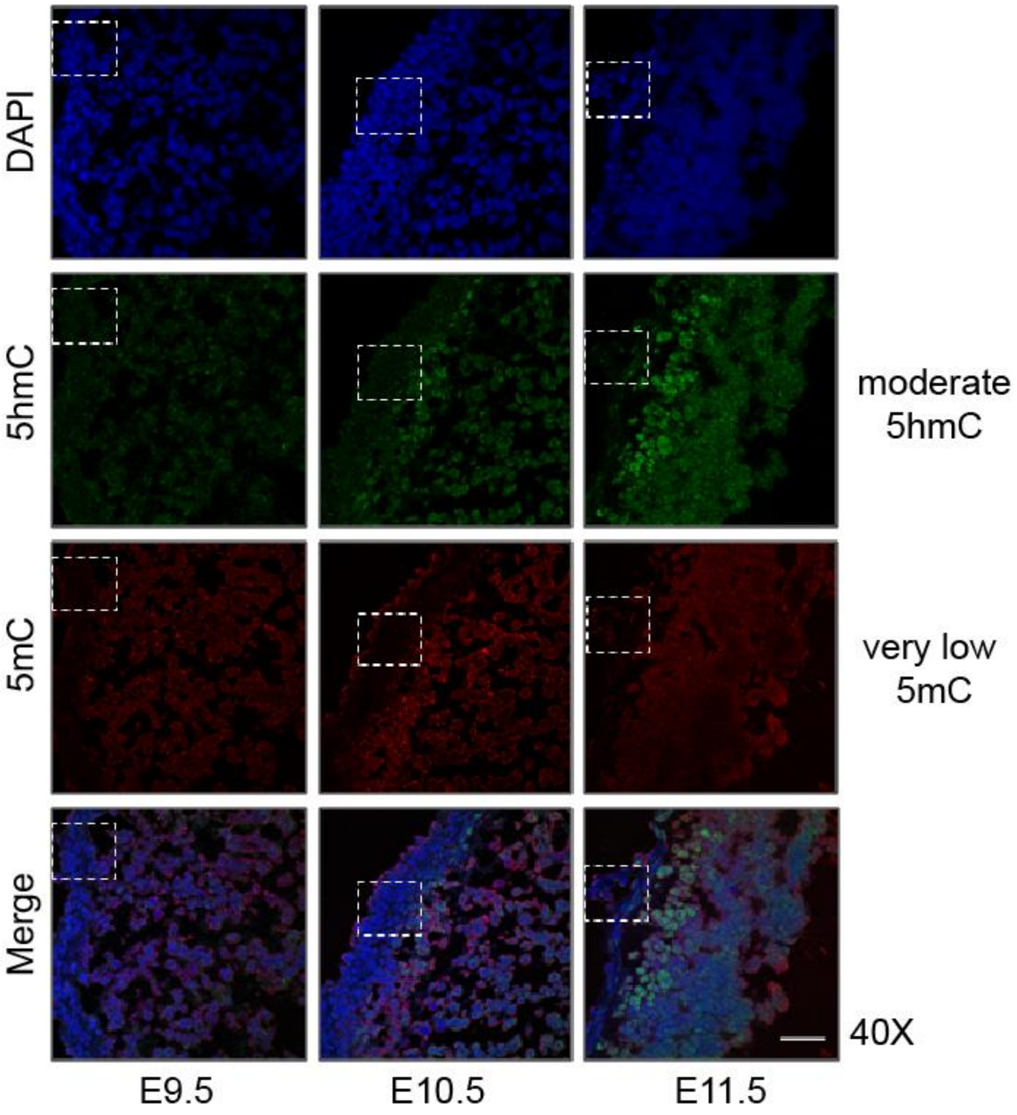

Figure 4.5: 5mC and 5hmC double immunostaining in E9.5 to E11.5 mouse embryonic surface ectodermal tissues. First row: cryosectioned tissues showing nuclear DNA counterstained with DAPI (blue). Second row: primary antibody against 5hmC (green). Third row: antibody against 5mC (red). Fourth row: merged images of DAPI, 5hmC and 5mC. Columns 1 to 3: representative mouse embryonic surface ectodermal tissue sections at stages from E9.5 to E11.5. Areas within the dashed boxes represent surface ectodermal tissues. Images were obtained using a confocal microscope with a 40X oil-immersion objective lens. Scale bar indicates 40 µm.

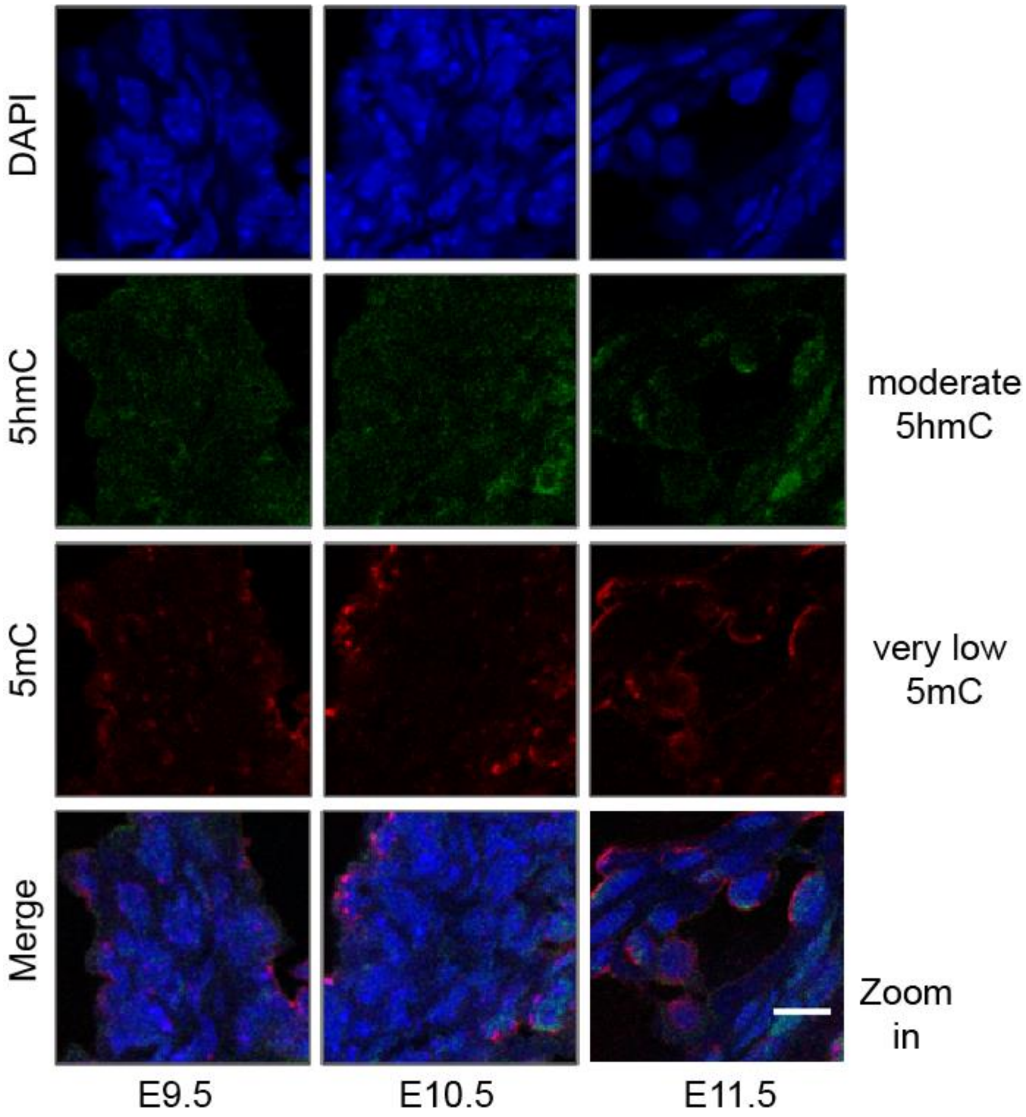

Figure 4.6: 5mC and 5hmC double immunostaining in E9.5 to E11.5 mouse embryonic surface ectodermal cell nuclei. First row: cryosectioned tissues showing nuclear DNA counterstained with DAPI (blue). Second row: primary antibody against 5hmC (green). Third row: antibody against 5mC (red). Fourth row: merged images of DAPI, 5hmC and 5mC. Columns 1 to 3: representative mouse embryonic surface ectodermal cell nuclei at stages from E9.5 to E11.5. The confocal images were obtained by zooming into areas within the dashed boxes shown in Figure 4.5. Scale bar indicates 10 µm.

4.2.3 5mC and 5hmC DNA methylation dynamics in developing mouse embryonic liver

The dynamics of 5mC and 5hmC during development of the embryonic mouse liver, examined at a magnification of 40X, are shown in **Figure 4.7**. The zoomed observations in **Figure 4.8** show the resulting dynamics at a higher resolution. 5mC and 5hmC display interesting dynamic patterns in developing liver. 5mC exhibits consistently low levels of staining throughout liver development (from E9.5 to E14.5) **(Figure 4.7 and 4.8 – 5mC)**. On the contrary, immunofluorescence experiments showed that the levels of 5hmC are low at E9.5. 5hmC levels become markedly increased at E10.5, reaching their maximum at E11.5. After reaching the maximum, 5hmC appears to remain constant at a relatively high level until E14.5 **(Figure 4.7 and 4.8 – 5hmC)**. The pattern of high 5hmC at later stages (from E12.5 to E14.5) apparently becomes much more scattered as at these stages of embryonic development, fetal liver becomes the main hematopoietic organ and is full of blood cells. Erythrocytes (red blood cells), the most numerous blood cells, are the easiest to identify as they generally have a rounded shape and are relatively uniform in size, making it easy to distinguish between the liver cells and red blood cells without using tissue-specific markers. Leukocytes (white blood cells), on the other hand, which are slightly larger than erythrocytes can be identified histologically by the complex shape of their nuclei. Several types of leukocytes have segmented nuclei, meaning that the nucleus is pinched off into two or more smaller segments that are still connected to each other. These results suggested that the dynamic nuclear changes in DNA methylation and hydroxymethylation states observed in liver were in good agreement with the model where the generation of 5hmC may correlate with the loss of old 5mC, but the observations were also found to be consistent with an involvement of *de novo* methylation in the generation of 5hmC.

As in other tissues, the liver immunofluorescence images showed that the 5mC signals are mainly localised in the heterochromatic regions but also at the nuclear periphery **(Figure 4.8 – 5mC)**, whereas 5hmC signals are mostly found in the euchromatic regions and are excluded from DAPI-dense foci **(Figure 4.8 – 5hmC)**. The observed staining patterns of 5hmC and 5mC are in agreement with the results obtained in Chapter 3, suggesting good reproducibility of 5mC and 5hmC when the same optimised protocols are used.

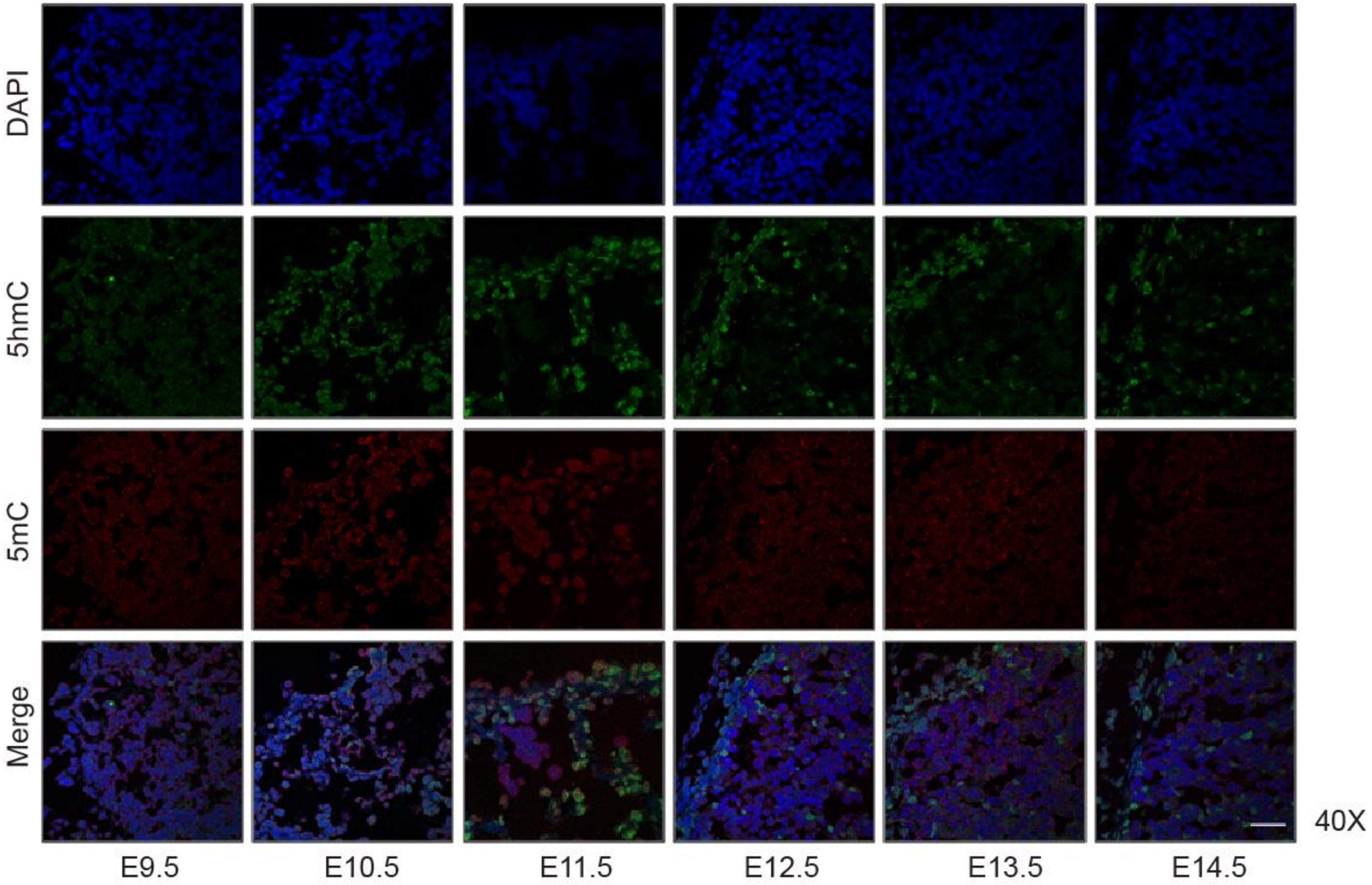

Figure 4.7: 5mC and 5hmC double immunostaining in E9.5 to E14.5 mouse embryonic liver tissue. First row: cryosectioned tissues showing nuclear DNA counterstained with DAPI (blue). Second row: primary antibody against 5hmC (green). Third row: with antibody against 5mC (red). Fourth row: merged images of DAPI, 5hmC and 5mC. Columns 1 to 6: representative mouse embryonic liver cryosections at stages from E9.5 to E14.5. Images were obtained using a confocal microscope with a 40X oil-immersion objective lens. Scale bar indicates 40 µm.

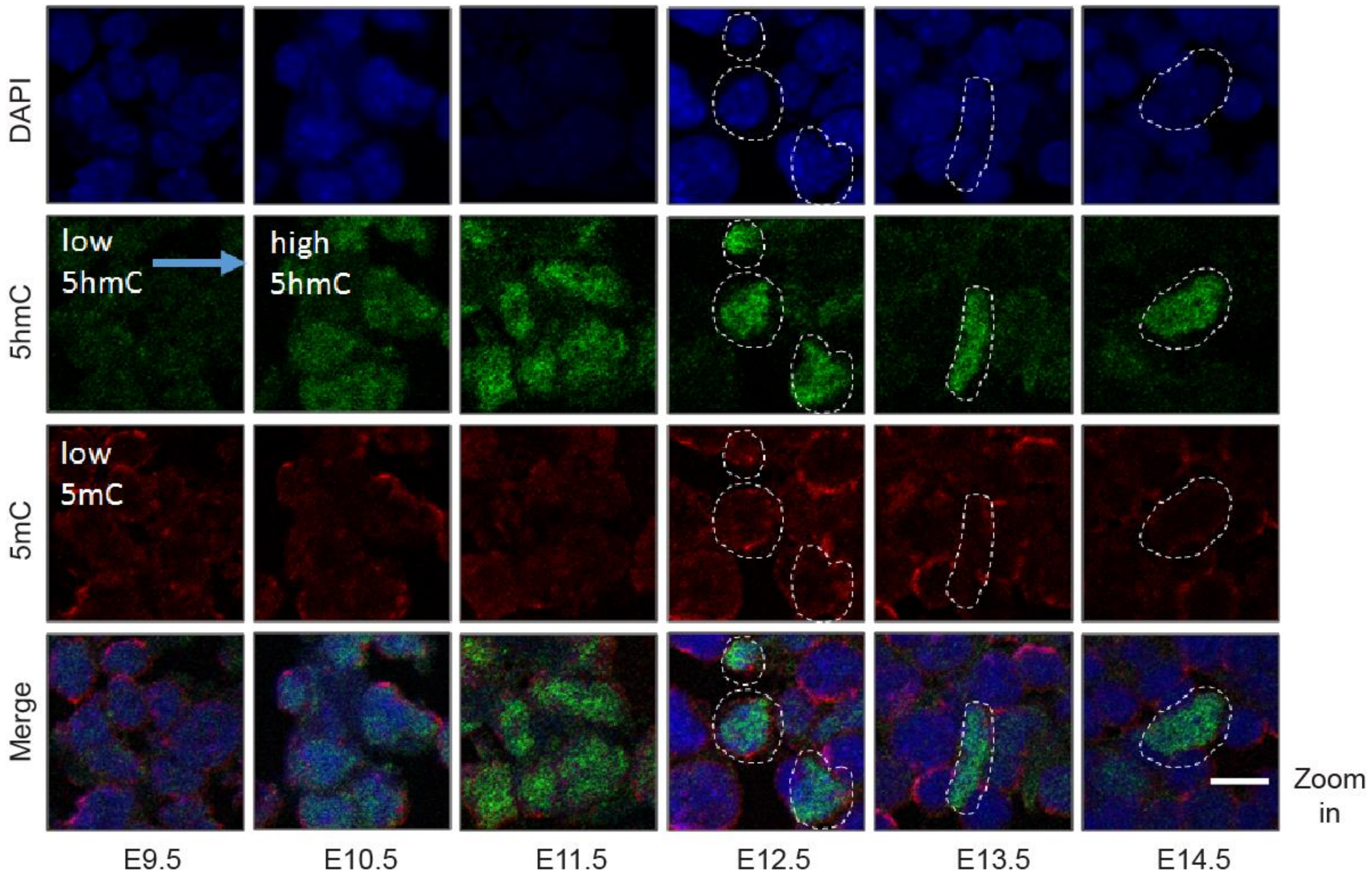

Figure 4.8: 5mC and 5hmC double immunostaining in E9.5 to E14.5 mouse embryonic liver cell nuclei. First row: cryosectioned tissues showing nuclear DNA counterstained with DAPI (blue). Second row: primary antibody against 5hmC (green). Third row: antibody against 5mC (red). Fourth row: merged images of DAPI, 5hmC and 5mC. Columns 1 to 6: representative mouse embryonic liver tissue sections at stages from E9.5 to E14.5. The confocal images were obtained by zooming into the images shown in Figure 4.7. The dashed circles represent liver cells. Scale bar indicates 10 µm.

4.2.4 5mC and 5hmC DNA methylation dynamics in developing mouse embryonic red blood cells

The dynamics of 5mC and 5hmC during development of the embryonic mouse red blood cells, examined at a magnification of 40X, are shown in **Figure 4.9**. Immunofluorescent staining of 5hmC and 5mC in red blood cells was performed as published genomic studies reported that whole blood has the lowest 5hmC content (Nestor et al., 2012; Stewart et al., 2015). The past reports are consistent with the immunostaining results obtained in the present study. 5mC and 5hmC display interesting dynamic patterns in the developing red blood cells. Immunofluorescence experiments showed high levels of staining for 5mC from E12.5 to E14.5 **(Figure 4.9 – 5mC)**, whereas for 5hmC, the levels of staining at the same stages of embryonic development are very low **(Figure 4.9 – 5hmC)**. The images of red blood cells in liver were only taken at E12.5, E13.5 and E14.5 as at the early stages of development, the progenitors of these cells were morphologically unrecognisable and indistinguishable. Definitive erythrocytes, which began to emerge from the fetal liver at E12.5, were easily identified because of their small, round nuclei and because they often presented in small clusters. These results suggested that the dynamic nuclear changes in DNA methylation and hydroxymethylation states observed in red blood cells were in good agreement with the model where the generation of 5hmC may correlate with the loss of old 5mC. Indeed, the opposite 5hmC/5mC levels observed in this study provide strong support for the hypothesis.

Blood cell immunofluorescence images also showed that the 5mC signals are to partly be localised in the DNA-dense heterochromatic regions **(Figure 4.9 – 5mC)**, whereas the low level 5hmC signals are predominantly located in the euchromatic regions and excluded from DAPI-dense foci **(Figure 4.9 – 5hmC)**. Moreover, the images also show that the intense immunofluorescence signals of 5mC are arranged predominantly at the nuclear periphery. The observed staining patterns of 5mC and 5hmC are in agreement with the results obtained in Chapter 3 suggesting that the optimised protocols for the detection of both 5mC and 5hmC are robust and highly reproducible between cryosections of different stages of mouse embryonic development.

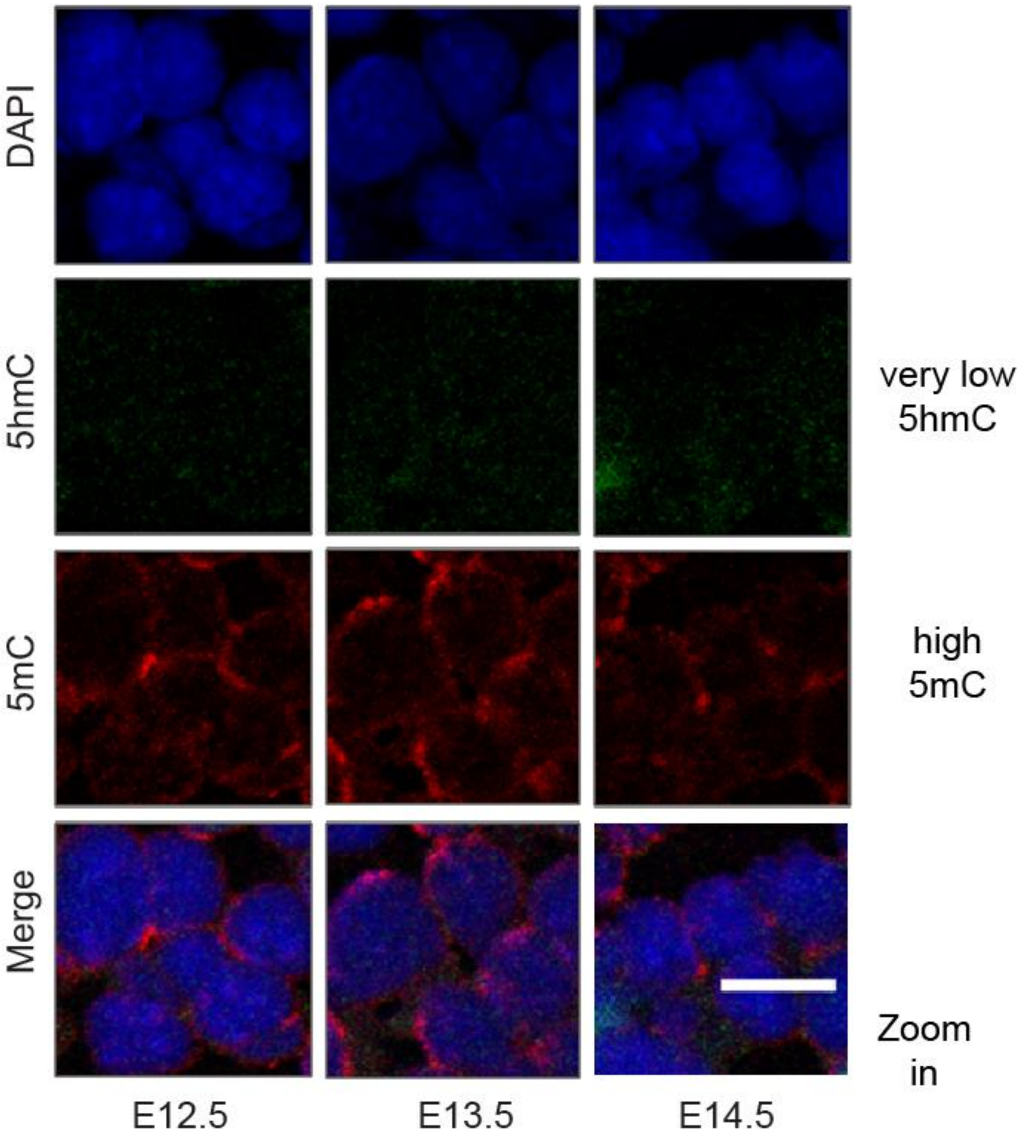

Figure 4.9: 5mC and 5hmC double immunostaining in E12.5 to E14.5 mouse embryonic red blood cells. First row: nuclear DNA counterstained with DAPI (blue). Second row: primary antibody against 5hmC (green). Third row: antibody against 5mC (red). Fourth row: merged images of DAPI, 5hmC and 5mC. Columns 1 to 3: representative mouse embryonic red blood cells in whole embryo cryosections at stages from E12.5 to E14.5. Images were obtained using a confocal microscope with a 40X oil-immersion objective lens. Scale bar indicates 10 µm.

4.2.5 5mC and 5hmC DNA methylation dynamics in developing mouse embryonic diaphragm

The dynamics of 5mC and 5hmC during development of the embryonic mouse diaphragm, examined at a magnification of 40X, are shown in **Figure 4.10**. The resulting dynamics are also shown at a higher image resolution using zoomed observations in **Figure 4.11**. 5mC and 5hmC display interesting dynamic patterns in the developing diaphragm. Immunofluorescence experiments showed that 5mC exhibits consistently low levels of staining throughout diaphragm development (from E9.5 to E14.5) **(Figure 4.10 and 4.11 – 5mC)**. 5hmC, on the other hand, shows low levels of staining at E9.5. Subsequently, at E10.5, 5hmC levels become markedly elevated. Following elevation, 5hmC appears to remain constant at a relatively high level until E14.5 **(Figure 4.10 and 4.11 – 5hmC)**. These results suggested that the dynamic nuclear changes in DNA methylation and hydroxymethylation states observed in diaphragm were in good agreement with the model where the generation of 5hmC may correlate with the loss of old 5mC, but these observations were also found to be consistent with an involvement of *de novo* methylation in the generation of 5hmC.

Analysis of diaphragm tissue immunofluorescence images also showed that the 5mC signals are partly localised in the heterochromatic regions **(Figure 4.10 and 4.11 – 5mC)**, whereas 5hmC signals are mainly detected in the euchromatic regions and excluded from DAPI-dense foci **(Figure 4.10 and 4.11 – 5hmC)**. Moreover, the images also show nuclei in which 5mC is arranged predominantly at the nuclear periphery. The observed staining patterns of 5mC and 5hmC are in line with the results obtained in Chapter 3 suggesting that the optimised protocols for the detection of both 5mC and 5hmC demonstrate high reproducibility and consistency of results between cryosections of different stages of mouse embryonic development.

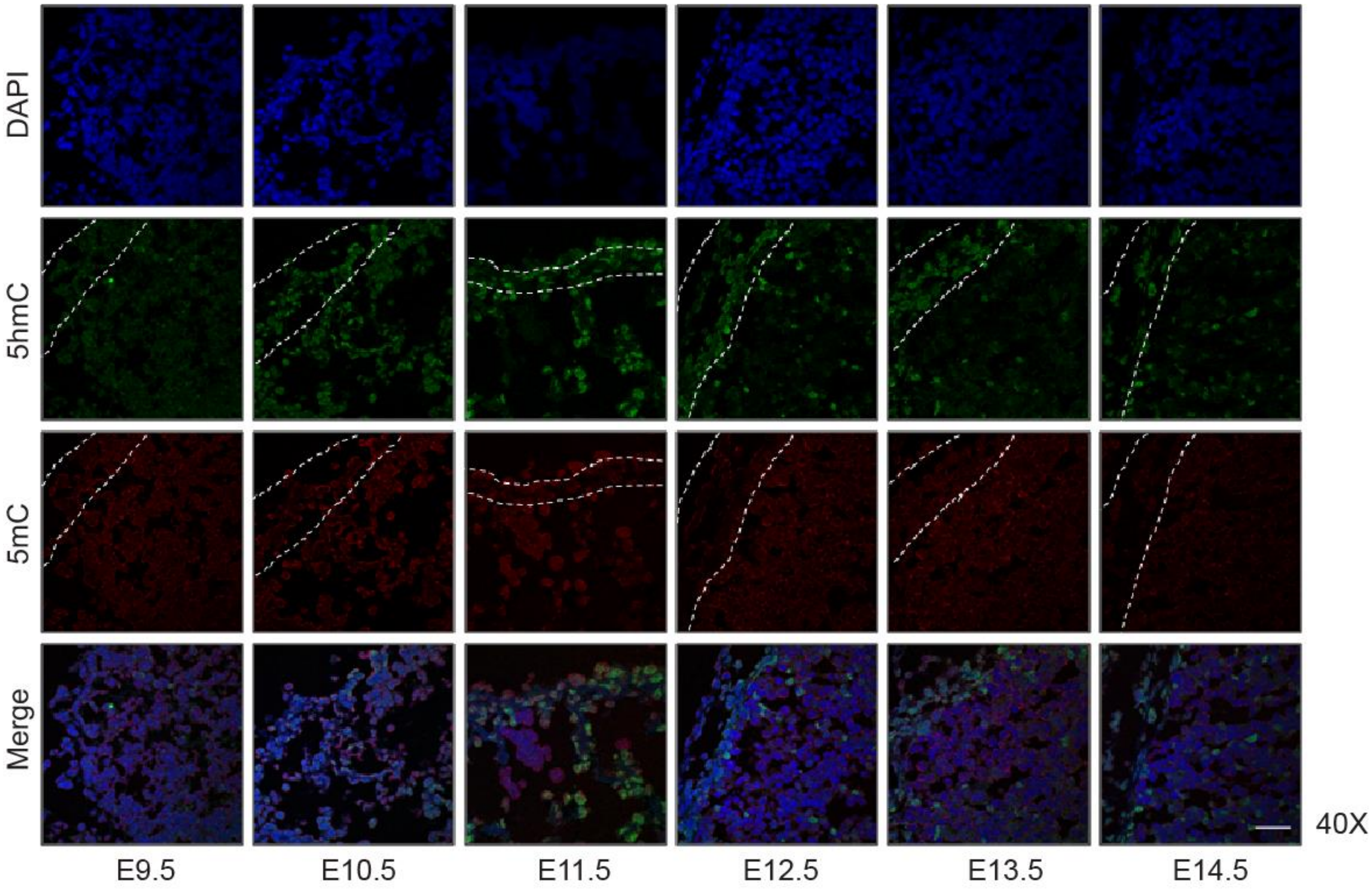

Figure 4.10: 5mC and 5hmC double immunostaining in E9.5 to E14.5 mouse embryonic diaphragm tissues. First row: cryosectioned tissues showing nuclear DNA counterstained with DAPI (blue). Second row: primary antibody against 5hmC (green). Third row: antibody against 5mC (red). Fourth row: merged images of DAPI, 5hmC and 5mC. Columns 1 to 6: representative mouse embryonic diaphragm tissue in whole embryo cryosections at stages from E9.5 to E14.5. Areas within the dashed lines represent diaphragm tissues. Images were obtained using a confocal microscope with a 40X oil-immersion objective lens. Scale bar indicates 40 µm.

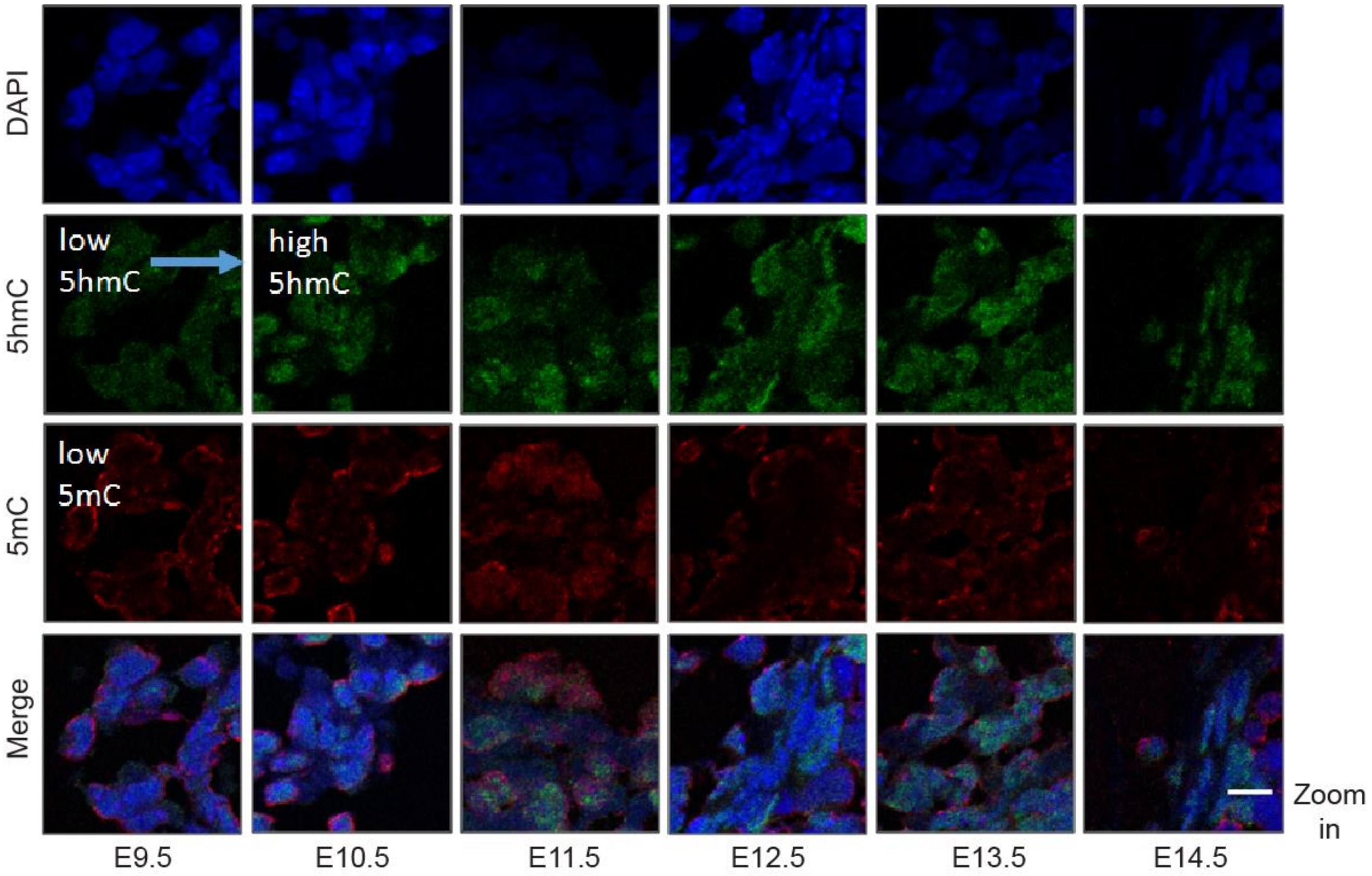

Figure 4.11: 5mC and 5hmC double immunostaining in E9.5 to E14.5 mouse embryonic diaphragm cell nuclei. First row: cryosectioned tissues showing nuclear DNA counterstained with DAPI (blue). Second row: primary antibody against 5hmC (green). Third row: antibody against 5mC (red). Fourth row: merged images of DAPI, 5hmC and 5mC. Columns 1 to 6: representative mouse embryonic diaphragm tissue cryosections at stages from E9.5 to E14.5. The confocal images were obtained by zooming into areas within the dashed lines shown in Figure 4.10. Scale bar indicates 10 µm.

4.2.6 5mC and 5hmC DNA methylation dynamics in developing mouse embryonic heart

The dynamics of 5mC and 5hmC during development of the embryonic mouse heart, examined at a magnification of 40X, are shown in **Figure 4.12**. The resulting dynamics are also shown at a higher image resolution using zoomed observations in **Figure 4.13** and **4.14**. 5mC and 5hmC display interesting dynamic patterns in the developing heart. Immunofluorescence experiments showed that the levels of 5mC are high at E9.5 and E10.5. At E11.5, 5mC levels begin to decrease and reach their minimum at E12.5. After reaching the minimum, 5mC appears to remain constant in both regions (trabecular **[Figure 4.13]** and compact myocardium **[Figure 4.14]**) at a relatively low level until E14.5 **(Figure 4.12 – 5mC)**. 5hmC, on the other hand, shows low levels of staining at E9.5 and E10.5. At E11.5, 5hmC levels begin to increase and reach their maximum at E12.5, coincident with the loss of 5mC. After reaching the maximum, 5hmC appears to remain constant in the trabecular compartment **(Figure 4.13)** at a relatively high level until E14.5, whereas in the compact myocardium **(Figure 4.14)**, 5hmC levels begin to decline shortly after E12.5 and reach their minimum at E13.5. 5hmC then stays constant at a relatively low level until E14.5 **(Figure 4.12 – 5hmC)**. These results suggested that the dynamic nuclear changes in DNA methylation and hydroxymethylation states observed in trabecular region were in good agreement with the model where the generation of 5hmC may correlate with the loss of old 5mC, but the observations were also found to be consistent with an involvement of *de novo* methylation in the generation of 5hmC. On the contrary, the dynamic nuclear changes in DNA methylation and hydroxymethylation states observed in compact myocardium were in line with the model where the 5hmC levels are controlled independently. There was clearly no significant correlation between the loss of 5mC and the generation of 5hmC at the global nuclear level.

Nuclear analysis of heart development immunofluorescence images also showed that the 5mC signals are largely distributed in the heterochromatic regions in addition to the nuclear periphery **(Figure 4.13 and 4.14 – 5mC)**, whereas 5hmC signals are predominantly located in the euchromatic regions and excluded from DAPI-dense foci **(Figure 4.13 and 4.14 – 5hmC)**. The observed staining patterns of 5mC and 5hmC are in agreement with the results obtained in Chapter 3 indicating that this good level of reproducibility is achieved using the optimised protocols for detecting 5mC and 5hmC.

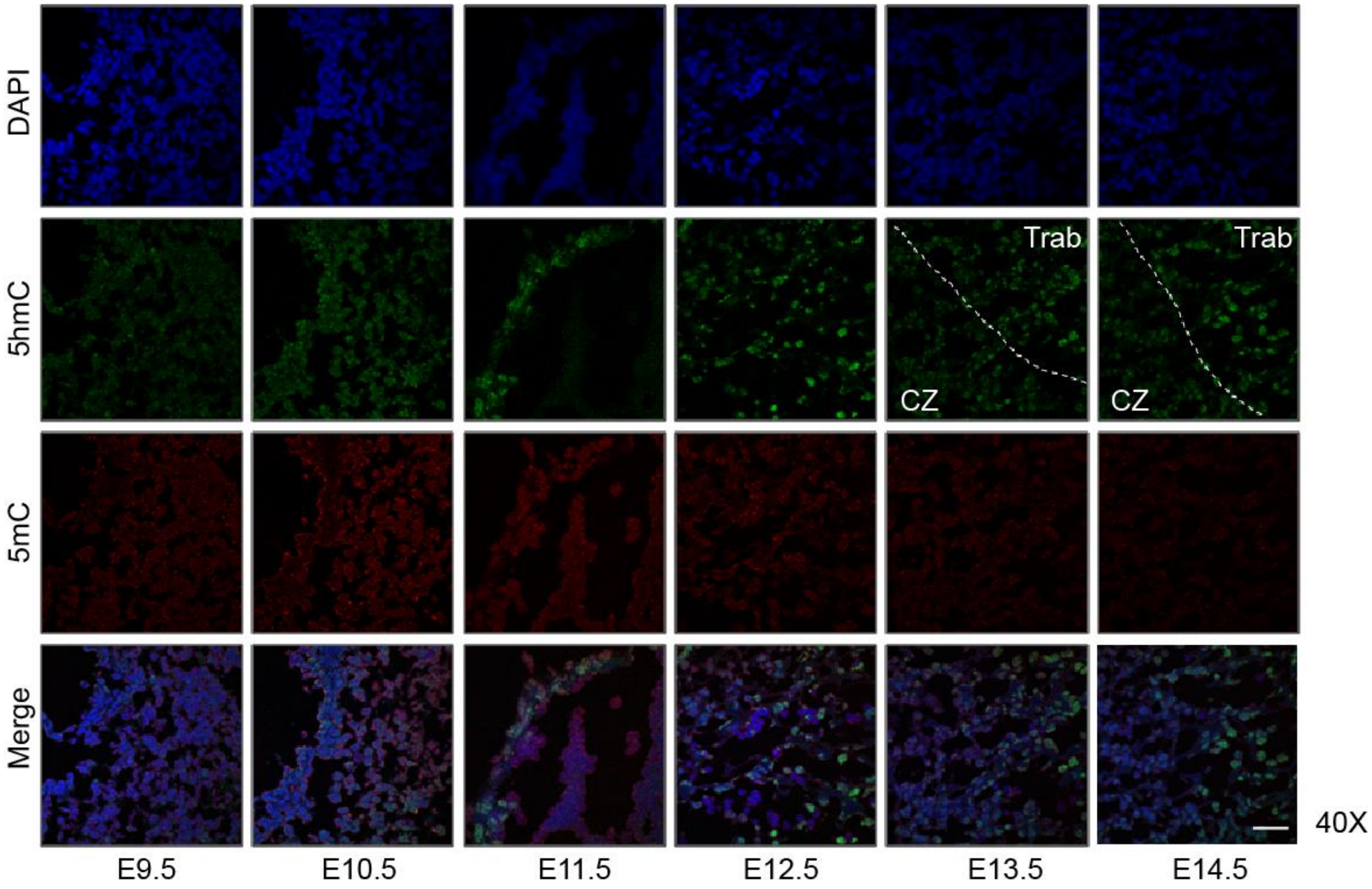

Figure 4.12: 5mC and 5hmC double immunostaining in E9.5 to E14.5 mouse embryonic heart tissues. First row: cryosectioned tissues showing nuclear DNA counterstained with DAPI (blue). Second row: primary antibody against 5hmC (green). Third row: antibody against 5mC (red). Fourth row: merged images of DAPI, 5hmC and 5mC. Columns 1 to 6: representative mouse embryonic heart tissue cryosections at stages from E9.5 to E14.5. The dashed lines highlight the boundary between the trabecular region (Trab) and the compact myocardium (CZ). Images were obtained using a confocal microscope with a 40X oil-immersion objective lens. Scale bar indicates 40 µm.

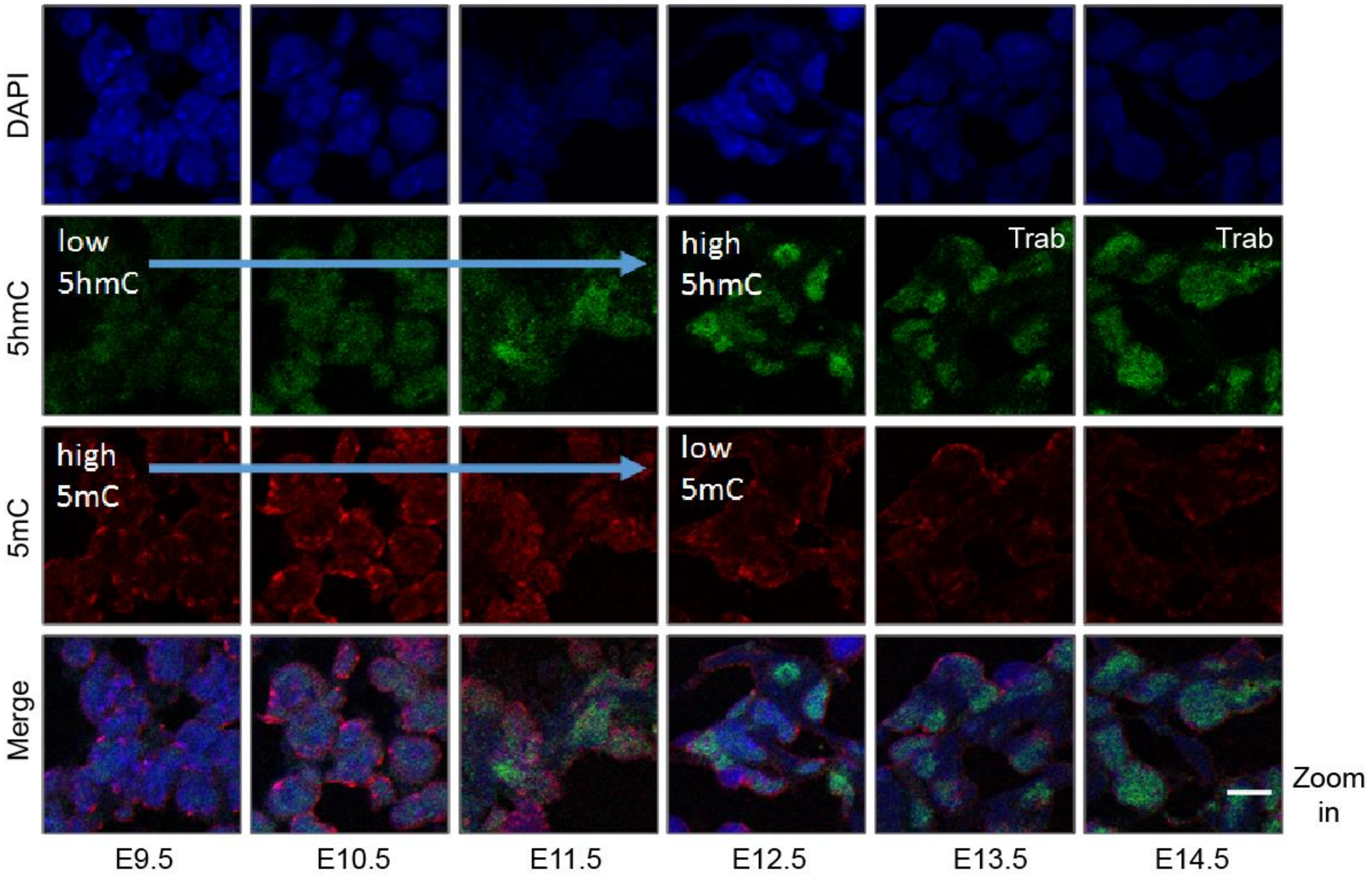

Figure 4.13: 5mC and 5hmC double immunostaining in E9.5 to E14.5 mouse embryonic heart cell nuclei. First row: cryosectioned tissues showing nuclear DNA counterstained with DAPI (blue). Second row: primary antibody against 5hmC (green). Third row: antibody against 5mC (red). Fourth row: merged images of DAPI, 5hmC and 5mC. Columns 1 to 6: representative mouse embryonic heart tissue cryosections at stages from E9.5 to E14.5. The confocal images at stages from E9.5 to E12.5 were obtained by zooming into the images shown in Figure 4.12, whereas the confocal images at stages E13.5 and E14.5 were obtained by zooming into the trabecular regions (Trab). Scale bar indicates 10 µm.

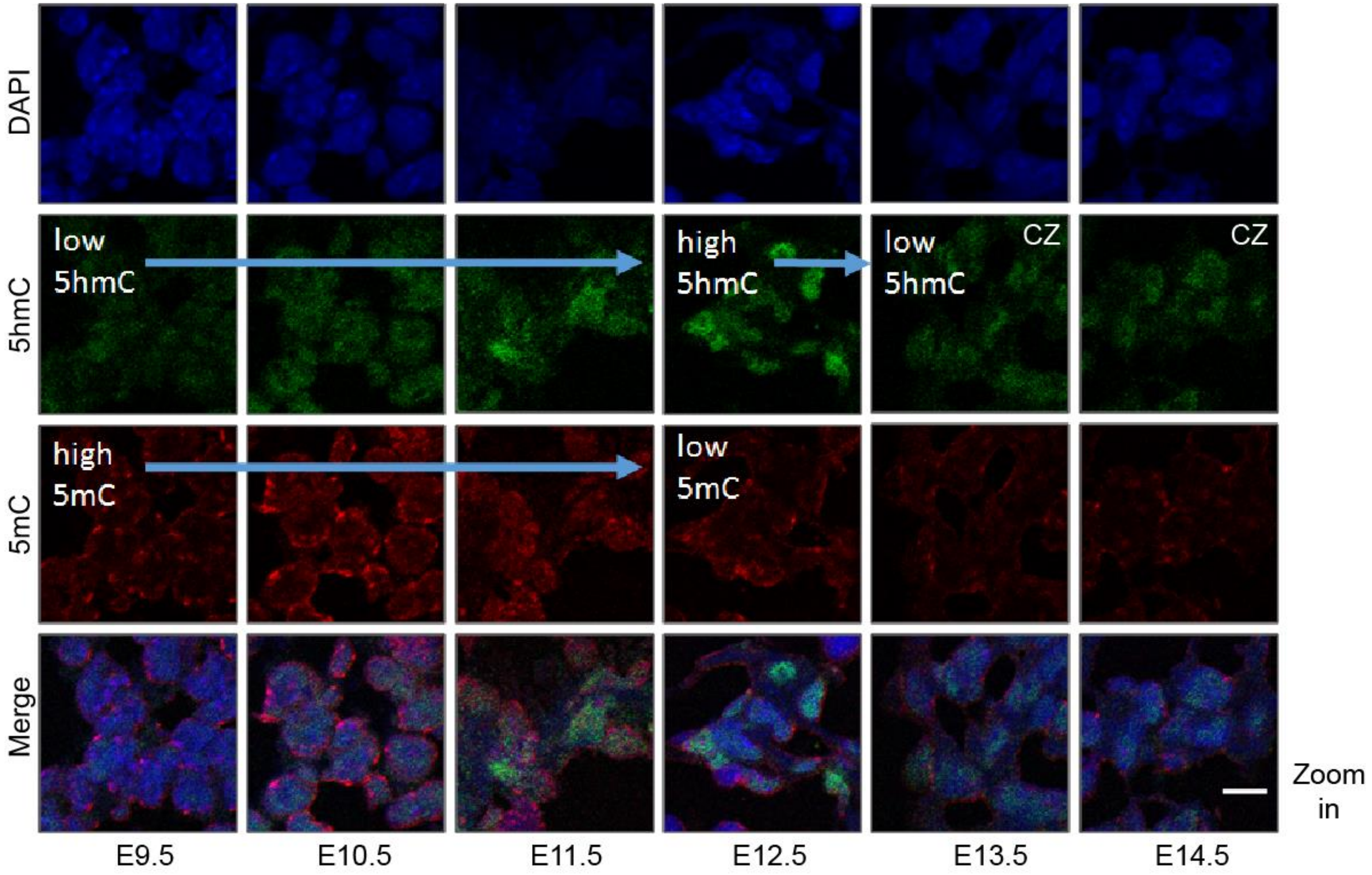

Figure 4.14: 5mC and 5hmC double immunostaining in E9.5 to E14.5 mouse embryonic heart cell nuclei. First row: cryosectioned tissues showing nuclear DNA counterstained with DAPI (blue). Second row: primary antibody against 5hmC (green). Third row: antibody against 5mC (red). Fourth row: merged images of DAPI, 5hmC and 5mC. Columns 1 to 6: representative mouse embryonic heart tissue cryosections at stages from E9.5 to E14.5. The confocal images at stages from E9.5 to E12.5 were obtained by zooming into the images shown in Figure 4.12, whereas the confocal images at stages E13.5 and E14.5 were obtained by zooming into the compact myocardium (CZ). Scale bar indicates 10 µm.

4.2.7 Quantification of 5mC and 5hmC staining patterns

Figure 4.15 and **4.16** show quantification of the 5mC and 5hmC signals in individual nuclei in E9.5 and E14.5 mouse embryonic diaphragm, liver, liver red blood cells, heart trabecular, heart compact myocardium and heart red blood cells. The levels of 5hmC in E14.5 red blood cells contained in liver and heart tissue are indeed lowest in this group. For diaphragm and liver, between E9.5 and E14.5, the levels of 5hmC are remarkably increased, for few cells in liver but spreading out over a wide range for diaphragm nuclei, whereas the levels of 5mC appear consistently lower. For heart trabecular nuclei, the levels of 5mC also show an apparent decrease between E9.5 and E14.5, whereas the levels of 5hmC nuclei are spread out and markedly higher at E14.5. For heart compact myocardium, the levels of 5mC are high at E9.5 and then become lower at E14.5, whereas for 5hmC, the levels between E9.5 and E14.5 show a modest increase compared to the trabeculae, which contain cells originating in the compact myocardium.

Overall, quantification analysis for 5mC and 5hmC displayed good consistency with immunostaining results.

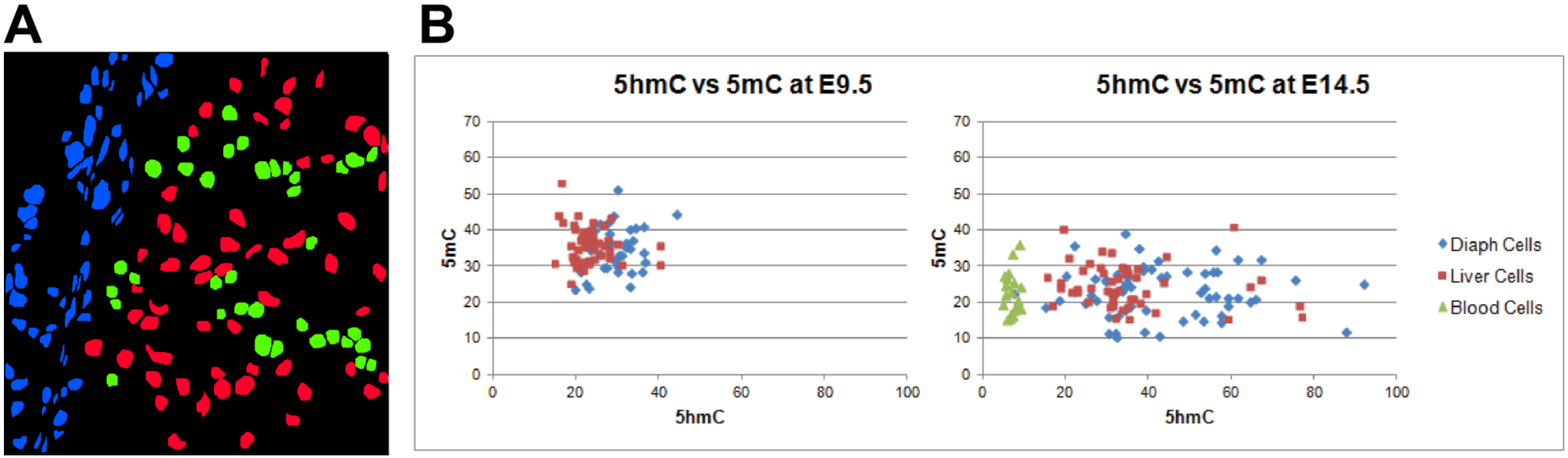

Figure 4.15: Quantification of the 5mC and 5hmC staining patterns in E9.5 and E14.5 mouse embryonic diaphragm, liver and blood cell nuclei. (A) Mask image of nuclei of E14.5 mouse embryonic diaphragm (blue), liver (red) and red blood cells (green) created using ImageJ (see Chapter 2, section 2.8) **(B)** A schematic showing of the results of quantification of 5mC and 5hmC signals in mouse embryonic diaphragm (blue), liver (red) and red blood cells (green) at E9.5 and E14.5.

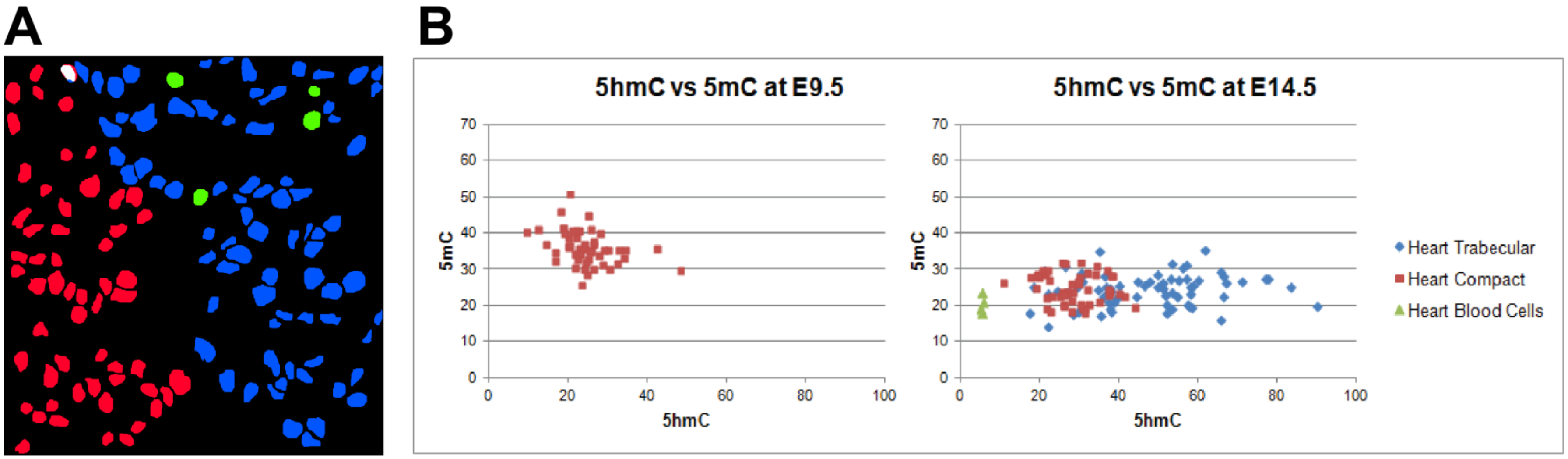

Figure 4.16: Quantification of the 5mC and 5hmC staining patterns in E9.5 and E14.5 mouse embryonic heart trabecular, heart compact myocardium and heart blood cell nuclei. (A) Mask image of nuclei of E14.5 mouse embryonic heart trabecular (blue), heart compact myocardium (red) and heart red blood cells (green) created using ImageJ (see Chapter 2, section 2.8) **(B)** A schematic showing of the results of quantification of 5mC and 5hmC signals in mouse embryonic heart trabecular (blue), heart compact myocardium (red) and heart red blood cells (green) at E9.5 and E14.5.

4.2.8 5mC immunostaining in E12.5 mouse embryonic primordial germ cells (PGCs)

Based on the finding that the genome-wide epigenetic states in PGCs undergo dramatic waves of reprogramming to remove DNA methylation, immunofluorescence double staining for 5mC in PGCs was subsequently performed as a necessary control to see whether the optimised protocol used for staining 5mC was capable of accurately detecting the hypomethylated state of PGCs in cryosections of E12.5 whole embryo mouse gonad. Moreover, the fluorescent signal results of 5mC erasure in PGCs were essentially required to help ensure the reliability and accuracy of 5mC results obtained in neocortex, surface ectoderm, liver, red blood cells, diaphragm and heart.

Mouse embryonic gonad at stage E12.5 was chosen for this experiment because at this stage of development the PGCs have migrated and reached their target tissue and settled in the fetal gonad. Furthermore, it has also been reported that, at E12.5, PGCs are in a hypomethylated state, suggesting that this embryonic stage is suitable for visualising DNA methylation changes (Yamaguchi et al., 2013). In addition, anti-Vasa antibody (DDX4/MVH) was used in this experiment as a PGC-specific marker.

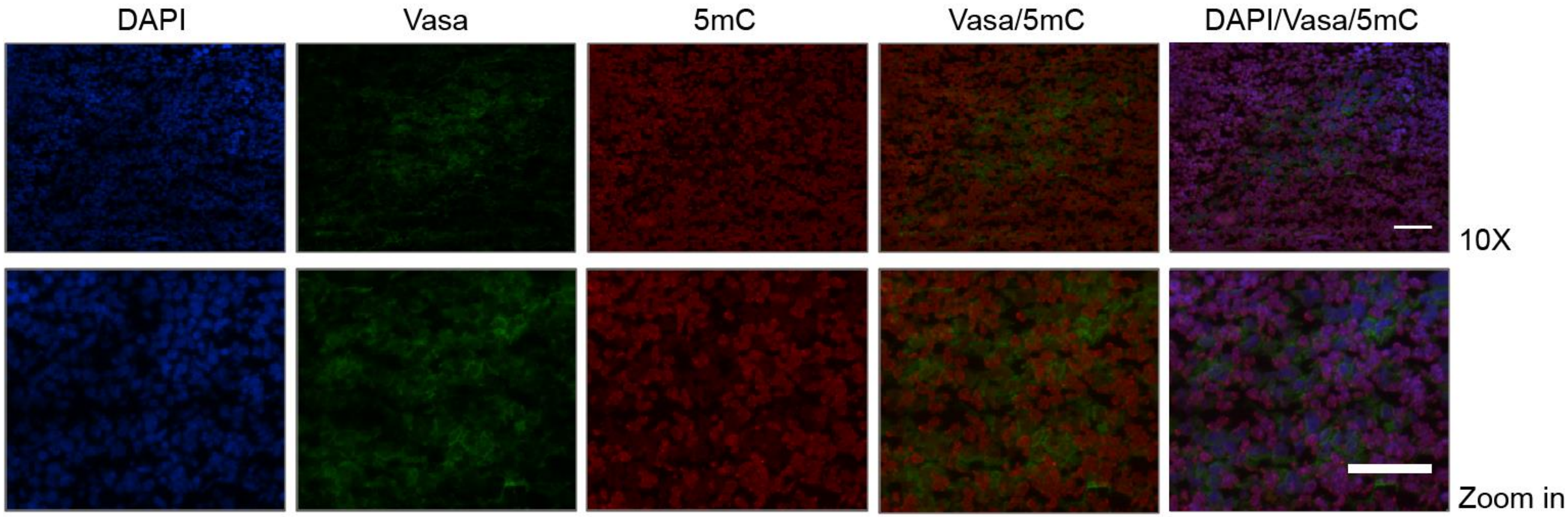

Figure 4.17: 5mC immunostaining in E12.5 mouse embryonic PGCs. First column: nuclear DNA counterstained with DAPI (blue). Second column: primary antibody against Vasa (green) highlighting PGC cells. Third column: primary antibody against 5mC (red). Fourth column: merged image of Vasa and 5mC. Fifth column: merged image of DAPI, Vasa and 5mC. Top row: Representative images of PGCs taken under 10X objective lens. Bottom row: zoomed-in portion of PGCs images in the top row. Vasa-positive PGCs were at hypomethylated states at mouse embryonic stage E12.5. Scale bar indicates 20 µm.

Figure 4.17 shows that the optimised protocol for 5mC immunostaining successfully detects a hypomethylated state in E12.5 PGCs. Representative immunofluorescence images show that cells that demonstrate direct association with Vasa-positive PGCs have indeed significantly lower 5mC staining levels. Consistent with other experimental findings, the result of the present experiment showed loss of DNA methylation in E12.5 PGCs. Furthermore, this experimental result also provided assurance that the hypomethylated DNA detected by our optimised 5mC immunostaining protocol in other mouse embryonic tissues was in fact reliable and accurate, and not due to local variations of in immunofluorescent staining.

Moreover, it is also shown that successful double immunostaining for 5mC and PGCs was achieved using the optimised protocol for immunodetection of 5mC, indicating that even under harsh DNA-denaturing conditions required by this procedure, anti-Vasa antibody was still found to stain positively for the germ cell-specific protein Vasa in the gonadal region (Figure 4.15 – Vasa). This result was therefore possible due to the compatibility of the PGCs immunostaining protocol with procedures requiring heat treatment. Tissue marker colocalisation on heat-denatured 5mC or 5hmC cryosections proved more problematic with other antibodies.

4.2.9 5mC and 5hmC single immunostainings in E14.5 mouse embryonic brain tissue: primary antibody specificity control

Since the dynamic study was performed by double staining with anti-5mC and anti-5hmC antibodies, there was a potential concern raised regarding the potential for cross-reactivity of the antibodies, as the 5mC and 5hmC modifications have very similar chemical structures. In addition, potential steric hindrance or antibody competition for closely located sites was a potential concern. Therefore, 5mC and 5hmC single immunostainings were performed as an additional control in order to confirm the specificity of the primary antibody binding affinity.

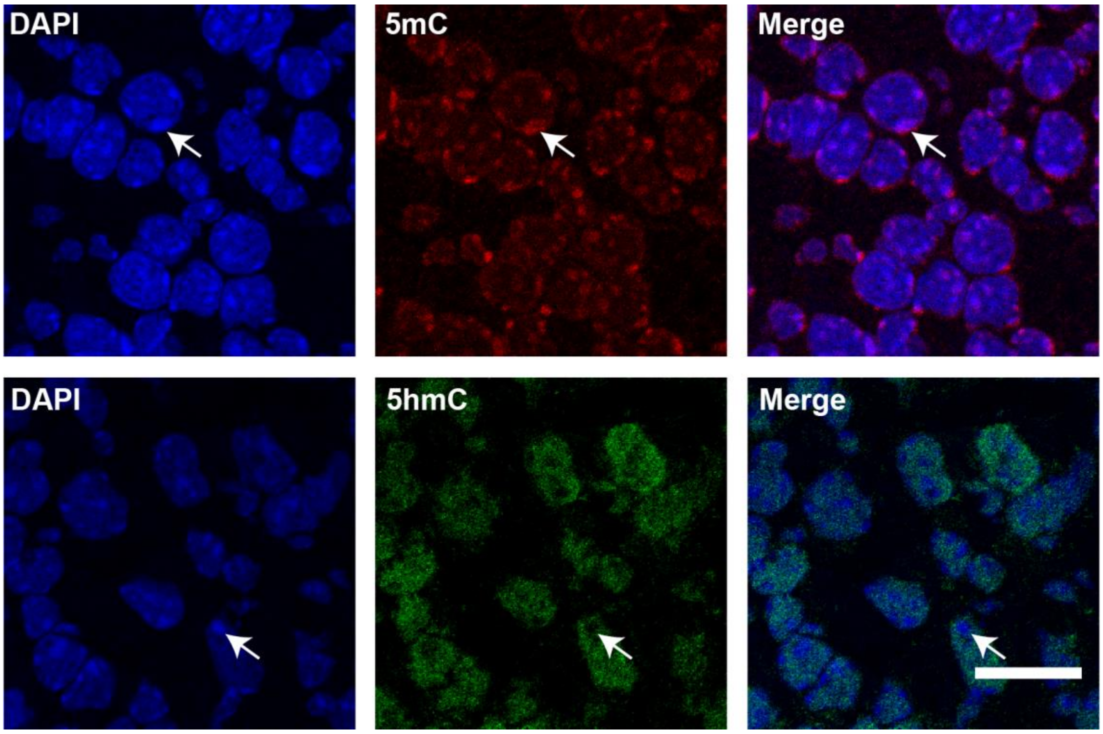

Figure 4.18: 5mC and 5hmC single immunostainings in E14.5 mouse embryonic brain cell nuclei. Left column: nuclear DNA counterstained with DAPI (blue). Middle column: primary antibodies against 5mC (red) and 5hmC (green). Top row, right column: merged image of DAPI and 5mC. Bottom row, right column: merged image of DAPI and 5hmC. Images were obtained using a confocal microscope with a 40X oil-immersion objective lens. 5mC signals mainly localise in DAPI-intense heterochromatic regions (top row, marked by arrows), whereas 5hmC signals primarily localise in euchromatic regions and exclude from the DAPI-bright granules (bottom row, marked by arrows). Scale bar indicates 20 µm.

Representative confocal immunofluorescence images show that the 5mC signals are robustly accumulated in DAPI-dense heterochromatic chromatin regions, while 5hmC signals are contrastingly distributed in DAPI-sparse euchromatic regions avoiding the DAPI-dense aggregates **(Figure 4.18)**. These results suggested that both antibodies against 5mC and 5hmC were indeed highly specific with no detectable cross-reactivity.

4.2.10 Enzyme immunostaining in E12.5 mouse embryonic tissues

The three enzymes of the mammalian Tet family (Tet1, Tet2 and Tet3) are responsible for the loss of 5mC and the production of 5hmC. Moreover, a recent study demonstrates that *de novo* DNA methylation could play a key role in the formation of 5hmC. Therefore, it was crucial to investigate the presence of these enzymes in order to discover the origin of 5hmC. Cryosections of E12.5 mouse tissues were immunostained with antibodies against Tet1, Tet2, Tet3 and DNMT3A. Day E12.5 embryo was chosen for this experiment because at this stage the dynamic range of high and low levels of 5mC and 5hmC was most apparent.

Detectable signals of Tet1, Tet2, Tet3 and DNMT3A are observed in neocortex **(Figure 4.19)**, liver **(Figure 4.20)**, diaphragm **(Figure 4.22)** and heart **(Figure 4.23)**. However, in red blood cells, no apparent signals of Tet1, Tet2, Tet3 and DNMT3A are detected **(Figure 4.21)**. The observation in the red blood cells was theoretically expected in view of the very low levels of 5hmC and high levels of 5mC staining in red blood cells. Immunofluorescent images of 5mC and 5hmC staining are shown in each of the figures **(Figure 4.19, 4.20, 4.21, 4.22, 4.23 – 5mC and 5hmC)** as comparative references of their staining levels. No results for surface ectoderm were obtained as at E12.5, this tissue was barely visible.

The confocal images further show interesting distribution patterns of Tet1, Tet2, Tet3 and DNMT3A. In neocortex, Tet1 signals are localised mainly in euchromatin regions, Tet2 signals are found mostly in heterochromatin regions, Tet3 distribution patterns are indistinguishable, and DNMT3A signals are enriched strongly in euchromatin regions **(Figure 4.19)**. In liver, all enzymes seem to be distributed preferentially in euchromatin regions **(Figure 4.20)**. Diaphragm appears to have distribution patterns of Tet1, Tet2, Tet3 and DNMT3A that are identical to enzymes distribution patterns in neocortex **(Figure 4.22)**. In heart, Tet1 signals are unclear, Tet2 signals are localised predominantly in heterochromatin regions, Tet3 and also DNMT3A signals are located preferentially in euchromatin regions **(Figure 4.23)**.

Overall, these observations were in agreement with the model where the loss of 5mC may trigger the formation of 5hmC, but the results were also consistent with an involvement of DNMT3A-driven *de novo* methylation in the production of 5hmC (Amouroux et al., 2016). In line with the previous studies, these findings also confirmed the important role of Tet1, Tet2, Tet3 and DNMT3A in mediating the accumulation of 5hmC. Their intranuclear distributions were in support of euchromatin-colocalised *de novo* 5mC methylation and 5hmC hydroxylation, in addition to heterochromatin-localised hydroxylation of old 5mC. However, it would be of great interest to see the dynamic patterns of these enzymes throughout embryonic development and investigate their correlation with 5mC and 5hmC dynamics in developing tissues.

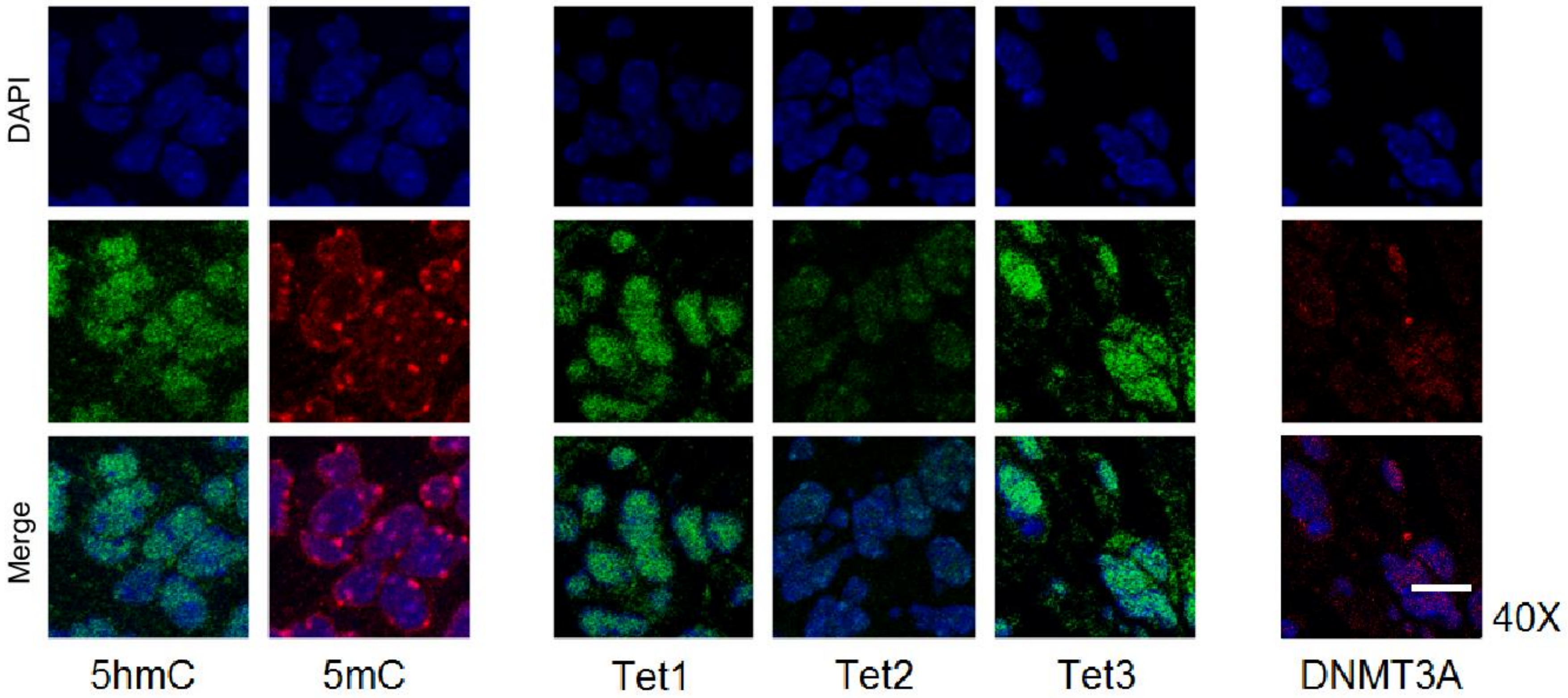

Figure 4.19: Tet1, Tet2, Tet3 and DNMT3A immunostainings in E12.5 mouse embryonic brain neocortical cell nuclei in whole embryo cryosections. Representative stainings of mouse embryonic brain neocortical cell nuclei in whole embryo cryosections are shown. First row: nuclear DNA counterstained with DAPI (blue). Second row, first panel: primary antibody against 5hmC (green). Second row, second panel: antibody against 5mC (red). Second row, third panel: antibody against Tet1 (green). Second row, fourth panel: antibody against Tet2 (green). Second row, fifth panel: antibody against Tet3 (green). Second row, sixth panel: antibody against DNMT3A (red). Third row: merged images. Images were obtained using a confocal microscope with a 40X oil-immersion objective lens. Indirect fluorescence signals of Tet1, Tet2, Tet3 and DNMT3A were detected. Scale bar indicates 10 µm.

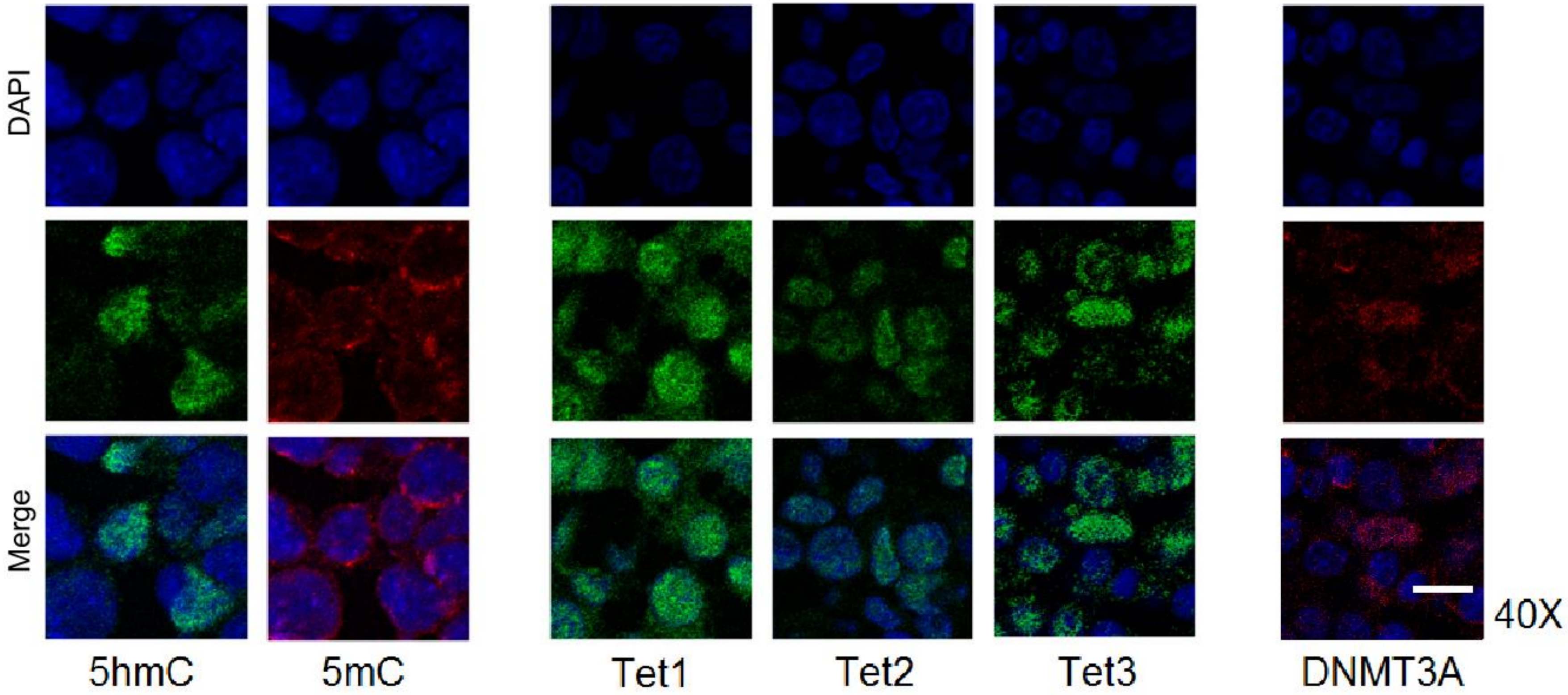

Figure 4.20: Tet1, Tet2, Tet3 and DNMT3A immunostainings in E12.5 mouse embryonic liver cell nuclei in whole embryo cryosections. Representative stainings of mouse embryonic liver cell nuclei are shown. First row: nuclear DNA counterstained with DAPI (blue). Second row, first panel: primary antibody against 5hmC (green). Second row, second panel: antibody against 5mC (red). Second row, third panel: antibody against Tet1 (green). Second row, fourth panel: antibody against Tet2 (green). Second row, fifth panel: antibody against Tet3 (green). Second row, sixth panel: antibody against DNMT3A (red). Third row: merged images. Images were obtained using a confocal microscope with a 40X oil-immersion objective lens. Tet1, Tet2, Tet3 and DNMT3A signals were observed. Scale bar indicates 10 µm.

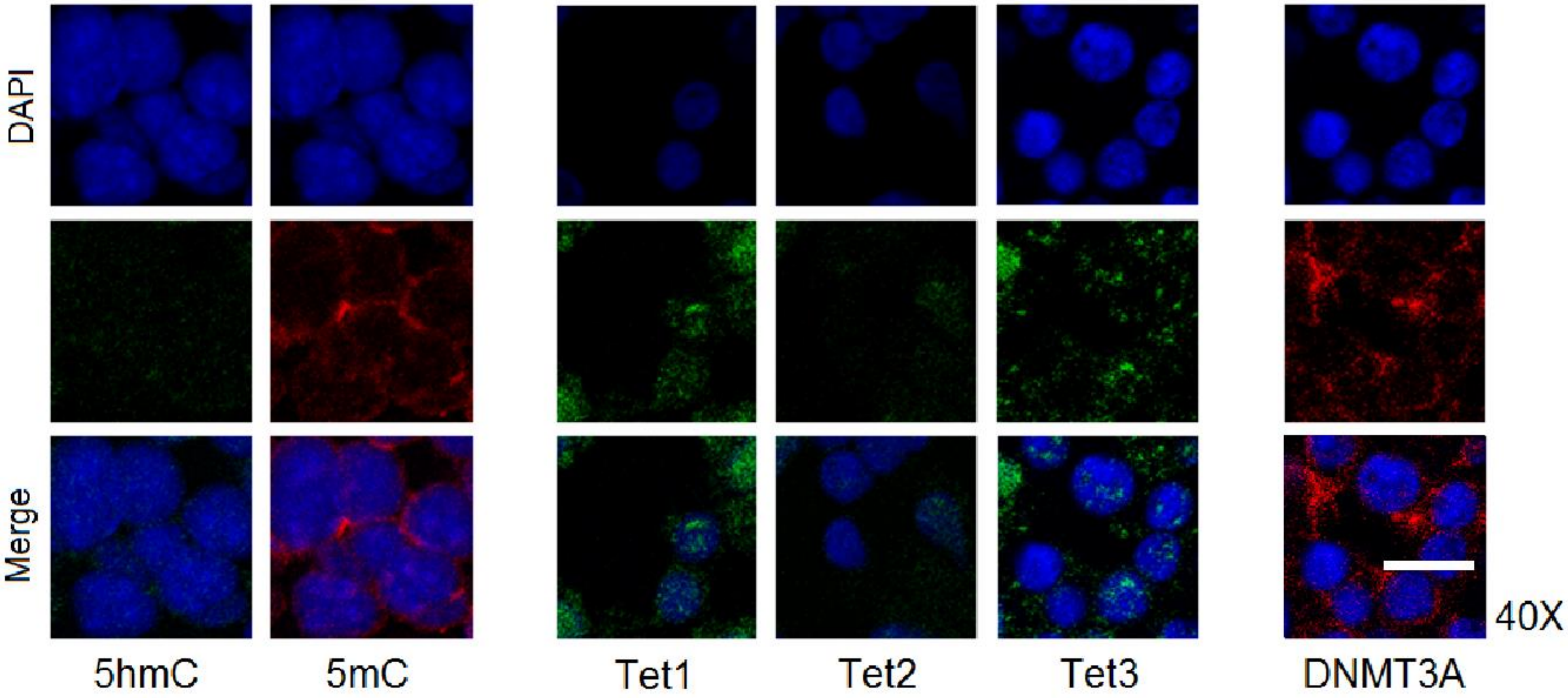

Figure 4.21: Tet1, Tet2, Tet3 and DNMT3A immunostainings in E12.5 mouse embryonic red blood cell nuclei in whole embryo cryosections. Representative stainings of mouse embryonic red blood cell nuclei are shown. First row: nuclear DNA counterstained with DAPI (blue). Second row, first panel: primary antibody against 5hmC (green). Second row, second panel: antibody against 5mC (red). Second row, third panel: antibody against Tet1 (green). Second row, fourth panel: antibody against Tet2 (green). Second row, fifth panel: antibody against Tet3 (green). Second row, sixth panel: antibody against DNMT3A (red). Third row: merged images. Images were obtained using a confocal microscope with a 40X oil-immersion objective lens. No apparent signals of Tet1, Tet2, Tet3 and DNMT3A were observed. Scale bar indicates 10 µm.

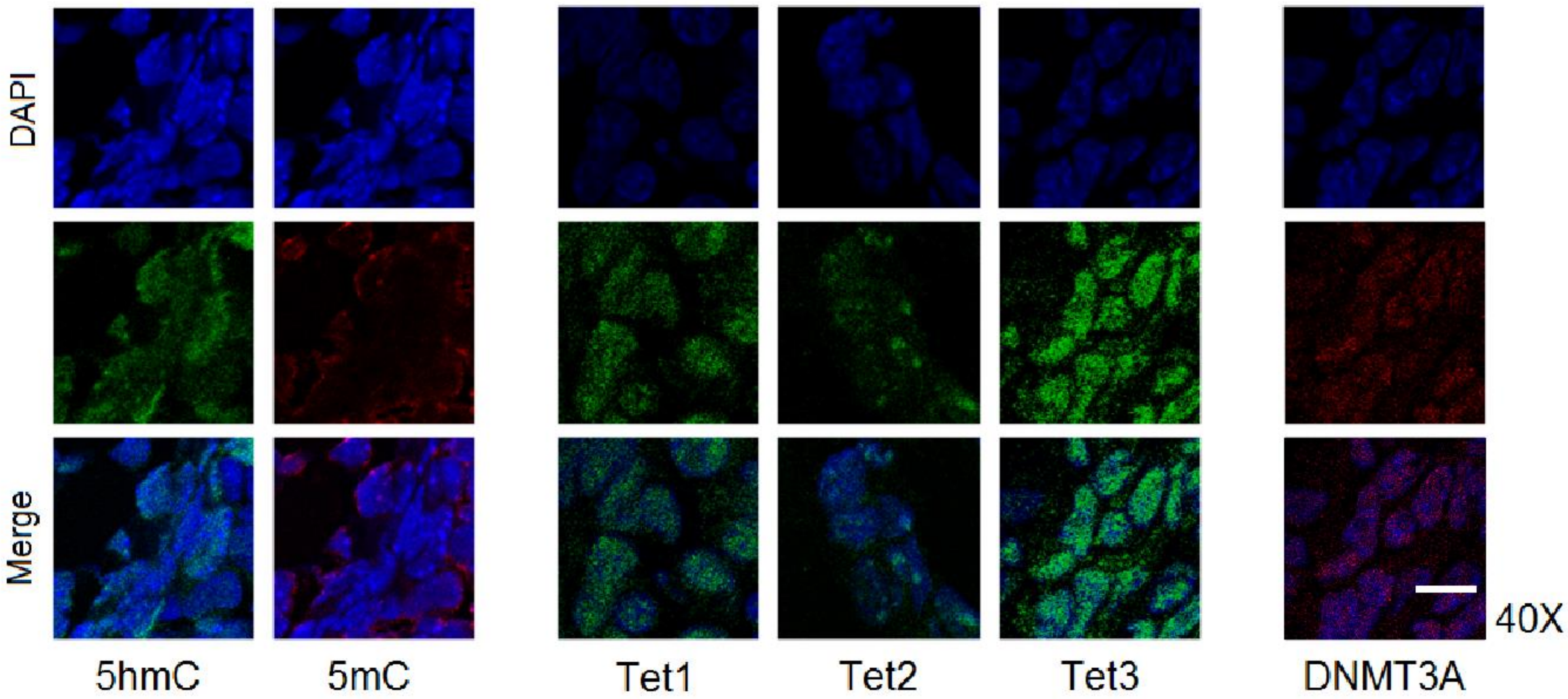

Figure 4.22: Tet1, Tet2, Tet3 and DNMT3A immunostainings in E12.5 mouse embryonic diaphragm cell nuclei in whole embryo cryosections. Representative stainings of mouse embryonic diaphragm cell nuclei are shown. First row: nuclear DNA counterstained with DAPI (blue). Second row, first panel: primary antibody against 5hmC (green). Second row, second panel: antibody against 5mC (red). Second row, third panel: antibody against Tet1 (green). Second row, fourth panel: antibody against Tet2 (green). Second row, fifth panel: antibody against Tet3 (green). Second row, sixth panel: antibody against DNMT3A (red). Third row: merged images. Images were obtained using a confocal microscope with a 40X oil-immersion objective lens. Detectable Tet1, Tet2, Tet3 and DNMT3A signals were present in mouse E12.5 diaphragm. Scale bar indicates 10 µm.

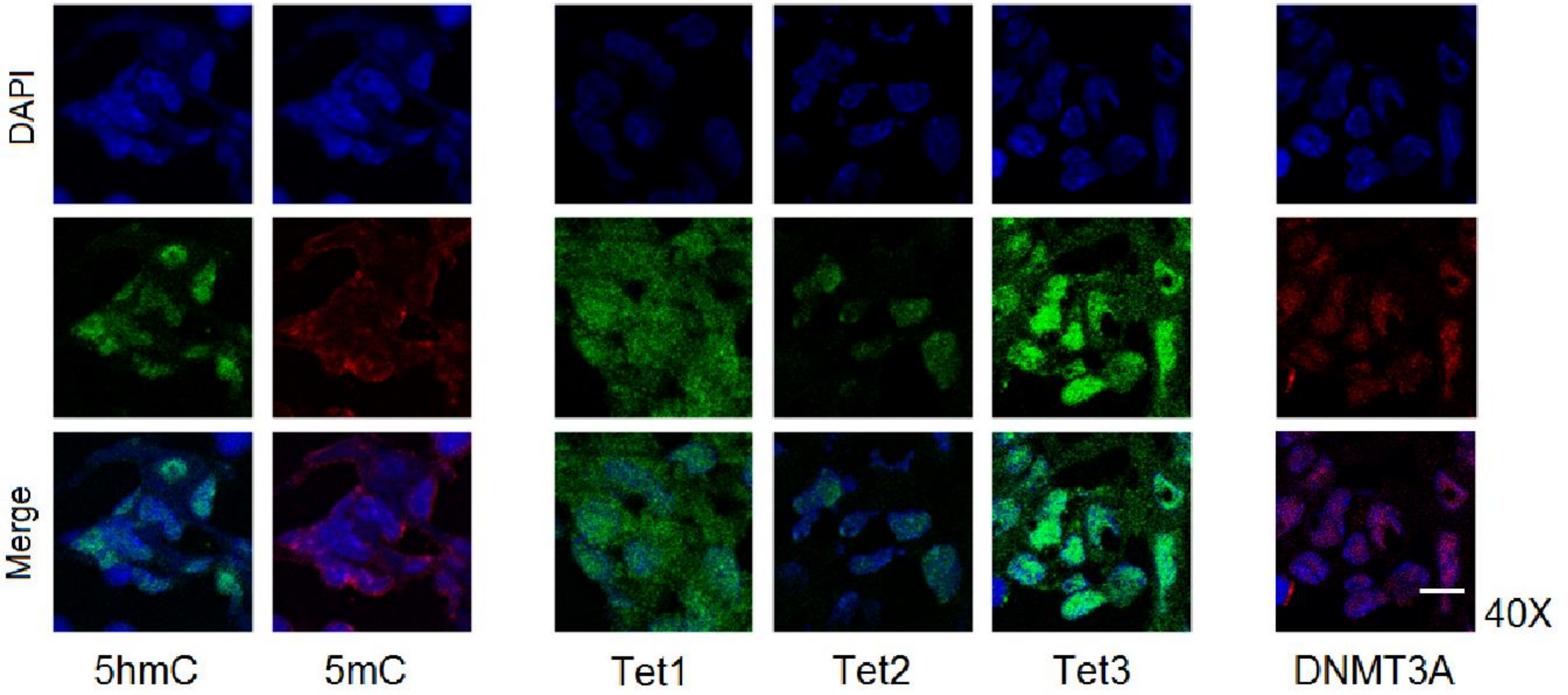

Figure 4.23: Tet1, Tet2, Tet3 and DNMT3A immunostainings in E12.5 mouse embryonic heart cell nuclei in whole embryo cryosections. Representative stainings of mouse embryonic heart cell nuclei are shown. First row: nuclear DNA counterstained with DAPI (blue). Second row, first panel: primary antibody against 5hmC (green). Second row, second panel: antibody against 5mC (red). Second row, third panel: antibody against Tet1 (green). Second row, fourth panel: antibody against Tet2 (green). Second row, fifth panel: antibody against Tet3 (green). Second row, sixth panel: antibody against DNMT3A (red). Third row: merged images. Images were obtained using a confocal microscope with a 40X oil-immersion objective lens. Tet1, Tet2, Tet3 and DNMT3A were present at detectable levels in mouse E12.5 heart. Scale bar indicates 10 µm.

4.3 Discussion

This chapter sought to explore DNA methylation states in terms of the cell type variations and the temporal changes of 5mC amongst developing mouse embryonic tissues and investigate their relationship with the formation and dynamics of 5hmC.

4.3.1 5mC and 5hmC dynamics in developing mouse embryonic tissues

Immunofluorescence observations revealed developmental tissue variations of 5mC, together with 5hmC, in brain neocortex, surface ectoderm, liver, red blood cells, diaphragm and heart. The optimised protocols used for 5mC and 5hmC detection in standardised conditions were able to display interesting dynamics across developmental stages. All tissues examined demonstrated distinct dynamic changes in 5mC and 5hmC patterns, except for liver and diaphragm, which showed some distribution-based similarity. Moreover, the dynamics of 5mC and 5hmC seemed to be tissue-specific, but again except for liver and diaphragm as they both appeared to share some features of similarity. Furthermore, both liver and diaphragm might also possess similarity in nuclear organisation of transcription for cellular differentiation. Apparently, heart showed much more dynamic changes in 5mC as well as 5hmC compared to other tissues, suggesting that nuclear organisation and DNA methylation state changes may be important for normal development of heart. On the contrary, 5mC in conjunction with 5hmC existed at highly elevated levels at certain developmental stages of neocortex, indicating that strong transcriptional silencing and activation states may be necessary for the development of neocortical zones.

Importantly, a recent study has reported significant levels of 5hmC in the cerebral cortex of the adult rat and its crucial role in the brain (Zheng et al., 2015). Another study also found significant enrichment of 5hmC in the adult mouse brain (Li and Liu, 2011). These results are consistent with Kriaucionis and Heintz who first reported discovery of 5hmC abundance in the adult mouse cortex and found that 5hmC was roughly 40% as abundant as 5mC in Purkinje cells (Kriaucionis and Heintz, 2009). Our findings likely explain the enrichment of 5hmC and 5mC as well as their important functions in the neocortex as variations between developing zones.

(Li and Liu, 2011) also found high distribution of 5hmC in human liver. The high levels of 5hmC observed in this study at later stages of liver development are found to be consistent with the published data describing 5hmC distribution in human tissues, suggesting that 5hmC may be necessary for the expression of hepatic genes. On the other hand, research studies on 5hmC in blood indicate that blood cells are strongly depleted of 5hmC (Gross et al., 2016; Nestor et al., 2012; Stewart et al., 2015). Consistent with the previous reports, confocal microscopy experiments also showed extremely low 5hmC levels in blood cells. For other tissue types, including surface ectoderm and diaphragm, less experimental literature on 5mC and 5hmC distributions is available. Thus, the data obtained from this study could provide new insights into the dynamics and distributions of both DNA modifications in these less-studied tissues. The same goes for heart, due to 5mC and 5hmC varying distribution levels throughout heart development, as an appropriate comparison with the literature could not be made.

However, a possible alternative explanation that could be made for high levels of 5hmC in neocortex and heart trabeculae is they both are the zones with low proliferative activity (Barazzuol et al., 2015; Luxán et al., 2013), indicating that both tissues are enriched with post-mitotic cells. These observations are in accordance with a previous study that suggests high 5hmC is associated with non-proliferating post-mitotic cells (Ruzov et al., 2011). Nevertheless, its function is not yet clear.

4.3.2 The origin of 5hmC during development

In order to investigate the relationship between 5mC and 5hmC, three proposed models to explain the formation of 5hmC were utilised. These included loss of 5mC, gain of 5hmC by Tet proteins **(Figure 4.24A)**, loss of 5mC, gain of 5hmC by Tet enzymes requiring DNMT3A **(Figure 4.24B)**, and 5hmC acting on its own without concerted active DNA demethylation. Immunofluorescence analysis of the possible correlation between the levels of 5mC and 5hmC discovered that the dynamic changes of 5mC and 5hmC during neocortical and compact myocardial development supported the model where the 5hmC may be an independent epigenetic mark with its own regulatory mechanism. In other developing tissues, including surface ectoderm, liver, red blood cells, diaphragm and cardiac trabeculae, dynamic changes in 5mC and 5hmC levels agreed closely with the model where the accumulation of 5hmC may be associated with the loss of old 5mC, but the observations were also consistent with an involvement of *de novo* DNA methyltransferase DNMT3A in the formation of 5hmC.

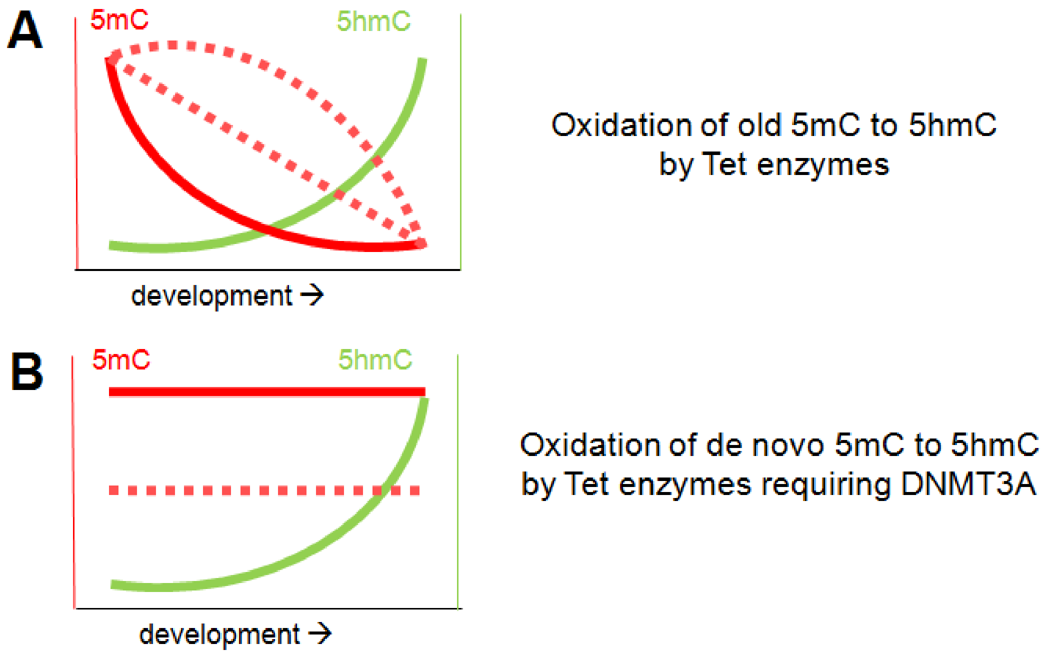

Figure 4.24: Model for 5hmC as *de novo* epigenetic mark. (A) Tet proteins catalyse the oxidation of old 5mC (red) to produce 5hmC (green). **(B)** Tet enzymes oxidise *de novo* 5mC (red), produced by *de novo* DNA methyltransferase DNMT3A, and yield 5hmC (green). Dashed red lines represent the possible levels of 5mC. Figure created from the model proposed by Amouroux et al. (2016).

Furthermore, the confocal image data describing the presence of all enzymes (Tet1, Tet2, Tet3, and DNMT3A) that are responsible for the production of 5hmC further confirmed the dynamic observed. A close inspection of the distribution patterns of enzymes suggests that DNMT3A 5mC may methylate euchromatin and euchromatic Tet1 (or Tet3, but less so Tet2) may render it into 5hmC in the euchromatin. Perhaps, these observations could therefore be taken in support of the *de novo* model, while more heterochromatin-localised Tet3 enzymes could hydroxylate old 5mC. However, it would be interesting to see the dynamic changes and distribution patterns of all those enzymes in the developing mouse tissues, not only at one stage of development, to further support the dynamic changes in 5mC and 5hmC.

Taken together, this study suggests two possible developmental roles of 5hmC, including its role as a transient intermediate product of Tet-mediated active cytosine demethylation which can be oxidised further to form another two oxidised cytosine bases and its role as a new, stable and independent epigenetic mark that could recruit its own protein readers. However, further investigation may be necessary in order to fully understand the function of 5hmC.

Chapter 5 - H3K9me3 and H3K27me3 histone methylation dynamics in developing mouse embryonic tissues

5.1 Introduction

It has become increasingly apparent that DNA methylation does not act independently, but instead there is a close teamwork between DNA methylation and histone modifications (Patel, 2016). Great interest has been placed in the relationship between DNA methylation and histone lysine methylation, as the two systems appear to be highly correlated with one another (Du et al., 2015a). DNA and histone methylation systems interact closely in the regulation of transcription and chromatin organisation (Cedar and Bergman, 2009). Both epigenetic marks are likely to work in concert in establishing patterns of gene silencing during normal development (Cheng, 2014). Interestingly, the epigenetic interplay can occur in two-way interactions, in which DNA methylation can either be influenced by histone lysine methylation or vice versa (Rose and Klose, 2014). Accumulating evidence suggests that this crosstalk may be achieved through an intricate network of interactions between DNA and histone lysine methyltransferases (Zhang et al., 2015).

Two histone marks, trimethylation of K9 and K27 on histone H3 (H3K9me3 and H3K27me3), are well known to be associated with constitutive and facultative heterochromatin formation, respectively, and gene repression (Boros et al., 2014). The epigenetic crosstalk between H3K9me and DNA methylation was first discovered several years ago by Tamaru and Selker (2001), demonstrating that DNA methylation is dependent on histone lysine methylation. Furthermore, trimethylation of H3K9 in particular has been shown to be very closely linked to cytosine methylation (Kim and Kim, 2012; Liu et al., 2013; Saksouk et al., 2015; Stewart et al., 2016). However, this crosstalk is not in agreement with the most recent study in mice (Zhao et al., 2016), which suggests that DNA maintenance methylation does not globally rely on H3K9 methylation.

Another important crosstalk between H3K27me3 and DNA methylation in directing transcriptional repression has also been reported (Reddington et al., 2013b). DNA methylation is necessary for the appropriate placement of H3K27me3, indicating that dysregulation of these two repressive mechanisms might be implicated in the development of many different types of cancer (Reddington et al., 2014). Interestingly, the relationship between H3K27me3 and DNA methylation is genomic region dependent, as these two epigenetic marks are found to be mutually exclusive in CpG dinucleotide-rich regions, whereas in other regions of H3K27me3 genomic enrichment, extensive overlap between these two mechanisms is apparent. Furthermore, the mutual exclusivity of H3K27me3 and DNA methylation may occur due to inhibition of PRC2 activity at DNA-methylated CpG-rich areas. Such inhibitory mechanism can be explained by epigenetic switching as reported in a previous study for prostate cancer cells (Gal-Yam et al., 2008). This study suggests that genes which are repressed by Polycomb complexes in normal prostate cells acquire CpG methylation and lose their H3K27me3 marks in the PC3 cancer cells. (Brinkman et al., 2012; de la Calle Mustienes et al., 2015; Yan et al., 2015).

Therefore, it was of considerable interest to explore the correlation between DNA methylation and histone lysine methylation particularly focusing on trimethylation at both H3K9 and H3K27 in order to gain an accurate and deeper understanding of this interesting relationship during development. Immunofluorescent staining technique was again employed in the experiments reported here. Dynamic nuclear changes in H3K9me3 and H3K27me3 states were identified in the developing brain neocortex and heart. The dynamic patterns of both histone markers were subsequently compared with the dynamics of 5mC demonstrated in Chapter 4. Neocortex and heart were selected for a comparative study because both tissues showed distinct dynamic patterns of 5mC.

Therefore, the aims of this chapter were:

1. To observe dynamic nuclear changes in H3K9me3 state during neocortex and heart development from E8.5 to E14.5 mouse whole embryonic stages.

2. To observe dynamic nuclear changes in H3K27me3 state during neocortex and heart development from E8.5 to E14.5 mouse whole embryonic stages.

3. To investigate the relationship between DNA methylation and histone lysine methylation in the developing neocortex and heart.

5.2 Results

Histone trimethylation dynamics at H3K9 and H3K27 were observed in whole embryo cryosections taken during mouse fetal development with results reported in brain neocortex and heart.

5.2.1 Dynamics of H3K9me3 during embryonic neocortical development in mouse

Figure 5.1 shows antibody staining patterns for H3K9me3 during embryonic neocortical development. Histone H3K9me3 displays consistently strong immunostaining in brain throughout development (embryonic days 8.5 to 14.5). Images of brain neocortical cell nuclei are shown in **Figure 5.2 – H3K9me3**. Confocal microscopy reveals that H3K9me3 immunostaining colocalises predominantly with DAPI brightly stained regions of high DNA density.

Furthermore, monoclonal RC2 antibody staining was used in this experiment to observe for intermediate filament nestin. RC2 staining is detected in the neocortical regions of E9.5 to E14.5 cryosections, but at E8.5, significantly less intense signal of RC2 is observed **(Figure 5.2 – RC2)**. H3K9me3 exhibits a high degree of colocalisation with nestin-expressing cells. This result suggested that high levels of H3K9me3 were positively associated with pluripotent neural progenitor cells.

It seemed that the patterns of H3K9me3 staining were similar to the patterns of 5mC staining described in Chapter 4. Fluorescence signals of these two epigenetic marks were found to be intense in the regions of neocortical tissue. These observations thus supported the research model which proposes that trimethylation of H3K9 works in combination with 5mC to promote gene silencing.

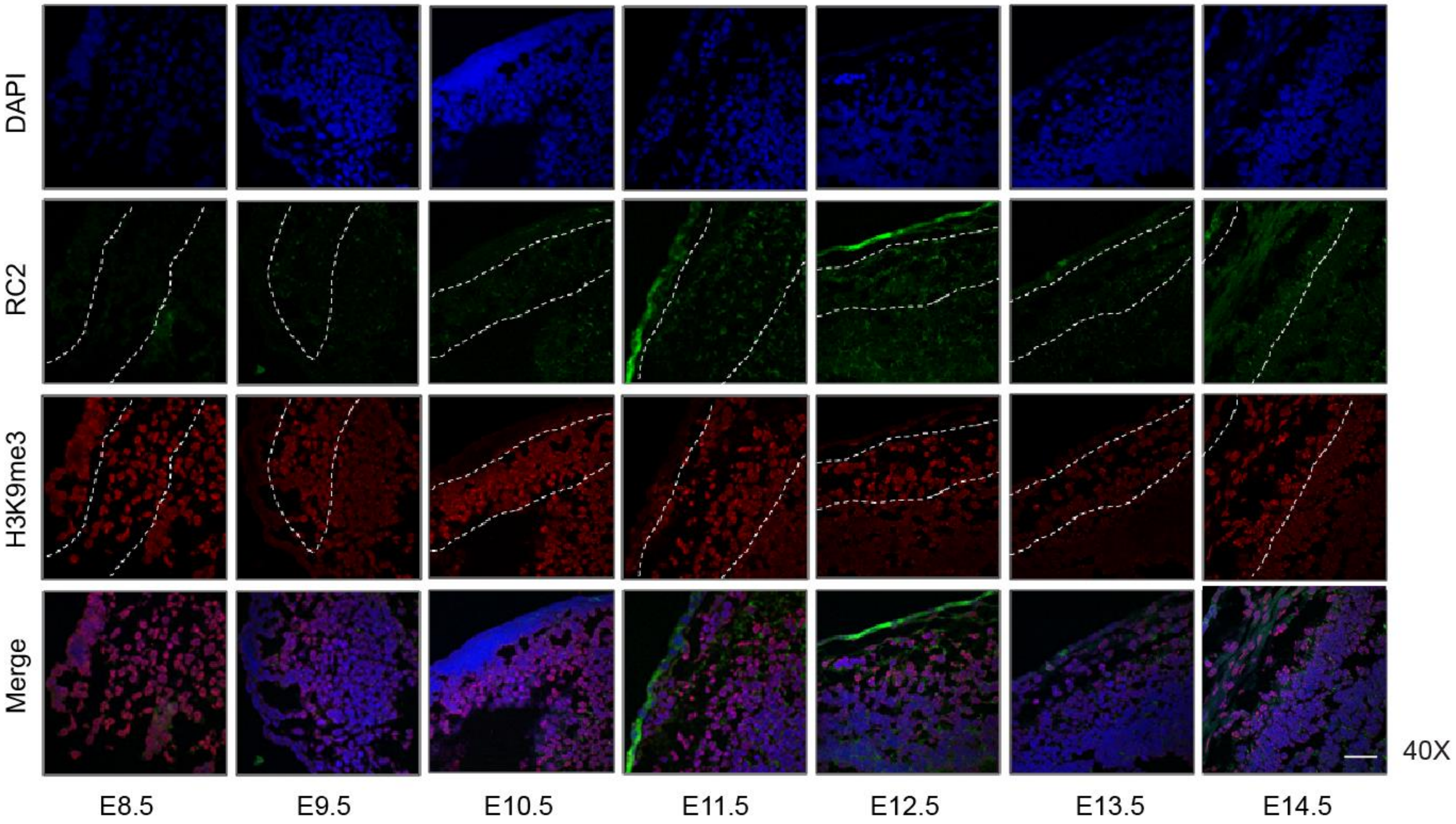

Figure 5.1: H3K9me3 immunostaining in E8.5 to E14.5 mouse embryonic brain neocortical tissues in whole embryo cryosections. First row: nuclear DNA counterstained with DAPI (blue). Second row: primary RC2 antibody against nestin (green). Third row: primary antibody against H3K9me3 (red). Fourth row: merged images of DAPI, nestin and H3K9me3. Columns 1 to 7: representative mouse embryonic brain neocortical tissue cryosections at stages from E8.5 to E14.5. Areas within the dashed lines represent neocortical tissues. Images were obtained using a confocal microscope with a 40X oil-immersion objective lens. Scale bar indicates 40 µm.

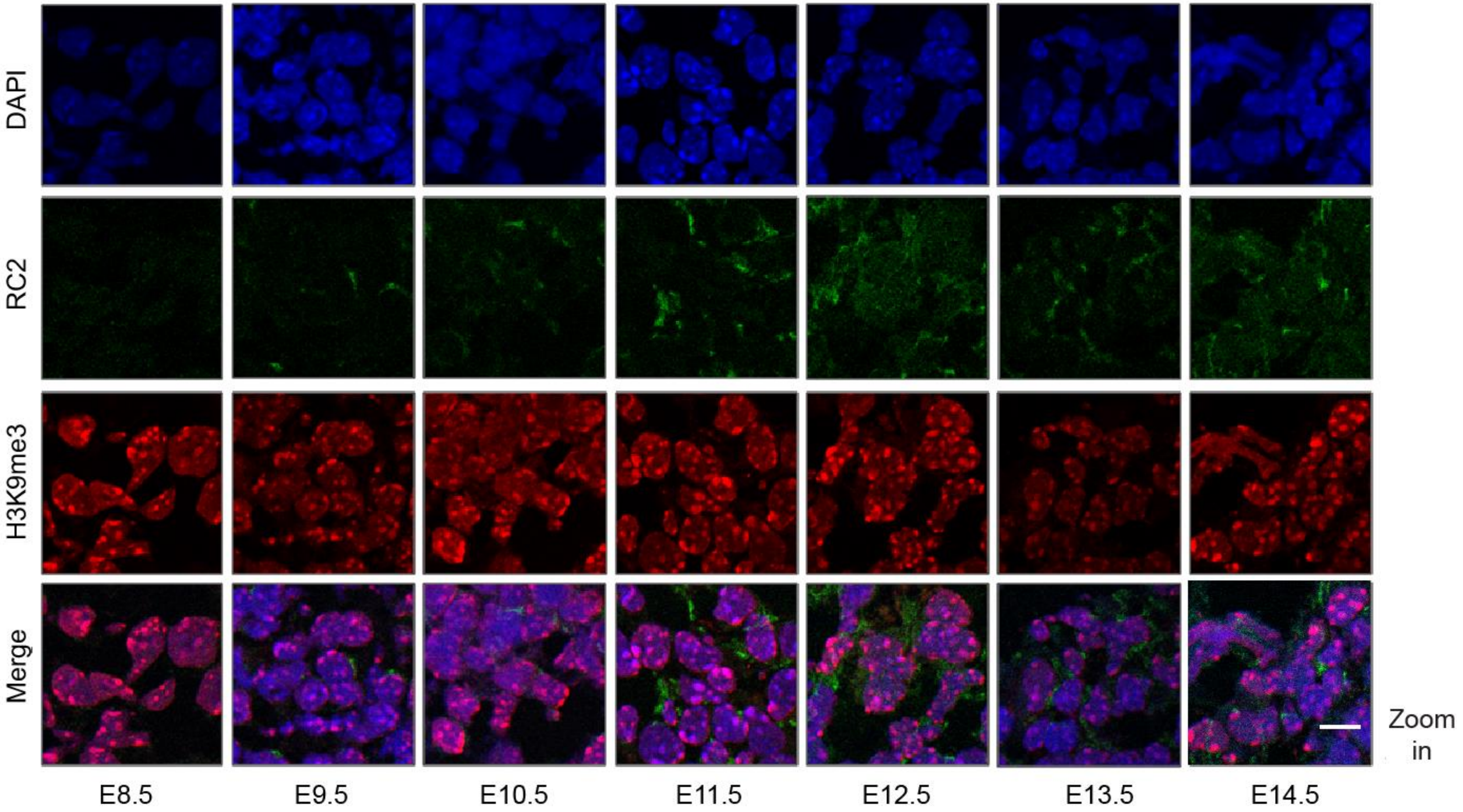

Figure 5.2: H3K9me3 immunostaining in E8.5 to E14.5 mouse embryonic brain neocortical cell nuclei. First row: nuclear DNA counterstained with DAPI (blue). Second row: primary RC2 antibody against nestin (green). Third row: primary antibody against H3K9me3 (red). Fourth row: merged images of DAPI, nestin and H3K9me3. Columns 1 to 7: representative mouse embryonic brain neocortical cell nuclei at stages from E8.5 to E14.5. The confocal images were obtained by zooming into areas within the dashed lines shown in Figure 5.1. Scale bar indicates 10 µm.

5.2.2 Dynamics of H3K27me3 during embryonic neocortical development in mouse

The dynamic changes of another classic repressive histone marker, trimethylation on H3K27, were also investigated in this study. H3K27me3 is a characteristic marker for facultative heterochromatin including X chromosome inactivation (Xi), whereas H3K9me3 is associated with constitutive heterochromatin typical for pericentromeric regions. Remarkably, H3K27me3 demonstrates a staining pattern similar to that of H3K9me3 in the developing mouse neocortex **(Figure 5.3)**. Immunofluorescence images show that H3K27me3 is maintained at consistently high levels throughout embryonic brain development (from E8.5 to E14.5) **(Figure 5.4 – H3K27me3)**. Moreover, inside each of the female cell nuclei, one large patch of Xi associated-H3K27me3 is detected.

Monoclonal RC2 antibody staining detects positive nestin signal in all stages of development except for E8.5, which demonstrates significantly weaker fluorescence signals **(Figure 5.4 – RC2)**. Like the H3K9me3 signal, this repressive histone modification also showing colocalisation with RC2-positive cells, providing a direct link between H3K27me3 and neural progenitor cells.

Interestingly, immunofluorescence microscopy for H3K27me3 revealed similar distribution patterns to H3K9me3 and 5mC, indicating that these three epigenetic marks were highly and mutually interconnected. Together, these findings suggest the importance of gene silencing in the developing neocortex.

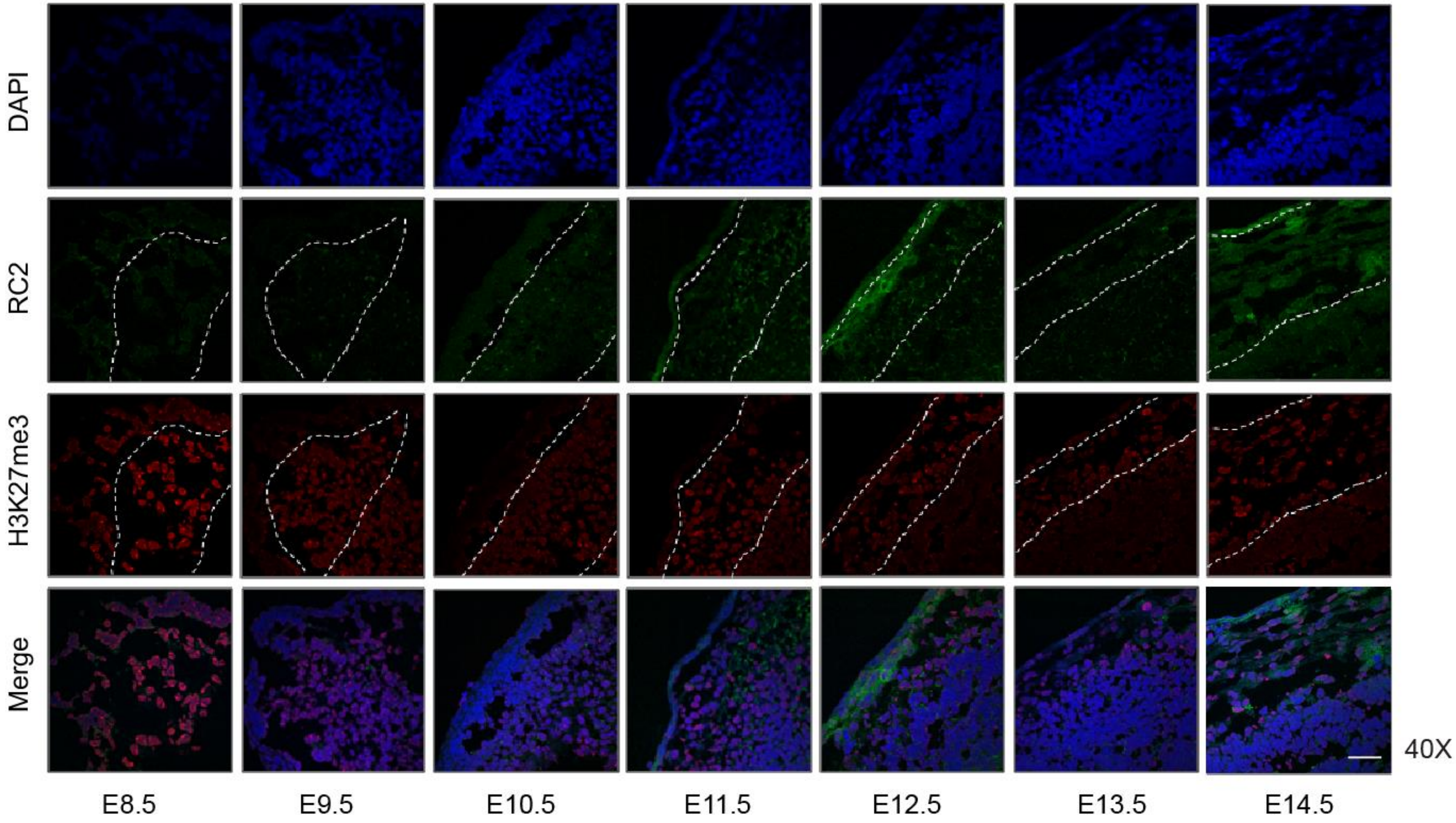

Figure 5.3: H3K27me3 immunostaining in E8.5 to E14.5 mouse embryonic brain neocortical tissues in whole embryo cryosections. First row: nuclear DNA counterstained with DAPI (blue). Second row: primary RC2 antibody against nestin (green). Third row: primary antibody against H3K27me3 (red). Fourth row: merged images of DAPI, nestin and H3K27me3. Columns 1 to 7: representative mouse embryonic brain neocortical tissue cryosections at stages from E8.5 to E14.5. Areas within the dashed lines represent neocortical tissues. Images were obtained using a confocal microscope with a 40X oil-immersion objective lens. Scale bar indicates 40 µm.

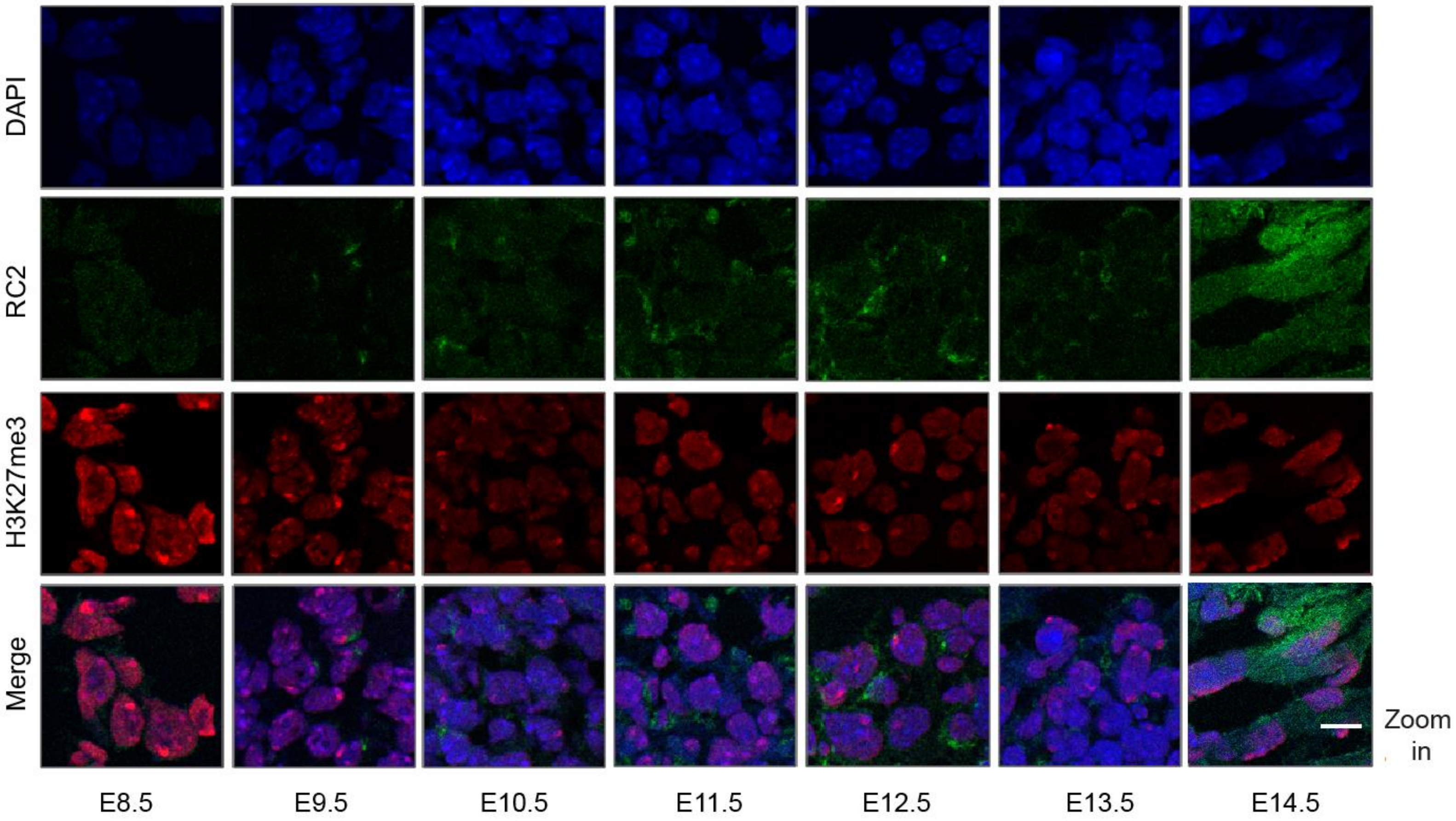

Figure 5.4: H3K27me3 immunostaining in E8.5 to E14.5 mouse embryonic brain neocortical cell nuclei. First row: nuclear DNA counterstained with DAPI (blue). Second row: primary RC2 antibody against nestin (green). Third row: primary antibody against H3K27me3 (red). Fourth row: merged images of DAPI, nestin and H3K27me3. Columns 1 to 7: representative mouse embryonic brain neocortical cell nuclei at stages from E8.5 to E14.5. The confocal images were obtained by zooming into areas within the dashed lines shown in Figure 5.3. Scale bar indicates 10 µm.

5.2.3 Dynamics of H3K9me3 during embryonic heart development in mouse

To further elucidate the relationship between H3K9me3 and 5mC, immunofluorescence detection of H3K9me3 was performed on cryosections of mouse embryonic heart. The dynamic nuclear organisation of H3K9me3 in the developing heart is shown in **Figure 5.5**. H3K9me3 is found at extremely high levels at E8.5. The levels of H3K9me3 then begin to decrease gradually between E9.5 to E11.5, reaching their lowest at E12.5. H3K9me3 is subsequently found to remain stable at very low levels until E14.5 **(Figure 5.6 - H3K9me3)**. These observations suggested that H3K9me3 during early heart development exhibited much more dynamics than in embryonic brain neocortex. Furthermore, confocal microscopy images also show significant enrichment of H3K9me3 signals in transcriptionally inactive heterochromatic regions.

Anti-cTnT antibody was used in this immunofluorescence experiment as a cardiac-specific marker. All embryonic stages show detectable fluorescence signals of cTnT except for E8.5 and E9.5, no apparent cTnT signals were observed **(Figure 5.6 - cTnT)**. The dynamic change pattern of H3K9me3 was examined closely at regions with high levels of cTnT staining.

The dynamic nuclear changes in H3K9 trimethylation during embryonic heart development correlated the best with the dynamics of 5mC observed in Chapter 4. These results further confirmed the strong correlation between H3K9me3 and 5mC.

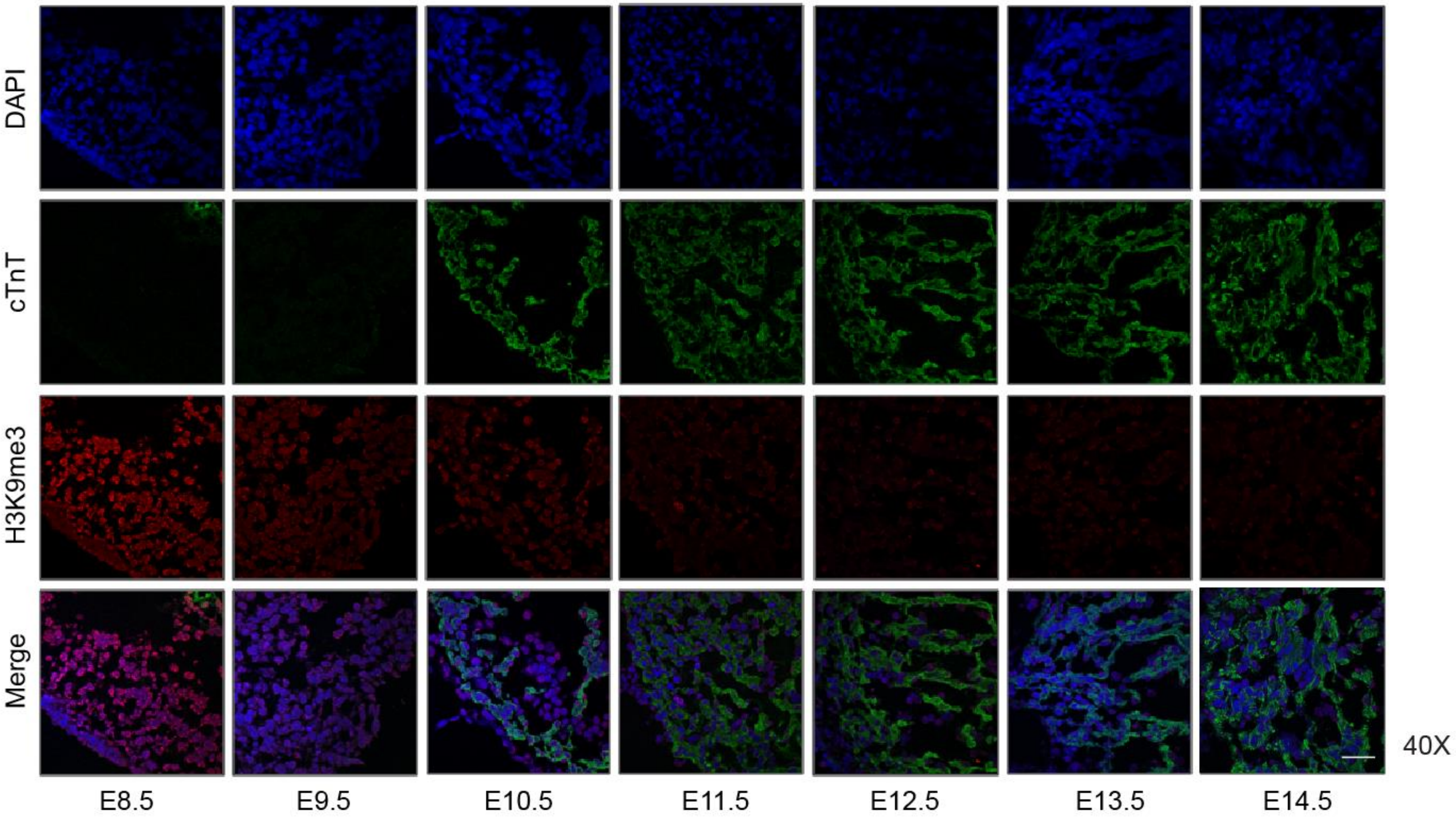

Figure 5.5: H3K9me3 immunostaining in E8.5 to E14.5 mouse embryonic heart tissues in whole embryo cryosections. First row: nuclear DNA counterstained with DAPI (blue). Second row: primary antibody against cTnT (green). Third row: primary antibody against H3K9me3 (red). Fourth row: merged images of DAPI, cTnT and H3K9me3. Columns 1 to 7: representative mouse embryonic heart tissue cryosections at stages from E8.5 to E14.5. Images were obtained using a confocal microscope with a 40X oil-immersion objective lens. Scale bar indicates 40 µm.

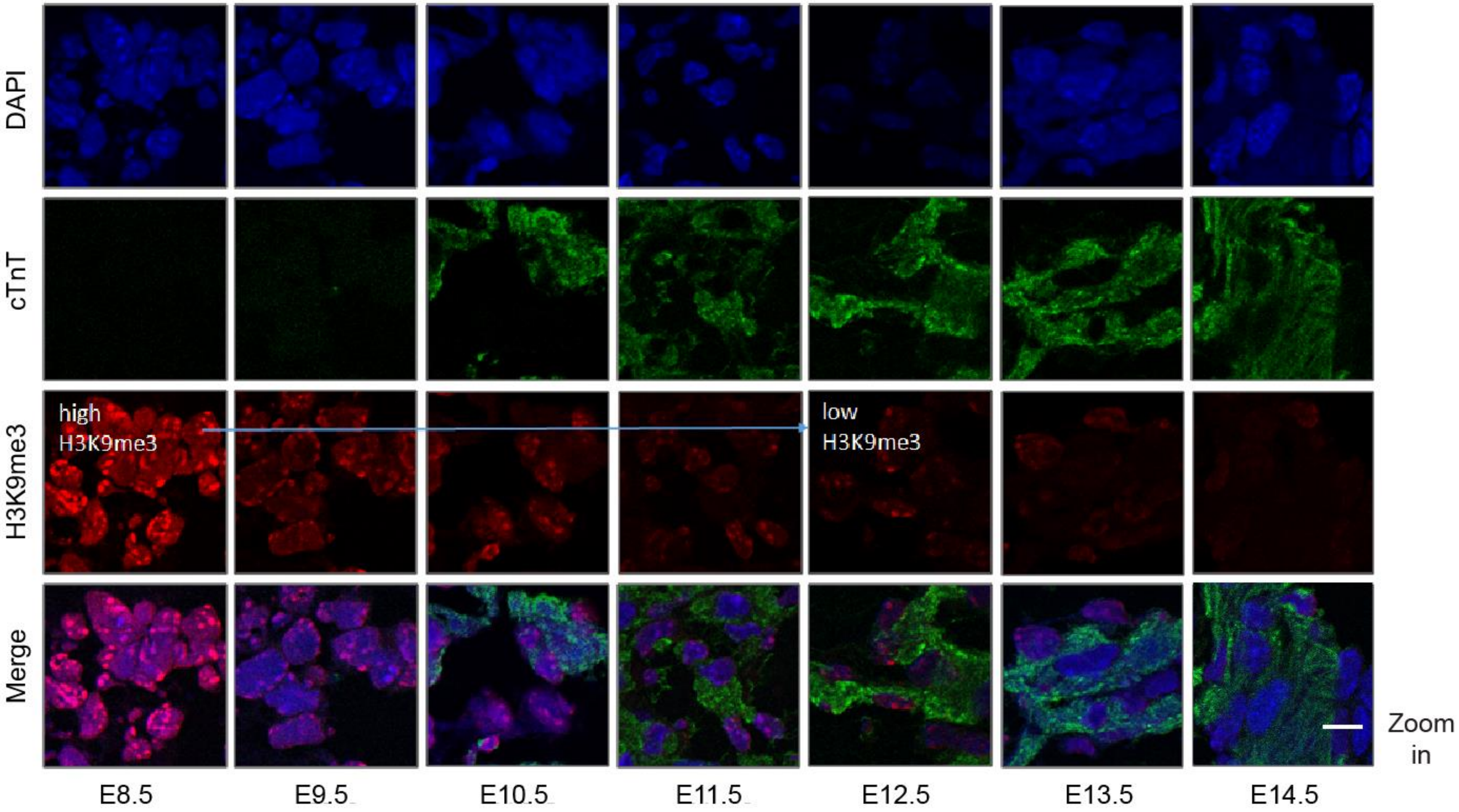

Figure 5.6: H3K9me3 immunostaining in E8.5 to E14.5 mouse embryonic heart cell nuclei. First row: nuclear DNA counterstained with DAPI (blue). Second row: primary antibody against cTnT (green). Third row: primary antibody against H3K9me3 (red). Fourth row: merged images of DAPI, cTnT and H3K9me3. Columns 1 to 7: representative mouse embryonic heart cell nuclei at stages from E8.5 to E14.5. The confocal images were obtained by zooming into the images shown in Figure 5.5. Scale bar indicates 10 µm.

5.2.4 Dynamics of H3K27me3 during embryonic heart development in mouse

The connection between H3K27me3 and 5mC was further explored in other mouse embryonic tissue in order to confirm the existence of crosstalk among different epigenetic pathways. As shown in **Figure 5.7**, the dynamic changes of H3K27me3 status in the developing heart follow the same pattern as H3K9me3. Representative confocal images show that at E8.5, H3K27me3 displays very high levels of detection. The subsequent decline in H3K27me3 levels was observed between E9.5 to E12.5. Following the decrease, H3K27me3 then stays constant at its lowest level until E14.5 **(Figure 5.8 - H3K27me3)**. These results clearly suggested that H3K27me3 in cardiomyocytes showed more dynamic behavior than neocortex during early embryonic brain development. The images also show the presence of an inactive X-associated H3K27me3-rich patch inside each of the female nuclei.

For cTnT staining, the signals are detected at all stages of embryonic development, except for E8.5 and E9.5, no detectable fluorescence signals were observed **(Figure 5.8 - cTnT)**. Changes in H3K27me3 distribution were observed within regions of cTnT-positive cardiomyocytes.

Again, a remarkable correlation was found among dynamic changes of H3K27me3, H3K9me3 and 5mC, pointing to a potential functional link between these three transcription-repressive marks during embryonic heart development.

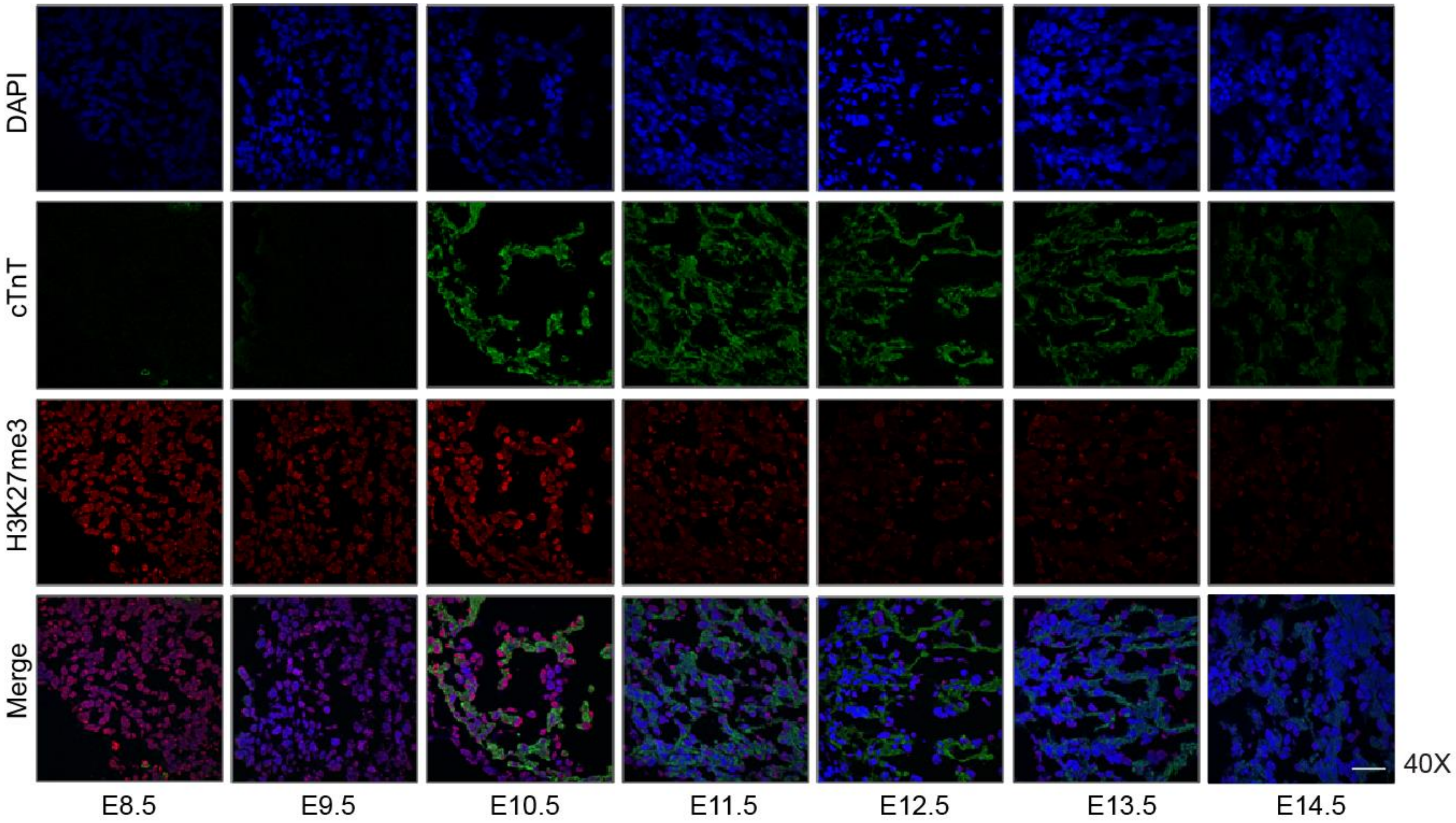

Figure 5.7: H3K27me3 immunostaining in E8.5 to E14.5 mouse embryonic heart tissues in whole embryo cryosections. First row: nuclear DNA counterstained with DAPI (blue). Second row: primary antibody against cTnT (green). Third row: primary antibody against H3K27me3 (red). Fourth row: merged images of DAPI, cTnT and H3K27me3. Columns 1 to 7: representative mouse embryonic heart tissue cryosections at stages from E8.5 to E14.5. Images were obtained using a confocal microscope with a 40X oil-immersion objective lens. Scale bar indicates 40 µm.

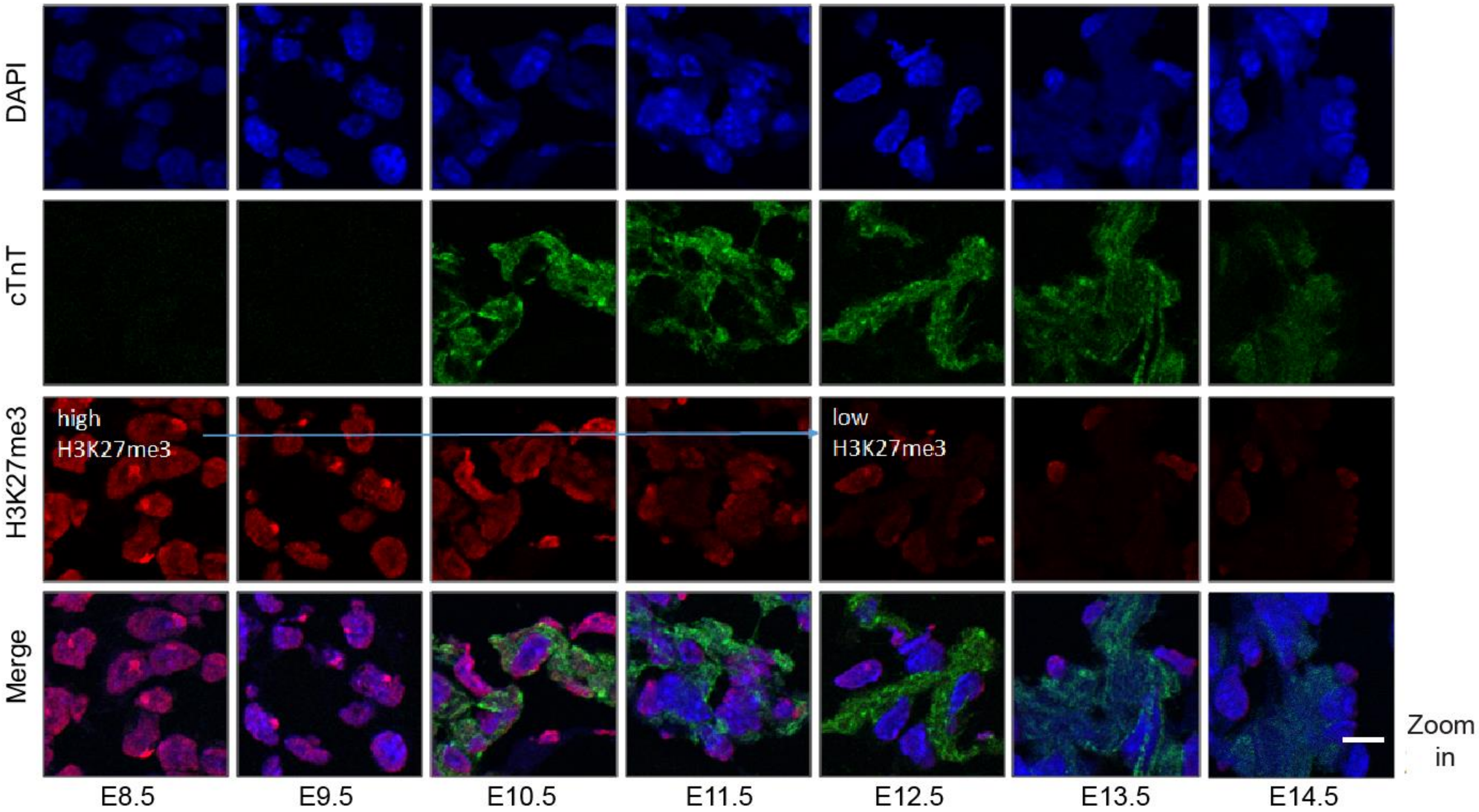

Figure 5.8: H3K27me3 immunostaining in E8.5 to E14.5 mouse embryonic heart cell nuclei. First row: nuclear DNA counterstained with DAPI (blue). Second row: primary antibody against cTnT (green). Third row: primary antibody against H3K27me3 (red). Fourth row: merged images of DAPI, cTnT and H3K27me3. Columns 1 to 7: representative mouse embryonic heart cell nuclei at stages from E8.5 to E14.5. The confocal images were obtained by zooming into the images shown in Figure 5.7. Scale bar indicates 10 µm.

5.2.5 Quantification of H3K9me3 staining patterns in heart

Figure 5.9 shows the quantification of H3K9me3 signals in individual nuclei in E9.5 mouse embryonic whole heart, and E14.5 heart where trabecular and compact myocardium have differentiated. For heart trabecular nuclei, the levels of H3K9me3 show an apparent decrease between E9.5 and E14.5. For heart compact myocardium, the levels between E9.5 and E14.5 show a stronger decrease compared to the trabeculae, which contain cells originating in the compact myocardium.

Overall, semi-quantificative analysis of H3K9me3 displayed good consistency with immunostaining results but additionally revealed a relative difference in H3K9me3 loss, which appears more marked in compact myocardium than in the trabeculae.

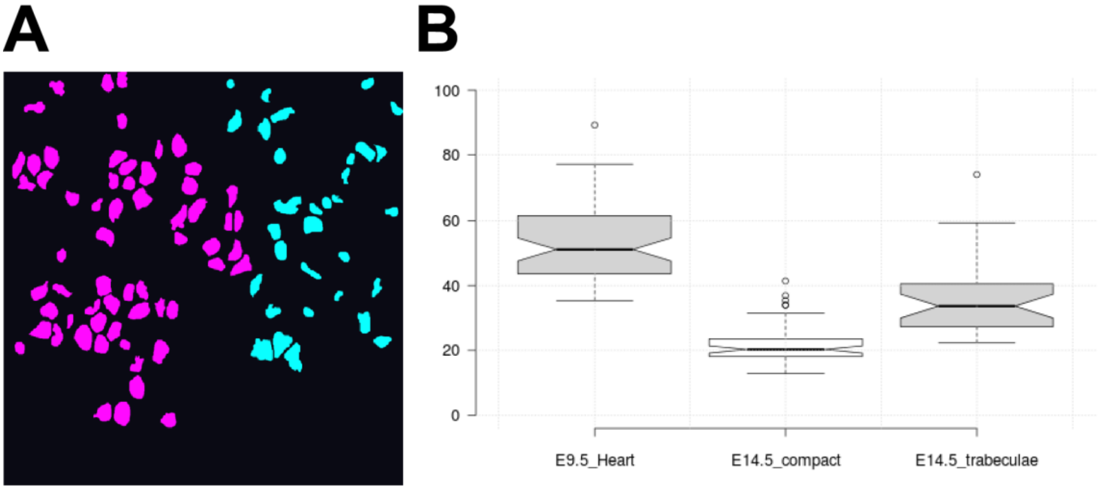

Figure 5.9: Quantification of the H3K9me3 staining patterns in E9.5 and E14.5 mouse embryonic heart cell nuclei. (A) E14.5 nuclei traced for trabecular (blue), compact (pink) myocardium **(B)** A notched boxplot showing the results of quantification of H3K9me3 signals in mouse embryonic whole heart at E9.5 and compact and trabecular myocardium at E14.5. Box plots represent medians (thick horizontal lines within boxes), interquartile ranges (IQRs), and ranges (excluding only values greater than ±1.58 times the IQR; outliers beyond this range are shown by individual open circles). The notches in the boxes are calculated as ±1.58 times IQR/√*n*, which correspond approximately to a 95% confidence interval.

5.3 Discussion

This chapter aimed to observe dynamic nuclear changes in H3K9me3 and H3K27me3 states during brain neocortical and heart development. The obtained data were subsequently used for comparative analysis with 5mC results in order to explore the correlation between these three epigenetic marks. H3K9me3 and H3K27me3 are markers for constitutive and facultative heterochromatin, respectively, and could report on the developmental dynamics of these heterochromatin compartments more specifically than 5mC alone. Standard histone immunohistochemistry protocol was used for detecting those histone markers.

5.3.1 H3K9me3 and H3K27me3 histone methylation dynamics in developing mouse embryonic tissues

The standardized staining procedure used for detecting H3K9me3 and H3K27me3 revealed interesting dynamic observations relating to both markers in the developing neocortex and heart. This analysis of the distribution patterns of H3K9me3 and H3K27me3 during neocortical development potentially discovered the existence of an interplay between these two marks. A similar result was obtained in the developing heart, where the levels of H3K9me3 and H3K27me3 displayed almost identical trends, further supporting this relationship. These observations clearly suggested a correlation that could signify possible mechanistic crosstalk between these two heterochromatin-related histone marks. For instance, H3K9me3 and H3K27me3 may function as a team to establish higher order chromatin structure across the nucleus. The obtained data are in excellent agreement with the growing body of histone literature reporting the complex connections between these two histone marks (Mozzetta et al., 2014; Sabbattini et al., 2014; Zhang et al., 2015).

Furthermore, the distribution patterns of H3K9me3 and H3K27me3 in the developing neocortex were far less dynamic than in the developing heart. Possible functional interplay between H3K9me3 and H3K27me3 mechanisms could be to ensure maintenance of heterochromatin and epigenetic gene silencing during early neocortical development. These findings are in line with previous research suggesting that H3K27me3 contributes to maintaining the undifferentiated state of neural progenitor cells (Pereira et al., 2010). The pattern of H3K9me3 distribution in the developing neocortex was found to be in good agreement with Western blot analysis that demonstrated stable level of H3K9me3 in the developing mouse brain, although the analysis was not done particularly in neocortex (Bártová et al., 2016). On the contrary, heart showed more dynamic behaviour of H3K9me3 and H3K27me3 than neocortex during early mouse development. The nuclear organisation in heart as revealed by the dynamic distributions of H3K9me3 and H3K27me3 raises the question whether it is crucial for proper heart function and formation. Moreover, chromatin organisation could also be necessary for cell differentiation and cell proliferation.

Constitutive heterochromatin, which is found predominantly at the pericentromeric regions of chromosomes is marked by H3K9me3 (Jamieson et al., 2016). Consistent with previous observations, detailed confocal microscopic analysis showed that H3K9me3 was highly enriched at the chromatin-dense chromocenters. Facultative heterochromatin, on the other hand, which is represented by X chromosome inactivation, is marked by H3K27me3 (Degl’Innocenti and D’Errico, 2017; Saksouk et al., 2014). In keeping with previous reports, H3K27me3 was indeed enriched on this facultative heterochromatin in female cells.

5.3.2 The relationship between DNA methylation and histone lysine methylation

Comparisons between DNA methylation and histone lysine methylation (H3K9me3 and H3K27me3) based on their distribution patterns in the developing neocortex and heart revealed a remarkably close relationship between these three epigenetic marks. This present study observed clear correlations in support of a functional crosstalk between the three major epigenetic repressive machineries. These three representatives of hetero- or inaccessible chromatin may establish cooperation to ensure transcription at specific genes is repressed for normal embryonic development.

HP1 proteins, which preferentially bind H3K9me3, play a key role in promoting the formation of highly condensed heterochromatin structures (Muramatsu et al., 2016). Interestingly, these proteins have been shown to interact and recruit DNMTs, providing a direct link to the interplay between H3K9me3 and DNA methylation (Hirabayashi and Gotoh, 2010; Lehnertz et al., 2003; Saksouk et al., 2015). In a similar fashion, PRC2 complex, which catalyses trimethylation of H3K27, has also been demonstrated to interact with all three DNMTs (Mohammad et al., 2009; Viré et al., 2006; Zhang et al., 2016b). Remarkably, another recent study has revealed the existence of a cooperation between HP1 and PRC2 complex, further confirming the tight correlation between the three repressive epigenetic markers (Boros et al., 2014). Taken together, the results we have newly observed in developing embryonic tissues indicate that repressive epigenetic systems may indeed be working together as part of a concerted transcriptional gene silencing mechanism during development.

Chapter 6 – Visualisation of DNA methylation using transgenic MBD-GFP mice

6.1 Introduction

Genetic engineering, also known as genetic modification or GM, involves taking a specific gene from one organism and incorporating it into a completely unrelated organism (Sadelain et al., 2012). Such inserted gene is called a transgene and the organism that is created by genetic manipulation techniques is referred to as a transgenic or genetically modified organism (GMO) (Scharfenberger et al., 2014). Researchers have employed the application of transgenes to study the development and function of proteins in organisms (Rongvaux et al., 2014). Furthermore, the introduction of foreign DNA, a process known as transgenesis, could potentially result in a phenotypic change in an individual organism (Kim et al., 2016).

A wide range of transgenic animals has been successfully generated for a variety of purposes. Examples of animal species include mice (Maeda et al., 2016), zebrafish (Kawakami et al., 2016), frogs (Takagi et al., 2013) and rabbits (Lang et al., 2016). Nevertheless, genetically modified mice are by far the most routinely used to study gene transfer (Doyle et al., 2012). This is because they are relatively inexpensive, easily housed and maintained, breed well and are convenient due to their small size (Kumar et al., 2009). Importantly, the mouse genome was sequenced early on and proves to be easily manipulated by transgenic technology (Haruyama et al., 2009). The application of this technique of gene transfer to early developing embryos has allowed researchers to produce more appropriate and reliable animal models for studying human development, diseases, and disorders (Cho et al., 2009).

A reporter or marker gene is a gene that is commonly used as an indicator to elucidate transgenic events. For instance, the reporter gene can be employed to visually detect the activity of a specific gene in tissues (Vacaru et al., 2014). One of the most frequently used reporter gene for transgenic research is Green Fluorescent Protein (GFP) (Chudakov et al., 2010; Moore et al., 2012). Transgenic mice expressing fluorescent proteins have become ideal tools for monitoring protein distribution and expression as well as dynamic cellular events by microscopy (Besser et al., 2015; Ueda et al., 2014).

One of the main current techniques available for studying DNA methylation is immunohistochemistry. However, in the case of immunohistochemistry, the intact structure of chromatin is destroyed by the heat treatment that is required in the optimised protocol for the successful binding of anti-5mC antibody to methylated DNA. Apart from immunohistochemistry technique, there is no appropriate method to visualise the dynamics of DNA methylation status in living cells or, particularly, in organisms.

Thus, to track and detect the dynamic changes in 5mC during development, part of this study's design relied on transgenic MBD-GFP mice to visualise DNA methylation in live cells and tissues. Embryos carrying a GFP fusion with a CpG methyl-binding domain (Human MBD1) were derived from transgenic mice generated by the lab and the collaborating lab prior to this study. MBD1 preferentially binds to methylated DNA at CpG sites. This transgenic line expresses a GFP-MBD fusion protein driven by a ubiquitous promoter of the CAG type. In this model, the injected transgene was integrated randomly into the genome. In addition, GFP reporter system used in this study allowed direct GFP fluorescence visualisation without the need to add exogenous substrates or cofactors for detection. Thus, the dynamic expression patterns of proteins can be followed in live embryos as well as whole organisms. Transgenic primary fibroblasts and cardiomyocytes from E13.5 – E14.5 embryos had been characterised *in vitro* in the lab, but the reporter fusion had not been characterised as a marker for MBD1 and its binding to 5mC during development, and therefore transgenic embryos were used in this experiment.

Therefore, the aims of this chapter were:

1. To investigate tissues undergoing dynamic nuclear changes in the state of 5mC during development from E10.5 to E14.5 in MBD-GFP mouse whole embryonic stages.

2. To investigate the correlation between the MBD-GFP results observed in transgenic mice and the 5mC results obtained in wild-type.

3. To characterise the transgenic MBD-GFP mouse.

6.2 Results

Native MBD-GFP protein signal was visible in primary cell cultures but was sensitive to the cryosection protocol. The signal was therefore amplified by immunostaining for GFP in order to characterise its expression during development. Immunostaining of whole mouse embryo cryosections at stages from E10.5 to E14.5 for MBD-GFP protein expression revealed the distribution of MBD-GFP **(Figure 6.1, 6.2, 6.3, 6.4 and 6.5)**. The highest levels of GFP expression were detected in heart, liver, brain and neural tube. However, no apparent developmental dynamics of GFP were observed. All four tissues displayed uniform levels of high GFP throughout embryonic development **(Figure 6.6, 6.7, 6.8, 6.9 - GFP)**.

Furthermore, the fluorescence images also show that in cell nuclei, the GFP signals are predominantly concentrated in the areas of intense DAPI which represent transcriptionally inactive heterochromatin. MBD-GFP nuclear distribution pattern was well correlated with patterns of 5mC nuclear distribution discussed in Chapter 4. The correlation between MBD-GFP and 5mC marks was also investigated at great length in Chapter 3, which showed detectable overlapping of intense GFP and 5mC signals in heterochromatin regions. However, developmental changes between MBD-GFP levels and the levels of 5mC states were not in agreement. These observations therefore throw doubt on whether the transgenic MBD-GFP mouse can prove to be a beneficial tool for visualisation of comparative DNA methylation levels in live tissues during development.

In addition, bright fluorescent signals of GFP in brain and neural tube demonstrated colocalisation with nestin-expressing cells **(Figure 6.8, 6.9 – RC2)**, suggesting that high 5mC contents in both tissues were associated with neural progenitor cells.

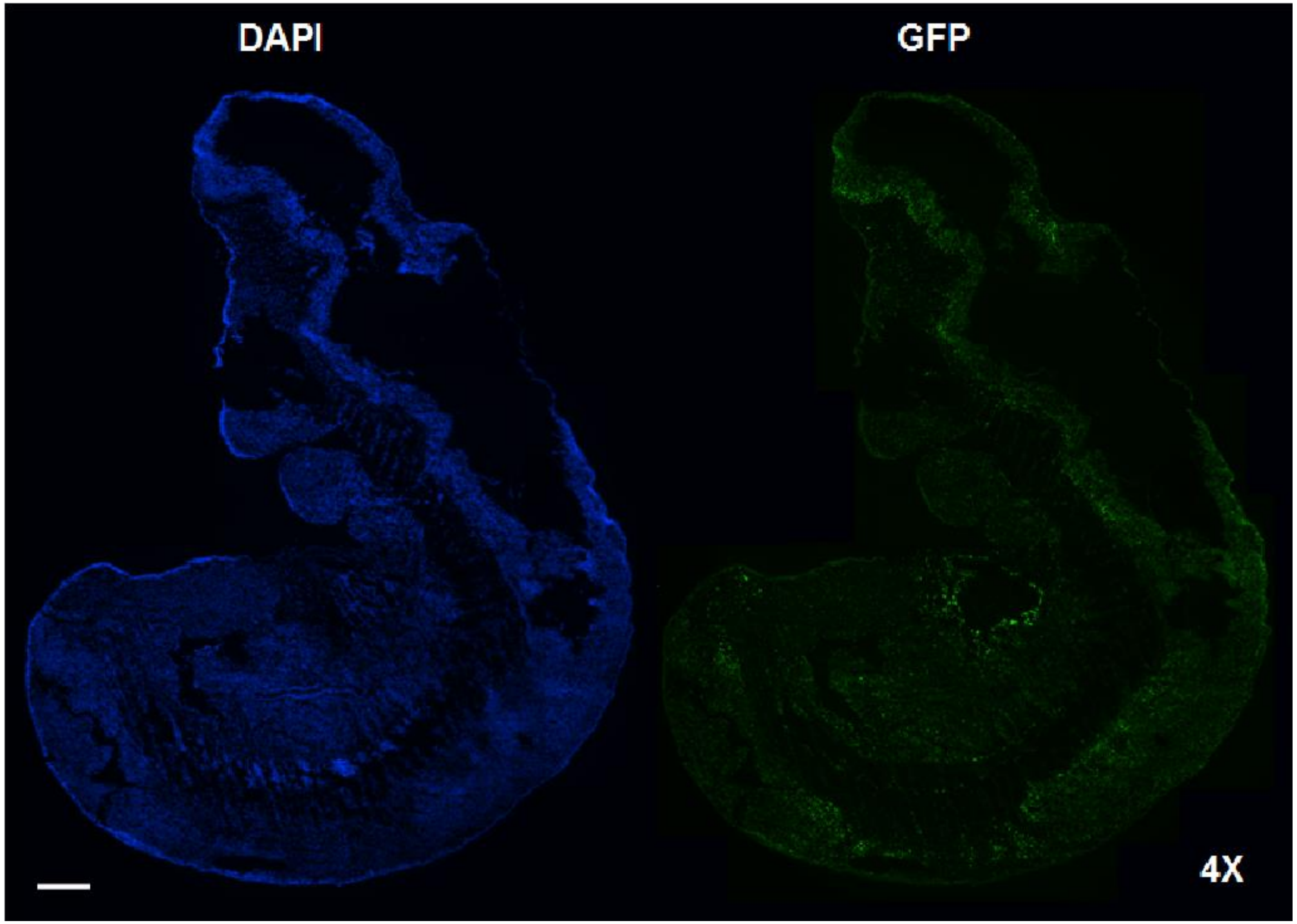

Figure 6.1: Immunostaining of whole mouse embryo cryosections at E10.5 for MBD-GFP protein expression. The representative mosaic fluorescent images of whole embryo cryosections are shown. Left image: nuclear DNA counterstained with DAPI (blue). Right image: antibody against GFP (green). Images were obtained using a fluorescence microscope with a 4X objective lens. High GFP fluorescence intensities are observed in heart, liver, brain and neural tube regions. Scale bar indicates 40 µm.

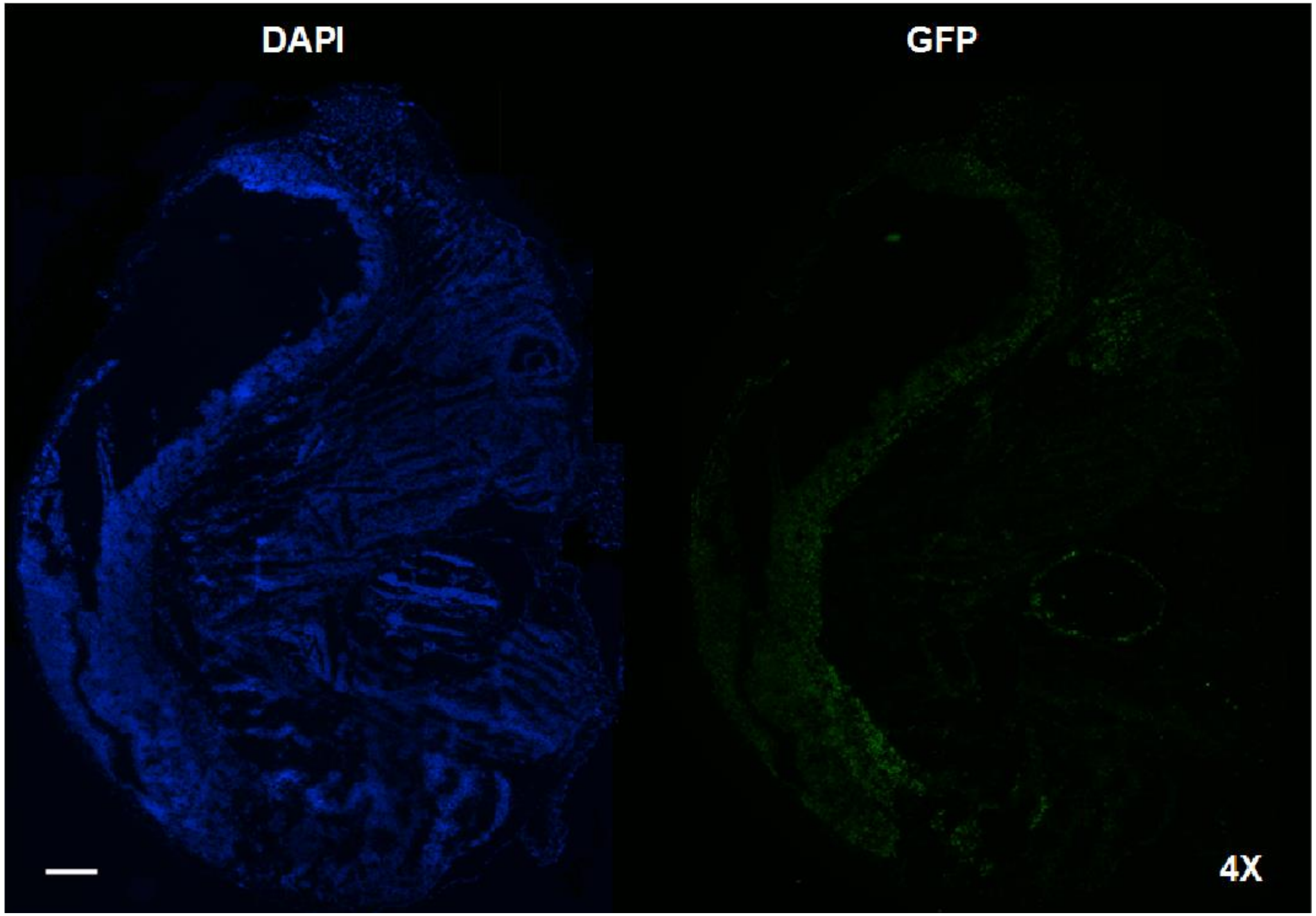

Figure 6.2: Immunostaining of whole mouse embryo cryosections at E11.5 for MBD-GFP protein expression. The representative mosaic fluorescent images of whole embryo cryosections are shown. Left image: nuclear DNA counterstained with DAPI (blue). Right image: antibody against GFP (green). Images were obtained using a fluorescence microscope with a 4X objective lens. High GFP signals are detected in heart, liver, brain and neural tube areas. Scale bar indicates 40 µm.

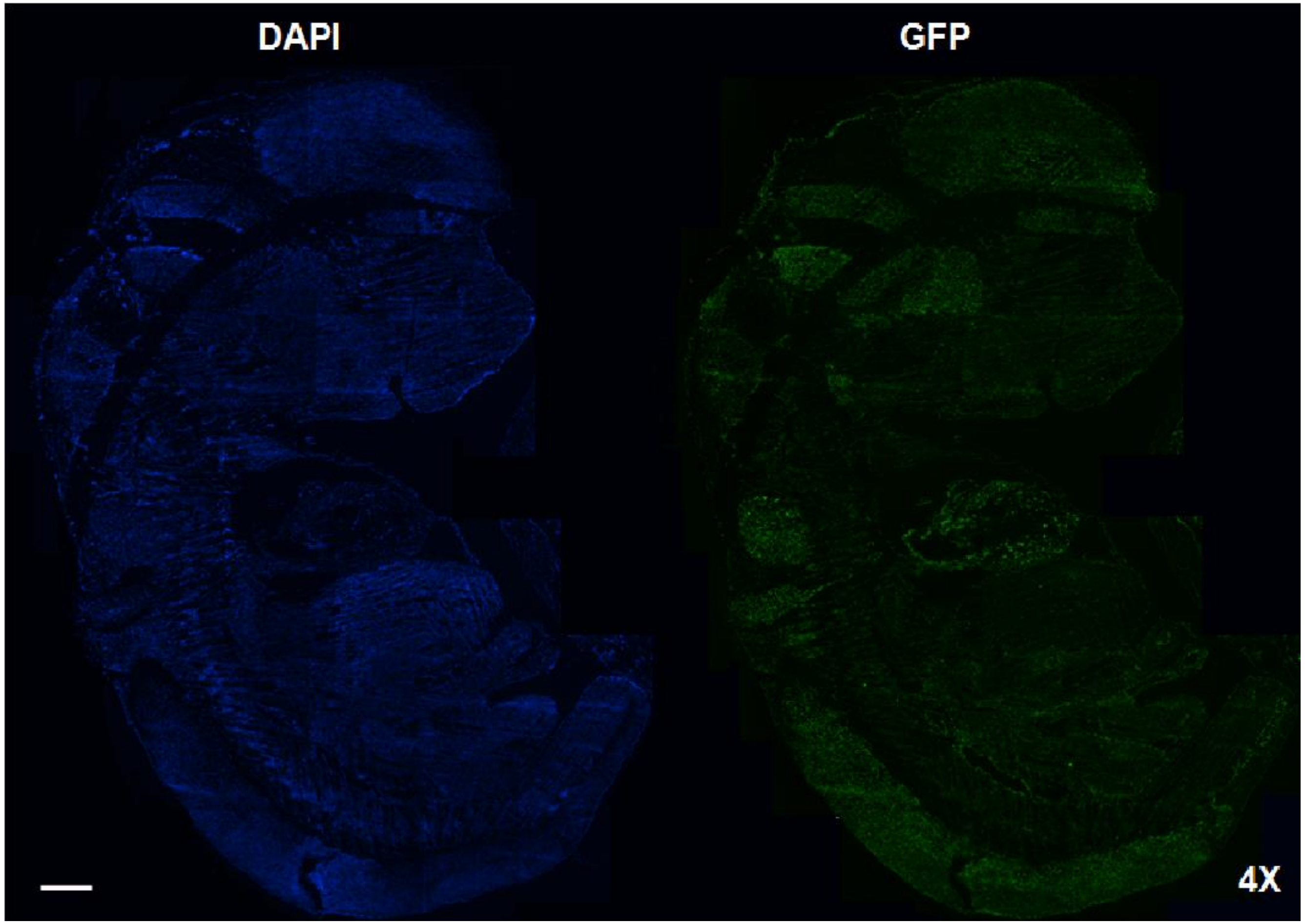

Figure 6.3: Immunostaining of whole mouse embryo cryosections at E12.5 for MBD-GFP protein expression. The representative mosaic fluorescent images of whole embryo cryosections are shown. Left image: nuclear DNA counterstained with DAPI (blue). Right image: antibody against GFP (green). Images were obtained using a fluorescence microscope with a 4X objective lens. Heart, liver, brain and neural tube exhibit high levels of GFP expression. Scale bar indicates 40 µm.

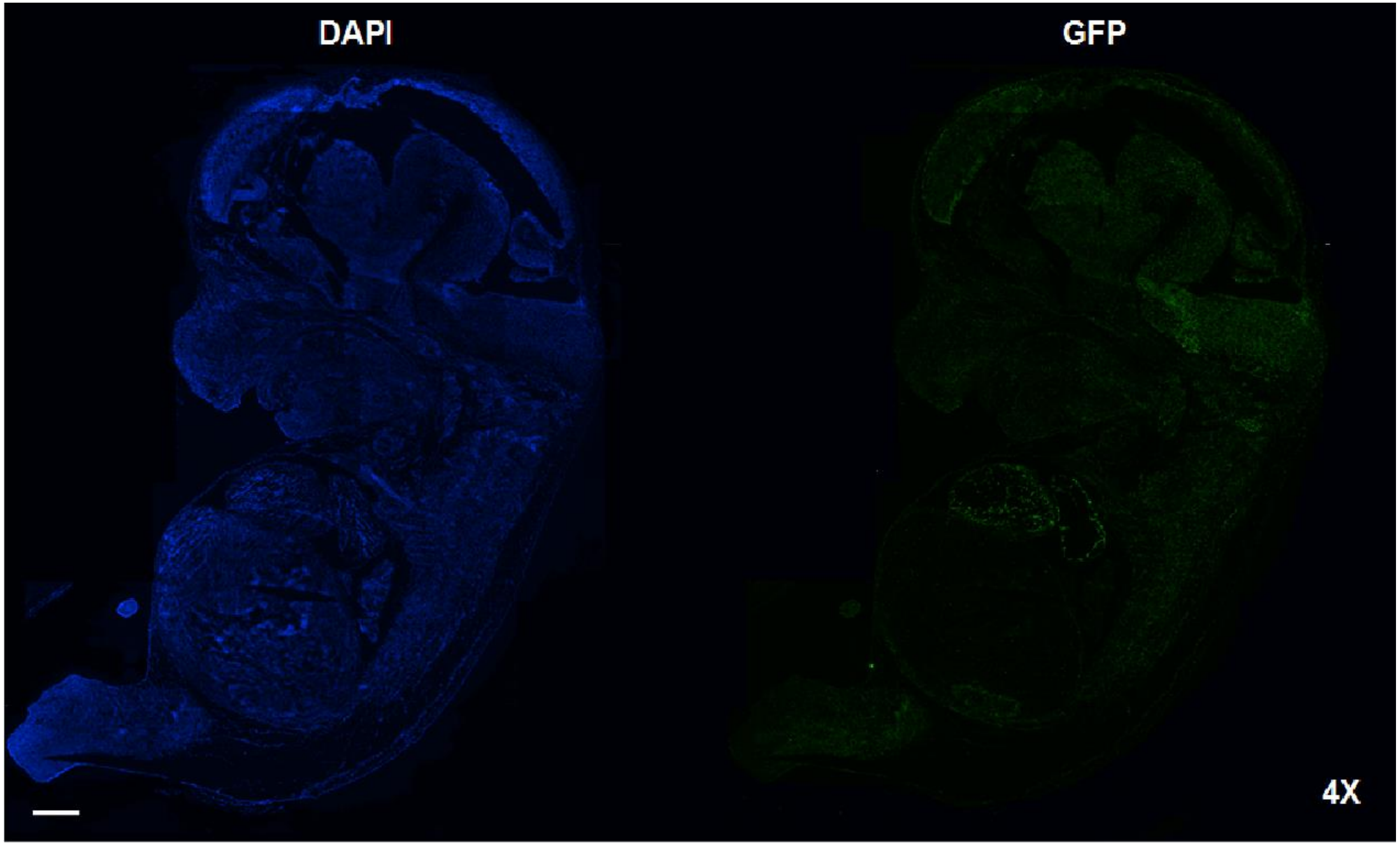

Figure 6.4: Immunostaining of whole mouse embryo cryosections at E13.5 for MBD-GFP protein expression. The representative mosaic fluorescent images of whole embryo cryosections are shown. Left image: nuclear DNA counterstained with DAPI (blue). Right image: antibody against GFP (green). Images were obtained using a fluorescence microscope with a 4X objective lens. Strong GFP fluorescence signals are observed in the regions of heart, liver, brain and neural tube. Scale bar indicates 40 µm.

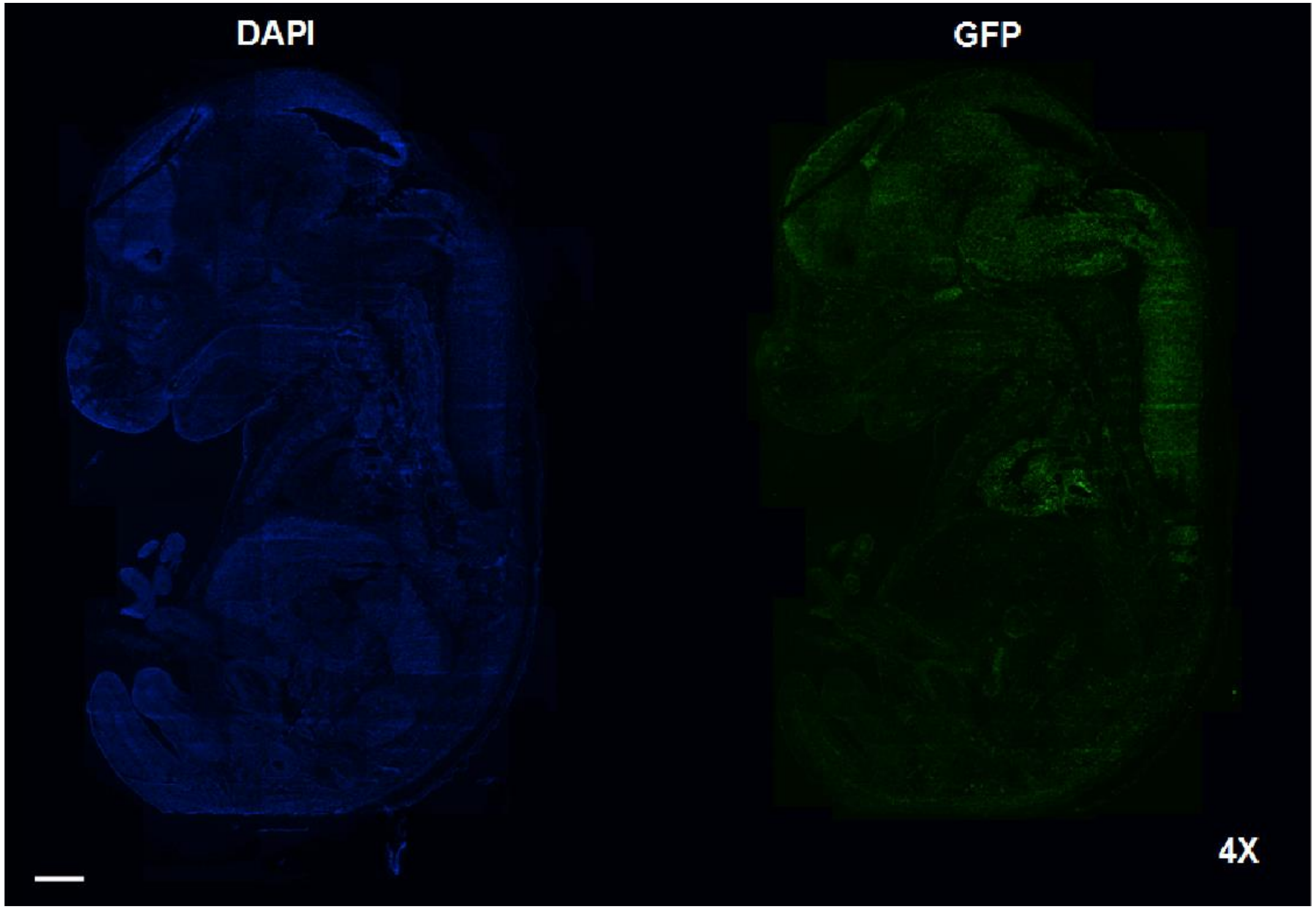

Figure 6.5: Immunostaining of whole mouse embryo cryosections at E14.5 for MBD-GFP protein expression. The representative mosaic fluorescent images of whole embryo cryosections are shown. Left image: nuclear DNA counterstained with DAPI (blue). Right image: antibody against GFP (green). Images were obtained using a fluorescence microscope with a 4X objective lens. GFP is expressed at high levels in heart, liver, brain and neural tube. Scale bar indicates 40 µm.

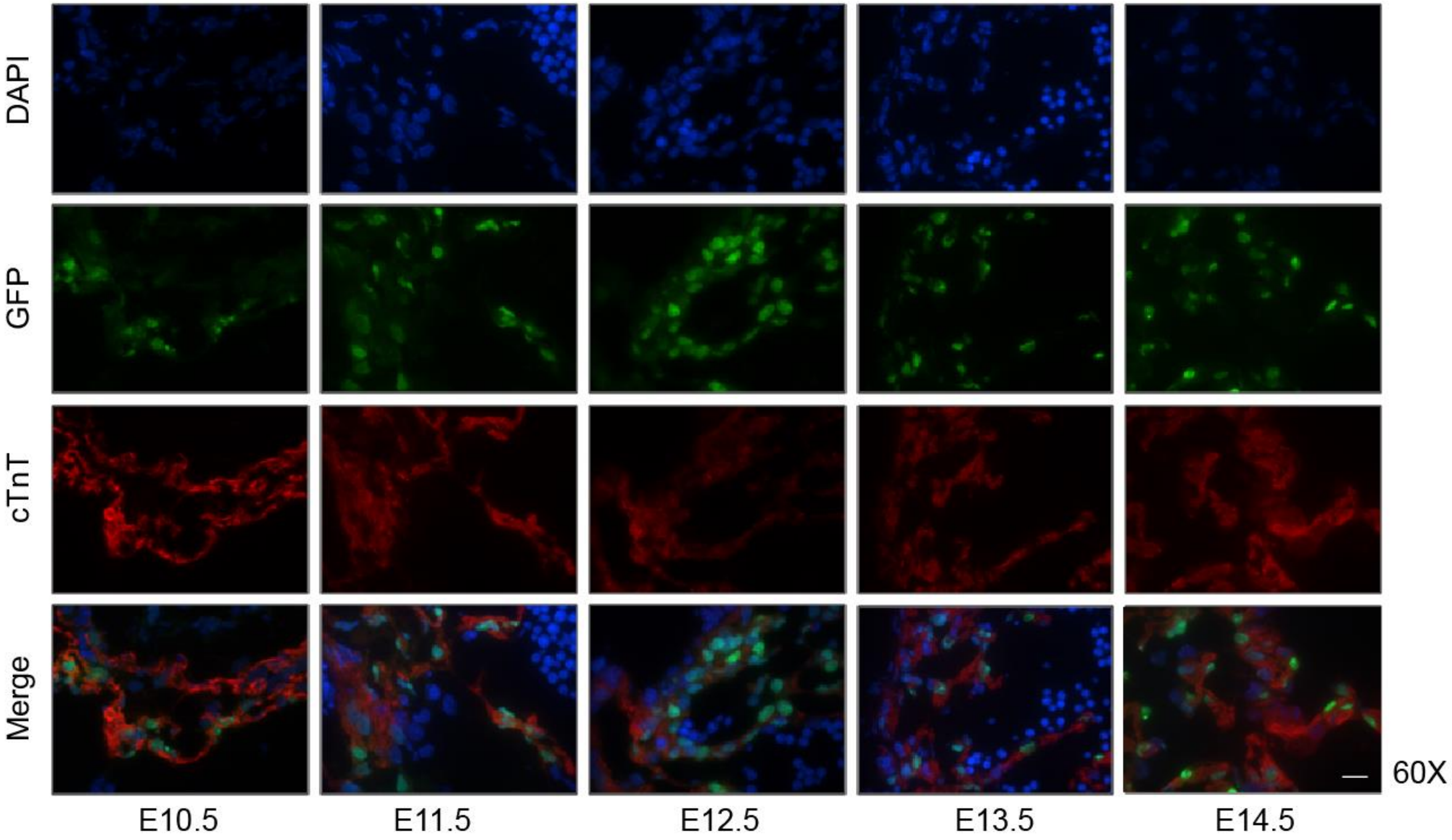

Figure 6.6: GFP immunostaining in E10.5 to E14.5 mouse embryonic heart cell nuclei. First row: nuclear DNA counterstained with DAPI (blue). Second row: primary antibody against GFP (green). Third row: antibody against cTnT (red). Fourth row: merged images of DAPI, GFP and cTnT. Columns 1 to 5: representative mouse embryonic heart cell nuclei at stages from E10.5 to E14.5. Images were obtained using a fluorescence microscope with a 60X objective lens. Scale bar indicates 30 µm.

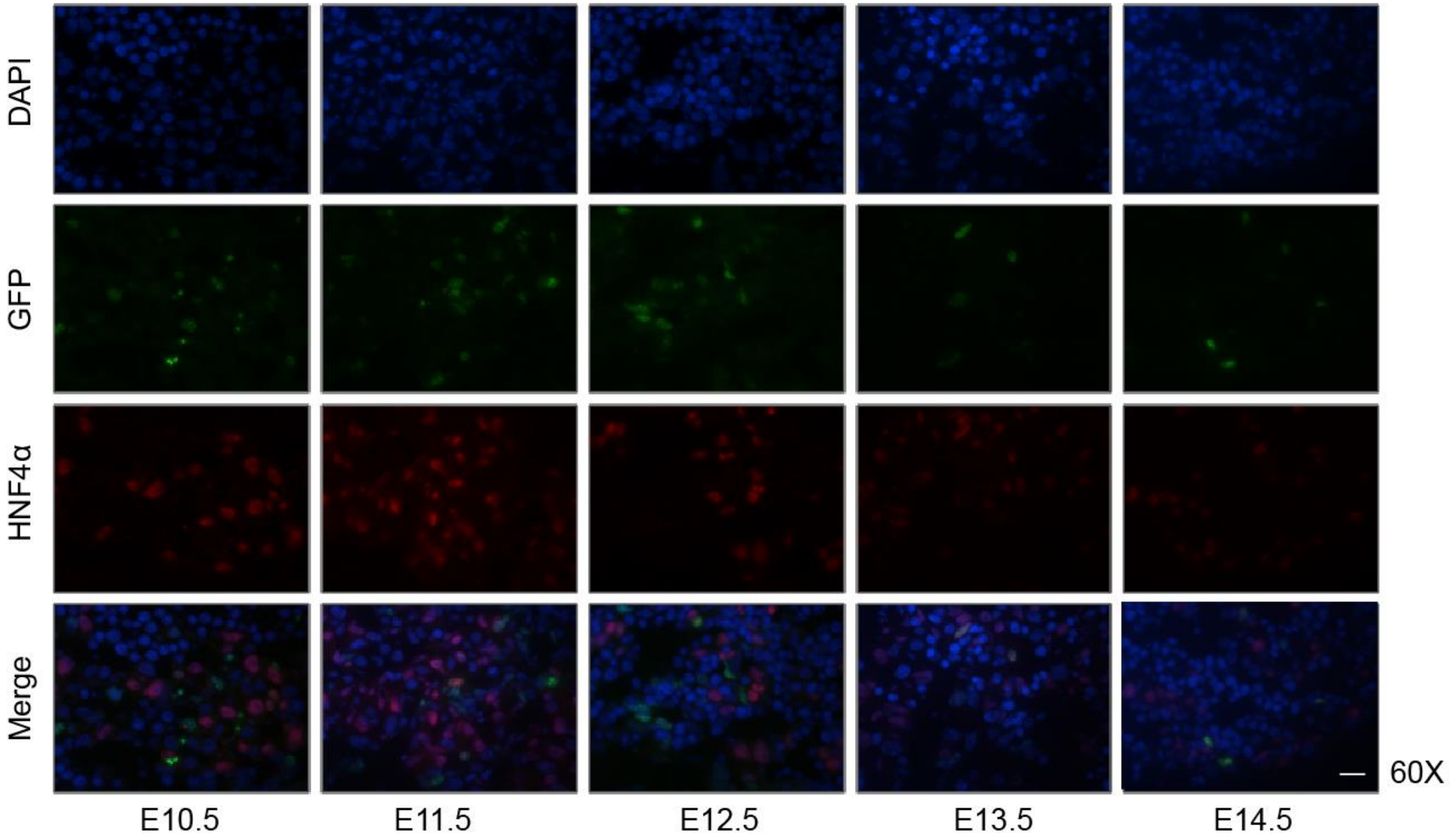

Figure 6.7: GFP immunostaining in E10.5 to E14.5 mouse embryonic liver cell nuclei. First row: nuclear DNA counterstained with DAPI (blue). Second row: primary antibody against GFP (green). Third row: antibody against HNF4α (red). Fourth row: merged images of DAPI, GFP and HNF4α. Columns 1 to 5: representative mouse embryonic liver cell nuclei at stages from E10.5 to E14.5. Images were obtained using a fluorescence microscope with a 60X objective lens. Scale bar indicates 30 μm.

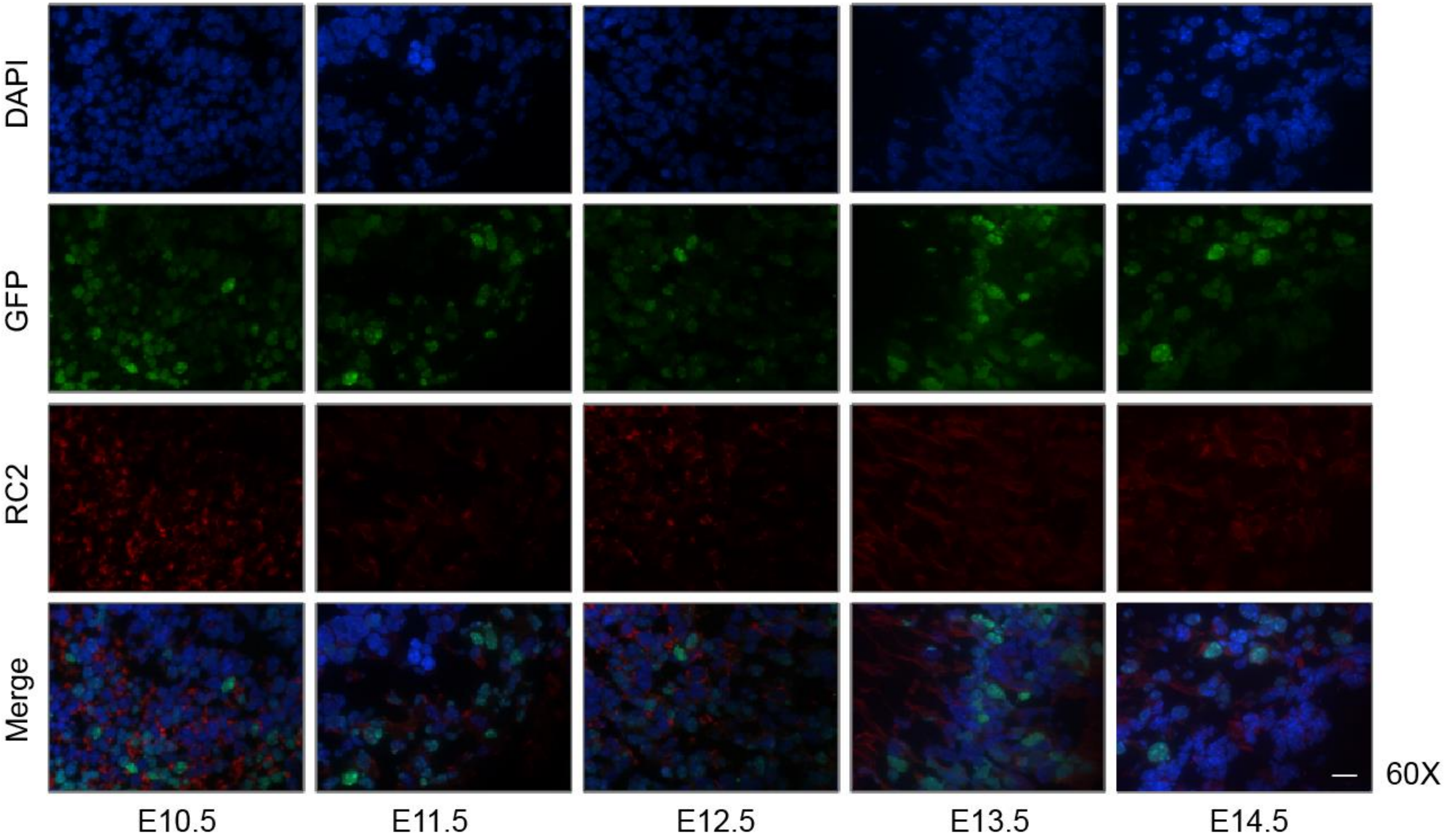

Figure 6.8: GFP immunostaining in E10.5 to E14.5 mouse embryonic brain cell nuclei. First row: nuclear DNA counterstained with DAPI (blue). Second row: primary antibody against GFP (green). Third row: antibody against RC2 (red). Fourth row: merged images of DAPI, GFP and RC2. Columns 1 to 5: representative mouse embryonic brain cell nuclei at stages from E10.5 to E14.5. Images were obtained using a fluorescence microscope with a 60X objective lens. Scale bar indicates 30 µm.

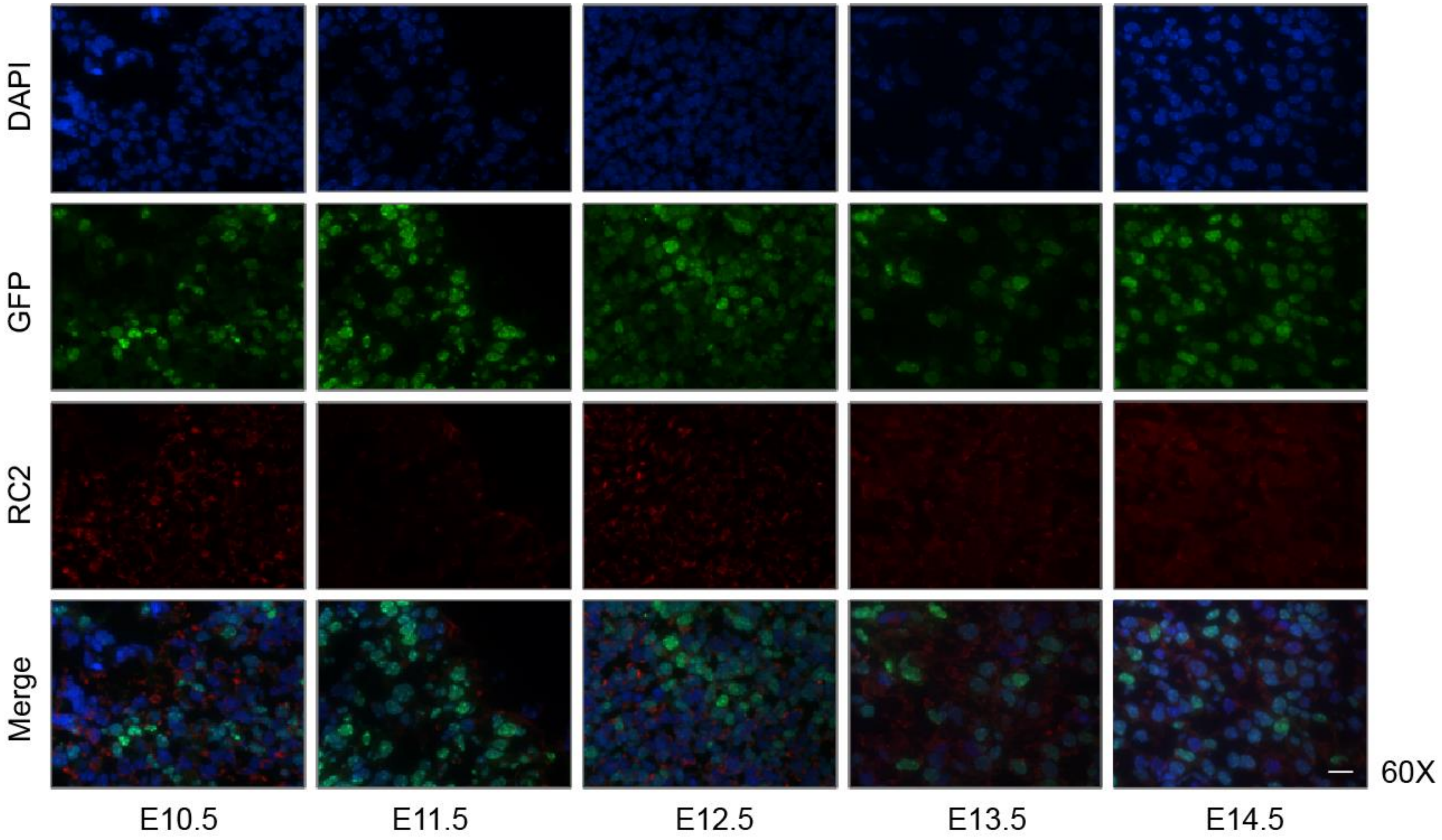

Figure 6.9: GFP immunostaining in E10.5 to E14.5 mouse embryonic neural tube cell nuclei. First row: nuclear DNA counterstained with DAPI (blue). Second row: primary antibody against GFP (green). Third row: antibody against RC2 (red). Fourth row: merged images of DAPI, GFP and RC2. Columns 1 to 5: representative mouse embryonic neural cell nuclei at stages from E10.5 to E14.5. Images were obtained using a fluorescence microscope with a 60X objective lens. Scale bar indicates 30 µm.

6.3 Discussion

This chapter aimed to identify tissues undergoing dynamic nuclear changes in 5mC in developing MBD-GFP mouse embryos. Immunostaining of whole mouse embryo cryosections for MBD-GFP protein expression revealed that no dynamic changes in levels comparable to those seen in 5mC levels were observed in the developing heart, liver, brain and neural tube. Moreover, MBD-GFP results also showed that the 5mC was found to be stable at high level throughout the development of these four tissues. MBD-GFP protein seemed therefore to be expressed in a tissue-specific pattern. The reason for this preferential expression in certain organs is unclear. This could be due to a combination of higher protein expression and lower protein turnover, while cell division rate could additionally influence protein levels. Therefore, the signals observed may not be comparable between tissues.

The localisation of MBD-GFP was also revealed by immunostaining with anti-GFP antibody. In the cell nuclei, GFP signals were found to be mainly located in the dense regions of heterochromatin, proving that the MBD-GFP probe can accurately recognise heterochromatin that contains hypermethylated DNA. Furthermore, the experimental results also suggested that the MBD-GFP probe successfully captured global status of 5mC in living conditions.

The distribution patterns of 5mC observed in transgenic mouse embryos were in keeping with the 5mC distribution patterns observed in Chapter 4. However, the dynamics of 5mC reported through MBD1-GFP binding in transgenic mouse embryos were in contradiction with the 5mC dynamics discovered in Chapter 4. The dynamics of 5mC in the developing heart and liver were compared between wild type and transgenic embryos. As for the brain, the 5mC dynamic result cannot be practically compared because the initial observation of 5mC dynamics in transgenic embryos was not specifically done in neocortex. Overall, this experiment yielded some unexpected results.

In addition, high fluorescence signals of both 5mC and GFP demonstrated colocalisation with high nestin-expressing cell populations. This result further confirmed that the high genomic content of 5mC was associated with neural progenitors.

Nevertheless, further investigation is required to provide a clear picture about how DNA methylation status is reported in transgenic MBD-GFP mouse. Moreover, additional experiments can be undertaken in order to characterise the transgenic mouse in more detail. One of the critical experiments that need to be performed is GFP detection in PGCs to investigate how this well-characterised global DNA demethylation event is represented. Furthermore, instead of using a fluorescence widefield microscope, the utilisation of confocal microscopy technique would offer high-contrast and extremely high-quality images that can attribute signal more specifically to individual cell nuclei. The results obtained for MBD-GFP, therefore, need to be further verified by confocal microscopy.

Chapter 7 - General discussion, conclusions and future works

Epigenetics, the study of non-DNA sequence-encoded heritable traits propagated through modifications in the genomic DNA and chromatin proteins, is of increasing importance in biomedicine. Epigenetic mechanisms are implicated in the regulation of gene expression patterns that are at the basis of cell type specification during development and are necessary for maintenance of healthy life (Moffat et al., 2012; Reddington et al., 2013a). Their malfunction contributes to common complex inflammatory, cardiovascular and oncogenic disease, as well as being implicated in the lifetime programming effects from foetal and environmental exposures (Rose et al., 2013; Sproul and Meehan, 2013).

This PhD study aimed to advance scientific understanding of the nuclear epigenetic dynamics during mammalian development. A few prominent examples of developmental DNA methylation changes have been characterised in zygotes and germ cells. However, DNA methylation dynamics of other tissues in mammalian development are currently under-investigated. This knowledge has relevance to understanding epigenetic maintenance of cell types in adult life and diseases such as cancer, and can contribute to cell reprogramming for regenerative medicine, as the early observations of zygotic programming led the way to the first cell reprogramming by nuclear transfer experiments (Campbell et al., 1996; Gurdon, 2006). Therefore, the first aim of this study was to discover tissues undergoing dynamic nuclear changes in DNA methylation during mouse development. These changes were then characterised in order to report on developmental tissue-specific differences in DNA methylation and associated histone marks. This study utilised comparative immunocytochemistry by immunofluorescence staining analysis as a main method to visualise DNA methylation states and other epigenetic marks in tissues.

7.1 Optimised immunostaining for studying DNA methylation states in tissues

The standard protocol for immunodetection of 5mC was initially thought to work on tissues as it worked on cells but certain steps required adaptation and rigorous optimisation **(see Chapter 3)**. The problem was attributed to the acid denaturation step as it appeared to be ineffective at denaturing nuclear DNA in cryosectioned tissues. Acid can also lead to a destruction of DNA, potentially resulting in non-representative binding of 5mC antibody. Thus, the acid-dependent DNA denaturation step was replaced with heat-mediated DNA denaturation and antigen retrieval, which was indeed able to successfully improve the detection of methylated DNA by properly denaturing the DNA and simultaneously reversing the formaldehyde crosslinking. Heat treatment seemed to aptly disassociate in every nucleus a double-stranded DNA into single strands without apparent DNA damage.

Nonetheless, the requirement of using heat to induce denaturation of DNA lowers the possibility of combining the optimised 5mC immunodetection protocol with tissue specific markers. The heat treatment conditions were found to be incompatible with the preservation of most protein epitopes. The use of tissue-specific markers in parallel could allow more precise attribution of nuclear signal to specific cell types than on the basis of anatomy alone. Therefore, further optimisation would be important particularly at the DNA denaturation step in order to be able to perform double immunostaining with tissue-specific markers and accurately detect 5mC in the tissue of interest.

7.2 5mC and 5hmC DNA methylation dynamics in developing mouse embryonic tissues

The successful 5mC immunodetection protocol was employed to examine developing mouse tissues across the embryo for variations in involvement and dynamics of DNA methylation states **(see Chapter 4)**. Immunofluorescence data of 5mC were subsequently used for comparative analysis with 5hmC dynamic observations. Thus, the second aim of this study is to investigate the origin of 5hmC in developing tissues **(see Chapter 4)**.

Detailed immunofluorescence analysis suggests novel possible DNA demethylation events in the developing tissues studied. The molecular events of 5mC loss and concomitant 5hmC gain coupled with the existence of enzymatic activities are consistent with previous DNA demethylation studies in zygotes and PGCs (Amouroux et al., 2016; Ruzov et al., 2011; Yamaguchi et al., 2013; Zhang et al., 2012a). This study also reveals the importance of nuclear organisation during early development of certain tissues. Chromatin may become more compacted or diffuse in response to developmental changes in gene expression. On the other hand, in some other tissues, particularly surface ectoderm and red blood cells, it seems like there is a need for switching genes respectively on or off throughout development, although the precise reason is still unclear, it is notable that erythrocytes undergo globin gene switching and eventually become enucleated (Chao et al., 2015). The findings, however, require further experimental investigation at the genomic level in order to seek the best explanation of the observations. Contrastingly, some tissues did not follow the classic events of CpG demethylation, but in fact confocal analysis of distribution levels were indicative that 5hmC appeared to work by itself without depending on other mechanisms. The apparent dynamic range observed for 5hmC levels was also greater than for 5mC levels, although this may be due to higher antibody affinity for the less abundant 5hmC epitope. A unique role of 5hmC has been reported in several studies (Hahn et al., 2013; Heras et al., 2017; Iurlaro et al., 2013; Li and O’Neill, 2013; Salvaing et al., 2012). However, the exact molecular mechanism of 5hmC is still under extensive investigation.

One possible explanation for elevated levels of 5hmC in certain stages of developing tissues could be due to higher oxygen conditions (Wenger et al., 2015). In support, a recent study suggests high oxygen levels trigger the enzymatic activity of Tet proteins (Chia et al., 2011). Tet enzymes utilise α-ketoglutarate (α-KG) and molecular oxygen to oxidise 5mC and yield 5hmC, indicating that high levels of oxygen may be associated with increase in Tet activity and generation of 5hmC. Furthermore, another recent study discovered that tumour hypoxia (i.e. oxygen-deficient tumour cells) induces hypermethylation of DNA by reducing the activity of Tet enzymes (Thienpont et al., 2016). Together, both studies have shown the important of oxygen in the production of 5hmC. In this study, high 5hmC levels were observed in the later stages of trabeculae development. It is conceivable that ventricular blood can diffuse into the trabecula and trigger the localised formation of 5hmC. This observation is further supported by very low levels of 5hmC in fetal red blood cells. These progenitor cells have not yet committed to oxygen transfer, therefore contain no oxygen (O’Connell et al., 2013). The enrichment of 5hmC in neocortex remains unsure although this study could speculate an involvement of cortical vascularisation.

An alternative mechanism relating to cell turnover may be based on DNA replication and mitotic index of the tissues, which could potentially enhance 5mC maintenance over 5hmC hydroxylation activities. It is notable that the heart trabecular tissues and the outer neocortex zones in which higher 5hmC levels were observed contain less mitotic cells that migrate from more proliferative zones.

These and other testable models will be investigated in future studies. In addition, more developing mouse embryonic tissues should be further explored for the dynamics of 5mC and 5hmC in order to better understand their precise role and mechanism.

7.3 H3K9me3 and H3K27me3 histone methylation dynamics in developing mouse embryonic tissues

The third aim of this study is to investigate relevant connections between DNA methylation and histone lysine methylation **(see Chapter 5)**. The overall levels and distribution patterns of H3K9me3 and H3K27me3 revealed tight correlations with 5mC distribution patterns. Furthermore, these three epigenetic marks were found to be enriched at their respective constitutive and facultative heterochromatic foci. This study suggests the existence of a possible mechanistic interplay between DNA methylation and histone lysine methylation. They may work in combination to establish higher order structures of heterochromatin across nuclear compartments and promote gene silencing.

Fascinatingly, the interplay between these three systems appears to work in a tissue-specific manner. In neocortex, a silenced state of heterochromatin may need to be maintained throughout development, whereas in heart, nuclear organisation may be necessary for normal development. Nevertheless, their mechanistic interplay in a tissue-specific manner is still not well understood. Importantly, these observations are worthy of attention but these exploratory findings need further investigation specifically at a genomic level.

Similar to 5mC, it would also be interesting to explore the existence of crosstalk between DNA hydroxymethylation and specific histone modifications that are marked for open chromatin, for instance H3K4me3. 5hmC was found to be correlated negatively with repressive histone marks H3K9me3 and H3K27me3 (Wen et al., 2014). Thus, it is worth carrying out this experiment in order to be able to reveal and better understand the complex crosstalk among different types of epigenetic modification.

7.4 Visualisation of DNA methylation using transgenic MBD-GFP mice

The last aim of this study was to visualise DNA methylation in tissues using a transgenic MBD-GFP mouse **(see Chapter 6)**. Immunofluorescence analysis revealed that the MBD-GFP probe can recognise correctly heterochromatin containing hypermethylated DNA. This study also provided strong evidence that the MBD-GFP signals were positively correlated with 5mC signals observed in wild-type tissue, suggesting that MBD-GFP results were in good agreement with the experimental control. MBD-GFP levels and dynamics observed in the developing neocortex seemed to follow the dynamics of 5mC in wild type. In contrast, MBD-GFP levels and dynamics observed in the developing heart and liver did not quite correlate with wild-type results. The stronger MBD-GFP signal in heart indicated that transgene expression in these particular tissues may not report on comparative 5mC levels between these tissues, despite correctly reporting on DNA methylation within each cell type. This transgenic MBD-GFP mouse warrants deeper investigation to further explain the immunofluorescence data.

7.5 Future improvements

A major advance in the field during the past few years has been the identification of 5hmC as the sixth base in the mammalian genome. 5hmC has since been the subject of extensive investigation providing a better understanding of its biological function. Furthermore, a commercial antibody targeting 5hmC has also become available since then. The available 5hmC antibody has therefore allowed us to unravel the presence and distribution of 5hmC in the developing mouse embryonic tissues. However, the present study focused mainly on one technique and thus able to report only on immunostaining data. Therefore, genomic data, which are currently lacking in this study, should be included to provide further support for the immunostaining technique. The recent development of 5hmC-specific antibodies has led to the development and application of an antibody-based enrichment technique known as hydroxymethylated DNA immunoprecipitation (hMeDIP), a technique analogous to methylated DNA immunoprecipitation (MeDIP). hMeDIP appears to provide an invaluable tool to evaluate locus-specific and genome-wide maps of 5hmC in mammalian DNA. Therefore, this technique should be employed alongside MeDIP and chromatin immunoprecipitation (ChIP) experiments, followed by next-generation sequencing (NGS) and bioinformatics analysis in order to obtain epigenetic information at the whole genome level.

7.6 Conclusions

In conclusion, the findings in this study have contributed more scientific understanding of DNA methylation dynamics and nuclear heterochromatin organisation during mammalian development, and its biological function in the specification and maintenance of cell lineages forming tissues and organs. This current knowledge may provide important insights into current barriers to cell fate reprogramming, which will be of benefit to cell regenerative biomedical technologies and understanding disease.

7.7 Future works

It would be of great interest to further identify 5hmC-rich cell populations. Therefore, for the next experiments, fluorescence activated cell sorting (FACS) will be performed to isolate cells that contain high levels of 5hmC. Genomic mapping will then be performed using methylated and hydroxymethylated DNA immunoprecipitation methods (MeDIP and hMeDIP, respectively) followed by next-generation sequencing (NGS) and bioinformatics analysis.

References

Aguilar-Sanchez, C. (2016). Epigenetic transitions in cardiovascular development and cell reprogramming. PhD Thesis. University of Edinburgh.

Alabert, C., and Groth, A. (2012). Chromatin replication and epigenome maintenance. Nat. Rev. Mol. Cell Biol. *13*, 153–167.

Albert, M., and Helin, K. (2010). Histone methyltransferases in cancer. Semin. Cell Dev. Biol. *21*, 209–220.

Allan, R.S. (2015). The epigenetic mechanisms that underlie health and disease. Immunol. Cell Biol. *93*, 224–225.

Allan, J., Cowling, G.J., Harborne, N., Cattini, P., Craigie, R., and Gould, H. (1981). Regulation of the higher-order structure of chromatin by histones H1 and H5. J. Cell Biol. *90*, 279–288.

Allan, J., Harborne, N., Rau, D.C., and Gould, H. (1982). Participation of core histone “tails” in the stabilization of the chromatin solenoid. J. Cell Biol. *93*, 285–297.

Allfrey, V.G., Faulkner, R., and Mirsky, A.E. (1964). Acetylation and methylation of histones and their possible role in the regulation of RNA synthesis. Proc. Natl. Acad. Sci. U. S. A. *51*, 786–794.

Allis, C.D., and Jenuwein, T. (2016). The molecular hallmarks of epigenetic control. Nat. Rev. Genet. *17*, 487–500.

Amouroux, R., Nashun, B., Shirane, K., Nakagawa, S., Hill, P.W.S., D’Souza, Z., Nakayama, M., Matsuda, M., Turp, A., Ndjetehe, E., et al. (2016). De novo DNA methylation drives 5hmC accumulation in mouse zygotes. Nat. Cell Biol. *18*, 225–233.

Avior, Y., Sagi, I., and Benvenisty, N. (2016). Pluripotent stem cells in disease modelling and drug discovery. Nat. Rev. Mol. Cell Biol. *17*, 170–182.

Bai, L., and Morozov, A.V. (2010). Gene regulation by nucleosome positioning. Trends Genet. *26*, 476–483.

Baker, M. (2011). Making sense of chromatin states. Nat. Methods *8*, 717–722.

Bannister, A.J., and Kouzarides, T. (2011). Regulation of chromatin by histone modifications. Cell Res. *21*, 381–395.

Barazzuol, L., Rickett, N., Ju, L., and Jeggo, P.A. (2015). Low levels of endogenous or X-ray-induced DNA double-strand breaks activate apoptosis in adult neural stem cells. J Cell Sci *128*, 3597–3606.

Barbierato, M., Argentini, C., and Skaper, S. (2012). Indirect Immunofluorescence Staining of Cultured Neural Cells. In Neurotrophic Factors, S.D. Skaper, ed. (Humana Press), pp. 235–246.

Barlow, D.P., and Bartolomei, M.S. (2014). Genomic Imprinting in Mammals. Cold Spring Harb. Perspect. Biol. *6*, a018382.

Barski, A., Cuddapah, S., Cui, K., Roh, T.-Y., Schones, D.E., Wang, Z., Wei, G., Chepelev, I., and Zhao, K. (2007). High-Resolution Profiling of Histone Methylations in the Human Genome. Cell *129*, 823–837.

Bártová, E., Večeřa, J., Krejčí, J., Legartová, S., Pacherník, J., and Kozubek, S. (2016). The level and distribution pattern of HP1β in the embryonic brain correspond to those of H3K9me1/me2 but not of H3K9me3. Histochem. Cell Biol. *145*, 447–461.

Beaujean, N., Salvaing, J., Abd Hadi, N.A., and Pennings, S. (2017). Antibody based detection of global nuclear DNA methylation in cells, tissue sections and mammalian embryos. (Springer New York), (in press).

Beck, S., Lee, B.-K., Rhee, C., Song, J., Woo, A.J., and Kim, J. (2014). CpG island-mediated global gene regulatory modes in mouse embryonic stem cells. Nat. Commun. *5*, 5490.

Bell, O., Tiwari, V.K., Thomä, N.H., and Schübeler, D. (2011). Determinants and dynamics of genome accessibility. Nat. Rev. Genet. *12*, 554–564.

Bernstein, B.E., Meissner, A., and Lander, E.S. (2007). The Mammalian Epigenome. Cell *128*, 669–681.

Besser, S., Sicker, M., Marx, G., Winkler, U., Eulenburg, V., Hülsmann, S., and Hirrlinger, J. (2015). A Transgenic Mouse Line Expressing the Red Fluorescent Protein tdTomato in GABAergic Neurons. PLOS ONE *10*, e0129934.

Bintu, L., Yong, J., Antebi, Y.E., McCue, K., Kazuki, Y., Uno, N., Oshimura, M., and Elowitz, M.B. (2016). Dynamics of epigenetic regulation at the single-cell level. Science *351*, 720–724.

Bird, A.P. (1986). CpG-rich islands and the function of DNA methylation. Nature *321*, 209–213.

Bird, A.P. (1987). CpG islands as gene markers in the vertebrate nucleus. Trends Genet. *3*, 342–347.

Biswas, M., Voltz, K., Smith, J.C., and Langowski, J. (2011). Role of Histone Tails in Structural Stability of the Nucleosome. PLOS Comput Biol *7*, e1002279.

Black, J.C., Van Rechem, C., and Whetstine, J.R. (2012). Histone Lysine Methylation Dynamics: Establishment, Regulation, and Biological Impact. Mol. Cell *48*, 491–507.

Blackledge, N.P., and Klose, R. (2011). CpG island chromatin. Epigenetics *6*, 147–152.

Bogdanovic, O., Long, S.W., van Heeringen, S.J., Brinkman, A.B., Gómez-Skarmeta, J.L., Stunnenberg, H.G., Jones, P.L., and Veenstra, G.J.C. (2011). Temporal uncoupling of the DNA methylome and transcriptional repression during embryogenesis. Genome Res. *21*, 1313–1327.

Boland, M.J., Nazor, K.L., and Loring, J.F. (2014). Epigenetic Regulation of Pluripotency and Differentiation. Circ. Res. *115*, 311–324.

Bonasio, R., Tu, S., and Reinberg, D. (2010). Molecular Signals of Epigenetic States. Science *330*, 612–616.

Boros, J., Arnoult, N., Stroobant, V., Collet, J.-F., and Decottignies, A. (2014). Polycomb Repressive Complex 2 and H3K27me3 Cooperate with H3K9 Methylation To Maintain Heterochromatin Protein 1α at Chromatin. Mol. Cell. Biol. *34*, 3662–3674.

Bowman, G.D., and Poirier, M.G. (2015). Post-translational modifications of histones that influence nucleosome dynamics. Chem. Rev. *115*, 2274–2295.

Branco, M.R., Ficz, G., and Reik, W. (2012). Uncovering the role of 5-hydroxymethylcytosine in the epigenome. Nat. Rev. Genet. *13*, 7–13.

Brinkman, A.B., Gu, H., Bartels, S.J.J., Zhang, Y., Matarese, F., Simmer, F., Marks, H., Bock, C., Gnirke, A., Meissner, A., et al. (2012). Sequential ChIP-bisulfite sequencing enables direct genome-scale investigation of chromatin and DNA methylation cross-talk. Genome Res. *22*, 1128–1138.

Budhavarapu, V.N., Chavez, M., and Tyler, J.K. (2013). How is epigenetic information maintained through DNA replication? Epigenetics Chromatin *6*, 32.

Bunkar, N., Pathak, N., Lohiya, N.K., and Mishra, P.K. (2016). Epigenetics: A key paradigm in reproductive health. Clin. Exp. Reprod. Med. *43*, 59–81.

Burry, R.W. (2011). Controls for Immunocytochemistry. J. Histochem. Cytochem. *59*, 6–12.

Cacabelos, R. (2016). Epigenetics of Brain Disorders: The Paradigm of Alzheimer ’s Disease. J. Alzheimers Dis. Park. *06*.

Cacabelos, R., and Torrellas, C. (2015). Epigenetics of Aging and Alzheimer’s Disease: Implications for Pharmacogenomics and Drug Response. Int. J. Mol. Sci. *16*, 30483–30543.

de la Calle Mustienes, E., Gómez-Skarmeta, J.L., and Bogdanović, O. (2015). Genome-wide epigenetic cross-talk between DNA methylation and H3K27me3 in zebrafish embryos. Genomics Data *6*, 7–9.

Campbell, K.H.S., McWhir, J., Ritchie, W.A., and Wilmut, I. (1996). Sheep cloned by nuclear transfer from a cultured cell line. Nature *380*, 64–66.

Cantone, I., and Fisher, A.G. (2013). Epigenetic programming and reprogramming during development. Nat. Struct. Mol. Biol. *20*, 282–289.

Cedar, H., and Bergman, Y. (2009). Linking DNA methylation and histone modification: patterns and paradigms. Nat. Rev. Genet. *10*, 295–304.

Chalfie, M., Tu, Y., Euskirchen, G., Ward, W.W., and Prasher, D.C. (1994). Green fluorescent protein as a marker for gene expression. Science *263*, 802–805.

Chao, R., Gong, X., Wang, L., Wang, P., and Wang, Y. (2015). CD71(high) population represents primitive erythroblasts derived from mouse embryonic stem cells. Stem Cell Res. *14*, 30–38.

Chatterjee, R., and Vinson, C. (2012). CpG methylation recruits sequence specific transcription factors essential for tissue specific gene expression. Biochim. Biophys. Acta BBA - Gene Regul. Mech. *1819*, 763–770.

Chen, T., and Dent, S.Y.R. (2014). Chromatin modifiers and remodellers: regulators of cellular differentiation. Nat. Rev. Genet. *15*, 93–106.

Chen, C.-C., Wang, K.-Y., and Shen, C.-K.J. (2012). The Mammalian de Novo DNA Methyltransferases DNMT3A and DNMT3B Are Also DNA 5-Hydroxymethylcytosine Dehydroxymethylases. J. Biol. Chem. *287*, 33116–33121.

Cheng, X. (2014). Structural and Functional Coordination of DNA and Histone Methylation. Cold Spring Harb. Perspect. Biol. *6*, a018747.

Cheng, Y., Bernstein, A., Chen, D., and Jin, P. (2015). 5-Hydroxymethylcytosine: A new player in brain disorders? Exp. Neurol. *268*, 3–9.

Chi, P., Allis, C.D., and Wang, G.G. (2010). Covalent histone modifications: miswritten, misinterpreted, and miserased in human cancers. Nat. Rev. Cancer *10*, 457–469.

Chia, N., Wang, L., Lu, X., Senut, M.-C., Brenner, C.A., and Ruden, D.M. (2011). Hypothesis: Environmental regulation of 5-hydroxymethylcytosine by oxidative stress. Epigenetics *6*, 853–856.

Cho, A., Haruyama, N., and Kulkarni, A.B. (2009). Generation of Transgenic Mice. Curr. Protoc. Cell Biol. Editor. Board Juan Bonifacino Al *CHAPTER*, Unit-19.11.

Choudhury, S.R., Fitzpatrick, Z., Harris, A.F., Maitland, S.A., Ferreira, J.S., Zhang, Y., Ma, S., Sharma, R.B., Gray-Edwards, H.L., Johnson, J.A., et al. (2016). In Vivo Selection Yields AAV-B1 Capsid for Central Nervous System and Muscle Gene Therapy. Mol. Ther. *24*, 1247–1257.

Chouliaras, L., Mastroeni, D., Delvaux, E., Grover, A., Kenis, G., Hof, P.R., Steinbusch, H.W.M., Coleman, P.D., Rutten, B.P.F., and van den Hove, D.L.A. (2013). Consistent decrease in global DNA methylation and hydroxymethylation in the hippocampus of Alzheimer's disease patients. Neurobiol. Aging *34,* 2091–2099.

Chow, J.C., Ciaudo, C., Fazzari, M.J., Mise, N., Servant, N., Glass, J.L., Attreed, M., Avner, P., Wutz, A., Barillot, E., et al. (2010). LINE-1 Activity in Facultative Heterochromatin Formation during X Chromosome Inactivation. Cell *141*, 956–969.

Chudakov, D.M., Matz, M.V., Lukyanov, S., and Lukyanov, K.A. (2010). Fluorescent Proteins and Their Applications in Imaging Living Cells and Tissues. Physiol. Rev. *90*, 1103–1163.

Clouaire, T., Webb, S., Skene, P., Illingworth, R., Kerr, A., Andrews, R., Lee, J.-H., Skalnik, D., and Bird, A. (2012). Cfp1 integrates both CpG content and gene activity for accurate H3K4me3 deposition in embryonic stem cells. Genes Dev. *26*, 1714–1728.

Cyranoski, D. (2014). Stem cells: The black box of reprogramming. Nature *516*, 162–164.

Daxinger, L., and Whitelaw, E. (2010). Transgenerational epigenetic inheritance: More questions than answers. Genome Res. *20*, 1623–1628.

Deans, C., and Maggert, K.A. (2015). What Do You Mean, "Epigenetic"? Genetics *199*, 887–896.

Deaton, A.M., and Bird, A. (2011). CpG islands and the regulation of transcription. Genes Dev. *25*, 1010–1022.

Deaton, A.M., Webb, S., Kerr, A.R.W., Illingworth, R.S., Guy, J., Andrews, R., and Bird, A. (2011). Cell type–specific DNA methylation at intragenic CpG islands in the immune system. Genome Res. *21*, 1074–1086.

Degl'Innocenti, A., and D'Errico, A. (2017). Regulatory Features for Odorant Receptor Genes in the Mouse Genome. Front. Genet. *8*.

Delatte, B., Deplus, R., and Fuks, F. (2014). Playing TETris with DNA modifications. EMBO J. *33*, 1198–1211.

DesJarlais, R., and Tummino, P.J. (2016). Role of Histone-Modifying Enzymes and Their Complexes in Regulation of Chromatin Biology. Biochemistry (Mosc.) *55*, 1584–1599.

Dimitrova, E., Turberfield, A.H., and Klose, R.J. (2015). Histone demethylases in chromatin biology and beyond. EMBO Rep. *16*, 1620–1639.

Diotel, N., Mérot, Y., Coumailleau, P., Gueguen, M.-M., Sérandour, A.A., Salbert, G., and Kah, O. (2017). 5-hydroxymethylcytosine marks postmitotic neural cells in the adult and developing vertebrate central nervous system. J. Comp. Neurol. *525*, 478–497.

Domcke, S., Bardet, A.F., Adrian Ginno, P., Hartl, D., Burger, L., and Schübeler, D. (2015). Competition between DNA methylation and transcription factors determines binding of NRF1. Nature *528*, 575–579.

Dong, X., and Weng, Z. (2013). The correlation between histone modifications and gene expression. Epigenomics *5*, 113–116.

Doyle, A., McGarry, M.P., Lee, N.A., and Lee, J.J. (2012). The construction of transgenic and gene knockout/knockin mouse models of human disease. Transgenic Res. *21*, 327–349.

Du, J., Johnson, L.M., Jacobsen, S.E., and Patel, D.J. (2015a). DNA methylation pathways and their crosstalk with histone methylation. Nat. Rev. Mol. Cell Biol. *16*, 519–532.

Du, Q., Luu, P.-L., Stirzaker, C., and Clark, S.J. (2015b). Methyl-CpG-binding domain proteins: readers of the epigenome. Epigenomics *7*, 1051–1073.

Duncan, E.J., Gluckman, P.D., and Dearden, P.K. (2014). Epigenetics, plasticity, and evolution: How do we link epigenetic change to phenotype? J. Exp. Zoolog. B Mol. Dev. Evol. *322*, 208–220.

D’Urso, A., and Brickner, J.H. (2014). Mechanisms of epigenetic memory. Trends Genet. TIG *30*, 230–236.

Duymich, C.E., Charlet, J., Yang, X., Jones, P.A., and Liang, G. (2016). DNMT3B isoforms without catalytic activity stimulate gene body methylation as accessory proteins in somatic cells. Nat. Commun. *7*, 11453.

Ehrlich, M., and Ehrlich, K.C. (2014). DNA cytosine methylation and hydroxymethylation at the borders. Epigenomics *6*, 563–566.

Eisenstein, M. (2016). A simpler twist of fate. Nature *534*, 421–423.

Ezponda, T., and Licht, J.D. (2014). Molecular Pathways: Deregulation of Histone 3 Lysine 27 Methylation in Cancer—Different Paths, Same Destination. Clin. Cancer Res. Off. J. Am. Assoc. Cancer Res. *20*, 5001–5008.

Falkenberg, K.J., and Johnstone, R.W. (2014). Histone deacetylases and their inhibitors in cancer, neurological diseases and immune disorders. Nat. Rev. Drug Discov. *13*, 673–691.

Fedoriw, A., Mugford, J., and Magnuson, T. (2012). Genomic Imprinting and Epigenetic Control of Development. Cold Spring Harb. Perspect. Biol. *4*, a008136.

Feinberg AP, and Fallin M (2015). Epigenetics at the crossroads of genes and the environment. JAMA *314*, 1129–1130.

Feng, S., Jacobsen, S.E., and Reik, W. (2010). Epigenetic reprogramming in plant and animal development. Science *330*, 622–627.

Ficz, G., Branco, M.R., Seisenberger, S., Santos, F., Krueger, F., Hore, T.A., Marques, C.J., Andrews, S., and Reik, W. (2011). Dynamic regulation of 5-hydroxymethylcytosine in mouse ES cells and during differentiation. Nature *473*, 398–402.

Filippakopoulos, P., and Knapp, S. (2014). Targeting bromodomains: epigenetic readers of lysine acetylation. Nat. Rev. Drug Discov. *13*, 337–356.

Fischle, W. (2008). Talk is cheap--cross-talk in establishment, maintenance, and readout of chromatin modifications. Genes Dev. *22*, 3375–3382.

Fischle, W., Mootz, H.D., and Schwarzer, D. (2015). Synthetic histone code. Curr. Opin. Chem. Biol. *28*, 131–140.

Flaus, A., and Owen-Hughes, T. (2017). Unlocking the nucleosome. Science *355*, 245–246.

Fowler, C.B., Evers, D.L., O'Leary, T.J., and Mason, J.T. (2011). Antigen retrieval causes protein unfolding: evidence for a linear epitope model of recovered immunoreactivity. J. Histochem. Cytochem. Off. J. Histochem. Soc. *59*, 366–381.

Franco, I., Ortiz-López, L., Roque-Ramírez, B., Ramírez-Rodríguez, G.B., and Lamas, M. (2017). Pharmacological inhibition of DNA methyltransferase 1 promotes neuronal differentiation from rodent and human nasal olfactory stem/progenitor cell cultures. Int. J. Dev. Neurosci. *58*, 65–73.

Fuchs, S.M., Kizer, K.O., Braberg, H., Krogan, N.J., and Strahl, B.D. (2012). RNA Polymerase II Carboxyl-terminal Domain Phosphorylation Regulates Protein Stability of the Set2 Methyltransferase and Histone H3 Di- and Trimethylation at Lysine 36. J. Biol. Chem. *287*, 3249–3256.

Füllgrabe, J., Hajji, N., and Joseph, B. (2010). Cracking the death code: apoptosis-related histone modifications. Cell Death Differ. *17*, 1238–1243.

Gal-Yam, E.N., Egger, G., Iniguez, L., Holster, H., Einarsson, S., Zhang, X., Lin, J.C., Liang, G., Jones, P.A., and Tanay, A. (2008). Frequent switching of Polycomb repressive marks and DNA hypermethylation in the PC3 prostate cancer cell line. Proc. Natl. Acad. Sci. U. S. A. *105*, 12979–12984.

Gao, J., Ma, Y., Fu, H.-L., Luo, Q., Wang, Z., Xiao, Y.-H., Yang, H., Cui, D.-X., and Jin, W.-L. (2016). Non-catalytic roles for TET1 protein negatively regulating neuronal differentiation through srGAP3 in neuroblastoma cells. Protein Cell *7*, 351–361.

Gardiner-Garden, M., and Frommer, M. (1987). CpG islands in vertebrate genomes. J. Mol. Biol. *196*, 261–282.

Geisler, S.J., and Paro, R. (2015). Trithorax and Polycomb group-dependent regulation: a tale of opposing activities. Dev. Camb. Engl. *142*, 2876–2887.

Gendrel, A.-V., Tang, Y.A., Suzuki, M., Godwin, J., Nesterova, T.B., Greally, J.M., Heard, E., and Brockdorff, N. (2013). Epigenetic Functions of Smchd1 Repress Gene Clusters on the Inactive X Chromosome and on Autosomes. Mol. Cell. Biol. *33*, 3150–3165.

Gibney, E.R., and Nolan, C.M. (2010). Epigenetics and gene expression. Heredity *105*, 4–13.

Giehr, P., Kyriakopoulos, C., Ficz, G., Wolf, V., and Walter, J. (2016). The Influence of Hydroxylation on Maintaining CpG Methylation Patterns: A Hidden Markov Model Approach. PLoS Comput. Biol. *12*, e1004905.

Gilbert, S.F. (2012). Commentary: “The Epigenotype” by C.H. Waddington. Int. J. Epidemiol. *41*, 20–23.

Gillette, T.G., and Hill, J.A. (2015). Readers, Writers, and Erasers Chromatin as the Whiteboard of Heart Disease. Circ. Res. *116*, 1245–1253.

Ginno, P.A., Lott, P.L., Christensen, H.C., Korf, I., and Chédin, F. (2012). R-loop formation is a distinctive characteristic of unmethylated human CpG island promoters. Mol. Cell *45*, 814–825.

Goto, S., Morigaki, R., Okita, S., Nagahiro, S., and Kaji, R. (2015). Development of a highly sensitive immunohistochemical method to detect neurochemical molecules in formalin-fixed and paraffin-embedded tissues from autopsied human brains. Front. Neuroanat. *9*, 22.

Graham, E., Moss, J., Burton, N., Armit, C., Richardson, L., and Baldock, R. (2015). The atlas of mouse development eHistology resource. Development *142*, 1909–1911.

Greer, E.L., and Shi, Y. (2012). Histone methylation: a dynamic mark in health, disease and inheritance. Nat. Rev. Genet. *13*, 343–357.

Grégoire, L., Haudry, A., and Lerat, E. (2016). The transposable element environment of human genes is associated with histone and expression changes in cancer. BMC Genomics *17*, 588.

Grewal, S.I.S., and Jia, S. (2007). Heterochromatin revisited. Nat. Rev. Genet. *8*, 35–46.

Gross, D.S., Chowdhary, S., Anandhakumar, J., and Kainth, A.S. (2015). Chromatin. Curr. Biol. *25*, R1158–R1163.

Gross, J.A., Lefebvre, F., Lutz, P.-E., Bacot, F., Vincent, D., Bourque, G., and Turecki, G. (2016). Variations in 5-methylcytosine and 5-hydroxymethylcytosine among human brain, blood, and saliva using oxBS and the Infinium MethylationEPIC array. Biol. Methods Protoc. *1*.

Grskovic, M., Javaherian, A., Strulovici, B., and Daley, G.Q. (2011). Induced pluripotent stem cells — opportunities for disease modelling and drug discovery. Nat. Rev. Drug Discov. *10*, 915–929.

Gurdon, J.B. (2006). From Nuclear Transfer to Nuclear Reprogramming: The Reversal of Cell Differentiation. Annu. Rev. Cell Dev. Biol. *22*, 1–22.

Hackett, J.A., Reddington, J.P., Nestor, C.E., Dunican, D.S., Branco, M.R., Reichmann, J., Reik, W., Surani, M.A., Adams, I.R., and Meehan, R.R. (2012). Promoter DNA methylation couples genome-defence mechanisms to epigenetic reprogramming in the mouse germline. Development *139*, 3623–3632.

Hackett, J.A., Sengupta, R., Zylicz, J.J., Murakami, K., Lee, C., Down, T.A., and Surani, M.A. (2013). Germline DNA Demethylation Dynamics and Imprint Erasure Through 5-Hydroxymethylcytosine. Science *339*, 448–452.

Hahn, M., Dambacher, S., and Schotta, G. (2010). Heterochromatin dysregulation in human diseases. J. Appl. Physiol. *109*, 232–242.

Hahn, M.A., Qiu, R., Wu, X., Li, A.X., Zhang, H., Wang, J., Jui, J., Jin, S.-G., Jiang, Y., Pfeifer, G.P., et al. (2013). Dynamics of 5-hydroxymethylcytosine and chromatin marks in Mammalian neurogenesis. Cell Rep. *3*, 291–300.

Hahn, M.A., Szabó, P.E., and Pfeifer, G.P. (2014). 5-Hydroxymethylcytosine: A stable or transient DNA modification? Genomics *104*, 314–323.

Hajkova, P. (2011). Epigenetic reprogramming in the germline: towards the ground state of the epigenome. Philos. Trans. R. Soc. B Biol. Sci. *366*, 2266–2273.

Handy, D.E., Castro, R., and Loscalzo, J. (2011). Epigenetic Modifications: Basic Mechanisms and Role in Cardiovascular Disease. Circulation *123*, 2145–2156.

Harraghy, N., Calabrese, D., Fisch, I., Girod, P.-A., LeFourn, V., Regamey, A., and Mermod, N. (2015). Epigenetic regulatory elements: Recent advances in understanding their mode of action and use for recombinant protein production in mammalian cells. Biotechnol. J. *10*, 967–978.

Harshman, S.W., Young, N.L., Parthun, M.R., and Freitas, M.A. (2013). H1 histones: current perspectives and challenges. Nucleic Acids Res. *41*, 9593–9609.

Hartono, S.R., Korf, I.F., and Chédin, F. (2015). GC skew is a conserved property of unmethylated CpG island promoters across vertebrates. Nucleic Acids Res. *43*, 9729–9741.

Haruyama, N., Cho, A., and Kulkarni, A.B. (2009). Overview: Engineering transgenic constructs and mice. Curr. Protoc. Cell Biol. Editor. Board Juan Bonifacino Al *CHAPTER*, Unit-19.10.

He, H., Gonzalez, M., Zhang, F., and Li, F. (2014). DNA replication components as regulators of epigenetic inheritance—lesson from fission yeast centromere. Protein Cell *5*, 411–419.

He, X.-J., Chen, T., and Zhu, J.-K. (2011a). Regulation and function of DNA methylation in plants and animals. Cell Res. *21*, 442–465.

He, Y.-F., Li, B.-Z., Li, Z., Liu, P., Wang, Y., Tang, Q., Ding, J., Jia, Y., Chen, Z., Li, L., et al. (2011b). Tet-Mediated Formation of 5-Carboxylcytosine and Its Excision by TDG in Mammalian DNA. Science *333*, 1303–1307.

van Heeringen, S.J., Akkers, R.C., van Kruijsbergen, I., Arif, M.A., Hanssen, L.L.P., Sharifi, N., and Veenstra, G.J.C. (2014). Principles of nucleation of H3K27 methylation during embryonic development. Genome Res. *24*, 401–410.

Heitz, E. (1928). Das Heterochromatin der Moose. Jahrb Wiss Bot. *69*, 762–818.

Heras, S., Smits, K., De Schauwer, C., and Van Soom, A. (2017). Dynamics of 5-methylcytosine and 5-hydroxymethylcytosine during pronuclear development in equine zygotes produced by ICSI. Epigenetics Chromatin *10*, 13.

Hergeth, S.P., and Schneider, R. (2015). The H1 linker histones: multifunctional proteins beyond the nucleosomal core particle. EMBO Rep. *16*, 1439–1453.

Hill, P.W.S., Amouroux, R., and Hajkova, P. (2014). DNA demethylation, Tet proteins and 5-hydroxymethylcytosine in epigenetic reprogramming: An emerging complex story. Genomics *104*, 324–333.

Hirabayashi, Y., and Gotoh, Y. (2010). Epigenetic control of neural precursor cell fate during development. Nat. Rev. Neurosci. *11*, 377–388.

Hiragami-Hamada, K., Soeroes, S., Nikolov, M., Wilkins, B., Kreuz, S., Chen, C., De La Rosa-Velázquez, I.A., Zenn, H.M., Kost, N., Pohl, W., et al. (2016). Dynamic and flexible H3K9me3 bridging via HP1β dimerization establishes a plastic state of condensed chromatin. Nat. Commun. *7*, 11310.

Hirschi, K.K., Li, S., and Roy, K. (2014). Induced Pluripotent Stem Cells for Regenerative Medicine. Annu. Rev. Biomed. Eng. *16*, 277–294.

Hochberg, Z., Feil, R., Constancia, M., Fraga, M., Junien, C., Carel, J.-C., Boileau, P., Le Bouc, Y., Deal, C.L., Lillycrop, K., et al. (2011). Child health, developmental plasticity, and epigenetic programming. Endocr. Rev. *32*, 159–224.

Højfeldt, J.W., Agger, K., and Helin, K. (2013). Histone lysine demethylases as targets for anticancer therapy. Nat. Rev. Drug Discov. *12*, 917–930.

Howat, W.J., and Wilson, B.A. (2014). Tissue fixation and the effect of molecular fixatives on downstream staining procedures. Methods *70*, 12–19.

Hu, L., Li, Z., Cheng, J., Rao, Q., Gong, W., Liu, M., Shi, Y.G., Zhu, J., Wang, P., and Xu, Y. (2013). Crystal Structure of TET2-DNA Complex: Insight into TET-Mediated 5mC Oxidation. Cell *155*, 1545–1555.

Huang, Y., and Rao, A. (2014). Connections between TET proteins and aberrant DNA modification in cancer. Trends Genet. *30*, 464–474.

Huang, C., Xu, M., and Zhu, B. (2013). Epigenetic inheritance mediated by histone lysine methylation: maintaining transcriptional states without the precise restoration of marks? Phil Trans R Soc B *368*, 20110332.

Hussaini, S.M.Q., Jun, H., Cho, C.H., Kim, H.J., Kim, W.R., and Jang, M.-H. (2013). Heat-Induced Antigen Retrieval: An Effective Method to Detect and Identify Progenitor Cell Types during Adult Hippocampal Neurogenesis. J. Vis. Exp. JoVE.

Huypens, P., Sass, S., Wu, M., Dyckhoff, D., Tschöp, M., Theis, F., Marschall, S., de Angelis, M.H., and Beckers, J. (2016). Epigenetic germline inheritance of diet-induced obesity and insulin resistance. Nat. Genet. *48*, 497–499.

Inoue, A., Shen, L., Dai, Q., He, C., and Zhang, Y. (2011). Generation and replication-dependent dilution of 5fC and 5caC during mouse preimplantation development. Cell Res. *21*, 1670–1676.

Irimia, M., Tena, J.J., Alexis, M.S., Fernandez-Miñan, A., Maeso, I., Bogdanovic, O., de la Calle-Mustienes, E., Roy, S.W., Gómez-Skarmeta, J.L., and Fraser, H.B. (2012). Extensive conservation of ancient microsynteny across metazoans due to cis-regulatory constraints. Genome Res. *22*, 2356–2367.

Ito, S., D'Alessio, A.C., Taranova, O.V., Hong, K., Sowers, L.C., and Zhang, Y. (2010). Role of Tet proteins in 5mC to 5hmC conversion, ES cell self-renewal, and ICM specification. Nature *466*, 1129–1133.

Ito, S., Shen, L., Dai, Q., Wu, S.C., Collins, L.B., Swenberg, J.A., He, C., and Zhang, Y. (2011). Tet proteins can convert 5-methylcytosine to 5-formylcytosine and 5-carboxylcytosine. Science *333*, 1300–1303.

Iurlaro, M., Ficz, G., Oxley, D., Raiber, E.-A., Bachman, M., Booth, M.J., Andrews, S., Balasubramanian, S., and Reik, W. (2013). A screen for hydroxymethylcytosine and formylcytosine binding proteins suggests functions in transcription and chromatin regulation. Genome Biol. *14*, R119.

Iwasaki, W., Miya, Y., Horikoshi, N., Osakabe, A., Taguchi, H., Tachiwana, H., Shibata, T., Kagawa, W., and Kurumizaka, H. (2013). Contribution of histone N-terminal tails to the structure and stability of nucleosomes. FEBS Open Bio *3*, 363–369.

Izzo, A., and Schneider, R. (2010). Chatting histone modifications in mammals. Brief. Funct. Genomics *9*, 429–443.

Jafarpour, F., Hosseini, S.M., Ostadhosseini, S., Abbasi, H., Dalman, A., and Nasr-Esfahani, M.H. (2017). Comparative dynamics of 5-methylcytosine reprogramming and TET family expression during preimplantation mammalian development in mouse and sheep. Theriogenology *89*, 86–96.

Jamieson, K., Wiles, E.T., McNaught, K.J., Sidoli, S., Leggett, N., Shao, Y., Garcia, B.A., and Selker, E.U. (2016). Loss of HP1 causes depletion of H3K27me3 from facultative heterochromatin and gain of H3K27me2 at constitutive heterochromatin. Genome Res. *26*, 97–107.

Jensen, E.C. (2012). Use of Fluorescent Probes: Their Effect on Cell Biology and Limitations. Anat. Rec. Adv. Integr. Anat. Evol. Biol. *295*, 2031–2036.

Jenuwein, T., and Allis, C.D. (2001). Translating the Histone Code. Science *293*, 1074–1080.

Jeong, M., Sun, D., Luo, M., Huang, Y., Challen, G.A., Rodriguez, B., Zhang, X., Chavez, L., Wang, H., Hannah, R., et al. (2014). Large conserved domains of low DNA methylation maintained by Dnmt3a. Nat. Genet. *46*, 17–23.

Jin, C., Lu, Y., Jelinek, J., Liang, S., Estecio, M.R.H., Barton, M.C., and Issa, J.-P.J. (2014). TET1 is a maintenance DNA demethylase that prevents methylation spreading in differentiated cells. Nucleic Acids Res. gku372.

Jin, S.-G., Jiang, Y., Qiu, R., Rauch, T.A., Wang, Y., Schackert, G., Krex, D., Lu, Q., and Pfeifer, G.P. (2011). 5-hydroxymethylcytosine is strongly depleted in human cancers but its levels do not correlate with IDH1 mutations. Cancer Res. *71*, 7360–7365.

Jones, P.A. (2012). Functions of DNA methylation: islands, start sites, gene bodies and beyond. Nat. Rev. Genet. *13*, 484–492.

Jørgensen, H.F., Adie, K., Chaubert, P., and Bird, A.P. (2006). Engineering a high-affinity methyl-CpG-binding protein. Nucleic Acids Res. *34*, e96.

Justin, N., Zhang, Y., Tarricone, C., Martin, S.R., Chen, S., Underwood, E., De Marco, V., Haire, L.F., Walker, P.A., Reinberg, D., et al. (2016). Structural basis of oncogenic histone H3K27M inhibition of human polycomb repressive complex 2. Nat. Commun. *7*, 11316.

Kagiwada, S., Kurimoto, K., Hirota, T., Yamaji, M., and Saitou, M. (2013). Replication- coupled passive DNA demethylation for the erasure of genome imprints in mice. EMBO J. *32*, 340–353.

Kalashnikova, A.A., Rogge, R.A., and Hansen, J.C. (2016). Linker histone H1 and protein-protein interactions. Biochim. Biophys. Acta *1859*, 455–461.

Kato, T., and Iwamoto, K. (2014). Comprehensive DNA methylation and hydroxymethylation analysis in the human brain and its implication in mental disorders. Neuropharmacology *80*, 133–139.

Kaufman, M.H. (1992). The atlas of mouse development (London: Elsevier Academic Press).

Kaufman, P.D., and Rando, O.J. (2010). Chromatin as a potential carrier of heritable information. Curr. Opin. Cell Biol. *22*, 284–290.

Kawakami, K., Asakawa, K., Hibi, M., Itoh, M., Muto, A., and Wada, H. (2016). Chapter Three - Gal4 Driver Transgenic Zebrafish: Powerful Tools to Study Developmental Biology, Organogenesis, and Neuroscience. In Advances in Genetics, N.S. Foulkes, ed. (Academic Press), pp. 65–87.

Kelaini, S., Cochrane, A., and Margariti, A. (2014). Direct reprogramming of adult cells: avoiding the pluripotent state. Stem Cells Cloning Adv. Appl. *7*, 19–29.

Khare, T., Pai, S., Koncevicius, K., Pal, M., Kriukiene, E., Liutkeviciute, Z., Irimia, M., Jia, P., Ptak, C., Xia, M., et al. (2012). 5-hmC in the brain is abundant in synaptic genes and shows differences at the exon-intron boundary. Nat. Struct. Mol. Biol. *19*, 1037–1043.

Kim, J., and Kim, H. (2012). Recruitment and biological consequences of histone modification of H3K27me3 and H3K9me3. ILAR J. *53*, 232–239.

Kim, J., Vaish, V., Feng, M., Field, K., Chatzistamou, I., and Shim, M. (2016). Transgenic expression of cyclooxygenase-2 (COX2) causes premature aging phenotypes in mice. Aging *8*, 2392–2405.

Klose, R.J., and Bird, A.P. (2006). Genomic DNA methylation: the mark and its mediators. Trends Biochem. Sci. *31*, 89–97.

Kohl, J., Ng, J., Cachero, S., Ciabatti, E., Dolan, M.-J., Sutcliffe, B., Tozer, A., Ruehle, S., Krueger, D., Frechter, S., et al. (2014). Ultrafast tissue staining with chemical tags. Proc. Natl. Acad. Sci. U. S. A. *111*, E3805-3814.

Kondo, Y., Shen, L., Cheng, A.S., Ahmed, S., Boumber, Y., Charo, C., Yamochi, T., Urano, T., Furukawa, K., Kwabi-Addo, B., et al. (2008). Gene silencing in cancer by histone H3 lysine 27 trimethylation independent of promoter DNA methylation. Nat. Genet. *40*, 741–750.

Kothari, R.M., and Shankar, V. (1976). 5-Methylcytosine content in the vertebrate deoxyribonucleic acids: species specificity. J. Mol. Evol. *7*, 325–329.

Kouzarides, T. (2007). Chromatin Modifications and Their Function. Cell *128*, 693–705.

Kraus, T.F.J., Guibourt, V., and Kretzschmar, H.A. (2014). 5-Hydroxymethylcytosine, the “Sixth Base”, during brain development and ageing. J. Neural Transm. *122*, 1035–1043.

Kraus, T.F.J., Kilinc, S., Steinmaurer, M., Stieglitz, M., Guibourt, V., and Kretzschmar, H.A. (2015). Profiling of methylation and demethylation pathways during brain development and ageing. J. Neural Transm. *123*, 189–203.

Kriaucionis, S., and Heintz, N. (2009). The nuclear DNA base 5-hydroxymethylcytosine is present in Purkinje neurons and the brain. Science *324*, 929–930.

Kriukienė, E., Liutkevičiūtė, Z., and Klimašauskas, S. (2012). 5-Hydroxymethylcytosine – the elusive epigenetic mark in mammalian DNA. Chem. Soc. Rev. *41*, 6916–6930.

Kumar, T.R., Larson, M., Wang, H., McDermott, J., and Bronshteyn, I. (2009). Transgenic mouse technology: principles and methods. Methods Mol. Biol. Clifton NJ *590*, 335–362.

Lalonde, M.-E., Cheng, X., and Côté, J. (2014). Histone target selection within chromatin: an exemplary case of teamwork. Genes Dev. *28*, 1029–1041.

Lan, J., Lepikhov, K., Giehr, P., and Walter, J. (2017). Histone and DNA methylation control by H3 serine 10/threonine 11 phosphorylation in the mouse zygote. Epigenetics Chromatin *10*, 5.

Landan, G., Cohen, N.M., Mukamel, Z., Bar, A., Molchadsky, A., Brosh, R., Horn-Saban, S., Zalcenstein, D.A., Goldfinger, N., Zundelevich, A., et al. (2012). Epigenetic polymorphism and the stochastic formation of differentially methylated regions in normal and cancerous tissues. Nat. Genet. *44*, 1207–1214.

Lander, E.S., Linton, L.M., Birren, B., Nusbaum, C., Zody, M.C., Baldwin, J., Devon, K., Dewar, K., Doyle, M., FitzHugh, W., et al. (2001). Initial sequencing and analysis of the human genome. Nature *409*, 860–921.

Lang, C.N., Koren, G., and Odening, K.E. (2016). Transgenic rabbit models to investigate the cardiac ion channel disease long QT syndrome. Prog. Biophys. Mol. Biol. *121*, 142–156.

Lee, J.J., Vilain, R.E., Granter, S.R., Hu, N.R., Bresler, S.C., Xu, S., Frank, A.H., Mihm, M.C., Saw, R.P.M., Fletcher, C.D., et al. (2017). 5-Hydroxymethylcytosine is a nuclear biomarker to assess biological potential in histologically ambiguous heavily pigmented melanocytic neoplasms. J. Cutan. Pathol. *44*, 249–255.

Lehnertz, B., Ueda, Y., Derijck, A.A.H.A., Braunschweig, U., Perez-Burgos, L., Kubicek, S., Chen, T., Li, E., Jenuwein, T., and Peters, A.H.F.M. (2003). Suv39h-mediated histone H3 lysine 9 methylation directs DNA methylation to major satellite repeats at pericentric heterochromatin. Curr. Biol. CB *13*, 1192–1200.

Li, E., and Zhang, Y. (2014). DNA Methylation in Mammals. Cold Spring Harb. Perspect. Biol. *6*, a019133.

Li, G., and Reinberg, D. (2011). Chromatin higher-order structures and gene regulation. Curr. Opin. Genet. Dev. *21*, 175–186.

Li, Q., and Zhang, Z. (2012). Linking DNA replication to heterochromatin silencing and epigenetic inheritance. Acta Biochim. Biophys. Sin. *44*, 3–13.

Li, W., and Liu, M. (2011). Distribution of 5-Hydroxymethylcytosine in Different Human Tissues. J. Nucleic Acids *2011*, e870726.

Li, Y., and O'Neill, C. (2013). 5′-methylcytosine and 5′-hydroxymethylcytosine Each Provide Epigenetic Information to the Mouse Zygote. PLOS ONE *8*, e63689.

Li, D., Guo, B., Wu, H., Tan, L., and Lu, Q. (2015a). TET Family of Dioxygenases: Crucial Roles and Underlying Mechanisms. Cytogenet. Genome Res. *146*, 171–180.

Li, L., Chen, B.-F., and Chan, W.-Y. (2015b). An epigenetic regulator: methyl-CpG-binding domain protein 1 (MBD1). Int. J. Mol. Sci. *16*, 5125–5140.

Li, X., Liu, Y., Salz, T., Hansen, K.D., and Feinberg, A. (2016). Whole-genome analysis of the methylome and hydroxymethylome in normal and malignant lung and liver. Genome Res. *26*, 1730–1741.

Liu, F., Wang, L., Perna, F., and Nimer, S.D. (2016a). Beyond transcription factors: how oncogenic signalling reshapes the epigenetic landscape. Nat. Rev. Cancer *16*, 359–372.

Liu, X., Gao, Q., Li, P., Zhao, Q., Zhang, J., Li, J., Koseki, H., and Wong, J. (2013). UHRF1 targets DNMT1 for DNA methylation through cooperative binding of hemi-methylated DNA and methylated H3K9. Nat. Commun. *4*, 1563.

Liu, Y., Giannopoulou, E.G., Wen, D., Falciatori, I., Elemento, O., Allis, C.D., Rafii, S., and Seandel, M. (2016b). Epigenetic profiles signify cell fate plasticity in unipotent spermatogonial stem and progenitor cells. Nat. Commun. *7*, 11275.

Liutkevičiūtė, Z., Kriukienė, E., Ličytė, J., Rudytė, M., Urbanavičiūtė, G., and Klimašauskas, S. (2014). Direct Decarboxylation of 5-Carboxylcytosine by DNA C5- Methyltransferases. J. Am. Chem. Soc. *136*, 5884–5887.

Long, H.K., King, H.W., Patient, R.K., Odom, D.T., and Klose, R.J. (2016). Protection of CpG islands from DNA methylation is DNA-encoded and evolutionarily conserved. Nucleic Acids Res. gkw258.

Lorthongpanich, C., Cheow, L.F., Balu, S., Quake, S.R., Knowles, B.B., Burkholder, W.F., Solter, D., and Messerschmidt, D.M. (2013). Single-Cell DNA-Methylation Analysis Reveals Epigenetic Chimerism in Preimplantation Embryos. Science *341*, 1110–1112.

Luger, K., Dechassa, M.L., and Tremethick, D.J. (2012). New insights into nucleosome and chromatin structure: an ordered state or a disordered affair? Nat. Rev. Mol. Cell Biol. *13*, 436–447.

Luxán, G., Casanova, J.C., Martínez-Poveda, B., Prados, B., D'Amato, G., MacGrogan, D., Gonzalez-Rajal, A., Dobarro, D., Torroja, C., Martinez, F., et al. (2013). Mutations in the NOTCH pathway regulator MIB1 cause left ventricular noncompaction cardiomyopathy. Nat. Med. *19*, 193–201.

Maarel, S.M. van der (2008). Epigenetic mechanisms in health and disease. Ann. Rheum. Dis. *67*, iii97-iii100.

Maeda, S., Djukic, B., Taneja, P., Yu, G.-Q., Lo, I., Davis, A., Craft, R., Guo, W., Wang, X., Kim, D., et al. (2016). Expression of A152T human tau causes age- dependent neuronal dysfunction and loss in transgenic mice. EMBO Rep. *17*, 530–551.

Maiti, A., and Drohat, A.C. (2011). Thymine DNA Glycosylase Can Rapidly Excise 5-Formylcytosine and 5-Carboxylcytosine POTENTIAL IMPLICATIONS FOR ACTIVE DEMETHYLATION OF CpG SITES. J. Biol. Chem. *286*, 35334–35338.

Maity, B., Sheff, D., and Fisher, R.A. (2013). Immunostaining: detection of signaling protein location in tissues, cells and subcellular compartments. Methods Cell Biol. *113*, 81–105.

Malan-Müller, S., Seedat, S., and Hemmings, S.M.J. (2014). Understanding posttraumatic stress disorder: insights from the methylome. Genes Brain Behav. *13*, 52–68.

Maresca, A., Zaffagnini, M., Caporali, L., Carelli, V., and Zanna, C. (2015). Dna Methyltransferase 1 Mutations and Mitochondrial Pathology: Is Mtdna Methylated? Genet. Disord. *6*, 90.

Margueron, R., and Reinberg, D. (2010). Chromatin structure and the inheritance of epigenetic information. Nat. Rev. Genet. *11*, 285–296.

Marmorstein, R., and Zhou, M.-M. (2014). Writers and Readers of Histone Acetylation: Structure, Mechanism, and Inhibition. Cold Spring Harb. Perspect. Biol. *6*, a018762.

Maurano, M.T., Wang, H., John, S., Shafer, A., Canfield, T., Lee, K., and Stamatoyannopoulos, J.A. (2015). Role of DNA Methylation in Modulating Transcription Factor Occupancy. Cell Rep. *12*, 1184–1195.

McAllister, T.E., England, K.S., Hopkinson, R.J., Brennan, P.E., Kawamura, A., and Schofield, C.J. (2016). Recent Progress in Histone Demethylase Inhibitors. J. Med. Chem. *59*, 1308–1329.

McGinty, R.K., and Tan, S. (2015). Nucleosome Structure and Function. Chem. Rev. *115*, 2255–2273.

Meehan, R.R., Dunican, D.S., Ruzov, A., and Pennings, S. (2005). Epigenetic silencing in embryogenesis. Exp. Cell Res. *309*, 241–249.

Meloni, M. (2016). Political Biology: Science and Social Values in Human Heredity from Eugenics to Epigenetics (Springer).

Menafra, R., Brinkman, A.B., Matarese, F., Franci, G., Bartels, S.J.J., Nguyen, L., Shimbo, T., Wade, P.A., Hubner, N.C., and Stunnenberg, H.G. (2014). Genome-Wide Binding of MBD2 Reveals Strong Preference for Highly Methylated Loci. PLOS ONE *9*, e99603.

Messerschmidt, D.M., Knowles, B.B., and Solter, D. (2014). DNA methylation dynamics during epigenetic reprogramming in the germline and preimplantation embryos. Genes Dev. *28*, 812–828.

Meyer, P. (2015). Epigenetic variation and environmental change. J. Exp. Bot. *66*, 3541–3548.

Miao, Z., He, Y., Xin, N., Sun, M., Chen, L., Lin, L., Li, J., Kong, J., Jin, P., and Xu, X. (2015). Altering 5-hydroxymethylcytosine modification impacts ischemic brain injury. Hum. Mol. Genet. *24*, 5855–5866.

Migicovsky, Z., and Kovalchuk, I. (2011). Epigenetic memory in mammals. Epigenomics Epigenetics *2*, 28.

Minkovsky, A., Sahakyan, A., Rankin-Gee, E., Bonora, G., Patel, S., and Plath, K. (2014). The Mbd1-Atf7ip-Setdb1 pathway contributes to the maintenance of X chromosome inactivation. Epigenetics Chromatin *7*, 12.

Moffat, M., Reddington, J.P., Pennings, S., and Meehan, R.R. (2012). DNA Methylation in Mammalian and Non-Mammalian Organisms.

Mohammad, H.P., Cai, Y., McGarvey, K.M., Easwaran, H., Van Neste, L., Ohm, J.E., O'Hagan, H.M., and Baylin, S.B. (2009). Polycomb CBX7 promotes initiation of heritable repression of genes frequently silenced with cancer-specific DNA hypermethylation. Cancer Res. *69*, 6322–6330.

Mohan, M., Herz, H.-M., and Shilatifard, A. (2012). Snapshot: Chromatin Lysine Methylase Complexes: Transcriptional Regulation and Epigenetics. Cell *149*, 498–498.e1.

Moore, A.M., Borschel, G.H., Santosa, K.A., Flagg, E.R., Tong, A.Y., Kasukurthi, R., Newton, P., Yan, Y., Hunter, D.A., Johnson, P.J., et al. (2012). A transgenic rat expressing green fluorescent protein (GFP) in peripheral nerves provides a new hindlimb model for the study of nerve injury and regeneration. J. Neurosci. Methods *204*, 19–27.

Moore, L.D., Le, T., and Fan, G. (2013). DNA Methylation and Its Basic Function. Neuropsychopharmacology *38*, 23–38.

Morera, L., Lübbert, M., and Jung, M. (2016). Targeting histone methyltransferases and demethylases in clinical trials for cancer therapy. Clin. Epigenetics *8*, 57.

Mozzetta, C., Pontis, J., Fritsch, L., Robin, P., Portoso, M., Proux, C., Margueron, R., and Ait-Si-Ali, S. (2014). The histone H3 lysine 9 methyltransferases G9a and GLP regulate polycomb repressive complex 2-mediated gene silencing. Mol. Cell *53*, 277–289.

Mozzetta, C., Boyarchuk, E., Pontis, J., and Ait-Si-Ali, S. (2015). Sound of silence: the properties and functions of repressive Lys methyltransferases. Nat. Rev. Mol. Cell Biol. *16*, 499–513.

Munari, E., Chaux, A., Vaghasia, A.M., Taheri, D., Karram, S., Bezerra, S.M., Gonzalez Roibon, N., Nelson, W.G., Yegnasubramanian, S., Netto, G.J., et al. (2016). Global 5-Hydroxymethylcytosine Levels Are Profoundly Reduced in Multiple Genitourinary Malignancies. PloS One *11*, e0146302.

Münzel, M., Globisch, D., Brückl, T., Wagner, M., Welzmiller, V., Michalakis, S., Müller, M., Biel, M., and Carell, T. (2010). Quantification of the Sixth DNA Base Hydroxymethylcytosine in the Brain. Angew. Chem. Int. Ed. *49*, 5375–5377.

Muramatsu, D., Kimura, H., Kotoshiba, K., Tachibana, M., and Shinkai, Y. (2016). Pericentric H3K9me3 Formation by HP1 Interaction-defective Histone Methyltransferase Suv39h1. Cell Struct. Funct. *41*, 145–152.

Musselman, C.A., Khorasanizadeh, S., and Kutateladze, T.G. (2014). Towards understanding methyllysine readout. Biochim. Biophys. Acta *1839*, 686–693.

Nabel, C.S., Jia, H., Ye, Y., Shen, L., Goldschmidt, H.L., Stivers, J.T., Zhang, Y., and Kohli, R.M. (2012). AID/APOBEC deaminases disfavor modified cytosines implicated in DNA demethylation. Nat. Chem. Biol. *8*, 751–758.

Nakamura, K.C., Kameda, H., Koshimizu, Y., Yanagawa, Y., and Kaneko, T. (2008). Production and Histological Application of Affinity-purified Antibodies to Heat-denatured Green Fluorescent Protein. J. Histochem. Cytochem. *56*, 647–657.

Nakamura, R., Tsukahara, T., Qu, W., Ichikawa, K., Otsuka, T., Ogoshi, K., Saito, T.L., Matsushima, K., Sugano, S., Hashimoto, S., et al. (2014). Large hypomethylated domains serve as strong repressive machinery for key developmental genes in vertebrates. Dev. Camb. Engl. *141*, 2568–2580.

Neri, F., Incarnato, D., and Oliviero, S. (2015). DNA methylation and demethylation dynamics. Oncotarget *6*, 34049–34050.

Nestor, C.E., Ottaviano, R., Reddington, J., Sproul, D., Reinhardt, D., Dunican, D., Katz, E., Dixon, J.M., Harrison, D.J., and Meehan, R.R. (2012). Tissue type is a major modifier of the 5-hydroxymethylcytosine content of human genes. Genome Res. *22*, 467–477.

Nestor, C.E., Ottaviano, R., Reinhardt, D., Cruickshanks, H.A., Mjoseng, H.K., McPherson, R.C., Lentini, A., Thomson, J.P., Dunican, D.S., Pennings, S., et al. (2015). Rapid reprogramming of epigenetic and transcriptional profiles in mammalian culture systems. Genome Biol. *16*, 11.

Nightingale, K.P. (2015). CHAPTER 1:Epigenetics – What it is and Why it Matters. In CHAPTER 1:Epigenetics – What It Is and Why It Matters, pp. 1–19.

Noble, D. (2015). Conrad Waddington and the origin of epigenetics. J. Exp. Biol. *218*, 816–818.

Nowak, R.P., Tumber, A., Johansson, C., Che, K.H., Brennan, P., Owen, D., and Oppermann, U. (2016). Advances and challenges in understanding histone demethylase biology. Curr. Opin. Chem. Biol. *33*, 151–159.

O’Connell, T.X., Pedigo, R.A., and Blair, T.E. (2013). Crush Step 1 E-Book: The Ultimate USMLE Step 1 Review (Elsevier Health Sciences).

Odell, I.D., and Cook, D. (2013). Immunofluorescence Techniques. J. Invest. Dermatol. *133*, 1–4.

Pástor, M.V.D. (2010). Direct immunofluorescent labeling of cells. Methods Mol. Biol. Clifton NJ *588*, 135–142.

Pastor, W.A., Pape, U.J., Huang, Y., Henderson, H.R., Lister, R., Ko, M., McLoughlin, E.M., Brudno, Y., Mahapatra, S., Kapranov, P., et al. (2011). Genome-wide mapping of 5-hydroxymethylcytosine in embryonic stem cells. Nature *473*, 394–397.

Pastor, W.A., Aravind, L., and Rao, A. (2013). TETonic shift: biological roles of TET proteins in DNA demethylation and transcription. Nat. Rev. Mol. Cell Biol. *14*, 341–356.

Pastore, C. (2017). DNA Nanotechnology: A nucleosome clamp. Nat. Nanotechnol. *12*, 4–4.

Patel, D.J. (2016). A Structural Perspective on Readout of Epigenetic Histone and DNA Methylation Marks. Cold Spring Harb. Perspect. Biol. *8*, a018754.

Patel, M., and Yang, S. (2010). Advances in Reprogramming Somatic Cells to Induced Pluripotent Stem Cells. Stem Cell Rev. *6*, 367–380.

Penn, N.W., Suwalski, R., O'Riley, C., Bojanowski, K., and Yura, R. (1972). The presence of 5-hydroxymethylcytosine in animal deoxyribonucleic acid. Biochem. J. *126*, 781–790.

Pennings, S., Allan, J., and Davey, C.S. (2005). DNA methylation, nucleosome formation and positioning. Brief. Funct. Genomic. Proteomic. *3*, 351–361.

Pepenella, S., Murphy, K.J., and Hayes, J.J. (2014). Intra- and inter-nucleosome interactions of the core histone tail domains in higher-order chromatin structure. Chromosoma *123*, 3–13.

Pereira, J.D., Sansom, S.N., Smith, J., Dobenecker, M.-W., Tarakhovsky, A., and Livesey, F.J. (2010). Ezh2, the histone methyltransferase of PRC2, regulates the balance between self-renewal and differentiation in the cerebral cortex. Proc. Natl. Acad. Sci. U. S. A. *107*, 15957–15962.

Peters, J. (2014). The role of genomic imprinting in biology and disease: an expanding view. Nat. Rev. Genet. *15*, 517–530.

Pfeifer, G.P., Kadam, S., and Jin, S.-G. (2013). 5-hydroxymethylcytosine and its potential roles in development and cancer. Epigenetics Chromatin *6*, 10.

Piyathilake, C.J., Niveleau, A., and Grizzle, W. (2004). Role of Global Methylation of DNA in Lung Carcinoma. In Handbook of Immunohistochemistry and in Situ Hybridization of Human Carcinomas, pp. 181–187.

Popp, C., Dean, W., Feng, S., Cokus, S.J., Andrews, S., Pellegrini, M., Jacobsen, S.E., and Reik, W. (2010). Genome-wide erasure of DNA methylation in mouse primordial germ cells is affected by Aid deficiency. Nature *463*, 1101–1105.

Portela, A., and Esteller, M. (2010). Epigenetic modifications and human disease. Nat. Biotechnol. *28*, 1057–1068.

Potok, M.E., Nix, D.A., Parnell, T.J., and Cairns, B.R. (2013). Reprogramming the maternal zebrafish genome after fertilization to match the paternal methylation pattern. Cell *153*, 759–772.

Probst, A.V., Dunleavy, E., and Almouzni, G. (2009). Epigenetic inheritance during the cell cycle. Nat. Rev. Mol. Cell Biol. *10*, 192–206.

Prokopuk, L., Stringer, J.M., Hogg, K., Elgass, K.D., and Western, P.S. (2017). PRC2 is required for extensive reorganization of H3K27me3 during epigenetic reprogramming in mouse fetal germ cells. Epigenetics Chromatin *10*, 7.

Pueschel, R., Coraggio, F., and Meister, P. (2016). From single genes to entire genomes: the search for a function of nuclear organization. Development *143*, 910–923.

Putiri, E.L., and Robertson, K.D. (2010). Epigenetic mechanisms and genome stability. Clin. Epigenetics *2*, 299–314.

Rajagopal, J., and Stanger, B.Z. (2016). Plasticity in the Adult: How Should the Waddington Diagram Be Applied to Regenerating Tissues? Dev. Cell *36*, 133–137.

Rao P, P., and Kumar D, R. (2016). Recent understanding of ectodermal dysplasia. Int. J. Adv. Res. *4*, 703–707.

Reddington, J.P., Pennings, S., and Meehan, R.R. (2013a). Non-canonical functions of the DNA methylome in gene regulation. Biochem. J. *451*, 13–23.

Reddington, J.P., Perricone, S.M., Nestor, C.E., Reichmann, J., Youngson, N.A., Suzuki, M., Reinhardt, D., Dunican, D.S., Prendergast, J.G., Mjoseng, H., et al. (2013b). Redistribution of H3K27me3 upon DNA hypomethylation results in de-repression of Polycomb target genes. Genome Biol. *14*, R25.

Reddington, J.P., Sproul, D., and Meehan, R.R. (2014). DNA methylation reprogramming in cancer: does it act by re-configuring the binding landscape of Polycomb repressive complexes? BioEssays News Rev. Mol. Cell. Dev. Biol. *36*, 134–140.

Rhie, S.K., Hazelett, D.J., Coetzee, S.G., Yan, C., Noushmehr, H., and Coetzee, G.A. (2014). Nucleosome positioning and histone modifications define relationships between regulatory elements and nearby gene expression in breast epithelial cells. BMC Genomics *15*, 331.

Ridzuan, M.A.M., Moon, R.W., Knuepfer, E., Black, S., Holder, A.A., and Green, J.L. (2012). Subcellular Location, Phosphorylation and Assembly into the Motor Complex of GAP45 during Plasmodium falciparum Schizont Development. PLOS ONE *7*, e33845.

Rivera, C., Gurard-Levin, Z.A., Almouzni, G., and Loyola, A. (2014). Histone lysine methylation and chromatin replication. Biochim. Biophys. Acta BBA - Gene Regul. Mech. *1839*, 1433–1439.

Rodríguez-Paredes, M., and Esteller, M. (2011). Cancer epigenetics reaches mainstream oncology. Nat. Med. 330–339.

Rongvaux, A., Willinger, T., Martinek, J., Strowig, T., Gearty, S.V., Teichmann, L.L., Saito, Y., Marches, F., Halene, S., Palucka, A.K., et al. (2014). Development and function of human innate immune cells in a humanized mouse model. Nat. Biotechnol. *32*, 364–372.

Rose, N.R., and Klose, R.J. (2014). Understanding the relationship between DNA methylation and histone lysine methylation. Biochim. Biophys. Acta BBA - Gene Regul. Mech. *1839*, 1362–1372.

Rose, C.M., Driesche, S. van den, Meehan, R.R., and Drake, A.J. (2013). Epigenetic reprogramming: preparing the epigenome for the next generation. Biochem. Soc. Trans. *41*, 809–814.

Rose, C.M., van den Driesche, S., Sharpe, R.M., Meehan, R.R., and Drake, A.J. (2014). Dynamic changes in DNA modification states during late gestation male germ line development in the rat. Epigenetics Chromatin *7*, 19.

Rothbart, S.B., and Strahl, B.D. (2014). Interpreting the language of histone and DNA modifications. Biochim. Biophys. Acta BBA - Gene Regul. Mech. *1839*, 627–643.

Rothbauer, U., Zolghadr, K., Tillib, S., Nowak, D., Schermelleh, L., Gahl, A., Backmann, N., Conrath, K., Muyldermans, S., Cardoso, M.C., et al. (2006). Targeting and tracing antigens in live cells with fluorescent nanobodies. Nat. Methods *3*, 887–889.

Roundtree, I.A., and He, C. (2016). RNA epigenetics — chemical messages for posttranscriptional gene regulation. Curr. Opin. Chem. Biol. *30*, 46–51.

Ruzov, A., Tsenkina, Y., Serio, A., Dudnakova, T., Fletcher, J., Bai, Y., Chebotareva, T., Pells, S., Hannoun, Z., Sullivan, G., et al. (2011). Lineage-specific distribution of high levels of genomic 5-hydroxymethylcytosine in mammalian development. Cell Res. *21*, 1332–1342.

Saadeh, H., and Schulz, R. (2014). Protection of CpG islands against de novo DNA methylation during oogenesis is associated with the recognition site of E2f1 and E2f2. Epigenetics Chromatin *7*, 26.

Sabbattini, P., Sjoberg, M., Nikic, S., Frangini, A., Holmqvist, P.-H., Kunowska, N., Carroll, T., Brookes, E., Arthur, S.J., Pombo, A., et al. (2014). An H3K9/S10 methyl-phospho switch modulates Polycomb and Pol II binding at repressed genes during differentiation. Mol. Biol. Cell *25*, 904–915.

Sadelain, M., Papapetrou, E.P., and Bushman, F.D. (2012). Safe harbours for the integration of new DNA in the human genome. Nat. Rev. Cancer *12*, 51–58.

Saitou, M., Kagiwada, S., and Kurimoto, K. (2012). Epigenetic reprogramming in mouse pre-implantation development and primordial germ cells. Development *139*, 15–31.

Saksouk, N., Barth, T.K., Ziegler-Birling, C., Olova, N., Nowak, A., Rey, E., Mateos-Langerak, J., Urbach, S., Reik, W., Torres-Padilla, M.-E., et al. (2014). Redundant Mechanisms to Form Silent Chromatin at Pericentromeric Regions Rely on BEND3 and DNA Methylation. Mol. Cell *56*, 580–594.

Saksouk, N., Simboeck, E., and Déjardin, J. (2015). Constitutive heterochromatin formation and transcription in mammals. Epigenetics Chromatin *8*, 3.

Salvaing, J., Aguirre-Lavin, T., Boulesteix, C., Lehmann, G., Debey, P., and Beaujean, N. (2012). 5-Methylcytosine and 5-Hydroxymethylcytosine Spatiotemporal Profiles in the Mouse Zygote. PLOS ONE *7*, e38156.

Santos, F., and Dean, W. (2006). Using immunofluorescence to observe methylation changes in mammalian preimplantation embryos. Methods Mol. Biol. Clifton NJ *325*, 129–137.

Sarraf, S.A., and Stancheva, I. (2004). Methyl-CpG binding protein MBD1 couples histone H3 methylation at lysine 9 by SETDB1 to DNA replication and chromatin assembly. Mol. Cell *15*, 595–605.

Saxonov, S., Berg, P., and Brutlag, D.L. (2006). A genome-wide analysis of CpG dinucleotides in the human genome distinguishes two distinct classes of promoters. Proc. Natl. Acad. Sci. *103*, 1412–1417.

Scharfenberger, L., Hennerici, T., Király, G., Kitzmüller, S., Vernooij, M., and Zielinski, J.G. (2014). Transgenic Mouse Technology in Skin Biology: Generation of Complete or Tissue-Specific Knockout Mice. J. Invest. Dermatol. *134*, 1–5.

Schiesser, S., Hackner, B., Pfaffeneder, T., Müller, M., Hagemeier, C., Truss, M., and Carell, T. (2012). Mechanism and Stem-Cell Activity of 5-Carboxycytosine Decarboxylation Determined by Isotope Tracing. Angew. Chem. Int. Ed. *51*, 6516–6520.

Schneider, C.A., Rasband, W.S., and Eliceiri, K.W. (2012). NIH Image to ImageJ: 25 years of image analysis. Nat. Methods *9*, 671–675.

Schübeler, D. (2015). Function and information content of DNA methylation. Nature *517*, 321–326.

Schuettengruber, B., Martinez, A.-M., Iovino, N., and Cavalli, G. (2011). Trithorax group proteins: switching genes on and keeping them active. Nat. Rev. Mol. Cell Biol. *12*, 799–814.

Schwämmle, V., Aspalter, C.-M., Sidoli, S., and Jensen, O.N. (2014). Large Scale Analysis of Co-existing Post-translational Modifications in Histone Tails Reveals Global Fine Structure of Cross-talk. Mol. Cell. Proteomics *13*, 1855–1865.

Schwämmle, V., Sidoli, S., Ruminowicz, C., Wu, X., Lee, C.-F., Helin, K., and Jensen, O.N. (2016). Systems level analysis of histone H3 post-translational modifications reveals features of PTM crosstalk in chromatin regulation. Mol. Cell. Proteomics mcp.M115.054460.

Seisenberger, S., Peat, J.R., Hore, T.A., Santos, F., Dean, W., and Reik, W. (2013a). Reprogramming DNA methylation in the mammalian life cycle: building and breaking epigenetic barriers. Philos. Trans. R. Soc. B Biol. Sci. *368*.

Seisenberger, S., Peat, J.R., and Reik, W. (2013b). Conceptual links between DNA methylation reprogramming in the early embryo and primordial germ cells. Curr. Opin. Cell Biol. *25*, 281–288.

Seto, E., and Yoshida, M. (2014). Erasers of Histone Acetylation: The Histone Deacetylase Enzymes. Cold Spring Harb. Perspect. Biol. *6*, a018713.

Shi, Z., and Stack, Ms. (2015). An Update on Immunohistochemistry in Translational Cancer Research. Cancer Transl. Med. *1*, 115.

Shi, W., Dirim, F., Wolf, E., Zakhartchenko, V., and Haaf, T. (2004a). Methylation reprogramming and chromosomal aneuploidy in in vivo fertilized and cloned rabbit preimplantation embryos. Biol. Reprod. *71*, 340–347.

Shi, Y., Lan, F., Matson, C., Mulligan, P., Whetstine, J.R., Cole, P.A., Casero, R.A., and Shi, Y. (2004b). Histone Demethylation Mediated by the Nuclear Amine Oxidase Homolog LSD1. Cell *119*, 941–953.

Shukla, A., Sehgal, M., and Singh, T.R. (2015). Hydroxymethylation and its potential implication in DNA repair system: A review and future perspectives. Gene *564*, 109–118.

Simon, M., North, J.A., Shimko, J.C., Forties, R.A., Ferdinand, M.B., Manohar, M., Zhang, M., Fishel, R., Ottesen, J.J., and Poirier, M.G. (2011). Histone fold modifications control nucleosome unwrapping and disassembly. Proc. Natl. Acad. Sci. *108*, 12711–12716.

Smith, Z.D., and Meissner, A. (2013). DNA methylation: roles in mammalian development. Nat. Rev. Genet. *14*, 204–220.

Song, C.-X., Szulwach, K.E., Fu, Y., Dai, Q., Yi, C., Li, X., Li, Y., Chen, C.-H., Zhang, W., Jian, X., et al. (2011). Selective chemical labeling reveals the genome-wide distribution of 5-hydroxymethylcytosine. Nat. Biotechnol. *29*, 68–72.

Song, Y., Wu, F., and Wu, J. (2016). Targeting histone methylation for cancer therapy: enzymes, inhibitors, biological activity and perspectives. J. Hematol. Oncol.J Hematol Oncol *9*, 49.

Sormani, G., Haerter, J.O., Lövkvist, C., and Sneppen, K. (2016). Stabilization of epigenetic states of CpG islands by local cooperation. Mol. Biosyst. *12*, 2142–2146.

Soshnev, A.A., Josefowicz, S.Z., and Allis, C.D. (2016). Greater Than the Sum of Parts: Complexity of the Dynamic Epigenome. Mol. Cell *62*, 681–694.

Sproul, D., and Meehan, R.R. (2013). Genomic insights into cancer-associated aberrant CpG island hypermethylation. Brief. Funct. Genomics *12*, 174–190.

Stewart, K.R., Veselovska, L., and Kelsey, G. (2016). Establishment and functions of DNA methylation in the germline. Epigenomics *8*, 1399–1413.

Stewart, S.K., Morris, T.J., Guilhamon, P., Bulstrode, H., Bachman, M., Balasubramanian, S., and Beck, S. (2015). oxBS-450K: A method for analysing hydroxymethylation using 450K BeadChips. Methods *72*, 9–15.

Strahl, B.D., and Allis, C.D. (2000). The language of covalent histone modifications. Nature *403*, 41–45.

Stringer, J.M., Barrand, S., and Western, P. (2013). Fine-tuning evolution: germ-line epigenetics and inheritance. Reproduction *146*, R37–R48.

Sun, H., Kennedy, P.J., and Nestler, E.J. (2013). Epigenetics of the Depressed Brain: Role of Histone Acetylation and Methylation. Neuropsychopharmacology *38*, 124–137.

Sun, W., Zang, L., Shu, Q., and Li, X. (2014). From development to diseases: The role of 5hmC in brain. Genomics *104*, 347–351.

Surani, M.A. (2015). Human Germline: A New Research Frontier. Stem Cell Rep. *4*, 955–960.

Suzuki, T., and Miyata, N. (2011). Lysine demethylases inhibitors. J. Med. Chem. *54*, 8236–8250.

Swenson, E.S., Price, J.G., Brazelton, T., and Krause, D.S. (2007). Limitations of Green Fluorescent Protein as a Cell Lineage Marker. STEM CELLS *25*, 2593–2600.

Szymanska, M., Fosdahl, A.M., Raiborg, C., Dietrich, M., Liestøl, K., Stang, E., and Bertelsen, V. (2016). Interaction with epsin 1 regulates the constitutive clathrin-dependent internalization of ErbB3. Biochim. Biophys. Acta BBA - Mol. Cell Res. *1863*, 1179–1188.

Tahiliani, M., Koh, K.P., Shen, Y., Pastor, W.A., Bandukwala, H., Brudno, Y., Agarwal, S., Iyer, L.M., Liu, D.R., Aravind, L., et al. (2009). Conversion of 5-Methylcytosine to 5-Hydroxymethylcytosine in Mammalian DNA by MLL Partner TET1. Science *324*, 930–935.

Takagi, C., Sakamaki, K., Morita, H., Hara, Y., Suzuki, M., Kinoshita, N., and Ueno, N. (2013). Transgenic Xenopus laevis for live imaging in cell and developmental biology. Dev. Growth Differ. *55*, 422–433.

Takahashi, K., and Yamanaka, S. (2006). Induction of Pluripotent Stem Cells from Mouse Embryonic and Adult Fibroblast Cultures by Defined Factors. Cell *126*, 663–676.

Takahashi, K., and Yamanaka, S. (2013). Induced pluripotent stem cells in medicine and biology. Development *140*, 2457–2461.

Takahashi, K., and Yamanaka, S. (2016). A decade of transcription factor-mediated reprogramming to pluripotency. Nat. Rev. Mol. Cell Biol. *17*, 183–193.

Tamaru, H. (2010). Confining euchromatin/heterochromatin territory: jumonji crosses the line. Genes Dev. *24*, 1465–1478.

Tamaru, H., and Selker, E.U. (2001). A histone H3 methyltransferase controls DNA methylation in Neurospora crassa. Nature *414*, 277–283.

Tammen, S.A., Friso, S., and Choi, S.-W. (2013). Epigenetics: the link between nature and nurture. Mol. Aspects Med. *34*, 753–764.

Tan, L., and Shi, Y.G. (2012). Tet family proteins and 5-hydroxymethylcytosine in development and disease. Dev. Camb. Engl. *139*, 1895–1902.

Tang, W.W.C., Kobayashi, T., Irie, N., Dietmann, S., and Surani, M.A. (2016). Specification and epigenetic programming of the human germ line. Nat. Rev. Genet. *17*, 585–600.

Taylor, G.C.A., Eskeland, R., Hekimoglu-Balkan, B., Pradeepa, M.M., and Bickmore, W.A. (2013). H4K16 acetylation marks active genes and enhancers of embryonic stem cells, but does not alter chromatin compaction. Genome Res. *23*, 2053–2065.

Teif, V.B., Vainshtein, Y., Caudron-Herger, M., Mallm, J.-P., Marth, C., Höfer, T., and Rippe, K. (2012). Genome-wide nucleosome positioning during embryonic stem cell development. Nat. Struct. Mol. Biol. *19*, 1185–1192.

Teif, V.B., Beshnova, D.A., Vainshtein, Y., Marth, C., Mallm, J.-P., Höfer, T., and Rippe, K. (2014). Nucleosome repositioning links DNA (de)methylation and differential CTCF binding during stem cell development. Genome Res. *24*, 1285–1295.

Tessarz, P., and Kouzarides, T. (2014). Histone core modifications regulating nucleosome structure and dynamics. Nat. Rev. Mol. Cell Biol. *15*, 703–708.

Therizols, P., Illingworth, R.S., Courilleau, C., Boyle, S., Wood, A.J., and Bickmore, W.A. (2014). Chromatin decondensation is sufficient to alter nuclear organization in embryonic stem cells. Science *346*, 1238–1242.

Thienpont, B., Steinbacher, J., Zhao, H., D'Anna, F., Kuchnio, A., Ploumakis, A., Ghesquière, B., Van Dyck, L., Boeckx, B., Schoonjans, L., et al. (2016). Tumour hypoxia causes DNA hypermethylation by reducing TET activity. Nature *537*, 63–68.

Thinnes, C.C., England, K.S., Kawamura, A., Chowdhury, R., Schofield, C.J., and Hopkinson, R.J. (2014). Targeting histone lysine demethylases — Progress, challenges, and the future. Biochim. Biophys. Acta BBA - Gene Regul. Mech. *1839*, 1416–1432.

Thomson, J.P., Skene, P.J., Selfridge, J., Clouaire, T., Guy, J., Webb, S., Kerr, A.R.W., Deaton, A., Andrews, R., James, K.D., et al. (2010). CpG islands influence chromatin structure via the CpG-binding protein Cfp1. Nature *464*, 1082–1086.

Thomson, J.P., Ottaviano, R., Unterberger, E.B., Lempiäinen, H., Muller, A., Terranova, R., Illingworth, R.S., Webb, S., Kerr, A.R.W., Lyall, M.J., et al. (2016). Loss of Tet1-Associated 5-Hydroxymethylcytosine Is Concomitant with Aberrant Promoter Hypermethylation in Liver Cancer. Cancer Res. *76*, 3097–3108.

Tian, Z., Tolić, N., Zhao, R., Moore, R.J., Hengel, S.M., Robinson, E.W., Stenoien, D.L., Wu, S., Smith, R.D., and Paša-Tolić, L. (2012). Enhanced top-down characterization of histone post-translational modifications. Genome Biol. *13*, R86.

Tomizawa, S., and Sasaki, H. (2012). Genomic imprinting and its relevance to congenital disease, infertility, molar pregnancy and induced pluripotent stem cell. J. Hum. Genet. *57*, 84–91.

Triantaphyllopoulos, K.A., Ikonomopoulos, I., and Bannister, A.J. (2016). Epigenetics and inheritance of phenotype variation in livestock. Epigenetics Chromatin *9*, 31.

Trojer, P., and Reinberg, D. (2007). Facultative Heterochromatin: Is There a Distinctive Molecular Signature? Mol. Cell *28*, 1–13.

Tsukada, Y., Fang, J., Erdjument-Bromage, H., Warren, M.E., Borchers, C.H., Tempst, P., and Zhang, Y. (2006). Histone demethylation by a family of JmjC domain-containing proteins. Nature *439*, 811–816.

Turner, B.M. (2000). Histone acetylation and an epigenetic code. BioEssays *22*, 836–845.

Ueda, J., Maehara, K., Mashiko, D., Ichinose, T., Yao, T., Hori, M., Sato, Y., Kimura, H., Ohkawa, Y., and Yamagata, K. (2014). Heterochromatin dynamics during the differentiation process revealed by the DNA methylation reporter mouse, MethylRO. Stem Cell Rep. *2*, 910–924.

Vacaru, A.M., Vitale, J., Nieves, J., and Baron, M.H. (2014). Generation of Transgenic Mouse Fluorescent Reporter Lines for Studying Hematopoietic Development. Methods Mol. Biol. Clifton NJ *1194*, 289–312.

Vaissière, T., Sawan, C., and Herceg, Z. (2008). Epigenetic interplay between histone modifications and DNA methylation in gene silencing. Mutat. Res. *659*, 40–48.

Vallot, C., Ouimette, J.-F., and Rougeulle, C. (2016). Establishment of X chromosome inactivation and epigenomic features of the inactive X depend on cellular contexts. BioEssays News Rev. Mol. Cell. Dev. Biol.

Vela, D., and Buja, L.M. (2016). Pathological Assessment of Experimental Models of Stem Cell and Other Regenerative Therapies. In Stem Cell and Gene Therapy for Cardiovascular Disease, (Academic Press), pp. 13–23.

Verdin, E., and Ott, M. (2015). 50 years of protein acetylation: from gene regulation to epigenetics, metabolism and beyond. Nat. Rev. Mol. Cell Biol. *16*, 258–264.

Vinod, K.R., Jones, D., and Udupa, V. (2016). A simple and effective heat induced antigen retrieval method. MethodsX *3*, 315–319.

Viré, E., Brenner, C., Deplus, R., Blanchon, L., Fraga, M., Didelot, C., Morey, L., Van Eynde, A., Bernard, D., Vanderwinden, J.-M., et al. (2006). The Polycomb group protein EZH2 directly controls DNA methylation. Nature *439*, 871–874.

Vollert, C.T., Moree, W.J., Gregory, S., Bark, S.J., and Eriksen, J.L. (2015). Formaldehyde scavengers function as novel antigen retrieval agents. Sci. Rep. *5*, 17322.

Waddington, C.H. (1942). The epigenotype. Endeavour *1*, 18.

Waddington, C.H. (1957). The Strategy of the Genes; a Discussion of Some Aspects of Theoretical Biology (London: Allen & Unwin).

Wagner, M., Steinbacher, J., Kraus, T.F.J., Michalakis, S., Hackner, B., Pfaffeneder, T., Perera, A., Müller, M., Giese, A., Kretzschmar, H.A., et al. (2015). Age-Dependent Levels of 5-Methyl-, 5-Hydroxymethyl-, and 5-Formylcytosine in Human and Mouse Brain Tissues. Angew. Chem. Int. Ed. *54*, 12511–12514.

Wagner, T., Robaa, D., Sippl, W., and Jung, M. (2014). Mind the methyl: methyllysine binding proteins in epigenetic regulation. ChemMedChem *9*, 466–483.

Walker, D.M., and Gore, A.C. (2011). Transgenerational neuroendocrine disruption of reproduction. Nat. Rev. Endocrinol. *7*, 197–207.

Wang, C.-Z., and Zhu, B. (2015). You are never alone: crosstalk among epigenetic players. Sci. Bull. *60*, 899–904.

Wang, H., and Matise, M. (2013). Immunofluorescence Staining with Frozen Mouse or Chick Embryonic Tissue Sections. In Neural Development, R. Zhou, and L. Mei, eds. (Humana Press), pp. 175–188.

Wang, F., Yang, Y., Lin, X., Wang, J.-Q., Wu, Y.-S., Xie, W., Wang, D., Zhu, S., Liao, Y.-Q., Sun, Q., et al. (2013). Genome-wide loss of 5-hmC is a novel epigenetic feature of Huntington’s disease. Hum. Mol. Genet. *22*, 3641–3653.

Wang, J., Lawry, S.T., Cohen, A.L., and Jia, S. (2014). Chromosome boundary elements and regulation of heterochromatin spreading. Cell. Mol. Life Sci. CMLS *71*, 4841–4852.

Weber, A.R., Krawczyk, C., Robertson, A.B., Kuśnierczyk, A., Vågbø, C.B., Schuermann, D., Klungland, A., and Schär, P. (2016). Biochemical reconstitution of TET1–TDG–BER-dependent active DNA demethylation reveals a highly coordinated mechanism. Nat. Commun. *7*.

Wen, L., Li, X., Yan, L., Tan, Y., Li, R., Zhao, Y., Wang, Y., Xie, J., Zhang, Y., Song, C., et al. (2014). Whole-genome analysis of 5-hydroxymethylcytosine and 5-methylcytosine at base resolution in the human brain. Genome Biol. *15*, R49.

Wenger, R.H., Kurtcuoglu, V., Scholz, C.C., Marti, H.H., and Hoogewijs, D. (2015). Frequently asked questions in hypoxia research. Hypoxia *3*, 35–43.

Westhorpe, F.G., and Straight, A.F. (2015). The Centromere: Epigenetic Control of Chromosome Segregation during Mitosis. Cold Spring Harb. Perspect. Biol. *7*, a015818.

Whitelaw, E. (2015). Disputing Lamarckian epigenetic inheritance in mammals. Genome Biol. *16*.

Wight, A., Yang, D., Ioshikhes, I., and Makrigiannis, A.P. (2016). Nucleosome Presence at AML-1 Binding Sites Inversely Correlates with Ly49 Expression: Revelations from an Informatics Analysis of Nucleosomes and Immune Cell Transcription Factors. PLOS Comput Biol *12*, e1004894.

Wijst, M.G.P. van der, Venkiteswaran, M., Chen, H., Xu, G.-L., Plösch, T., and Rots, M.G. (2015). Local chromatin microenvironment determines DNMT activity: from DNA methyltransferase to DNA demethylase or DNA dehydroxymethylase. Epigenetics *10*, 671–676.

Williamson, I., Eskeland, R., Lettice, L.A., Hill, A.E., Boyle, S., Grimes, G.R., Hill, R.E., and Bickmore, W.A. (2012). Anterior-posterior differences in HoxD chromatin topology in limb development. Dev. Camb. Engl. *139*, 3157–3167.

Winter, S., and Fischle, W. (2010). Epigenetic markers and their cross-talk. Essays Biochem. *48*, 45–61.

Wong, M.D., Eede, M.C. van, Spring, S., Jevtic, S., Boughner, J.C., Lerch, J.P., and Henkelman, R.M. (2015). 4D atlas of the mouse embryo for precise morphological staging. Development *142*, 3583–3591.

Wright, R., and Saul, R.A. (2013). Epigenetics and Primary Care. Pediatrics *132*, S216–S223.

Wu, H., and Zhang, Y. (2011). Mechanisms and functions of Tet protein-mediated 5-methylcytosine oxidation. Genes Dev. *25*, 2436–2452.

Wu, H., and Zhang, Y. (2014). Reversing DNA Methylation: Mechanisms, Genomics, and Biological Functions. Cell *156*, 45–68.

Wu, H., and Zhang, Y. (2015). Charting oxidized methylcytosines at base resolution. Nat. Struct. Mol. Biol. *22*, 656–661.

Wu, S.C., and Zhang, Y. (2010). Active DNA demethylation: many roads lead to Rome. Nat. Rev. Mol. Cell Biol. *11*, 607–620.

Wyatt, G.R., and Cohen, S.S. (1952). A new pyrimidine base from bacteriophage nucleic acids. Nature *170*, 1072–1073.

Xu, S., Li, W., Zhu, J., Wang, R., Li, Z., Xu, G.-L., and Ding, J. (2013). Crystal structures of isoorotate decarboxylases reveal a novel catalytic mechanism of 5-carboxyl-uracil decarboxylation and shed light on the search for DNA decarboxylase. Cell Res. *23*, 1296–1309.

Yamagata, K., Yamazaki, T., Miki, H., Ogonuki, N., Inoue, K., Ogura, A., and Baba, T. (2007). Centromeric DNA hypomethylation as an epigenetic signature discriminates between germ and somatic cell lineages. Dev. Biol. *312*, 419–426.

Yamaguchi, S., Hong, K., Liu, R., Inoue, A., Shen, L., Zhang, K., and Zhang, Y. (2013). Dynamics of 5-methylcytosine and 5-hydroxymethylcytosine during germ cell reprogramming. Cell Res. *23*, 329–339.

Yamazaki, T., Yamagata, K., and Baba, T. (2007). Time-lapse and retrospective analysis of DNA methylation in mouse preimplantation embryos by live cell imaging. Dev. Biol. *304*, 409–419.

Yan, H., Zhang, D., Liu, H., Wei, Y., Lv, J., Wang, F., Zhang, C., Wu, Q., Su, J., and Zhang, Y. (2015). Chromatin modifications and genomic contexts linked to dynamic DNA methylation patterns across human cell types. Sci. Rep. *5*, 8410.

Yang, H., Liu, Y., Bai, F., Zhang, J.-Y., Ma, S.-H., Liu, J., Xu, Z.-D., Zhu, H.-G., Ling, Z.-Q., Ye, D., et al. (2013). Tumor development is associated with decrease of TET gene expression and 5-methylcytosine hydroxylation. Oncogene *32*, 663–669.

Yang, Z., Jiang, W., Liu, F., Zhou, Y., Yin, H., and Ai, S. (2015). A novel electrochemical immunosensor for the quantitative detection of 5-hydroxymethylcytosine in genomic DNA of breast cancer tissue. Chem. Commun. Camb. Engl. *51*, 14671–14673.

Yao, B., Lin, L., Street, R.C., Zalewski, Z.A., Galloway, J.N., Wu, H., Nelson, D.L., and Jin, P. (2014). Genome-wide alteration of 5-hydroxymethylcytosine in a mouse model of fragile X-associated tremor/ataxia syndrome. Hum. Mol. Genet. *23*, 1095–1107.

Yao, B., Christian, K.M., He, C., Jin, P., Ming, G., and Song, H. (2016). Epigenetic mechanisms in neurogenesis. Nat. Rev. Neurosci. *advance online publication*.

Yoo, Y., Park, J.H., Weigel, C., Liesenfeld, D.B., Weichenhan, D., Plass, C., Seo, D.-G., Lindroth, A.M., and Park, Y.J. (2017). TET-mediated hydroxymethylcytosine at the Pparγ locus is required for initiation of adipogenic differentiation. Int. J. Obes.

Zhang, F., Liu, Y., Zhang, Z., Li, J., Wan, Y., Zhang, L., Wang, Y., Li, X., Xu, Y., Fu, X., et al. (2016a). 5-hydroxymethylcytosine loss is associated with poor prognosis for patients with WHO grade II diffuse astrocytomas. Sci. Rep. *6*, 20882.

Zhang, P., Su, L., Wang, Z., Zhang, S., Guan, J., Chen, Y., Yin, Y., Gao, F., Tang, B., and Li, Z. (2012a). The Involvement of 5-Hydroxymethylcytosine in Active DNA Demethylation in Mice. Biol. Reprod. *86*.

Zhang, T., Cooper, S., and Brockdorff, N. (2015). The interplay of histone modifications - writers that read. EMBO Rep. *16*, 1467–1481.

Zhang, X., Wen, H., and Shi, X. (2012b). Lysine methylation: beyond histones. Acta Biochim. Biophys. Sin. *44*, 14–27.

Zhang, Y.-Y., Huang, S.-H., Zhou, H.-R., Chen, C.-J., Tian, L.-H., and Shen, J.-Z. (2016b). Role of HOTAIR in the diagnosis and prognosis of acute leukemia. Oncol. Rep. *36*, 3113–3122.

Zhao, Q., Zhang, J., Chen, R., Wang, L., Li, B., Cheng, H., Duan, X., Zhu, H., Wei, W., Li, J., et al. (2016). Dissecting the precise role of H3K9 methylation in crosstalk with DNA maintenance methylation in mammals. Nat. Commun. *7*, 12464.

Zheng, T., Lv, Q., Lei, X., Yin, X., and Zhang, B. (2015). Spatial Distribution of 5-Hydroxymethyl Cytosine in Rat Brain and Temporal Distribution in Striatum. Neurochem. Res. *40*, 688–697.

Zhong, X., Wang, Q.-Q., Li, J.-W., Zhang, Y.-M., An, X.-R., and Hou, J. (2017). Ten-Eleven Translocation-2 (Tet2) Is Involved in Myogenic Differentiation of Skeletal Myoblast Cells in Vitro. Sci. Rep. *7*.

Zhou, F.C., Resendiz, M., Lo, C.-L., and Chen, Y. (2016). Cell-Wide DNA De-Methylation and Re-Methylation of Purkinje Neurons in the Developing Cerebellum. PLOS ONE *11*, e0162063.

Zhou, V.W., Goren, A., and Bernstein, B.E. (2011). Charting histone modifications and the functional organization of mammalian genomes. Nat. Rev. Genet. *12*, 7–18.

Zhu, J., He, F., Hu, S., and Yu, J. (2008). On the nature of human housekeeping genes. Trends Genet. *24*, 481–484.